

# New methods for the $\gamma$ -ray spectroscopy with position-sensitive detector systems

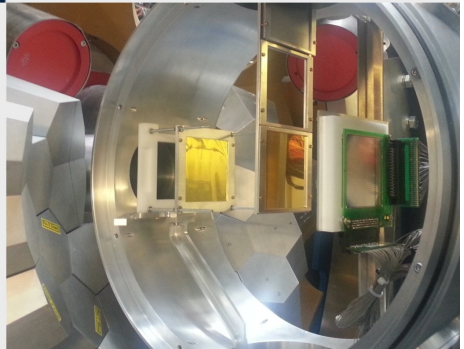
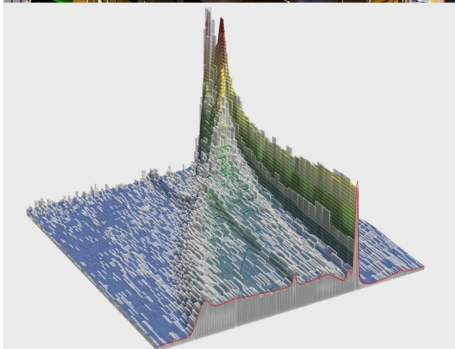
Neue Methoden für die  $\gamma$ -Spektroskopie mit positionsempfindlichen Detektorsystemen

Vom Fachbereich Physik der Technischen Universität Darmstadt zur Erlangung des akademischen Grades eines Doktors der Naturwissenschaften (Dr. rer. nat.) genehmigte Dissertation von Christian Stahl M.Sc. aus Limburg  
Juli 2015 – Darmstadt – D 17



TECHNISCHE  
UNIVERSITÄT  
DARMSTADT

Fachbereich Physik  
Institut für Kernphysik  
AG Pietralla



This work was  
supported by

**HIC**  
for **FAIR**  
Helmholtz International Center

&



Bundesministerium  
für Bildung  
und Forschung

under grants №  
05P09RDFN4  
05P12RDFN8

New methods for the  $\gamma$ -ray spectroscopy with position-sensitive detector systems  
Neue Methoden für die  $\gamma$ -Spektroskopie mit positionsempfindlichen Detektorsystemen

Genehmigte Dissertation von Christian Stahl M.Sc. aus Limburg

1. Gutachten: Prof. Dr. Dr. h.c. Norbert Pietralla
2. Gutachten: Prof. Dr. Thomas Aumann

Tag der Einreichung: 30.6.2015

Tag der Prüfung: 28.07.2015

Darmstadt – D 17

**On the cover:**

Top left: AGATA demonstrator at the Laboratori Nazionali di Legnaro (Photograph provided by Daniele Ceccato, University of Padova and INFN-LNL).

Bottom left: Fit of a two-dimensional lineshape to an experimental data set by the continuous-angle Doppler-Shift Attenuation Method.

Bottom right: Experimental setup of PreSPEC-AGATA experiment S426.

Bitte zitieren Sie dieses Dokument als:

URN: [urn:nbn:de:tuda-tuprints-49556](http://nbn-resolving.org/urn:nbn:de:tuda-tuprints-49556)

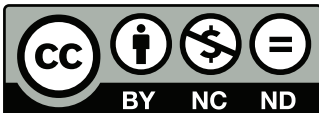
URL: <http://tuprints.ulb.tu-darmstadt.de/id/eprint/4955>

Dieses Dokument wird bereitgestellt von tuprints,

E-Publishing-Service der TU Darmstadt

<http://tuprints.ulb.tu-darmstadt.de>

[tuprints@ulb.tu-darmstadt.de](mailto:tuprints@ulb.tu-darmstadt.de)



Die Veröffentlichung steht unter folgender Creative Commons Lizenz:

Namensnennung – Keine kommerzielle Nutzung – Keine Bearbeitung 3.0 Deutschland

<http://creativecommons.org/licenses/by-nc-nd/3.0/de/>

---

# Abstract

This doctoral thesis describes two new experimental techniques for in-beam  $\gamma$ -ray spectroscopy that exploit the position-sensitivity of the latest generation of high-purity Germanium detectors, so-called  $\gamma$ -ray tracking detectors. These detectors allow to determine the interaction points of  $\gamma$ -ray quanta within the detector material with unrivaled accuracy.

The *continuous-angle Doppler-Shift Attenuation Method* extends the well-known DSA Method for the measurement of nuclear level lifetimes by providing a complete description of the observed characteristic, Doppler-broadened  $\gamma$ -ray lineshapes as a function of the energy and detection polar angle of the  $\gamma$ -rays. The method's power is demonstrated by the precise lifetime determination of the  $2_1^+$  and  $3_1^-$  state of  $^{136}\text{Xe}$  from data taken with the AGATA demonstrator.

The method of *Coulex-Multipolarimetry with relativistic heavy-ion beams* allows for the measurement of electromagnetic multipole-mixing ratios of  $\gamma$ -radiation. The core of the method is the determination of velocity-dependent Coulomb excitation cross sections at two different relativistic ion energies. These can be determined in one single measurement by distinguishing excitations in two spatially separated targets via different observed Doppler-shifts that can be reliably separated in  $\gamma$ -ray tracking detectors. This method was employed during the PreSPEC-AGATA campaign in the experiment S426 at GSI's FRS in 2014.

---



---

# Zusammenfassung

Diese Doktorarbeit beschreibt zwei neuartige experimentelle Methoden für die in-beam  $\gamma$ -Spektroskopie, welche die Positionsempfindlichkeit der neuesten Generation von hochreinen Germanium-Detektoren, sog.  $\gamma$ -ray tracking Detektoren, ausnutzen. Diese Detektoren erlauben die Bestimmung der Wechselwirkungspunkte von  $\gamma$ -Quanten innerhalb des Detektormaterials mit bisher unerreichter Genauigkeit.

Die *winkel-kontinuierliche Doppler-Shift Attenuation Methode* erweitert die bekannte DSA-Methode zur Messung von Kernzustandslebensdauern durch die vollständige Beschreibung der beobachteten charakteristischen, Doppler-verbreiteten Linienformen als Funktion der  $\gamma$ -Energie und des Polarwinkels ihres Nachweisortes. Die Leistungsfähigkeit der Methode wird demonstriert anhand der präzisen Bestimmung der Lebensdauern des  $2_1^+$ - und  $3_1^-$ -Zustands von  $^{136}\text{Xe}$  aus Daten, die mit dem AGATA-Demonstrator genommen wurden.

Die Methode der *Coulex-Multipolarimetrie mit relativistischen Ionenstrahlen* erlaubt die Messung elektromagnetischer Multipol-Mischungsverhältnisse von  $\gamma$ -Strahlung. Der Kern der Methode besteht in der Messung von geschwindigkeitsabhängigen Wirkungsquerschnitten für Coulomb-Anregung bei zwei verschiedenen relativistischen Ionenenergien. Diese werden in einer einzigen Messung bestimmt, indem Anregungen in zwei räumlich getrennten Targets durch unterschiedliche detektierte Doppler-Verschiebungen in  $\gamma$ -ray tracking Detektoren verlässlich getrennt werden. Die Methode wurde 2014 bei der PreSPEC-AGATA - Kampagne im Experiment S426 am FRS der GSI eingesetzt.

---



---

# Contents

<b>1. Introduction</b>	<b>1</b>
<b>2. Basic Principles</b>	<b>9</b>
2.1. Coulomb excitation theory . . . . .	9
2.1.1. Semi-classical approach . . . . .	9
2.1.2. Excitation probabilities and cross sections for sub-barrier beam energy . . . . .	12
2.1.3. Excitation probabilities and cross sections for relativistic beam energy . . . . .	14
2.1.4. General aspects . . . . .	16
2.2. Decay of excited nuclear states . . . . .	18
2.3. Doppler effect and relativistic transformations . . . . .	21
2.4. $\gamma$ -ray angular correlations . . . . .	22
<b>3. <math>\gamma</math>-ray tracking arrays</b>	<b>29</b>
3.1. Arrays of high-purity germanium detectors . . . . .	29
3.2. From segmented detectors to $\gamma$ -ray tracking arrays . . . . .	31
3.2.1. Pulse Shape Analysis . . . . .	32
3.2.2. Tracking . . . . .	35
3.3. AGATA and GRETA . . . . .	39
3.4. Possibilities arising from $\gamma$ -ray tracking arrays . . . . .	44
<b>4. The continuous-angle Doppler-Shift Attenuation Method</b>	<b>47</b>
4.1. Measurement of nuclear level lifetimes: An introduction . . . . .	47
4.1.1. Experimental techniques for lifetime measurements . . . . .	48
4.1.2. The Doppler-Shift Attenuation Method (DSAM) . . . . .	48
4.2. Principle of the continuous-angle DSA Method . . . . .	60
4.3. Formalism of the continuous-angle DSA Method . . . . .	67
4.4. Extensions of the continuous-angle DSA Method . . . . .	79
4.4.1. The differential caDSA Method . . . . .	79
4.4.2. The geometric caDSA Method . . . . .	89

---

<b>5. Coulex-Multipolarimetry with relativistic heavy-ion beams</b>	<b>97</b>
5.1. Purpose . . . . .	97
5.2. Principle . . . . .	98
5.3. Method . . . . .	101
5.3.1. Experimental setup . . . . .	101
5.3.2. Expected yields and peak areas . . . . .	102
5.3.3. Peak separation . . . . .	107
5.3.4. Lifetime effects . . . . .	110
5.3.5. Doppler correction / optimization . . . . .	113
<b>6. First experiments employing the new methods</b>	<b>117</b>
6.1. The $2^+_{1,MS}$ state of $^{140}\text{Ba}$ and level lifetimes of $^{136}\text{Xe}$ . . . . .	118
6.1.1. Setup of LNL experiment 09.08 . . . . .	121
6.1.2. Data Preparation . . . . .	124
6.1.3. Analysis of the data for $^{140}\text{Ba}$ populated by $\alpha$ -transfer . . . . .	141
6.1.4. caDSAM measurement: Level lifetimes of $^{136}\text{Xe}$ . . . . .	145
6.1.5. Coulex analysis: Transition strengths in $^{136}\text{Xe}$ . . . . .	165
6.1.6. Discussion of the results for $^{136}\text{Xe}$ . . . . .	177
6.2. Identification of the $\pi p_{3/2} \rightarrow \pi p_{1/2}$ spin-flip transition in $^{85}\text{Br}$ . . . . .	192
6.2.1. PreSPEC-AGATA experiment S426 . . . . .	194
6.2.2. Perspectives for the data-analysis . . . . .	208
<b>7. Potential impact of the new methods</b>	<b>213</b>
<b>8. Summary &amp; Outlook</b>	<b>217</b>
<b>A. Criteria for "safe" Coulomb-excitation</b>	<b>221</b>
<b>B. Implementation of the caDSA Method</b>	<b>223</b>
B.1. Program StopSim . . . . .	223
B.2. Details of the caDSAM formalism and the program APCAD . . . . .	229
B.3. Implementation of the differential caDSAM . . . . .	246
B.4. Implementation of the geometric caDSAM . . . . .	247
<b>C. Reaction kinematics</b>	<b>251</b>
<b>D. Additional spectra for LNL experiment 08.09</b>	<b>253</b>
D.1. Particle spectra and gates for reaction channel selection . . . . .	253
D.2. Determination of parameters defining the setup geometry . . . . .	258

---

<b>E. Reduced M1 transition strength for a <math>p_{1/2} \rightarrow p_{3/2}</math> spin-flip transition</b>	<b>261</b>
<b>Bibliography</b>	<b>265</b>
<b>List of Figures</b>	<b>287</b>
<b>List of Tables</b>	<b>295</b>
<b>List of publications</b>	<b>297</b>
<b>Acknowledgements</b>	<b>301</b>
<b>Lebenslauf (curriculum vitae)</b>	<b>303</b>

---



# 1 Introduction

When I attended my first lecture in nuclear structure physics as an undergraduate student, I was surprised to learn that the mechanisms forming the structure of atomic nuclei are not completely understood. There is no theoretical model capable of describing the properties of all nuclei including light, heavy, stable and radioactive systems. The forces that govern the interaction between nuclei, i.e. the electromagnetic, weak and strong interaction, are understood on a fundamental level in terms of the theories of electroweak interaction [Gla80, Wei80, Sal80, Hoo72] and quantum chromodynamics (QCD) [Mar78, Kog83]. This leads to the standard model of particle physics [Oli14], a very successful descriptive and predictive theory of subatomic particles and fields. In the high-energy regime of particle physics, the QCD can be treated perturbatively with respect to the strong coupling constant  $\alpha_s$  (asymptotic freedom [Gro05, Pol05, Wil05]), and the degrees of freedom are quarks and gluons. At low energy scales relevant to nuclear physics  $\alpha_s$  becomes  $\sim 1$  (see Fig. 1.1), resulting in quark confinement and the break-down of perturbation theory as function of the coupling constant. Therefore, alternative approaches are needed to derive nuclear forces from QCD in its non-perturbative regime, where the effective degrees of freedom are nucleons and pions.

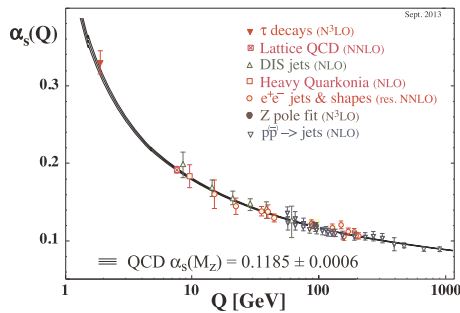


**Figure 1.1.:** Measured values of the strong coupling constant  $\alpha_s$  as a function of the energy scale  $Q$ . Large values of  $\alpha_s$  hinder the application of perturbation theory to QCD at low energy. Figure taken from [Oli14]. Details ibidem.

The resulting nuclear forces that are responsible for the nuclear binding are residual color forces, much like the van der Waals forces between neutral molecules [Epe09]. Significant progress in extracting nuclear forces from QCD has been achieved in the last years by the application of chiral effective field theory ( $\chi$ EFT). The advantage of nuclear forces derived from  $\chi$ EFT over phenomenological forces are their founding on the underlying theory of strong interaction -QCD- (which in particular also applies to three-nucleon forces), the naturally arising ordering of the importance of terms contributing to the Lagrangian and, resulting from this, the possibility to estimate errors of calculated observables [Epe09, Mac11].

Starting from nuclear forces, the nuclear many-body problem has to be solved in order to perform calculations of nuclear properties. Its complexity rises dramatically with the number of nucleons involved. Consequently, “full” *ab initio*

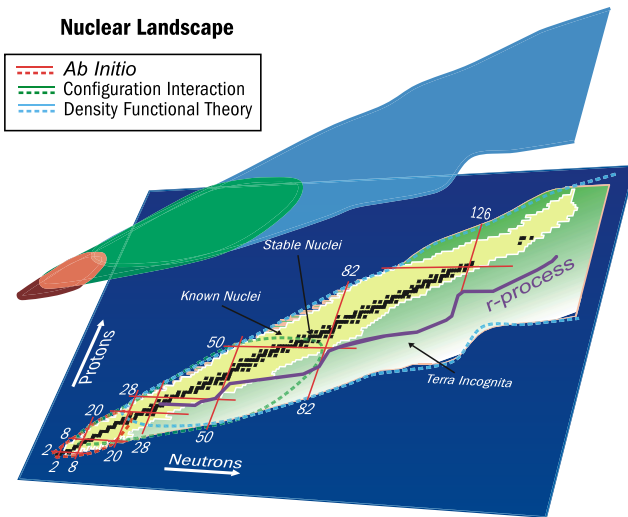


**Figure 1.2.:** Rough classification of computational methods suitable to solve the nuclear many-body problem for different regions of the nuclear chart, limited by the computing power available today. *Ab initio* methods can be applied to light nuclei only (red). Medium-mass nuclei are reachable by “configuration interaction” (shell-model) methods (green), whereas heavy nuclei can be approached by density functional methods (blue). Figure taken from [Dea08] and slightly modified. © IOP Publishing. Reproduced with permission. All rights reserved.

---

calculations can be performed only for light nuclei up to  $A \approx 15$  [Bar13, Epe14] with the computing power available today. *Ab initio* calculations for medium-mass nuclei can be performed by the application of effective truncation schemes (like *importance truncation* [Rot07], or *coupled cluster* methods [Kow04, Bin14]) and renormalization of the interactions [Bog10, Tsu11]. Shell-model calculations with phenomenological interactions fitted to experimental spectroscopic data are suitable for nuclei near closed shells, taking into account a very limited number of valence nuclei situated around the Fermi energy [Cau05, Bro88, Ots01]. Phenomenological microscopic models like the Quasiparticle Phonon Model (QPM) [Ber99] or self-consistent mean-field approaches (e.g. based on energy density functionals (EDF) [Ben03]) and phenomenological collective models like geometrical models [Boh75] or algebraic models [Ari75, Ari77] provide descriptions of nuclei with model-dependent limitations throughout the nuclear chart. Summarizing the above, the complex nature of the atomic nucleus today still lacks a unified, predictive and applicable theoretical description that is solidly founded on underlying principles.

Rich phenomena arise from the many-body two-fluid quantum nature of the atomic nucleus like its collective behavior [Boh52, Ari75], its shell-structure [Hax49, Goe50] and excitation modes related to its isospin degree of freedom such as Mixed-Symmetry States [Boh84, Pie08]. Their investigation helps to shed light on the mechanisms underlying nuclear structure and to improve the theoretical models describing it. In particular, the systematic study of nuclear structure as a function of proton- and neutron-number has proven to be a sensitive approach to investigate nuclear interactions. For example, the “regular” proton and neutron magic numbers (2,8,20,28,50,82), as they appear at the valley of stability, have been known and understood for many decades [Goe50]. Experimental results of the last years provide more and more examples for the appearance of “new” magic numbers at the extremes of isospin, like the doubly-magic nature of the  $N_\nu = 32, 34$  nuclei  $^{52,54}\text{Ca}$  [Wie13, Ste13] or the  $N_\nu = 16$  nucleus  $^{24}\text{O}$  [Kan09], and the disappearance of “regular” magic numbers like in the  $N_\nu = 28$  nucleus  $^{42}\text{Si}$  [Bas07]. These examples of shell-evolution have been traced back to shifts of single-particle energies driven by the monopole part of the tensor force [Ots05, Ots10a], a non-central component of the nuclear force, and by the presence of three-nucleon forces [Hol14, Hol13, Ots10b]. These findings highlight the importance of studying exotic nuclei.

The study of exotic nuclei far off stability has been rendered possible by the advent of radioactive ion beam (RIB) facilities. Today, a variety of RIB facilities are in operation (e.g. at NSCL, MI, USA; TRIUMF, Kanada; GANIL, France; REX-ISOLDE,



**Figure 1.3.:** Present (small red dots) and future (large white dots) major RIB facilities worldwide. Figure reprinted from [Rar07] with permission by the National Academy of Sciences, Courtesy of the National Academies Press, Washington, D.C.

CERN; GSI, Germany; RIKEN, Japan; ...), and a new generation of RIB facilities (like FRIB, MI, USA; Spiral2, France; HIE-ISOLDE, CERN; FAIR, Germany; SPES, Italy; ...) is under construction (see e.g. [Blu13] for an overview). The gain in intensity (and energy) of the RIBs produced by these new facilities results in an increasing number of exotic nuclei that become accessible for nuclear structure studies as well as in new possibilities for more precise experiments. Furthermore, the measurement of more observables in exotic nuclei such as spectroscopic factors, gyromagnetic ratios and electromagnetic transition strengths also for non-yrast states are now becoming feasible.

The developments for the production of RIBs are accompanied by the development of the next generation of  $\gamma$ -ray detector systems. Enhanced sensitivity results from the excellent timing properties with at the same time good energy resolution and high efficiency of recently available  $\text{LaBr}_3$  scintillation detectors [Loe01], and especially from the development of  $\gamma$ -ray tracking arrays [Wal14] such as AGATA [Akk12] and GRETA/GRETINA [Lee04, Pas13]. Via their superior position resolution, these  $\gamma$ -ray tracking detectors do not only raise the experimental sensitivity by providing an unrivaled energy resolution after Doppler correction of the energy of  $\gamma$ -rays emitted in-flight [Rec09a]. They also make new techniques for active background suppression possible [Don10] and open up a new field for experimental techniques that are founded upon the ability to precisely and continuously measure the emission direction of  $\gamma$ -rays.

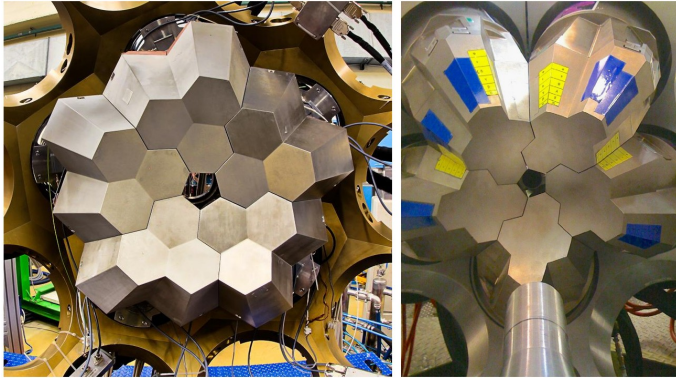


**Figure 1.4.:**  $\gamma$ -ray tracking detectors significantly raise the sensitivity of  $\gamma$ -ray spectroscopy experiments, in particular for in-beam spectroscopy of relativistic ion beams, by their unrivaled position resolution and render possible a new class of experimental techniques. Left: AGATA Demonstrator with 15 crystals arranged in 5 triple-clusters. Photograph provided by Daniele Ceccato, University of Padova and INFN-LNL. Right: GRETINA with 20 crystals arranged in 5 clusters. Figure reprinted from [Pas13] with permission from Elsevier.

In this thesis, two novel experimental techniques tailored to  $\gamma$ -ray spectroscopy with  $\gamma$ -ray tracking detectors and their first application to in-beam  $\gamma$ -ray spectroscopy experiments are presented.

The basic principles underlying the developed methods and performed experiments are briefly introduced in Chapter 2, followed by a discussion of the development, the features and the possibilities arising from  $\gamma$ -ray tracking detectors in Chapter 3.

In Chapter 4 the *continuous-angle Doppler-Shift Attenuation Method* (caDSAM), a further development of the Doppler-Shift Attenuation Method (DSAM) adapted to  $\gamma$ -ray tracking detectors in general and to experiments with (relativistic) RIBs in particular is presented. The DSA Method is suited to measure nuclear level lifetimes in the range from  $\sim 10$  fs to  $\sim 10$  ps by the analysis of characteristic shapes of Doppler-broadened  $\gamma$ -ray lines. The caDSAM makes use of the possibility to measure the polar  $\gamma$ -ray detection angle precisely and continuously with  $\gamma$ -ray tracking detectors and provides consistent descriptions of the characteristic, Doppler-broadened  $\gamma$ -ray lines as a function of both  $\gamma$ -ray energy and detection polar angle. Modifications of the caDSAM that extend the lifetime sensitivity to

---

$\sim 200$  ps (“*geometric caDSAM*”) and provide suitable experimental conditions for measurements with relativistic and radioactive ion beams (“*differential caDSAM*”) are discussed in Chapter 4.4.

A novel method for the measurement of  $\gamma$ -ray multipole mixing ratios  $\delta$  is presented in Chapter 5. The method of *Coulex-Multipolarimetry with relativistic heavy-ion beams* is based on the comparison of cross sections for Coulomb excitation (Coulex) at two different relativistic beam energies [Sta15]. By the use of two thick targets in a distance of  $\sim 10$  cm, excitations at two beam energies can be observed in one single measurement. Exploiting the superb angular resolution of  $\gamma$ -ray tracking detectors, excitations in either of the targets can be separated by different registered Doppler-shifts. This method allows for the determination of  $\delta$  also in cases where the emission of the  $\gamma$ -rays occurs isotropic in the emitter rest frame and conventional methods are not applicable.

In Chapter 6, applications of the two methods in experiments conducted at the Laboratori Nazionali di Legnaro and the PreSPEC-AGATA setup are presented.

The caDSAM was used to precisely determine the level lifetime of the  $2_1^+$  and  $3_1^-$  states of  $^{136}\text{Xe}$ . Transition strengths for all other  $2_i^+$  levels of  $^{136}\text{Xe}$  up to  $i = 7$  could be determined or, at least, constrained by a Coulex analysis relative to the  $2_1^+$  lifetime. The results are compared to microscopic calculations and discussed in the context of the nuclear structure of  $^{136}\text{Xe}$  and neighboring nuclei.

During the 2014 PreSPEC-AGATA campaign, the method of Coulex-Multipolarimetry was applied for the absolute measurement of the reduced  $M1$ -transition strength between the  $\pi p_{\frac{3}{2}}$ -dominated ground-state of  $^{85}\text{Br}$  and a candidate for its  $\pi p_{\frac{1}{2}}$  spin-orbit partner in order to identify the transition between these states as a spin-flip transition. The layout and the sensitivity of the experiment are discussed. The complicated analysis of the experimental data is ongoing and subject of another doctoral thesis, hence only a discussion of the perspectives for the data analysis can be given. However, in the particle-hole partner-nucleus of  $^{85}\text{Br}$ ,  $^{87}\text{Rb}$ , the  $\pi p_{\frac{1}{2}} \rightarrow \pi p_{\frac{3}{2}}$  spin-flip transition was also uniquely identified within this work [Sta13], albeit by another (non-standard) method.

These two applications of the novel methods developed within this work highlight two major competing aspects of nuclear structure: Collectivity and single-particle excitations, reflecting the many-body quantum nature of the atomic nucleus. The electromagnetic matrix elements derived from the analysis of the  $^{136}\text{Xe}$  data provide a valuable testing ground for nuclear structure models for collective nuclear vibrations, while the identification of single-particle states, like via the spin-flip

---

transitions in  $^{85}\text{Br}$  and in  $^{87}\text{Rb}$ , directly yields effective single-particle energy differences that serve as input for shell-model calculations and as benchmark observable for nuclear interactions in that mass region.

The potential impact of the two new methods for future experiments is discussed in Chapter 7, followed by a summary and an outlook in Chapter 8.



---

## 2 Basic Principles

This chapter reviews previous work relevant for the new experimental methods and their applications discussed in this thesis. These basic principles concern the excitation of atomic nuclei by Coulomb excitation (Section 2.1), the decay of the excited states (Section 2.2), effects on  $\gamma$ -radiation emitted in the nuclear de-excitation (Section 2.3) and the angular correlations of the  $\gamma$ -radiation (Section 2.4). The detection of  $\gamma$ -radiation in state-of-the-art  $\gamma$ -ray tracking detectors is discussed in the following Chapter 3. The references used are given in each chapter.

---

### 2.1 Coulomb excitation theory

---

This section is based on Reference [Ald56b, Ald75] for the general discussion and the low-energy case and on Reference [Win79] for the relativistic case. The Coulomb excitation process is discussed for the excitation of a target nucleus in the electromagnetic field of a passing projectile nucleus. The excitation of the projectile can be described accordingly if the relevant quantities for the target nucleus (mass, charge, matrix elements etc.) are interchanged with the quantities for the projectile nucleus.

---

#### 2.1.1 Semi-classical approach

---

Coulomb excitation (abbr.: Coulex) is the electromagnetic excitation of an atomic nucleus by the electromagnetic field of another nucleus. The interaction between a projectile- and target nucleus is purely electromagnetic, if the nuclei are sufficiently separated such that their radii do not overlap during the whole scattering process. The condition for this "safe" Coulomb excitation is discussed in Appendix A. If this condition is fulfilled, also the length scale of the trajectory of the projectile in the scattering process, quantified by its half distance of closest approach  $a$  to the target nucleus, is small compared to the de Broglie wavelength  $\lambda$  of the relative motion of the two particles:

$$\eta = \frac{a}{\lambda} \gg 1. \quad (2.1)$$

The parameter  $\eta$  is called the Sommerfeld parameter, and the fulfillment of  $\eta \gg 1$  implies that the motion of the projectile can be described by classical trajectories.

In this case, the cross section for Coulomb exciting a final state  $|f\rangle$  from the ground state  $|0\rangle$  can be expressed as

$$\left(\frac{d\sigma}{d\Omega}\right)_f = \left(\frac{d\sigma}{d\Omega}\right)_{Ruth} P_f, \quad (2.2)$$

where  $(d\sigma/d\Omega)_{Ruth}$  is the Rutherford scattering cross section and  $P_f$  is the excitation probability defined via the excitation amplitudes  $a_f$  by

$$P_f = (2J_0 + 1)^{-1} \sum_{M_0 M_f} |a_f|^2. \quad (2.3)$$

$J_0$  is the ground state spin. The excitation probability  $P_f$  is averaged over all magnetic substates  $M_0$  of the initial state and summed over all magnetic substates  $M_f$  of the final state. For small excitation probabilities  $P_f \ll 1$ , the excitation amplitudes can be obtained in first order perturbation theory where the electromagnetic interaction  $V(\vec{r}(t))$  is treated as small perturbation. This treatment of Coulomb excitation in first order perturbation theory is reviewed in this chapter. A treatment of Coulomb excitation beyond this approximation is discussed in Chapter 2.1.4.

The time-dependent Schrödinger equation for the projectile nucleus moving along the trajectory  $\vec{r}(t)$  in the electromagnetic field  $V$  of the target nucleus is given by

$$i\hbar \frac{\partial}{\partial t} |\Psi(t)\rangle = [H_0 + V(\vec{r}(t))] |\Psi(t)\rangle. \quad (2.4)$$

Its solutions are the time-dependent states

$$|\Psi(t)\rangle = \sum_n a_n(t) e^{-iE_n t/\hbar} |n\rangle, \quad (2.5)$$

where  $|n\rangle$  are the eigenstates of the Hamiltonian of the free nucleus  $H_0$  with eigenvalues (energies)  $E_n$ . Substituting Equation 2.5 into 2.4 defines a set of differential equations for the amplitudes  $a_n(t)$ :

$$i\hbar \dot{a}_n(t) = \sum_m \langle n|V(\vec{r}(t))|m\rangle e^{i(E_n - E_m)t/\hbar} a_m(t). \quad (2.6)$$

The amplitudes are time-independent for  $t = \pm\infty$  where the electromagnetic interaction vanishes. Before the scattering process, it is assumed that the nucleus is in its ground state, i.e.  $a_n(t = -\infty) = \delta_{n0}$ , and the square of the amplitude

$a_n(t = \infty)$  defines the probability to find the system in state  $|n\rangle$  after the scattering. This amplitude in the final state is given in first order perturbation theory by

$$a_f \equiv a_{J_f M_f, J_0 M_0} = \frac{1}{i\hbar} \int_{-\infty}^{+\infty} \langle J_f M_f | V(\vec{r}(t)) | J_0 M_0 \rangle e^{i(E_f - E_0)t/\hbar} dt. \quad (2.7)$$

$J_{f(0)}$  denotes the spin of the excited state (ground state) and  $M_{f(0)}$  is its magnetic quantum number.

The projectile experiences the electromagnetic field of the target nucleus  $V(\vec{r}(t))$  as a pulsed field. Hence, an excited state  $|f\rangle$  can only be excited by this field if the time duration of the pulse, i.e. the collision time, is short or comparable to the nuclear period  $T = 2\pi/\omega$  characteristic for the transition. The collision time  $\tau$  is quantified by the time needed by the projectile to travel the half distance of closest approach to the target nucleus  $a$  and the characteristic nuclear frequency is given by  $\omega = (E_f - E_i)/\hbar$ . The quantity

$$\xi = \tau \omega = \frac{a}{\gamma v} \frac{E_f - E_i}{\hbar} \quad (2.8)$$

is the adiabaticity parameter that measures the ratio between collision time and characteristic nuclear period. In Equation (2.8),  $v$  is the velocity of relative motion between the projectile and target nucleus and  $\gamma = (1 - v^2/c^2)^{-1/2}$  is the Lorentz factor. For experiments with beam energies below the Coulomb barrier,  $a$  can be estimated from the distance of closest approach for a central collision. For relativistic beam energies and scattering angles sufficiently small to obey the condition for "safe" Coulomb excitation, it can be estimated by the impact parameter  $b$ :

$$a_{lowE} = \frac{Z_p Z_t e^2}{m_0 v^2} \text{ and } a_{highE} = b, \quad (2.9)$$

where  $Z_p$  and  $Z_t$  are the proton number of projectile and target nuclei, respectively, and  $m_0$  is the reduced mass of projectile and target. The dependence of the Coulomb excitation cross section on the adiabaticity of the process is expressed by a function  $f(\xi)$  with the properties

$$\begin{aligned} f(\xi) &= 1 \text{ for } \xi = 0 \\ f(\xi) &\sim e^{-\pi\xi} \text{ for } \xi \gg 1. \end{aligned} \quad (2.10)$$

Hence, excitation is exponentially suppressed for large values of  $\xi$ , known as adiabatic cutoff. This limits the excitation energy reachable at beam energies below the

Coulomb barrier to 1-2 MeV in a single excitation step. It can be circumvented to a certain extent in multi-step excitations (see Section 2.1.4) that occur at moderate beam energies when using heavy projectiles and heavy target nuclei. Under these conditions, first order perturbation theory as discussed here is no longer applicable and the reader is referred to Reference [Ald75] and the discussion of higher order effects in Section 2.1.4. At relativistic beam energies, the significantly higher projectile velocities also allow the excitation of higher-lying states up to  $\sim 10$  MeV in a one-step process.

The excitation amplitudes (2.3) are obtained by a multipole expansion of the electromagnetic field  $V(\vec{r}(t))$  and evaluating Equation (2.7) along the path  $\vec{r}(t)$  of the projectile. For sub-barrier beam-energies, the path can be described by classical Rutherford trajectories and for relativistic beam energies, an approximation of the projectile path by a straight line is appropriate for impact parameters  $b$  fulfilling the conditions for "safe" Coulomb excitation. The classical treatment of the projectile trajectory combined with a quantum-mechanical treatment of the excitation process is denoted as semi-classical approach. Results for the excitation probabilities  $P_f$  at sub-barrier and relativistic beam energies employing the semi-classical approach and first order perturbation theory are presented in the following two sub-sections.

---

### 2.1.2 Excitation probabilities and cross sections for sub-barrier beam energy

---

At beam energies below the Coulomb barrier ("*sub-barrier energies*"), the excitation probabilities for transitions of multipole order  $\lambda$  and electric or magnetic radiation character  $\sigma = E, M$  can be expressed as

$$P_{f,\sigma} = \sum_{\lambda} \left| \chi_f^{(\sigma\lambda)} \right|^2 R_{\sigma\lambda}^2(\vartheta, \xi). \quad (2.11)$$

The first factor  $\chi_f^{(\sigma\lambda)}$  describes the  $\lambda$ -pole excitation probability for a center-of-mass scattering angle  $\vartheta = \pi$  and adiabaticity  $\xi = 0$ . It is denoted as excitation strength function. The second factor  $R_{\sigma\lambda}^2(\vartheta, \xi)$  describes the excitation probability relative to that special condition. The excitation amplitude corresponding to  $P_{f,\sigma}$  via the relation (2.3) is given by

$$a_{J_f M_f, J_0 M_0}^{\sigma} = -i \sum_{\lambda} (-1)^{J_0 - M_0} \sqrt{2J_0 + 1} \sqrt{2\lambda + 1} \begin{pmatrix} J_0 & \lambda & J_f \\ -M_0 & \mu & M_f \end{pmatrix} \chi_f^{(\sigma\lambda)} R_{\sigma\lambda\mu}(\vartheta, \xi). \quad (2.12)$$

Here,  $\begin{pmatrix} J_0 & \lambda & J_f \\ -M_0 & \mu & M_f \end{pmatrix}$  denotes the Wigner 3-j symbol.

For electric excitations, the strength function is given by

$$\chi_f^{(E\lambda)} = \frac{4\sqrt{\pi}(\lambda-1)! Z_p e \langle J_0 \| \mathcal{O}(E\lambda) \| J_f \rangle}{(2\lambda+1)!! \hbar v a^\lambda \sqrt{2J_0+1}}. \quad (2.13)$$

where  $\langle J_0 \| \mathcal{O}(E\lambda) \| J_f \rangle$  is the reduced matrix element for an electric  $\lambda$ -pole transition between the initial state  $|J_0\rangle$  and the final state  $|J_f\rangle$  and

$$R_{E\lambda}^2(\vartheta, \xi) = \sum_{\mu} |R_{E\lambda\mu}(\vartheta, \xi)|^2 = \left| \frac{(2\lambda-1)!!}{(\lambda-1)!} \right|^2 \frac{\pi}{2\lambda+1} \sum_{\mu} |Y_{\lambda\mu}(\pi/2, 0) I_{\lambda\mu}(\vartheta, \xi)|^2. \quad (2.14)$$

The quantities  $R_{E\lambda\mu}(\vartheta, \xi)$  are denoted as orbital integrals. They depend on the choice of the coordinate system. Explicit expressions are given in [Ald75]. In contrast, the squares of their absolute values summed over  $\mu$  appearing in Equation (2.14) are independent of the choice of the coordinate system. The function  $I_{\lambda\mu}(\vartheta, \xi)$  is the Coulomb excitation function and given by

$$I_{\lambda\mu}(\vartheta, \xi) = \int_{-\infty}^{\infty} \frac{[\cosh(w) + \epsilon + i\sqrt{\epsilon^2 - 1} \sinh(w)]^\mu}{[\epsilon \cosh(w) + 1]^{\lambda+\mu}} e^{i\xi[\epsilon \sinh(w)+w]} dw, \quad (2.15)$$

where  $\epsilon = \sin(\vartheta/2)^{-1}$  denotes the excentricity of the hyperbolic projectile orbit. Because of the spherical harmonics  $Y_{\lambda\mu}(\pi/2, 0)$ , only the excitation functions  $I_{\lambda\mu}(\vartheta, \xi)$  with even values of  $\lambda + \mu$  contribute to Equation (2.14). Tabulated values of  $I_{\lambda\mu}(\vartheta, \xi)$  can be found in Reference [Ald56a].

For magnetic excitations, the strength function is given by

$$\chi_f^{(M\lambda)} = \frac{4\sqrt{\pi}((\lambda-1)! Z_p e \langle J_0 \| \mathcal{O}(E\lambda) \| J_f \rangle)}{(2\lambda+1)!! \hbar c a^\lambda \sqrt{2J_0+1}} \quad (2.16)$$

and the summed squares of the orbital integrals are given by

$$R_{M\lambda}^2(\vartheta, \xi) = \left| \frac{(2\lambda-1)!!}{\lambda!} \right|^2 \frac{\pi}{2\lambda+3} \times \sum_{\mu} [(\lambda+1)^2 - \mu^2] |Y_{\lambda+1,\mu}(\pi/2, 0) I_{\lambda+1,\mu}(\vartheta, \xi)|^2 \cot^2(\vartheta/2). \quad (2.17)$$

In general, electric and magnetic excitations can interfere. Therefore, the total excitation amplitude is given by

$$\begin{aligned}
 a_{J_f M_f, J_0 M_0} &= a_{J_f M_f, J_0 M_0}^E + a_{J_f M_f, J_0 M_0}^M \\
 &= -i \sum_{\lambda} (-1)^{J_0 - M_0} \sqrt{2J_0 + 1} \sqrt{2\lambda + 1} \begin{pmatrix} J_0 & \lambda & J_f \\ -M_0 & \mu & M_f \end{pmatrix} \\
 &\quad \times \left\{ \chi_f^{(E\lambda)} R_{E\lambda\mu}(\vartheta, \xi) + \chi_f^{(M\lambda)} R_{M\lambda\mu}(\vartheta, \xi) \right\}.
 \end{aligned} \tag{2.18}$$

However, due to the selection rules for electromagnetic transitions, two nuclear states can never be connected by electric and magnetic multipole matrix elements of the same multipolarity. Therefore, interference terms in the excitation probabilities (2.11) and the excitation cross section (2.19) cancel if the initial state is unpolarized (see Section 2.4 for a discussion of polarization and alignment of nuclear states).

In this case, the differential cross section for Coulomb excitation at sub-barrier energies in first order perturbation theory is given by

$$\begin{aligned}
 \frac{d\sigma}{d\Omega} &= \sum_{\lambda} \left( \frac{d\sigma_{E\lambda}}{d\Omega} + \frac{d\sigma_{M\lambda}}{d\Omega} \right) \text{ with} \\
 \frac{d\sigma_{E\lambda}}{d\Omega} &= \frac{a^2}{4 \sin^4(\vartheta/2)} \left| \chi_f^{(E\lambda)} \right|^2 R_{E\lambda}^2(\vartheta, \xi) \text{ and} \\
 \frac{d\sigma_{M\lambda}}{d\Omega} &= \frac{a^2}{4 \sin^4(\vartheta/2)} \left| \chi_f^{(M\lambda)} \right|^2 R_{M\lambda}^2(\vartheta, \xi).
 \end{aligned} \tag{2.19}$$

Here,  $a = (Z_p Z_t e^2)/(m_0 v^2)$  is again the half distance of closest approach for a central collision.

---

### 2.1.3 Excitation probabilities and cross sections for relativistic beam energy

---

It was previously mentioned that for the calculation of the Coulomb excitation probabilities in the case of relativistic beam energies, the path of the projectile can be approximated by a straight line, passing the target nucleus at a distance of closest approach given by the impact parameter  $b$ . This is valid in the case that the impact parameter is sufficiently large to fulfill the condition of "safe" Coulomb excitation, i.e. it is ensured that the interaction between target and projectile nucleus is purely electromagnetic (see Appendix A). The scattering angle in the laboratory system  $\theta$  for an impact parameter  $b$  is given by

$$\theta \approx \frac{2Z_p Z_t e^2}{\gamma m_p v^2 b}. \tag{2.20}$$

The excitation amplitudes in this straight line approximation are given by

$$\begin{aligned}
 a_{J_f M_f, J_0 M_0} = & -i \frac{Z_p e}{\hbar \gamma v} \sum_{\sigma \lambda \mu} (-1)^{J_0 - M_0 + \mu} \sqrt{2\lambda + 1} \left( \frac{E_f - E_0}{\hbar c} \right)^\lambda \begin{pmatrix} J_0 & \lambda & J_f \\ -M_0 & -\mu & M_f \end{pmatrix} \\
 & \times \langle J_0 \parallel \mathcal{O}(\sigma \lambda) \parallel J_f \rangle G_{\sigma \lambda \mu} \left( \frac{c}{v} \right) K_\mu(\xi(b))
 \end{aligned} \tag{2.21}$$

Here,  $K_\mu(\xi(b))$  are modified Bessel functions of second kind, evaluated at the adiabaticity parameter  $\xi$  for the impact parameter  $b$  as defined in Equations (2.8) and (2.9). The functions  $K_\mu(\xi(b))$  have a similar meaning for the excitation amplitudes as the functions  $R_{\sigma \lambda}(\vartheta, \xi)$  in the non-relativistic case, i.e. they describe an exponential suppression of the excitation for large adiabaticity  $\xi \gg 1$ . The functions  $G_{\sigma \lambda \mu}(c/v)$  for the electric excitation ( $\sigma = E$ ) and  $\mu \geq 0$  are given by

$$\begin{aligned}
 G_{E \lambda \mu} \left( \frac{c}{v} \right) = & i^{\lambda + \mu} \frac{4\sqrt{\pi}}{\lambda(2\lambda + 1)!!} \sqrt{\frac{(\lambda - \mu)!}{(\lambda + \mu)!}} \left( \left( \frac{c}{v} \right)^2 - 1 \right)^{-\frac{1}{2}} \\
 & \times \left( \frac{(\lambda + 1)(\lambda + \mu)}{2\lambda + 1} P_{\lambda - 1}^\mu \left( \frac{c}{v} \right) - \frac{\lambda(\lambda - \mu + 1)}{2\lambda + 1} P_{\lambda + 1}^\mu \left( \frac{c}{v} \right) \right)
 \end{aligned} \tag{2.22}$$

and for magnetic excitations ( $\sigma = M$ ) and  $\mu \geq 0$  they are given by

$$G_{M \lambda \mu} \left( \frac{c}{v} \right) = i^{\lambda + \mu + 1} \frac{4\sqrt{\pi}}{\lambda(2\lambda + 1)!!} \sqrt{\frac{(\lambda - \mu)!}{(\lambda + \mu)!}} \left( \left( \frac{c}{v} \right)^2 - 1 \right)^{-\frac{1}{2}} \mu P_\lambda^\mu \left( \frac{c}{v} \right). \tag{2.23}$$

$P_\lambda^\mu(x)$  are associated Legendre functions. The values of  $G_{\sigma \lambda \mu}(c/v)$  for  $\mu < 0$  are given by the relations

$$\begin{aligned}
 G_{E \lambda - \mu}(c/v) &= (-1)^\mu G_{E \lambda \mu}(c/v) \\
 G_{M \lambda - \mu}(c/v) &= -(-1)^\mu G_{M \lambda \mu}(c/v).
 \end{aligned} \tag{2.24}$$

The expression for the excitation amplitudes is very similar to that in the case of sub-barrier beam energies. In analogy to Equation (2.12), an excitation strength function for the straight line approximation for relativistic beam energies can be approximated by

$$\chi_{f,SL}^{(E\lambda)} \simeq \frac{Z_p e}{\hbar v b^\lambda} \langle J_0 \parallel \mathcal{O}(E\lambda) \parallel J_f \rangle \tag{2.25}$$

and

$$\chi_{f,SL}^{(M\lambda)} \simeq \frac{Z_p e}{\hbar c b^\lambda} \langle J_0 \parallel \mathcal{O}(M\lambda) \parallel J_f \rangle. \quad (2.26)$$

The cross section  $\sigma_f$  for Coulomb excitation of the final state  $|J_f\rangle$  is obtained from Equations (2.3) and (2.21) by integrating over all impact parameters larger than the minimum impact parameter  $b_{min}$  which satisfies the condition for "safe" Coulomb excitation (Appendix A):

$$\sigma_f = \left( \frac{Z_p e}{\hbar c} \right)^2 \sum_{\sigma\lambda\mu} \left( \frac{E_f - E_0}{\hbar c} \right)^{2\lambda-1} \frac{|\langle J_0 \parallel \mathcal{O}(\sigma\lambda) \parallel J_f \rangle|^2}{2J_0 - 1} \left| G_{\sigma\lambda\mu} \left( \frac{c}{v} \right) \right|^2 g_\mu(\xi(b_{min})), \quad (2.27)$$

where  $g_\mu(\xi)$  is defined by

$$\begin{aligned} g_\mu(\xi) &= 2\pi \left( \frac{E_f - E_0}{\hbar\gamma v} \right)^2 \int_{b_{min}}^{\infty} b |K_\mu(\xi(b))|^2 db \\ &= \pi\xi^2 \left[ |K_{|\mu|+1}(\xi)|^2 - |K_{|\mu|}(\xi)|^2 - \frac{2\mu}{\xi} K_{|\mu|+1}(\xi)K_{|\mu|}(\xi) \right]. \end{aligned} \quad (2.28)$$

---

## 2.1.4 General aspects

---

In first order perturbation theory, the Coulomb-excitation cross section for one-step excitations is directly proportional to the square of the magnitude of the reduced matrix element of the electromagnetic operators with respect to initial and final state. This is apparent from Equations (2.13 / 2.16), (2.19) and (2.27). Hence, they are also directly proportional to the reduced transition strengths

$$B(\sigma\lambda, J_0 \rightarrow J_f) = \frac{1}{2J_i + 1} |\langle J_f \parallel \mathcal{O}(\sigma\lambda) \parallel J_0 \rangle|^2. \quad (2.29)$$

This makes Coulomb excitation a very useful tool for the study of nuclear collectivity.

Comparison of Equation (2.13) with Equation (2.16) and of Equation (2.25) with Equation (2.26) shows that

$$\chi_f^{(M\lambda)} = \frac{v}{c} \chi_f^{(E\lambda)} \frac{\langle J_0 \parallel \mathcal{O}(M\lambda) \parallel J_f \rangle}{\langle J_0 \parallel \mathcal{O}(E\lambda) \parallel J_f \rangle}. \quad (2.30)$$

This relation between electric and magnetic excitation strengths originates in the difference in magnitude of the electric field  $\vec{E}$  and the magnetic field  $\vec{B}$  created by a moving electric charge,

$$|\vec{B}| = \frac{v}{c} |\vec{E}|, \quad (2.31)$$

and results in a suppression of the cross section for magnetic Coulomb excitations by a factor  $\beta^2 = v^2/c^2$  with respect to electric excitations. As a consequence,  $M1$  excitations are negligible at sub-barrier beam energies. However, at relativistic beam energies, cross sections for  $M1$  Coulomb excitations can be comparable to  $E2$  excitations. The latter property and the different velocity dependence of electric and magnetic Coulomb excitation cross sections are exploited by the Coulex-Multipolarimetry Method developed within this work (see Chapter 5).

The excitation amplitudes (2.12) and (2.21) determine the population of the magnetic substates  $M_f$  of the excited state  $|J_f\rangle$  and, hence, the angular distribution of the  $\gamma$ -radiation de-populating the excited state (see Section 2.4).

For central collisions ( $\vartheta = \pi$ ) at sub-barrier energies, no angular momentum is transferred in direction of the incoming beam. With the quantization axis chosen to be the direction of the incoming beam, only the term with  $\mu = 0$  contributes. Consequently, for an excitation from an initial state with  $J_0 = 0$ , only the  $M_f = 0$  substate of the excited state  $|J_f\rangle$  is populated in central collisions. This means that the nuclear spins are oriented perpendicular to the quantization axis. Such a spin-orientation is denoted as "oblate". For smaller center-of-mass scattering angles  $\vartheta < \pi$ , also the terms with  $\mu \neq 0$  contribute and the distribution of magnetic substate population smears out but the oblate character of the spin orientation is preserved.

In the swift collisions that occur at relativistic beam energies and impact parameters that fulfill the conditions for "safe" Coulomb excitation, the substates  $M_f = \pm J_f$  are populated predominantly. Such a spin orientation is denoted as "prolate".

In the previous sections, Coulomb excitation was treated in first order perturbation theory. Higher order effects have been neglected. These higher order effects include the excitation of a final state  $|J_f\rangle$  via intermediate states  $|J_g\rangle$ . Excitation via intermediate states is denoted as multi-step Coulomb excitation and allows for the excitation of states of higher spins and higher excitation energies than in the discussed one-step process. It occurs especially at moderate beam energies close to the Coulomb barrier when using heavy projectiles and heavy target nuclei, resulting in large values of the excitation strength  $\chi$  defined in Equations (2.13) and

---

(2.16). Also, states  $|J_f\rangle$  that do not exhibit a sizable transition matrix element  $\langle J_0 || \mathcal{O}(\sigma\lambda) || J_f \rangle$  to the ground state  $|J_0\rangle$ , but that are strongly connected to an intermediate state  $|J_g\rangle$  which in turn is strongly connected to the ground state, can be excited by multi-step Coulomb excitation.

Another second order effect in Coulomb excitation is the multi-step excitation where the intermediate state is another magnetic substate of an excited state. Then, the second "excitation process" is basically a change of the magnetic substate of the excited nuclear level. This process is known as reorientation effect [Boe68, Häu74]. The cross section for this process involves the diagonal electric quadrupole matrix element connecting the magnetic substates of the excited state  $\langle J_f || \mathcal{O}(E2) || J_f \rangle$ . This results in sensitivity of the excitation cross section to the quadrupole moment of the excited state  $|J_f\rangle$ .

The importance of these second-order processes can be inferred from the excitation strength function  $\chi$  (Equations 2.13, 2.16 and 2.25, 2.26). If  $\chi$  is comparable to unity for any nuclear state, higher order corrections have to be taken into account, either by higher-order corrections to the discussed formalism or by the explicit solution of the time dependent Schrödinger equation (2.4) or, equivalently, by the solution of the set of differential Equations (2.6). For a further discussion of higher-order effects and higher-order corrections to the presented formalism, the reader is referred to References [Ald56b, Ald75].

A treatment of Coulomb-excitation by numerical solution of the set of differential Equations (2.6) also accounting for higher-order effects can conveniently be performed by the use of existing computer programs. For Coulomb excitation at energies near the Coulomb barrier, reference is made to the computer programs CLX [Owe] and GOSIA [Czo83, Cli12]. For Coulomb excitation at relativistic energies, reference is made to the computer program DWEIKO [Ber03].

For the experimental situations discussed in this thesis in sections 6.1 and 6.2, higher order effects are negligible.

---

## 2.2 Decay of excited nuclear states

---

The mathematical description of chains of radioactive decay is covered in many standard text-books on nuclear physics (e. g. [Kra87, Hey04, MK02]). The form of the equations presented here is derived from those and slightly modified, suitable for the problems discussed in this thesis.

The number of decays  $A(t)$  of an excited nuclear state in the time interval  $(t, t+dt)$  is given by

$$A(t) = \frac{1}{\tau}N(t) \quad (2.32)$$

where  $N(t)$  denotes the number of nuclei in the excited state at time  $t$  and  $\tau$  the mean lifetime of the state. If that nuclear state is exclusively populated directly in a nuclear reaction at  $t=0$ , the number of nuclei in that state obeys the differential equation

$$\dot{N}(t) = -\frac{1}{\tau}N(t), \quad (2.33)$$

where  $\dot{N}(t)$  denotes the time-derivative of  $N(t)$ . The solution to Eq. (2.33) for the initial condition  $N(t=0) = N_0$  is given by

$$N(t) = \frac{N_0}{\tau} e^{-t/\tau}. \quad (2.34)$$

In the following, the case is discussed that the excited state is also populated by the decay of other, higher-lying states that have been populated at  $t=0$ .

Consider a set of nuclear states  $(1, 2, \dots, n)$  that are connected by the linear decay chain

$$n \rightarrow n-1 \rightarrow n-2 \rightarrow \dots \rightarrow 2 \rightarrow 1. \quad (2.35)$$

The mean lifetime of state  $i$  is  $\tau_i$ . Let  $N_0$  be the total number of nuclei that are in an excited state at  $t=0$  and let  $b_i$  be the fraction of excited nuclei that are in state  $i$  at  $t=0$ . The number of nuclei in the highest-lying state  $n$  at time  $t$ ,  $N_n(t)$ , is again given by Equations (2.33) and (2.34):

$$\begin{aligned} \dot{N}_n(t) &= -\frac{1}{\tau_n}N_n(t) \text{ and} \\ N_n(t) &= \frac{b_n N_0}{\tau_n} e^{-t/\tau_n}, \end{aligned} \quad (2.36)$$

but the number of nuclei in lower-lying states  $i < n$  is described by the differential equations

$$\dot{N}_i(t) = -\frac{1}{\tau_i}N_i(t) + \frac{1}{\tau_{i+1}}N_{i+1}(t). \quad (2.37)$$

The first term describes the de-population of state  $i$  by its decay, the second term describes its population by the decay of the next higher-lying state  $i+1$ . The

solution for the last state in the decay chain of Eq. (2.35),  $N_1(t)$ , is given by the general Bateman solution [Bat10, Pre02] for the initial conditions  $N_i(t) = \delta_{in} b_n N_0$ :

$$N_1(t) = \tau_1 b_n N_0 \sum_{m=1}^n K_{n,m} e^{-t/\tau_m} \text{ where} \quad (2.38)$$

$$K_{n,m} = \frac{\tau_m^{(n-2)}}{\prod_{\substack{j=1, \\ j \neq m}}^n (\tau_m - \tau_j)}.$$

For the more general initial conditions  $N_i(t) = b_i N_0$  with  $\sum_i b_i = 1$ , decay chains starting at every state  $i$  with  $b_i \neq 0$  have to be added up. The solution for every chain is given by Equation (2.38), and together with  $K_{1,1} = 1/\tau_1$ , the solution for the last state in the chain is given by

$$N_1(t) = \sum_i \tau_1 b_i N_0 \sum_{m=1}^i K_{i,m} e^{-t/\tau_m}. \quad (2.39)$$

If a state is fed by several chains that are not connected by decays between the chains, each chain can be regarded individually. The decay function  $N_1(t)$  of the last state in the decay-chains is then given by a sum of decays after direct population of that state as in Eq. (2.34) and by decays of that state after its population by each of the decay chains using Equation (2.39). This is depicted in Figure 2.1.

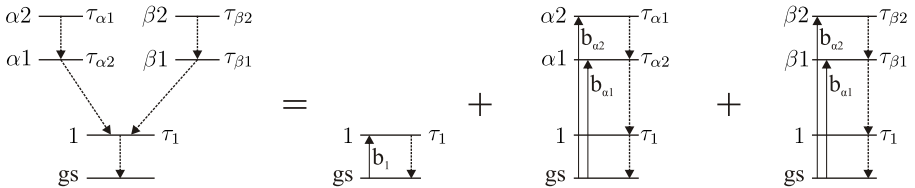


**Figure 2.1.:** Feeding of state '1' by two different decay chains,  $\alpha$  and  $\beta$ . If there are no transitions between the decay chains, the decay function  $N_1(t)$  of state '1' can be expressed as sum over the direct population of state '1' (Equation 2.34) and population by the decay chains  $\alpha$  and  $\beta$  (Equation 2.39).

If there are transitions between the different chains feeding a state, the set of differential Equations (2.37) has to be modified. Expressions for decay functions describing such "branching" feeding patterns can be found e.g. in Reference [Mor03].

---

## 2.3 Doppler effect and relativistic transformations

---

This chapter reviews relations from [Jac62, p. 360ff] and [Les10]. All effects and transformations are discussed in terms of  $\gamma$ -radiation emitted from a nucleus moving in the laboratory frame. The following notation is used:

- Quantities defined (measured) in the laboratory frame are labeled with the superscript  $L$ .
- Quantities defined (measured) in the rest frame of the recoiling nucleus are labeled with the superscript  $RN$ .
- Polar angles in spherical coordinates are denoted by  $\theta$ , azimuth angles by  $\phi$ .
- The direction of motion of the nucleus is denoted by  $(\theta_N, \phi_N)$  and its velocity relative to the laboratory frame is  $\beta = v/c$ .
- The emission direction of the  $\gamma$ -radiation is denoted by  $(\theta_\gamma, \phi_\gamma)$ .

### Doppler-effect

The energy of the  $\gamma$ -radiation emitted in the  $RN$  frame is  $E_0$ . Due to the relativistic Doppler-effect, a detector resting in the laboratory frame detects a shifted energy

$$E' = E_0 \frac{\sqrt{1 - \beta^2}}{1 - \beta \cos \alpha^L} \quad (2.40)$$

where  $\alpha^L$  is the angle between the nucleus' direction of motion and the emission direction of the  $\gamma$ -radiation, measured in the laboratory frame.  $\alpha^L$  can be calculated from the relation

$$\cos \alpha^L = \cos \theta_\gamma^L \cos \theta_N^L + \sin \theta_\gamma^L \sin \theta_N^L \cos(\phi_\gamma^L - \phi_N^L). \quad (2.41)$$

If the nucleus moves along the  $z$ -axis ( $\theta_N^{L,RN} = 0$ ), then  $\alpha^L = \theta_\gamma^L$ .

### Transformation of angles

Due to the relativistic length contraction, the angles  $(\theta_\gamma, \phi_\gamma)$  measured in the  $RN$  reference and in the laboratory frame are different. The relation between them is

$$\begin{aligned} \theta_\gamma^{RN} &= \cos^{-1} \left( \frac{\cos \theta_\gamma^L - \cos \theta_N^L [\beta\gamma - (\gamma - 1) \cos \alpha^L]}{\gamma(1 - \beta \cos \alpha^L)} \right) \\ \phi_\gamma^{RN} &= \tan^{-1} \left( \frac{\sin \theta_\gamma^L \sin \phi_\gamma^L - \sin \theta_N^L \sin \phi_N^L [\beta\gamma - (\gamma - 1) \cos \alpha^L]}{\sin \theta_\gamma^L \cos \phi_\gamma^L - \sin \theta_N^L \cos \phi_N^L [\beta\gamma - (\gamma - 1) \cos \alpha^L]} \right). \end{aligned} \quad (2.42)$$

$\gamma = (1 - \beta^2)^{-\frac{1}{2}}$  is the Lorentz-factor. If the nucleus moves along the  $z$ -axis ( $\theta_N^{L,RN} = 0$ ,  $\alpha^L = \theta_\gamma^L$ ), then Eq. 2.42 reduces to

$$\begin{aligned}\theta_\gamma^{RN} &= \cos^{-1} \frac{\cos \theta_\gamma^L - \beta}{1 - \beta \cos \theta_\gamma^L} \\ \phi_\gamma^{RN} &= \phi_\gamma^L\end{aligned}\quad (2.43)$$

### Transformation of solid angles

Due to the Lorentz-boost, a solid angle element  $d\Omega_\gamma^L$  in the laboratory system, located in the direction of  $\gamma$ -ray emission, transforms to a solid angle element  $d\Omega_\gamma^{RN}$  in the rest-frame of the recoiling nucleus by

$$d\Omega_\gamma^{RN} = \frac{1 - \beta^2}{(1 - \beta \cos \alpha^L)^2} d\Omega_\gamma^L. \quad (2.44)$$

A useful relation to the Doppler-formula, Eq. 2.40, is given by

$$\frac{d\Omega_\gamma^{RN}}{d\Omega_\gamma^L} = \left( \frac{E'}{E_0} \right)^2. \quad (2.45)$$

---

## 2.4 $\gamma$ -ray angular correlations

---

In this section, the discussion of the case of axially symmetric nuclear orientation is based on [Gro65, Yam67] and the discussion of particle-gamma angular correlations is based on [Ryb70].

When an excited nuclear state  $|J_i\rangle$  with total angular momentum  $J_i$  de-excites by the emission of  $\gamma$ -radiation into a final state  $|J_f\rangle$  with total angular momentum  $J_f$ , there is an angular correlation between the emission direction of the  $\gamma$ -ray and a chosen quantization axis. This angular correlation depends on the orientation of the emitting nucleus, i.e. its magnetic sub-state  $m_i \in (-J_i, \dots, J_i)$  w.r.t. the quantization axis, and the orientation of the final state, i.e. its magnetic sub-state  $m_f \in (-J_f, \dots, J_f)$  w.r.t. the quantization axis. The correlation function  $F_\lambda^\mu(\theta)$  is defined by the multipole order  $\lambda$  of the transition with  $|J_i - J_f| \leq \lambda \leq J_i + J_f$  and  $\mu = m_f - m_i$ :

$$\begin{aligned}F_\lambda^\mu(\theta) &= \frac{1}{2\lambda(\lambda+1)} \left[ (\lambda(\lambda+1) - \mu(\mu+1)) \left| Y_\lambda^{\mu+1}(\theta) \right|^2 \right. \\ &\quad \left. + (\lambda(\lambda+1) - \mu(\mu-1)) \left| Y_\lambda^{\mu-1}(\theta) \right|^2 + 2\mu^2 \left| Y_\lambda^\mu(\theta) \right|^2 \right].\end{aligned}\quad (2.46)$$

$\theta$  denotes the polar angle between the quantization axis and the emission direction of the  $\gamma$ -ray, and  $Y_\lambda^\mu(\theta)$  are spherical harmonics. This relation and all following equations in this section are valid in the rest frame of the emitting nucleus.

The magnetic sub-states of the nuclear levels involved are not directly accessible experimentally. Therefore, the description of the directional correlation of the emitted  $\gamma$ -radiation is expressed as an average quantity valid for ensembles of ions with a given distribution of orientations with respect to a given quantization axis. In the following, the coordinate system is chosen such that the quantization axis is aligned with the z-axis.

The quantization axis (and, hence, the z-axis) should be chosen such that the experimental situation exhibits the highest possible symmetry w.r.t. this axis. The beam axis, the direction of motion of an excited nucleus after the excitation reaction, the emission direction of  $\gamma$ -rays from preceding transitions or e.g. of electrons from populating  $\beta$ -decays are proper choices for the quantization axis.

### Nuclear orientation with axial symmetry

The relative population of a magnetic sub-state  $m$  w.r.t. a given quantization axis is denoted by  $a_m$  with the normalization  $\sum_{m=-J}^{m=+J} a_m = 1$ . If all magnetic sub-states are populated uniformly ( $a_m = (2J + 1)^{-1}$ ), the  $\gamma$ -ray emission occurs isotropically in the rest frame of the emitting nucleus. If there is a non-uniform population of magnetic sub-states,  $a_m \neq (2J + 1)^{-1}$ , the nuclei are *oriented*. In this case, the  $\gamma$ -ray emission will in general exhibit an angular distribution that is characteristic for  $J_i$ ,  $J_f$ ,  $\lambda$  and  $a_m$ . If the distribution of nuclear orientation exhibits axial symmetry w.r.t. the quantization axis and additionally  $a_m = a_{-m}$ , the nuclei are called *aligned*. For spins oriented preferably along the quantization axis ( $m = \pm J$  dominates) the alignment is called *prolate*, for orientation preferably perpendicular to the quantization axis ( $m = 0$  dominates) it is called *oblate*. If  $a_m \neq a_{-m}$  the nuclei are called *polarized*. Hence, the  $\gamma$ -ray emission is always isotropic for  $J_i = 0$  and  $J_i = \frac{1}{2}$ , if the nucleus is aligned, only. These different types of axially symmetric nuclear orientation are visualized in Figure 2.2.

Nuclear orientation can be effected by  $\gamma$ -ray transitions, radioactive decays or certain reactions such as Coulomb excitation (see Chapter 2.1) populating the state  $J_i$ .

In this paragraph, it is assumed that the nuclear orientation exhibits axial symmetry w.r.t. the quantization axis.

The degree of orientation of order  $k$ ,  $f_k(J)$ , can be expressed as

$$f_k(J) = \binom{2k}{k}^{-1} J^{-k} \sum_m \sum_{\nu=0}^k (-1)^\nu \frac{(J-m)!(J+m)!}{(J-m-\nu)!(J+m-k+\nu)!} \binom{k}{\nu}^2 a_m \quad (2.47)$$

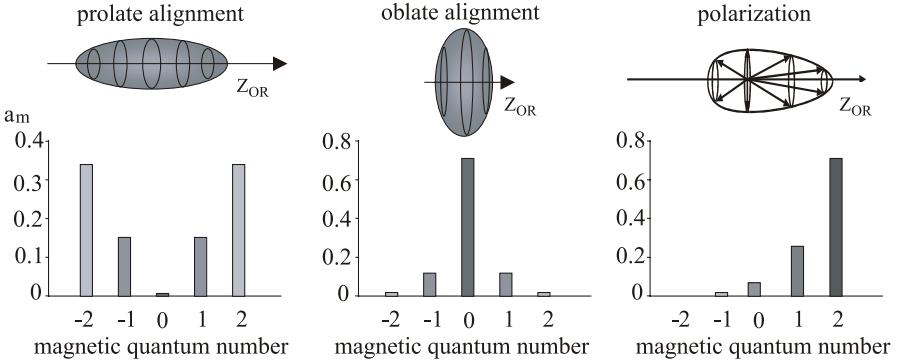


**Figure 2.2.:** Different types of axially symmetric nuclear orientation for a nuclear state with  $J_i = 2$ . The surfaces of the ellipsoids visualize the distribution of nuclear spin orientations. The figure was taken from [Ney03] and slightly modified. © IOP Publishing. Reproduced with permission. All rights reserved.

with  $k \geq 0$ . All  $f_k$  for  $k \geq 2J + 1$  vanish identically. In the case of nuclear alignment, all  $f_k$  with odd  $k$  vanish identically, and in the case of nuclear polarization, one or more  $f_k$  with odd  $k$  is different from zero. The statistical tensor  $\rho_k(J)$  is proportional to  $f_k(J)$  and given by

$$\rho_k(J) = \binom{2k}{k} J^k \sqrt{\frac{(2k+1)(2J+1)(2J-k)!}{(2J+k+1)!}} f_k(J). \quad (2.48)$$

If the initial state  $|J_i\rangle$  is populated by a preceding  $\gamma$ -ray transition from a nuclear state  $|J_0\rangle$ , then the relative population of the magnetic sub-states of the state  $|J_i\rangle$ ,  $a_{m_i}$ , can be calculated from the relative population of the magnetic sub-states of  $|J_0\rangle$ ,  $a_{m_0}$ , and the multipole order  $\lambda_0$  of the transition populating  $|J_i\rangle$ :

$$a_{m_i} = \sum_{m_0} a_{m_0} |\mathcal{C}_{J_0 m_0 \lambda_0 (m_i - m_0)}^{J_i m_i}|^2 \quad (2.49)$$

where  $\mathcal{C}_{j_1 m_1 j_2 m_2}^{J M} = \langle J M | j_1 m_1 j_2 m_2 \rangle$  is the Clebsch-Gordan coefficient for coupling  $|j_1 m_1\rangle$  and  $|j_2 m_2\rangle$  to  $|J M\rangle$ . For a chain of preceding transitions, Eq. (2.49) has to be applied repeatedly.

### Angular distribution in the polar angle $\theta$

Given the statistical tensor  $\rho_k(J_i)$  described above, the distribution  $W(\theta)$  of the emitted  $\gamma$ -radiation as a function of the polar angle  $\theta$  relative to the quantization axis can be expressed as

$$W(\theta) = \sum_k \rho_k(J_i) F_k P_k(\cos \theta). \quad (2.50)$$

$P_k(x)$  is the Legendre polynomial of order  $k$  and the  $F$ -coefficient  $F_k(\lambda \lambda' J_f J_i)$  is given by

$$F_k(\lambda \lambda' J_f J_i) = (-1)^{J_f - J_i - 1} \sqrt{(2\lambda + 1)(2\lambda' + 1)(2J_i + 1)} \mathcal{C}_{\lambda 1 \lambda' - 1}^{k 0} \mathcal{W}(J_i J_i \lambda \lambda'; k J_f) \quad (2.51)$$

where  $\mathcal{W}(j_1 j_2 J j_3; J_{12} J_{23})$  is Racah's  $W$ -coefficient. There exist plenty of tabulations<sup>1</sup> for  $\rho_k(J)$  and  $F_k(\lambda \lambda' J_f J_i)$ , e.g. [Yam67].

For pure transitions (only one multipole order occurs),  $\lambda' = \lambda$ . For mixed transitions ( $\lambda' = \lambda + 1$ ),  $F_k$  in Eq. (2.50) has to be replaced by

$$\left[ F_k(\lambda \lambda J_f J_i) + 2\delta_{\lambda'/\lambda} F_k(\lambda \lambda' J_f J_i) + \delta_{\lambda'/\lambda}^2 F_k(\lambda' \lambda' J_f J_i) \right] / (1 + \delta_{\lambda'/\lambda}^2). \quad (2.52)$$

$\delta_{\lambda'/\lambda}$  is the  $\lambda'/\lambda$  multipole mixing ratio (see Eq. 5.1).

It follows from the triangular condition for the Clebsch-Gordan coefficient in Eq. (2.51) that  $k \leq \lambda + \lambda'$ . For pure transitions, this means  $k \leq 2\lambda$ , and for mixed transitions with  $\lambda' = \lambda + 1$ , this means  $k \leq 2\lambda + 1$  (in practice, only the two lowest possible multipole orders play a role for the  $\gamma$ -transition).

Alternatively to Eq. (2.49), the population of the initial state  $|J_i\rangle$  by preceding  $\gamma$ -transitions  $\dots \rightarrow |J_1\rangle \xrightarrow{\lambda_1} |J_0\rangle \xrightarrow{\lambda_0} |J_i\rangle$  with multipolarities  $\lambda_n$  can also be taken into account in Eq. (2.50) by introducing a factor

$$U_k = U_k^0 U_k^1 \dots, \text{ where} \\ U_k^0 = \sqrt{(2J_0 + 1)(2J_1 + 1)} (-1)^{J_0 - J_i - \lambda_0} \mathcal{W}(J_0 J_0 J_i J_i; k \lambda_0) \text{ and} \quad (2.53) \\ U_k^n \text{ follow accordingly.}$$

In general, nuclei excited in a reaction where neither beam nor target are polarized will be aligned, only. As discussed above, all  $f_k$  and hence all  $\rho_k$  for odd  $k$  vanish identically in this case. Therefore, in this case, the angular distribution with respect to the beam axis can be written as

$$W(\theta) = 1 + \sum_{\text{even } k=2}^{2\min(L, J_i)} A_k P_k(\cos \theta) \quad (2.54)$$

with  $A_k = \rho_k(J_i) F_k$  and using the general property  $\rho_0 = F_0 = U_0 = 1$  as well as the conditions that  $k \leq 2J_i$ ,  $k \leq 2\lambda + 1$  and  $k$  even.

<sup>1</sup> In the tabulations,  $\rho_k(J)$  is often called  $B_k(J)$ , and  $F_k(\lambda \lambda' J_f J_i)$  is often called  $R_k(L L' J_f J_i)$

## Particle-gamma angular correlation

Up to here, it was assumed that there is axial symmetry of the nuclear orientation w.r.t. the quantization axis. This is the case if, for example, the orientation is realized by Coulomb excitation, the quantization axis is chosen to be the beam axis and the reaction products are not registered. However, if the reaction products are registered, a further directional correlation between the momentum vector of the excited particle and the emission directions of  $\gamma$ -rays can be observed. This correlation is called particle-gamma (p- $\gamma$ ) angular correlation.

Let the quantization axis be the beam axis and the origin be the vertex of the excitation reactions (and, for simplicity, also the emission point of the  $\gamma$ -rays). Let the excited nucleus be scattered into the direction  $(\theta_p, \phi_p = 0)$  (i.e. the azimuth scattering angle of the excited nucleus defines  $\phi = 0$ ), and let the  $\gamma$ -ray be emitted in the direction  $(\theta_\gamma, \phi_\gamma)$ . The p- $\gamma$  angular correlation describes a distribution of  $\gamma$ -ray intensity as a function of the azimuth angle  $\phi_\gamma$ , additionally to the angular distribution in the polar angle  $\theta_\gamma$ , as described in the previous paragraph.

The absence of the axial symmetry of the nuclear orientation w.r.t. the beam axis is reflected by a more general statistical tensor  $\rho_{kq}(J_i)$  with  $-k \leq q \leq k$ . It is related to a density matrix  $\rho_{mm'}$ , which can be considered as the extension of the relative population of the  $m$  sub-states  $a_m$  defined above. If axial symmetry is given,  $\rho_{mm'}$  is diagonal and  $\rho_{mm} \propto a_m$ . Generally, the statistical tensors  $\rho_{kq}(J_i)$  have to be calculated taking into account the excitation process (see [Ryb70] for a definition of  $\rho_{kq}$  and further details). In particular,

$$\rho_{00}(J_i) \propto \frac{d\sigma}{d\Omega_p} \quad (2.55)$$

where  $\frac{d\sigma}{d\Omega_p}$  denotes the differential excitation cross section. Computer codes for the calculation of excitation cross sections often also provide the statistical tensors  $\rho_{kq}$ . This is the case e.g. for the Coulomb-excitation code CLX (see Chapter 2.1 and [Owe]).

If the quantization axis is chosen to be the beam axis, it can be shown that all  $\rho_{kq}(J_i)$  are real (purely imaginary) if  $k$  is even (odd) [Ryb70]. Since only the case of nuclear alignment is discussed here, the following assumes that only even  $k$  occur (see paragraph “Nuclear orientation with axial symmetry”), and, hence,  $\rho_{kq}(J_i) \in \mathbb{R}$ .

With normalized statistical tensors

$$\hat{\rho}_{kq}(J_i) = \rho_{kq}(J_i) / \rho_{00}(J_i) \quad (2.56)$$

the p- $\gamma$  angular correlation can be expressed as

$$W(\theta_\gamma, \phi_\gamma) = 1 + \sum_{k \geq 2} \left( \hat{\rho}_{k0}(J_i) F_k P_k(\cos \theta_\gamma) + 2 \sum_{q > 0} \hat{\rho}_{kq}(J_i) F_k \cos(q\phi_\gamma) C_{kq}(\theta_\gamma, 0) \right) \quad (2.57)$$

where the  $C_{kq}(\theta_\gamma, 0)$  are related to associated Legendre functions  $P_k^q(x)$  by

$$C_{kq}(\theta_\gamma, 0) = (-1)^q [(k-q)!/(k+q)!]^{1/2} P_k^q(\cos \theta_\gamma), \quad \text{if } q \geq 0. \quad (2.58)$$

The first term in the sum of Eq. (2.57) describes the polar angular distribution of the  $\gamma$ -radiation and corresponds to Eq. (2.50). The second term describes the p- $\gamma$  angular correlation in the azimuth angle  $\phi_\gamma$ .

Via the  $C_{kq}(\theta_\gamma, 0)$ , the distribution in  $\phi_\gamma$  is a function of  $\theta_\gamma$ . The population of the  $m_i$  sub-states of  $|J_i\rangle$  is a function of the scattering angle  $\theta_p$  of an excitation reaction. Therefore, both the  $\gamma$ -ray angular distribution in  $\theta_\gamma$  and the p- $\gamma$  angular correlation in  $\phi_\gamma$  are functions of  $\theta_p$ .

### Normalization and transformation

Strictly speaking, the  $\gamma$ -ray angular distribution (Eqs. 2.50 and 2.54) and the p- $\gamma$  angular correlation (Eq. 2.57) have to be understood as emission densities into a solid angle element  $d\Omega$ , i.e. as functions

$$\frac{dW}{d\Omega}(\theta) \quad \text{and} \quad \frac{dW}{d\Omega}(\theta, \phi).$$

Their normalization is given by

$$\int_{\Omega} W(\theta) d\Omega = \int_{\Omega} W(\theta, \phi) d\Omega = 4\pi. \quad (2.59)$$

The above equations describe the  $\gamma$ -ray angular correlations in the rest frame of the emitting nuclei. If  $\gamma$ -radiation is emitted from nuclei in flight, the  $\gamma$ -ray angular correlations have to be transformed to the laboratory system in order to make a connection with experiments. Using the notations of Sec. 2.3, this transformation is given by

$$W(\theta_\gamma^L, \phi_\gamma^L) = W(\theta_\gamma^{RN}, \phi_\gamma^{RN}) \frac{d\Omega_\gamma^{RN}}{d\Omega_\gamma^L}. \quad (2.60)$$

Expressions for  $\theta_\gamma^L$  and  $\phi_\gamma^L$  in terms of  $\theta_\gamma^{RN}$  and  $\phi_\gamma^{RN}$  are given in Eqs. (2.42) and (2.43), and an expression for  $d\Omega_\gamma^{RN}/d\Omega_\gamma^L$  is given in Eq. (2.44).

The above coordinate transformations is well suited for numerical calculations or if a transformation of angular correlations can be done on an event-by-event basis. However, the closed analytical expressions of Eqs. (2.50) and (2.57) in terms of spherical harmonics, or rather in terms of  $P_n(\cos \theta)$  and  $P_k^q(\cos \theta)$  that can easily be expressed in terms of spherical harmonics, are generally lost after these transformations of coordinates. There exist approximate expressions for coordinate transformations of angular correlations in terms of spherical harmonics [Les10] that are accurate within 1% at moderate ion velocities up to  $\sim 15\%$ . However, simple analytical expressions can be derived in some special cases, e.g. if particular particle scattering angles are selected by particle detectors with small solid angle [Kra73] or if particle detectors with rotational symmetry w.r.t. the beam axis (like annular detectors) are used [Wol92, p. 116].

Alternatively, it may be desirable to change the quantization axis and calculate the angular correlations w.r.t. the new quantization axis. This is the case e.g. if statistical tensors are provided by a computer code with the direction of motion of an excited nucleus after an excitation reaction as quantization axis, but the angular correlations are to be evaluated in the laboratory frame w.r.t. the beam axis, independent from individual particle scattering directions. A change of quantization axis can be done by rotating the statistical tensor  $\rho_{kq}$  by the Euler angles  $(\phi, \theta, \psi)$ :

$$\rho'_{kq'} = \sum_q \rho_{kq} \mathcal{D}_{qq'}^{k*}(\phi, \theta, \psi). \quad (2.61)$$

Here,  $\mathcal{D}_{qq'}^{k*}(\phi, \theta, \psi)$  denotes the complex conjugate of the  $\mathcal{D}$ -function [Boh69, eq. (1A-38)].

---

## 3 $\gamma$ -ray tracking arrays

In this chapter, the generation of arrays of high-purity germanium (HPGe) detectors preceding  $\gamma$ -ray tracking arrays is discussed in Section 3.1. The transition from arrays of segmented detectors to  $\gamma$ -ray tracking arrays is described in Section 3.2. The main procedures applied in  $\gamma$ -ray tracking arrays, Pulse-Shape Analysis and tracking, are introduced in Section 3.2.1 and 3.2.2, respectively. The implementation of the concept of  $\gamma$ -ray tracking in the detector arrays AGATA and GRETA is presented in Section 3.3, followed by a discussion of the experimental possibilities arising from the development of  $\gamma$ -ray tracking arrays in Section 3.4.

The discussion of HPGe detectors in general is based on References [Ebe08, Lee03, Kno10], if not stated otherwise. The description of  $\gamma$ -ray-tracking detectors follows References [Akk12, Sim08, Wei03, Mic13].

---

### 3.1 Arrays of high-purity germanium detectors

---

Superb energy resolution for  $\gamma$ -rays in the order of 2% FWHM at 1.3 MeV photon energy is achieved with HPGe detectors. Therefore, these semiconductor radiation detectors are frequently used in  $\gamma$ -ray spectroscopy experiments since they were developed in the 1970's. The total detection efficiency achievable with arrays of HPGe detectors is mainly determined by the total amount of active detector material and the total solid angle covered by the detectors. The peak-to-background ratio and, hence, the experimental sensitivity to discrete  $\gamma$ -ray lines can be enhanced by identifying and rejecting  $\gamma$ -rays that escape from the active germanium detector material after depositing part of their energy by Compton scattering or pair production. This technique of Compton suppression is based on high-Z scintillation detectors placed around the HPGe detectors. If  $\gamma$ -rays deposit energy in these so-called anti-Compton shields, events where energy is coincidentally deposited in adjacent HPGe detectors are rejected.

Large  $4\pi$ -arrays of Compton-suppressed HPGe detectors were built and started operation in the 1990's. Their development was driven by the need to detect many coincident  $\gamma$ -rays from the decay cascades of excited nuclear states at high spin, so-called super- and hyperdeformed states [Nya84, GU93]. This application also calls for a high segmentation of the detectors arrays, achieved mainly by the combination of many individual detectors. The most advanced detector arrays of that

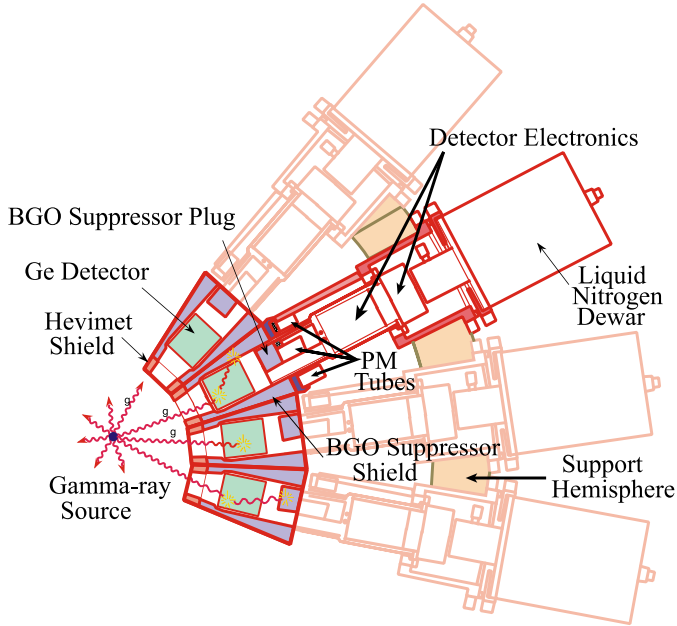


**Figure 3.1.:** Technical drawing of a part of the GAMMASPHERE detector array, consisting of 110 Compton-suppressed HPGe detectors. Figure reprinted from [Ebe08] with permission from Elsevier and slightly modified. See text for details.

kind are GAMMASPHERE [Lee97] (see Figure 3.1) which started operation at the Lawrence Berkeley National Laboratory (LBL), CA, USA, in 1993 and the EUROBALL III spectrometer [Sim97] which started operation at the Legnaro National Laboratory (LNL), Italy, in 1997.

At 1.3 MeV  $\gamma$ -ray energy, both systems have a total photopeak detection efficiency for  $\gamma$ -rays close to 10% and peak-to-total ratios around 65%. The germanium detectors of GAMMASPHERE and EUROBALL III cover 47% and 45% of the full  $4\pi$  solid angle, respectively. The remaining space is occupied to a large extent by the Compton suppressors. A granularity beyond the size of the germanium crystals is achieved by electric segmentation of the outer contacts of some of the GAMMASPHERE detector crystals. While each GAMMASPHERE detector is surrounded by an own Compton suppressor, the CLOVER detectors close to the  $\theta = 90^\circ$  position of EUROBALL III and the CLUSTER detectors at its backward angles are compos-

---

ite detectors, where multiple crystals share one Compton suppressor. In addition to the Compton suppression discussed previously, the full energy of  $\gamma$ -ray photons Compton-scattered between the multiple crystals of a composite detector is reconstructed by adding back the energy deposited in the individual crystals. This method is called Add-Back and is also applied in several subsequently developed detector arrays, such as the MINIBALL-array of composite, segmented detectors [War13].

Significantly higher sensitivity in terms of detection efficiency can only be achieved by covering a larger fraction of the total solid angle by active HPGe detectors. Hence, an "ultimate" HPGe detector array would consist of a full shell of germanium detectors without any Compton suppressors in between them. Theoretically, such an arrangement would have a total photopeak detection efficiency of 40-60%.

The problem with such a germanium shell is the impossibility to distinguish between cases where a single  $\gamma$ -ray emitted from the target position would scatter between two adjacent detectors and two  $\gamma$ -rays depositing their full energy in two neighboring detectors. This problem is also present in the EUROBALL CLUSTER detectors. It can only be overcome with a very high segmentation of a full germanium shell into 1000 detectors or more, making it unlikely that multiple  $\gamma$ -rays hit the detector coincidentally in neighboring crystals. This solution is financially excessively demanding and was not further pursued. Another approach to this problem is the concept of  $\gamma$ -ray tracking in highly segmented detectors, as discussed in the following paragraph.

The development of HPGe detector technology and its culmination in  $\gamma$ -ray tracking arrays is reviewed in References [Ebe08, Lee03].

---

### 3.2 From segmented detectors to $\gamma$ -ray tracking arrays

---

A  $\gamma$ -ray tracking array is a  $4\pi$  sphere of electrically highly segmented HPGe detectors. The segmentation is both in the longitudinal ("slices") and transverse ("pie sectors") direction of the germanium crystals (see Figure 3.2). The problem of assigning energy depositions in multiple detector segments to one or multiple  $\gamma$ -rays is approached by measuring the energy deposition, time and position of each interaction of  $\gamma$ -quanta in the detector material with high precision. The sequence of the interactions of a  $\gamma$ -quantum in a detector crystal is much faster than the time resolution of the detector. Therefore, it has to be determined by a software algorithm that also allows to distinguish between the interaction of a single or multiple  $\gamma$ -quanta with the detector material. This procedure is called tracking.

A precision for the determination of the interaction points of  $\gamma$ -rays inside the de-

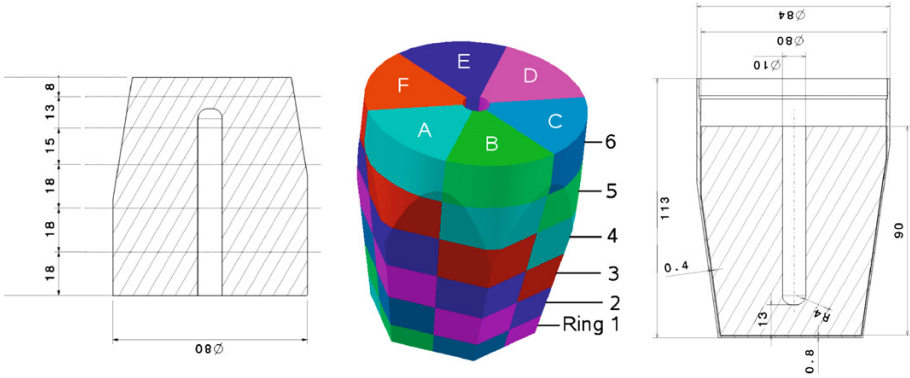


**Figure 3.2.:** Dimensions (left), 36-fold segmentation (center) and encapsulation (right) of an AGATA HPGe crystal. Dimensions are in millimeter. Figure reprinted from [Wie10] with permission from Elsevier.

tector better than the geometrical size of the segments can be achieved by the technique of Pulse Shape Analysis (PSA). This technique is based on the analysis of the temporal evolution of the electrical signals measured at the central contact of the detector crystal and at the contact of each segment.

---

### 3.2.1 Pulse Shape Analysis

---

When  $\gamma$ -rays deposit energy in a HPGe detector crystal, electron-hole pairs are created. These positive and negative charge carriers are separated by an applied high voltage and are collected in the inner (core, anode) and outer (segment, cathode) contacts. Before the charges are collected, they influence mirror charges on the inner and outer contacts, also in neighboring segments. The magnitudes of the mirror charges depend on the geometry of the crystal, but they are generally large if the charge is close to the contact, and small if it is far away from it. As long as positive and negative charge carriers are located at the same point, the influenced mirror charges compensate. Once they are separated, influenced mirror charges can be registered at the contacts due to the different positions of the positive and negative moving charges. If the negative charges approach the anode, they influence a positive mirror charge on it. That means that electrons drain off the anode. They are measured as negative charge in a preamplifier connected to the anode. The opposite occurs when the holes approach the cathode. Once the moving charge carriers reach the contacts, they compensate the mirror charges they had influenced.

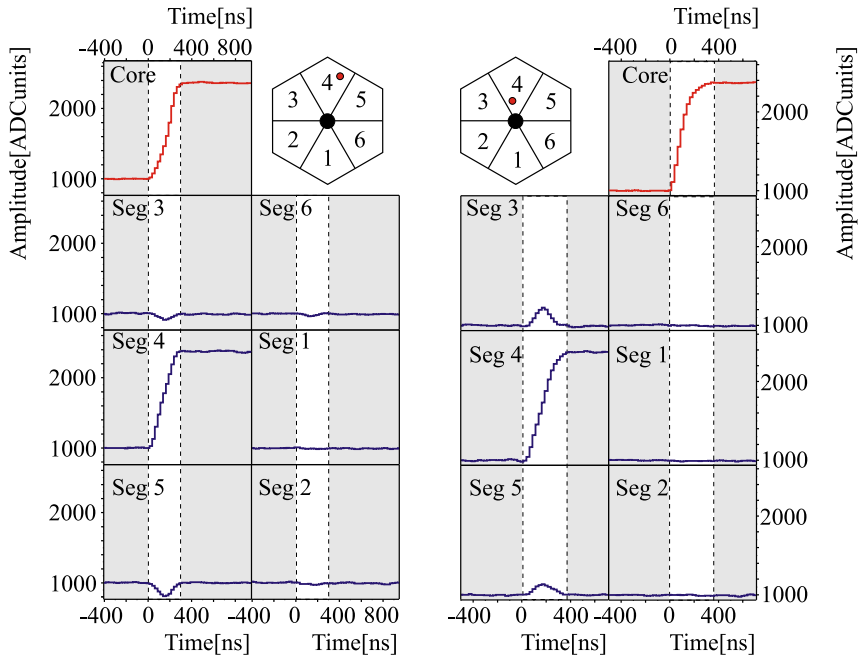


**Figure 3.3.:** Sketch of electric signals for two events registered in a segmented detector (left and right). In both cases, the energy is deposited in segment 4 (red dots). Net charges are registered in the core (red lines) and in segment 4. In neighboring segments, signals are induced by mirror charges (blue lines). Their relative amplitude is used to deduce the angle coordinate of the location of the energy deposition, and the radial coordinate is deduced from the time evolution of the net charge signal in the core. The figure was taken from Reference [Wei03] and slightly modified. See text for details.

Based on this interplay of the mirror charges influenced by the electrons and holes, the distance of an energy deposition from the electrodes can be inferred from the temporal evolution of the charge signals measured in the electrodes. This is exemplified in Figure 3.3. The top row shows the charge signal measured in the core contact. On the left side, signals are shown for an event where energy is deposited close to the outer contact. The holes are collected in the cathode of segment 4 very soon after the creation of the electron-hole pairs. The remaining electrons induce a positive mirror charge in the anode, which is measured as a negative charge in the

---

preamplifier as discussed above. This mirror charge slowly grows larger as the electrons approach the electrode. On the right hand side of Figure 3.3, the electrical signal measured for an event with energy-deposition close to the central contact is shown. Soon after the creation of the electron-hole pairs, the electrons reach the anode, resulting in a fast rise of the charge signal. The positive charges that move away from the central contact induce a negative mirror charge in the central contact, which is measured as a positive charge in the preamplifier. Therefore, the mirror charge influenced by the holes reduces the charge measured in the central contact. The magnitude of the mirror charge influenced by the holes decreases as the holes move to the outer cathode. Therefore, the reduction of the charge measured in the central contact decreases as the holes move towards the cathode.

Summarizing the above, an energy deposition close to the core contact results in a fast rise of the charge measured in the core preamplifier, an energy deposition at larger radii results in a slower rise of the measured charge.

Of course, the moving positive and negative charge carriers influence mirror charges not only in the electrodes of the segment in which the electron-hole pairs were created, but also in the electrodes of the neighboring segments. On the left side of Figure 3.3, the interaction is closer to segment 5 than to segment 3. In consequence, the influenced mirror charges in segment 5 are larger than in segment 3. Since the holes are collected soon after the interaction due to the close proximity to the outer contact, the positive mirror charges caused by the negatively charged electrons persist, resulting in negative charges measured in the preamplifiers of the cathodes. In contrast, the interaction close to the core and closer to segment 3 than to segment 5 on the right hand side of Figure 3.3 results in positive charges measured in the segments, and a larger signal is measured in segment 3 than in segment 5. By this relative amplitudes of the charge signals measured in the segment cathodes, a sensitivity to the polar coordinate of the interaction point is given. Sensitivity to the  $z$ -coordinate of the interaction arises in the same way from the longitudinal segmentation of the detector crystals as shown in Figure 3.2.

The discussed sensitivity of the charge signals measured in the central contact and the segment electrodes is used by the Pulse Shape Analysis to determine the three-dimensional position of the interactions of  $\gamma$ -rays in the detector crystal. If multiple interactions occur, the measured signals are superpositions of the discussed pulse shapes. In practice, the position determination is done by comparing measured signals to a database of reference signals for interactions at different, known positions in the detector crystal. Ideally, these databases are obtained from experimental data. This data is obtained by "scanning" the HPGe crystals with collimated  $\gamma$ -rays from sources, see e.g. [Dim09, Ha13, Goe13]. However, since this scanning proce-

---

ture is extremely time-consuming, calculated signal bases are usually used, where parameters defining the individual properties of the crystal such as the orientation of the crystal lattice and properties of the individual electronics channels such as crosstalk, preamplifier integration times and noise are obtained from a few experimental data points [Bru06a, Bru06b, Sch11a].

A variety of PSA algorithms for the comparison of pulse shapes in data bases with pulse shapes measured for individual events with the purpose to determine the interaction points of the registered  $\gamma$ -radiation has been developed. Examples are the adaptive Grid-Search [Ven04], the Particle-Swarm algorithm [Sch11b] or the Matrix Method [Ola06]. These algorithms differ by their demand in computing power and obtained position resolution, both for single hits per segment and for the case of multiple hits per segment. They are compared in Reference [Akk12]. A Position resolution in the order of 5 mm FWHM can be achieved for single-hit events. For details on the PSA, the reader is referred to the given references.

---

### 3.2.2 Tracking

---

The main interactions of  $\gamma$ -radiation with matter at the energies relevant for  $\gamma$ -ray spectroscopy of  $\sim 100$  keV to  $\sim 5$  MeV are the photoelectric effect, Compton scattering and pair production (see Figure 3.4 and Reference [Kno10] for details). The different interactions imply certain patterns of energy deposition and relations between the locations of energy deposition in subsequent interactions, as indicated on the left-hand side of Figure 3.5.

The leftmost drawing in Figure 3.5 illustrates the photoelectric effect. If it occurs, the full photon energy is deposited in one single, isolated interaction point. This process is dominant at photon energies below  $\sim 100$  keV. The central sketch in Figure 3.5 illustrates the hit pattern expected for Compton scattering events. Compton scattering is the dominant process for the photon energies relevant to  $\gamma$ -ray spectroscopy of  $\sim 100$  keV to  $\sim 10$  MeV. It usually results in a sequence of Compton scattering events where the photon energy is partially deposited at nearby sites before the remaining photon energy is fully deposited by a photoelectric effect. For example, a  $\gamma$ -ray with an energy of 1.3 MeV will undergo on average 3 Compton scattering events before the residual photon energy is fully absorbed by the occurrence of a photoelectric effect [Lee03]. Hereby, the scattering angle of the photon is correlated to the energy deposited in the detector in one Compton scattering event. The relation is given in the figure. On the right-hand side of the left part of Figure 3.5, the hit pattern expected of a pair production event is sketched. In this process, the total photon energy minus  $2 \times m_e c^2 = 1022$  keV needed to create an electron-positron pair is deposited in one interaction point. Two 511-keV  $\gamma$ -rays are created at approximately the same spot by the annihilation of the produced

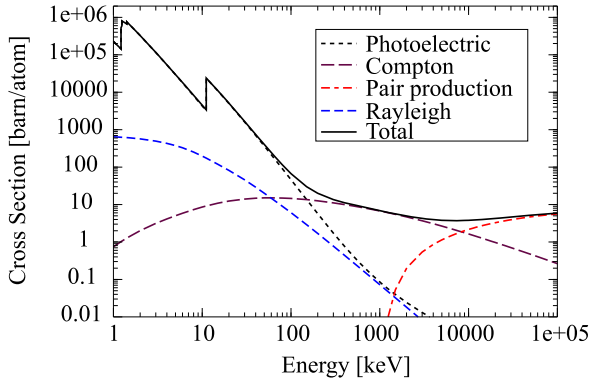


**Figure 3.4.:** Cross-section of the main processes for  $\gamma$ -ray-interaction with germanium. The figure was taken from Ref. [Mic13] and slightly modified. See [Kno10] for details.

positron. These two 511-keV  $\gamma$ -rays emitted in opposite directions in turn create new clusters of interaction points in vicinity to the site of pair production. The pair production process is dominant at photon energies exceeding  $\sim 10$  MeV.

It is the task of tracking algorithms to recognize these patterns in the set of interaction points and energy depositions provided by the Pulse Shape Analysis. From these patterns, the tracking algorithms identify the number of  $\gamma$ -rays that have been detected in an event, the sequence of their interactions and, thereby, their path in the detector crystals as well as the total energy deposited by each  $\gamma$  quantum. This is done by testing permutations of the sequence of the interactions for physical plausibility, assuming that the  $\gamma$ -rays have been emitted at a defined source position - usually the position of the reaction target. For the photoelectric effect, the plausibility can be tested in terms of the likelihood of the path length traveled by the photon in the germanium crystal before the interaction took place. For Compton scattering, plausibility of an interaction sequence can be checked by the relation of scattering angle and energy deposit in Compton scattering events, while for the pair production the deposit of the total energy minus 1022 keV in a central interaction point accompanied by the deposition of two times 511 keV at opposite sides is a good feature for identification.

In reality, often several  $\gamma$ -ray-quanta are detected simultaneously. Their interaction points have to be assigned to individual  $\gamma$ -rays by the tracking algorithm. The number of possible permutations for the sequence of identified interaction points

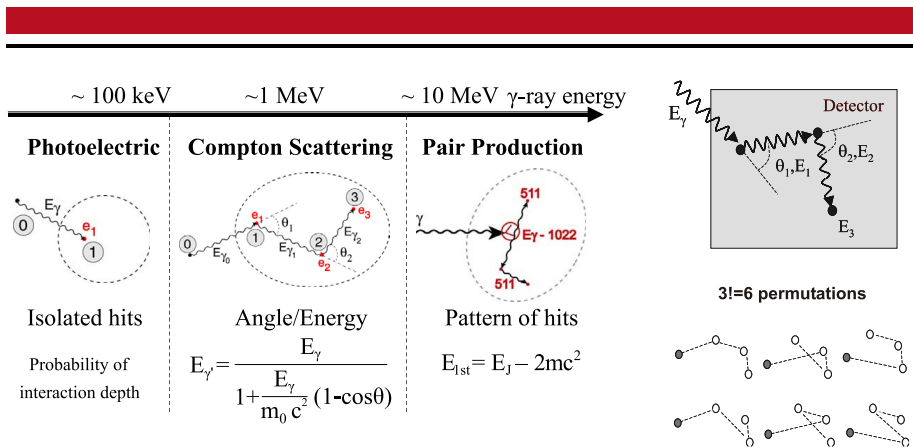


**Figure 3.5.:** Left: Expected interaction pattern for the three most important interactions of  $\gamma$ -rays with matter at the energies relevant for  $\gamma$ -ray spectroscopy and criteria for their identification (bottom). Figure reprinted from [Baz04] with permission from Elsevier and slightly modified.

Right: Permutations for an event with two Compton scattering events of a  $\gamma$ -ray, followed by its absorption by the photoelectric effect. The correct sequence of interactions can be inferred from the relation between Compton scattering angle and energy transfer (see middle part of left figure). See text for details. The figure was taken from Ref. [Lee03]. © IOP Publishing. Reproduced with permission. All rights reserved.

and their assignment to different  $\gamma$ -rays may become very large. For example, for the detection of 5  $\gamma$ -rays with an energy of 1.3 MeV each,  $5 \times 4 = 20$  interaction points are expected in total. The number of possible permutations of the interaction points and their assignment to different  $\gamma$ -rays exceeds  $10^{13}$  in this case<sup>1</sup>, rendering a test of every permutation practically impossible.

Therefore, the set of interaction points identified by the PSA is grouped into clusters as shown in Figure 3.6. One way to define these clusters is to assume that the interaction points belonging to one  $\gamma$ -ray lie within a certain solid angle, defined from the perspective of the assumed  $\gamma$ -ray vertex [LM04, Sch99]. This assumption is justified to a large extent by the relatively short mean-free path of  $\gamma$ -rays in germanium ( $\sim 2.5$  cm for 1.3 MeV photons [Rec09b]) and the fact that the dominant

<sup>1</sup> The number of possible permutations can be calculated [Mic13] by  $\sum_k S_n^k$ , where  $n$  is the number of  $\gamma$ -ray interaction points and  $S_n^k$  is the Stirling number of second kind giving the number of permutations for partitioning  $n$  objects into  $k$  non-empty subsets.

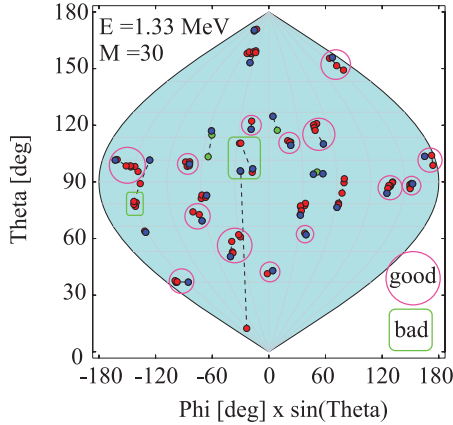


**Figure 3.6.:** Simulated interaction points of 30  $\gamma$ -rays with an energy of 1.33 MeV in an ideal  $4\pi$  germanium-shell. In polar coordinates with the origin at the  $\gamma$ -ray vertices, the interaction points form clusters. These are recognized by tracking-algorithms in order to deduce the number of  $\gamma$ -rays in an event and to reduce the number of permutations for the sequence of interactions. Nearby interactions of different  $\gamma$ -rays may lead to wrong assignments. The figure was taken from Ref. [Rec08] and slightly modified. See text for details.

effect at the relevant  $\gamma$ -ray energies, the Compton scattering, peaks under forward direction, the photoelectric effect results in an isolated interaction and the pair production also results in a relatively localized energy deposition, as shown in Figure 3.5. The possibility to scatter photons across a detector sphere, e.g. by Compton scattering, also has been taken into account in the clustering procedure. Alternative procedures for defining clusters of interaction points have been developed, see e.g. [Sul10, Did10].

Each of the clusters is assumed to contain the interaction points belonging to one single  $\gamma$ -ray emitted at a defined source position, and the number  $n!$  of permutations for the sequence of these  $n$  interaction points is manageable to test for plausibility. If no plausible sequence of the interaction points can be found, the clustering of all interactions may be modified.

This ansatz for tracking is denoted *forward tracking* and is implemented in several algorithms [Sch99, LM04, Piq04, Baz04]. An alternative ansatz, the *backward tracking* [Mar99, Mar02, Mil03] starts with searching an interaction point with  $\sim 100$ -250 keV energy deposition and assuming that this interaction point refers to

---

a photoelectric effect occurring at the end of the sequence of interactions. This approach is based on the observation that the last interaction in a sequence, the photoelectric effect, usually deposits  $\sim 100\text{-}250$  keV energy, irrespective of the original photon energy [Mar99]. The sequence of interactions is then reconstructed "backward", starting from that designated last interaction point. However, the forward-tracking algorithms have been shown to be more efficient for most applications [LM04].

The superb position resolution of about 5 mm FWHM that can be achieved by the PSA and the possibility to identify the first interaction points of  $\gamma$ -rays in the detector by tracking not only makes  $\gamma$ -ray tracking arrays very efficient and sensitive  $\gamma$ -ray spectrometers for experiments where high  $\gamma$ -ray multiplicities are measured, it also qualifies them as perfect tools for in-beam  $\gamma$ -ray spectroscopy of fast-moving ions. In such experiments,  $\gamma$ -rays are emitted by excited ions in-flight. Their spectroscopy demands a correction of the Doppler shift of the  $\gamma$ -ray energies that was discussed in Section 2.3.

The precision of that Doppler correction and, hence, the resolution of the Doppler-corrected  $\gamma$ -ray spectrum sensitively depends on the position resolution of the  $\gamma$ -ray detectors, since the Doppler effect is a function of the angle  $\alpha$  between the direction of motion of the emitting nucleus and the emission direction of the  $\gamma$ -ray (see Equation 2.40). The impact of the position resolution of the detector on the achievable resolution is demonstrated in Figure 3.7 and the experimental confirmation of the superb gain in energy resolution after Doppler correction by the position resolution of  $\gamma$ -ray tracking arrays is demonstrated in Figure 3.10.

---

### 3.3 AGATA and GRETA

---

The concept of  $\gamma$ -ray tracking introduced in the previous sections is currently being realized in two large-scale projects: The Gamma-Ray Energy Tracking Array (GRETA) [Lee03, Pas13] in the USA and the Advanced GAMMA Tracking Array (AGATA) [Akk12] in Europe. Both systems exhibit a very similar design with minor differences in the geometry of the HPGe crystals and aspects of the electronics. The main difference in the readout electronics used for AGATA and GRETA is that GRETA uses warm FETs for the preamplifiers reading out the segment contacts for easier maintenance and cold FETs only for the preamplifiers reading out the core signals, whereas AGATA uses cold FETs for all preamplifiers. The AGATA array will consist of 180 HPGe crystals with three different hexagonal, tapered shapes and 36-fold segmentation, arranged in 60 triples of crystals [Wie10] sharing one cryostat each. The shapes of the crystals are shown in Figure 3.8 together with the geometry of the full detector array. In contrast, GRETA will consist of 120 HPGe crystals



$$\Delta E^2 = \left( \frac{\partial E'}{\partial \beta} \Delta \beta \right)^2 + \left( \frac{\partial E'}{\partial \alpha} \Delta \alpha \right)^2 + \Delta E_{intr}^2$$

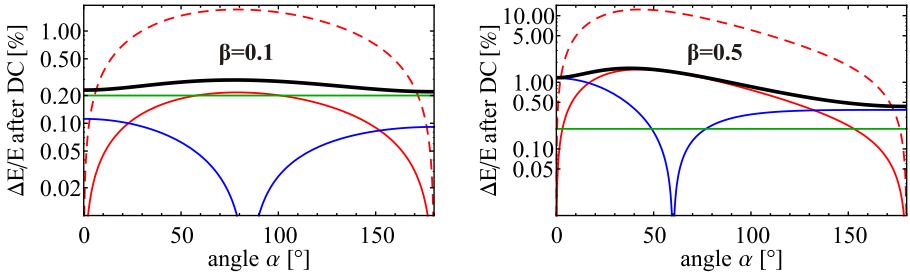


**Figure 3.7.:** Contributions to the energy resolution  $\Delta E$  obtained after Doppler correction (DC) as a function of the angle  $\alpha$  between the direction of motion of the emitting nucleus and the emission direction of the  $\gamma$ -ray (top formula). Green: Intrinsic energy resolution of HPGe detectors of  $\Delta E_{intr}/E \approx 2\%$ . Blue: Contribution by the relative uncertainty of the (measured) velocity of the emitting ion, assumed to be  $\Delta\beta/\beta = 1\%$ . Red: Contribution by the uncertainty of the (measured) angle  $\alpha$ , dominated by the uncertainty of the first interaction point of the  $\gamma$ -ray in the detector. Solid line: Position resolution  $\Delta x = 5$  mm as obtained in  $\gamma$ -ray tracking arrays, dashed line: Position uncertainty given by the size of the detector crystal,  $\Delta x = 40$  mm. A target-detector distance of 23.5 cm was assumed. Black line: Energy resolution  $\Delta E$  accounting for all contributions. Plots are shown for emitter velocities of 10% (left) and 50% (right) of the speed of light. Note the logarithmic scale of the Y-axes.

with two different hexagonal, tapered shapes and 36-fold segmentation arranged into 30 clusters, each containing four crystals sharing one cryostat. Due to these chosen geometries and the maximum size of HPGe crystals that can be manufactured, the inner radius of the GRETA array of about 18 cm will be slightly smaller than the inner radius of AGATA of 23.5 cm. From extensive Monte-Carlo simulation studies, a total photopeak detection efficiency of 43(28)% and a peak-to-total ratio of 59(43)% is expected at  $\gamma$ -ray multiplicity  $M_\gamma = 1(30)$  for the full AGATA array at a  $\gamma$ -ray energy of 1 MeV [Far10]. The same simulation applied to the geometry chosen for GRETA yields a total photopeak detection efficiency of 37(22)% and a peak-to-total ratio of 52(44)% is expected at  $\gamma$ -ray multiplicity  $M_\gamma = 1(30)$  and a  $\gamma$ -ray energy of 1 MeV [Far10].

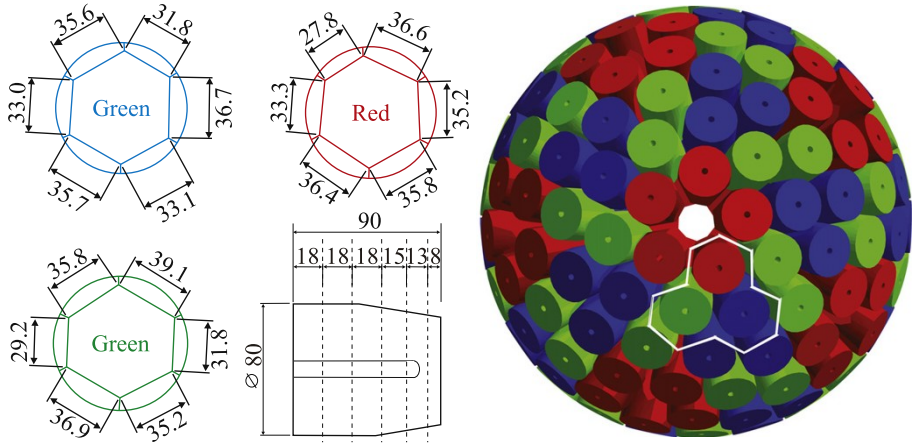


**Figure 3.8.:** Left: Geometry of the three slightly different hexagonal, tapered, 36-fold segmented HPGe crystals of AGATA, denoted as red, green and blue geometry, respectively.

**Right:** Geometry of all 180 crystals forming the full AGATA array. They are arranged in triple-clusters as indicated by the white line. The sphere is only interrupted by 12 pentagons (white spot) used for feeding through the beam pipe and instrumentation for target operation, beam diagnostics etc.

The figures were taken from Reference [Akk12] and slightly modified.

In a first stage, sub-arrays of both systems were built: The AGATA demonstrator consisting of 5 triple cluster with in total 15 crystals, and GRETINA [Lee04] with in total 28 crystals arranged in seven clusters. First experiences with both first-stage arrays have been made (see e.g. [Akk12, Pas13] and references therein). First physics experiments with the AGATA demonstrator were conducted at the Legnaro National Laboratory (LNL) in late 2010. An experiment employing the AGATA demonstrator at LNL conducted in 2011 is presented in this thesis in Chapter 6.1. First physics experiments employing GRETINA were conducted at the National Superconducting Cyclotron Laboratory (NSCL) at Michigan State University in mid of 2012. Figure 3.9 shows photographs of the first-stage arrays AGATA demonstrator and GRETINA.

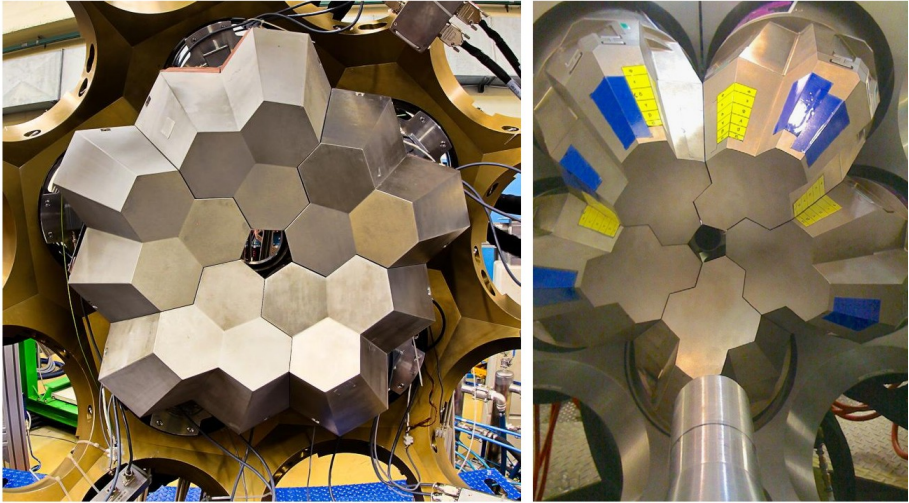


**Figure 3.9.:** **Left:** AGATA demonstrator with 15 crystals arranged in 5 triple-clusters. Photograph provided by Daniele Ceccato, University of Padova and INFN-LNL.  
**Right:** GRETINA with 20 crystals arranged in 5 clusters. Figure reprinted from [Pas13] with permission from Elsevier.

The superb capabilities for Doppler correction of the energy of  $\gamma$ -rays emitted in-flight have been demonstrated by experiments with a prototype AGATA triple-cluster detector at the university of Cologne [Rec08, Rec09b]. The Doppler-corrected  $\gamma$ -ray peak from the decay of the 1382-keV first excited  $3/2^-$ -state of  $^{49}\text{Ti}$ , populated in the transfer reaction  $^{48}\text{Ti}(d,p)^{49}\text{Ti}$ , is shown in Figure 3.10. Doppler correction has been performed using the position of the center of the hit crystals only, of the hit segments only, and using the position information provided by PSA employing the adaptive grid search algorithm [Ven04]. Energy resolutions of 35 keV, 14 keV and 4.8 keV FWHM have been obtained, respectively [Rec08]. The value obtained after PSA is in accordance with the design goal of a position resolution of 5 mm FWHM [Rec08, Rec09b].

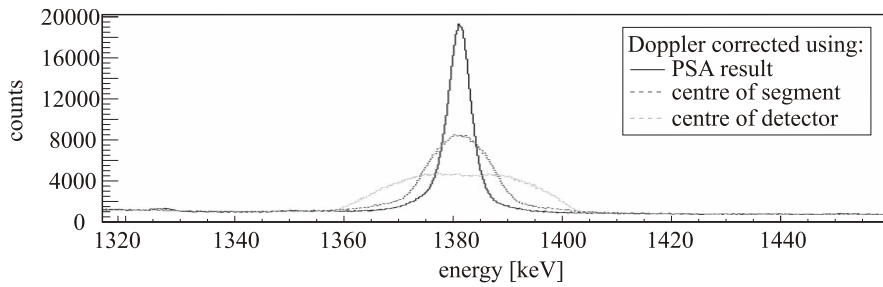


**Figure 3.10.:** Doppler-corrected  $\gamma$ -ray peak from the decay of the 1382-keV first excited  $3/2^-$ -state of  $^{49}\text{Ti}$  observed in a prototype AGATA detector. Doppler correction has been performed using the position of the center of the hit crystals only, of the hit segments only, and using the position information provided by PSA using the adaptive grid search algorithm [Ven04]. Energy resolutions of 35 keV, 14 keV and 4.8 keV FWHM have been obtained. Figure reprinted from [Rec09b] with permission from Elsevier and slightly modified. See text for details.

### 3.4 Possibilities arising from $\gamma$ -ray tracking arrays

The detection efficiency, peak-to-total ratio and energy resolution after Doppler correction of the energy of  $\gamma$ -rays emitted in-flight that are achievable with  $\gamma$ -ray tracking arrays such as AGATA and GRETA greatly enhance the sensitivity in  $\gamma$ -ray spectroscopy experiments. This sensitivity can be expressed in terms of the resolving power, a quantity that incorporates the energy resolution, peak-to-total ratio and total photopeak-efficiency of a detector. The resolving power of different generations of  $\gamma$ -ray detectors is shown in Figure 3.11, demonstrating the progress made by the development of  $\gamma$ -ray tracking detectors. The definition of the resolving power shown in the figure is given in Ref. [Lee03]. A direct impression of the gain in sensitivity can be obtained from simulation results shown in Figure 3.12.

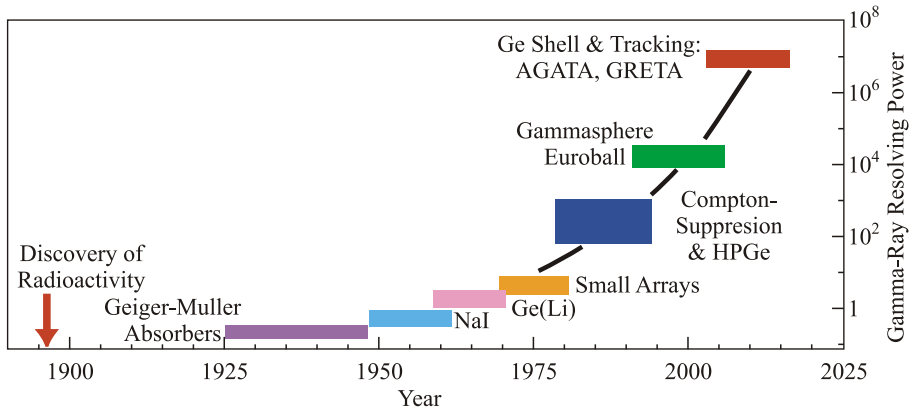


**Figure 3.11.:** Resolving power of different generations of  $\gamma$ -ray detectors. See Ref. [Lee03] and text for details. Figure taken from [Lee03] and slightly modified. © IOP Publishing. Reproduced with permission. All rights reserved.

The implications of this drastically increased sensitivity of  $\gamma$ -ray tracking arrays for  $\gamma$ -ray spectroscopy, especially for the spectroscopy of exotic isotopes, can already be divined from the results obtained with the existing first-stage arrays, the AGATA demonstrator and GRETINA. These results are discussed in view of future opportunities in numerous articles, e.g. [Lee03, Mac13, Lee13, Pod14, Rei14]. However, the ability to localize the individual interactions of  $\gamma$ -rays inside the detector material by PSA and inferring their sequence by tracking also opens up

---

possibilities for new applications. For example,  $\gamma$ -ray tracking arrays are highly sensitive Compton-polarimeters that allow the measurement of the linear polarization of  $\gamma$ -radiation [Ali12, Mel14, Biz15] and the detectors can be used as Compton-cameras [Rec09a]. The direct access to the digitized signals at the stage of PSA is a welcome chance to implement sophisticated corrections, such as the correction of damages to the detector caused by neutrons [Bru13], algorithms for  $\gamma$ -ray-neutron discrimination [Lju05, Ata09, Sen14] or algorithms increasing the time resolution of the detectors [Cre10, Sch11b].

Furthermore, a new class of experimental techniques is rendered possible by the development of  $\gamma$ -ray tracking arrays due to the high resolution in the energy *and* polar detection angle of  $\gamma$ -rays. Two such new techniques tailored to the use  $\gamma$ -ray tracking detectors were developed within this work. In a sense, they use this new type of detectors as an instrument that precisely measures the velocity and position of ions at the time of  $\gamma$ -ray emission. These new methods are presented in the following two chapters.

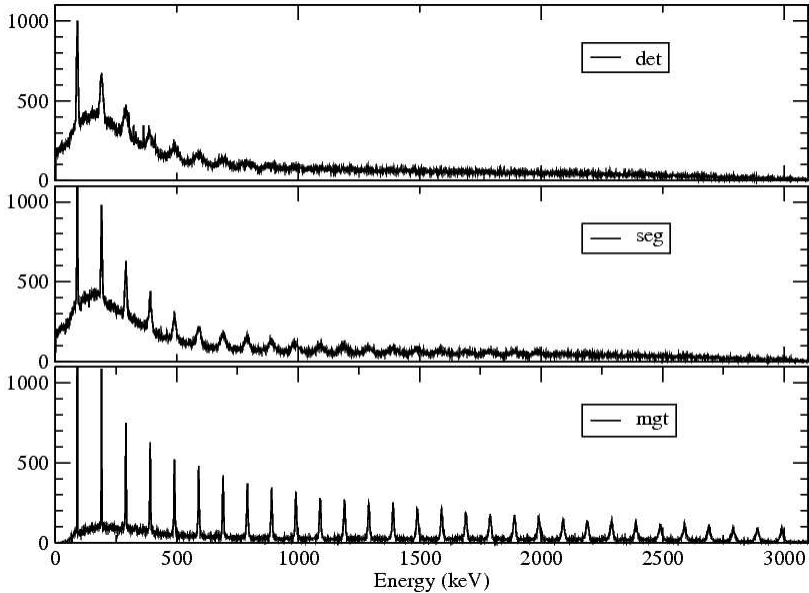


**Figure 3.12.:** Simulated spectra for the detection of a rotational cascade of 30  $\gamma$ -rays emitted at a velocity of  $\beta = 0.5$  with the full AGATA array. The Doppler correction has been performed using the position information of the crystal centers, segment centers and using the positions of first  $\gamma$ -ray interaction points obtained after tracking by the algorithm *mgt* [Baz04]. The spectrum in the top panel is comparable to those that can be obtained by Compton-suppressed  $4\pi$ -arrays such as GAMMASPHERE and EUROBALL. Figure taken from [Rec08].

---

## 4 The continuous-angle Doppler-Shift Attenuation Method

The continuous-angle Doppler-Shift Attenuation Method (caDSAM) is a further development of the well-known Doppler-Shift Attenuation Method (DSAM), adapting it for the use of position-sensitive HPGe detector arrays, the  $\gamma$ -ray tracking arrays. It was developed within this work and exploits the precise measurement of  $\gamma$ -ray polar detection angles by  $\gamma$ -ray tracking detectors as a "newly accessible" experimental observable. Extensions of the caDSAM technique qualify it especially for experiments with radioactive and relativistic ion beams and extend the range of lifetimes that can be sensitively measured.

Section 4.1 gives a short introduction to the measurement of nuclear level lifetimes in general (Section 4.1.1) and into the Doppler Shift Attenuation Method in particular (Section 4.1.2). Section 4.2 introduces the principle of the continuous-angle DSA Method and its advantages over the "conventional" DSA Method. The formalism underlying the caDSA Method is introduced in Section 4.3. The extensions of the method are discussed in Section 4.4.

Details of the formalism and the implementation of the method and its extensions into computer programs developed within this work are discussed in Appendix B.

---

### 4.1 Measurement of nuclear level lifetimes: An introduction

---

Reduced electromagnetic transition strengths  $B(\sigma\lambda, J_i \rightarrow J_f)$  for electric and magnetic transitions ( $\sigma = E, M$ ) and multipole order  $\lambda$  between initial and final nuclear states  $|J_i\rangle$  and  $|J_f\rangle$  are a valuable experimental observable, since they are sensitive to the wave functions of the nuclear states involved. This sensitivity is given via the reduced matrix element of the electromagnetic transition operator  $\langle J_f || \mathcal{O}(\sigma\lambda) || J_i \rangle$  [Boh69, eq. (3C-17)]:

$$B(\sigma\lambda, J_i \rightarrow J_f) = \frac{1}{2J_i + 1} \left| \langle J_f || \mathcal{O}(\sigma\lambda) || J_i \rangle \right|^2. \quad (4.1)$$

The lifetime  $\tau_i$  of the initial nuclear state  $|J_i\rangle$  is related to the reduced electromagnetic transition strengths by the relation [Boh69, eq. (3C-16)]

$$\frac{1}{\tau_i} = \sum_f \frac{8\pi(\lambda+1)}{\lambda[(2\lambda+1)!!]^2} \frac{1}{\hbar} \left(\frac{E_\gamma}{\hbar c}\right)^{2\lambda+1} B(\sigma\lambda, J_i \rightarrow J_f) (1 + \alpha_f), \quad (4.2)$$

where the summation is over all final states the initial state decays to.  $\alpha_f$  is the electron conversion coefficient of the decay  $i \rightarrow f$  and  $E_\gamma = E(J_i) - E(J_f)$  the energy of that decay. The width  $\Gamma_i$  of an isolated nuclear resonance state is connected to its lifetime by Fourier transformation via

$$\Gamma_i = \frac{\hbar}{\tau_i}. \quad (4.3)$$

---

#### 4.1.1 Experimental techniques for lifetime measurements

---

If all branching ratios of an excited nuclear state's decay channels and their electron conversion coefficients are known, the measurement of reduced transition strengths and level lifetimes is equivalent. This follows from Eq. 4.2. From Eq. 4.3, it is apparent that the measurement of transition widths and of lifetimes of nuclear states is equivalent.

There exists a variety of experimental methods for the measurement of reduced transition strengths, level lifetimes and transition widths, each with a particular range of applicability. They are listed and compared in terms of their range of applicability in Figure 4.1.

While the method of Coulomb excitation is discussed in Chapter 2.1 and the Doppler-Shift Attenuation Method (DSAM) is discussed in detail in the following section, the other methods mentioned in Figure 4.1 will not be discussed here. Reference is made to review articles on Nuclear Resonance Fluorescence (NRF) [Kne96], electron scattering ( $e, e'$ ) [Hei83], the Recoil Distance Doppler-Shift Method (RDDS or RDM) [Dew12] and electronic timing [Mac89, Mos89] and references therein.

---

#### 4.1.2 The Doppler-Shift Attenuation Method (DSAM)

---

The Doppler-Shift Attenuation Method is an experimental technique for the measurement of nuclear level lifetimes in the range from  $\sim 10$  fs [Mic13] to  $\sim 10$  ps [Bau12]. It is based on the observation of Doppler-shifted  $\gamma$ -ray energies while the nuclei emitting the  $\gamma$ -radiation are slowing down in matter. By the knowledge of

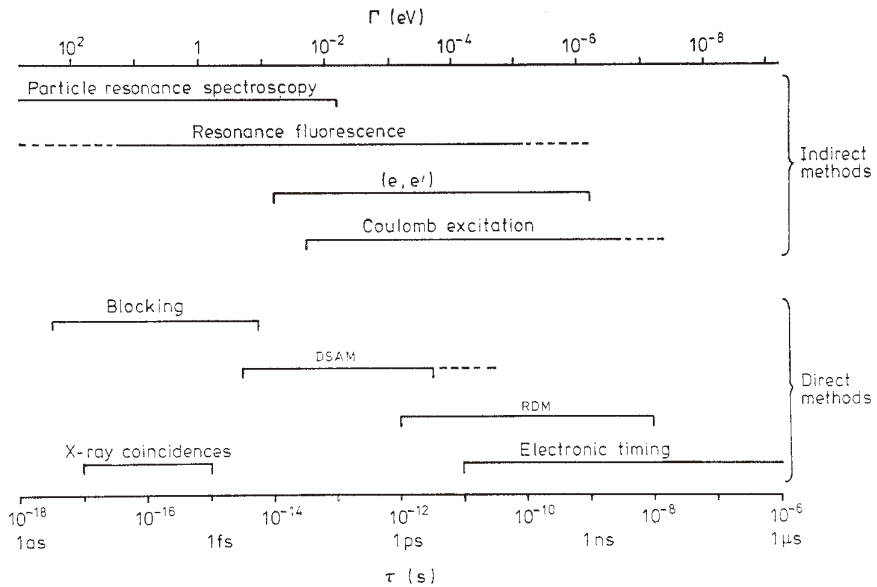


**Figure 4.1.:** Comparison of different experimental techniques for the measurement of nuclear level lifetimes (“direct” methods, bottom) or decay widths or transition strengths (“indirect” methods). The applicability of the methods to different ranges of level lifetimes is shown. The figure is taken from [Nol79]. © IOP Publishing. Reproduced with permission. All rights reserved.

the time dependence of the slowing-down process of the nuclei, the distribution of observed Doppler shifts can be related to the times at which the  $\gamma$ -radiation is emitted and, therefore, to the lifetime of the de-exciting nuclear state. Reviews of the method can be found e.g. in [Nol79, Ale78, Sch68]. A typical experimental setup for a DSAM measurement and the principle of the method is sketched in Figure 4.2. In the following, the principle of the DSA Method is outlined in a brief phenomenological manner, followed by a detailed discussion of central aspects.

### Principle of the DSA Method

Assume an ion beam impinges on a target and a reaction populating the excited state of interest occurs. After that reaction, the excited ion continues to propagate through the target and slows down. In Figure 4.2, the slowing-down process is sketched at the bottom left. If the de-excitation of the moving nucleus occurs soon

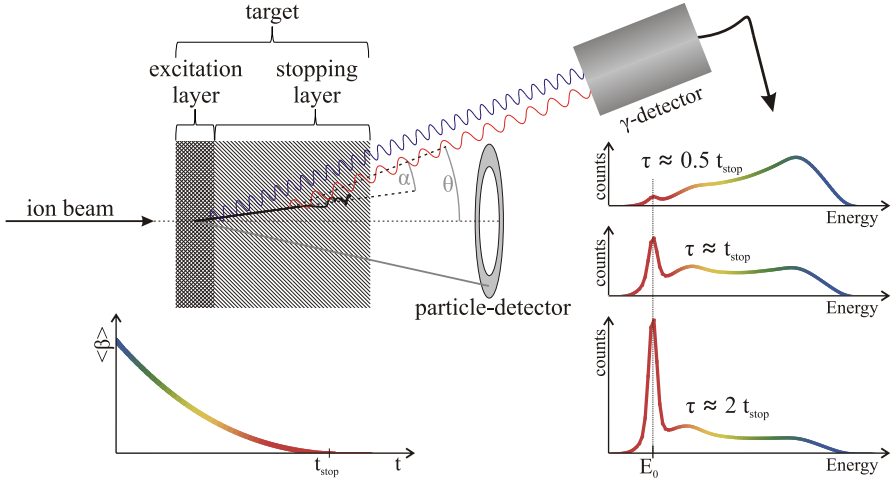


**Figure 4.2.:** Typical setup for a DSAM measurement and principle of the DSA Method. Exemplarily, a setup with a layered target and an annular particle detector under forward direction is shown, allowing to select reactions that occur in the thin excitation layer. The  $\gamma$ -ray detector is placed at an forward angle  $\theta$  in this example. The Doppler-broadened lineshapes depend on the angle  $\alpha$  between the momentum vector of the excited ion and the emission direction of the  $\gamma$ -ray as well as on the level lifetime  $\tau$  relative to the time  $t_{\text{stop}}$  the excited ions need to come to rest in the target material. Note the correspondence of the colors in the plot of the temporal velocity evolution (bottom left) and the resulting lineshapes (right). See text for details.

after the excitation (small time  $t$ ) at high velocity  $\beta$ , a  $\gamma$ -ray detector will detect a large Doppler shift according to Equation (2.40). Whether a  $\gamma$ -ray energy higher or lower than the transition energy  $E_0$  will be detected depends on the angle  $\alpha$  between the momentum vector of the emitting ion and the emission direction of the  $\gamma$ -ray. For most detector positions, the shift is larger in magnitude for a higher velocity  $\beta$  of the emitting ion. Consequently, for reduced ion velocities  $\beta$ , a reduced Doppler shift will be detected. If the emission occurs after the emitting ion has come to rest, no Doppler shift occurs and the transition energy  $E_0$  will be detected.

For simplicity, in the following it is assumed that the emitting ion moves in forward direction and the  $\gamma$ -ray detector is also positioned under a forward angle  $\theta$  (i.e. small angle  $\alpha$ ) as shown in Figure 4.2, resulting in detected Doppler-shifted

---

$\gamma$ -ray energies larger than  $E_0$ . Also, it is assumed that the nuclear state of interest is populated directly (no feeding), resulting in a simple exponential decay function (see Chapter 2.2) for the sake of simplicity.

Together with the temporal evolution of the velocities of the ions moving through the target material (sketched at the bottom left of Figure 4.2), the decay function  $A(t)$  (see Chapter 2.2) yields the distribution of ion velocities at the time of de-excitation. If the nuclear level lifetime  $\tau$  is short compared to the slowing-down time  $t_{stop}$ , the decays will occur predominantly at high ion velocities  $\beta$ . Consequently, large Doppler shifts are observed most frequently. This results in a lineshape as sketched in the upper right part of Figure 4.2. If the level lifetime is in the order of the slowing-down time, the fraction of decays occurring at reduced velocities or after the emitting ion has come to rest increases. For level lifetimes considerably larger than the slowing-down time, decays of ions at rest dominate and the transition energy  $E_0$  is detected predominantly. Lineshapes for these situations are sketched in the middle and lower right part of Figure 4.2.

In practice, the excitation and slowing-down process is modeled in terms of a Monte-Carlo simulation, yielding the temporal evolution of the velocities of an ensemble of ions after an excitation reaction. From these simulated ion velocity histories, lineshapes can be calculated for a given level lifetime. These calculated lineshapes are fitted to experimental data where the level lifetime is a free parameter, ultimately providing the measured level lifetime.

In the following, central aspects concerning the DSA Method and experiments employing it are discussed.

### Slowing-down process

For the description of the slowing-down process of heavy ions in matter, two different kinds of processes have to be differentiated. The interaction of the moving ion (and, in case of partial ionization, its electrons) with the electrons of the target material results in a large number of interactions such as elastic or inelastic scattering and charge-exchange reactions. Each of these reactions has only small influence on the magnitude of the ion momentum and its direction. On the scales relevant to the DSAM, this process of *electronic stopping* can be treated as a continuous process. In contrast, single collisions of the moving ions with the nuclei of the target material can lead to significant deviations of the magnitude and direction of the ion's momentum vector. The energy loss associated with these nuclear collisions is referred to as *nuclear stopping* and dominates the slowing-down process at low ion velocities below  $\sim 0.01c$ . It is expedient to treat these nuclear collisions individually in terms of a Monte-Carlo simulation.

---

At relativistic ion energies  $\gtrsim 200$  MeV/u resulting in velocities  $\gtrsim 0.5c$ , ions moving in matter are highly charged or even fully stripped. In this regime, the electronic stopping fully dominates the energy loss. By good knowledge of the charge-state distributions of the ions as they penetrate matter [Sch98b], reliable descriptions of the energy loss are available in this velocity regime [Sch98a, Wei00] which are based on the theory by Lindhard and Sørensen [Lin96].

At low ion velocities  $\beta \lesssim Z \cdot v_0$  (where  $v_0 = e^2/\hbar \approx c/137$  is the Bohr velocity and  $Z$  the atomic number of the beam ions or the target material), the specific electron configurations of the atomic shells of the beam ions and target atoms play an important role for the charge-exchange processes. In consequence, strong dependence of stopping powers on the atomic numbers of beam ions and target atoms is observed, an effect known as *Z1- and Z2-oscillations* [Gei02]. This hinders the possibility to find general expressions for stopping powers at low ion velocities. Instead, semi-empirical models and tabulations of experimental stopping powers are widely used for low ion energies, such as the tabulations by Northcliff and Schilling [Nor70], the model by Ziegler, Biersack and Littmann [Zie85] (incorporated into the software program SRIM [Zie10]) or the tables by the International Commission on Radiation Units and Measurements (ICRU) [Int05]. Analytical approaches to stopping powers at low energies have been made e.g. by Lindhard, Scharff, Schiøtt (LSS-theory, [Sig83, Lin61, Lin63]) and Blaugrund [Bla66].

Electronic and nuclear stopping powers for  $^{136}\text{Xe}$  ions slowing-down in solid tantalum extracted from the code SRIM [Zie10] are exemplarily shown in Figure 4.3. Due to the generally approximate character of stopping power descriptions at low energy, uncertainties of stopping powers induce a significant systematic uncertainty in the analysis of DSAM experiments. This is because a scaling of stopping powers is approximately equivalent to a scaling of the time-scale of the slowing-down process, directly influencing the nuclear level lifetimes extracted from DSAM measurements. For example, the mean deviation of stopping powers provided by the SRIM code from measured stopping powers is 4.3%. For 85% of the beam-target combinations for which experimental data are available, the agreement is within 10% [Zie10].

Reviews on the stopping power of ions in matter exist in abundance. Exemplarily, reference is made to the reviews by Geissel [Gei02] and Sigmund [Sig98].

### Target layout

Defining the ideal target for a particular DSAM experiment is a trade-off between a large excitation probability for the nuclear state of interest, a narrow velocity distribution of the ions after their excitation and stopping powers of the target ma-

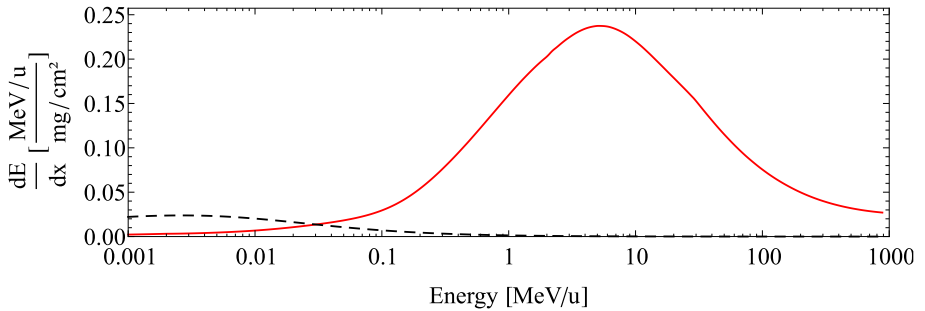


**Figure 4.3.:** Electronic (red, solid line) and nuclear (black, dashed line) stopping power of tantalum for  $^{136}\text{Xe}$  ions. The values are extracted from the computer program SRIM [Zie10] based on the semi-empirical model of Ziegler, Biersack and Littmann [Zie85].

materials resulting in a lineshape that is sensitive to the lifetime to be measured. The first point depends on the cross section for the reaction in the target material, the target(layer) thickness and the density of the material. The latter two points are discussed in this paragraph.

In the most simple case, DSAM experiments can be performed by the bombardment of unstructured, thick targets of any solid material. The choice of the material is governed by two considerations:

- When the target is bombarded with the beam, an efficient nuclear reaction populating the state of interest has to occur and
- The average time the excited ions need to come to rest in the target should be approximately equal to the lifetime that is to be measured (see Fig. 4.2).

Without loss of generality, the considerations on target layouts for DSAM experiments are discussed on the basis of the example of Coulomb excitation of a 546 MeV beam of  $^{136}\text{Xe}$  ions impinging on a target made of natural carbon. The blue line in Figure 4.4 (left) shows the distribution of velocities (i.e., their magnitude) of excited  $^{136}\text{Xe}$  nuclei directly after a Coulomb excitation reaction. The assumed target is solely made from carbon and is sufficiently thick to stop the ion beam. The velocity distribution of the ions directly after their excitation in a binary reaction is governed by two factors:

- The excitation cross section as a function of beam energy  $E$ , determining the number of excitations occurring at different ion velocities while the beam ions are slowing down in the target material.
- The differential excitation cross section as a function of scattering angle  $\theta$ ,  $\frac{d\sigma}{d\theta}$ , determining the distribution of scattering angles between the binary reaction partners.

The ion velocity after an excitation reaction at a given energy  $E$  and under a scattering angle  $\theta$  is given by the relations of the reaction kinematics (see Appendix C).

A narrow velocity distribution of the excited ions after the reaction is favorable because it generally results in more pronounced and more sensitive lineshape than a broad velocity distribution. This manifests itself in the lineshapes at large Doppler shifts in Figure 4.4 (right). In order to realize a sharp velocity distribution, the former factor can experimentally be limited by using a layered target. If it can be made sure that the nuclear reaction populating the state of interest occurs only in a certain target material, a thin layer of the respective material restricts the ion energies at which the reaction can occur. The energies are then bounded by the beam energy and the energy loss in the thin target layer. The subsequent target layers exclusively serve as "stoppers" for slowing down the excited ions in that case. Exemplarily, Figure 4.4 (left) shows the distribution of velocities of  $^{136}\text{Xe}$  nuclei Coulomb-excited on a  $0.5 \text{ mg/cm}^2$  layer of natural carbon (red line). The velocity profile is significantly sharpened compared to the situation of a thick target layer (blue line) where excitations can occur at any ion energy from the beam energy to zero. The distribution of velocities of ions directly after their excitation in a binary reaction caused by different occurring scattering angles can experimentally be limited by the use of a particle detector registering all but one of the reaction products. This is discussed in the following paragraph.

### Particle detection

The equations describing the kinematics of a binary collision (Appendix C) relate a particle's scattering angle with its kinetic energy after the collision (see also Figure 6.3, left-hand side). Corresponding relations can be derived for reactions with more than two particles (multiple beam-like or target-like reaction products) in the outgoing reaction channel [Bal63]. In the latter case, the momentum of one of the reaction products can be inferred, if the momentum of all other reaction products is measured and the masses of the reaction products and their excitation energies are known. Consequently, restricting the scattering angles of the reaction products via the geometry of a particle detector also imposes a criterion on their momentum (velocity) after the reaction. On the left-hand side of Figure 4.4, the velocity distri-

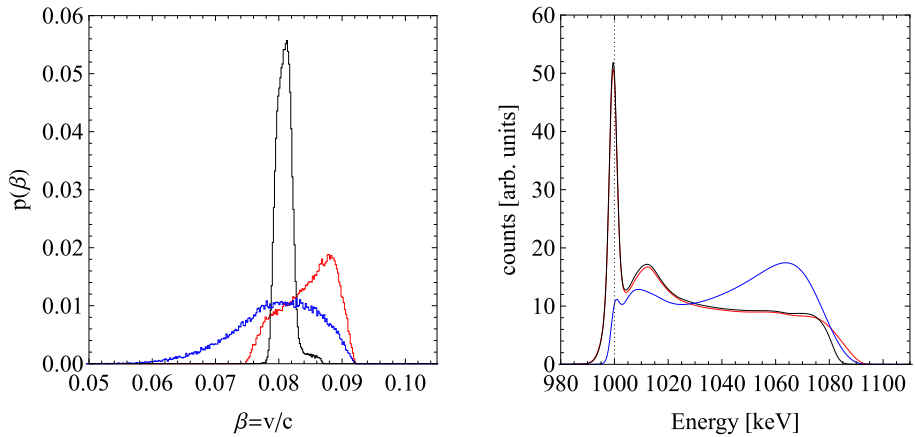


**Figure 4.4.:** **Left:** Velocity distributions of  $^{136}\text{Xe}$  nuclei directly after they have been Coulomb-excited on a target of natural carbon. A beam energy of exactly 546 MeV was assumed. The blue line shows the distribution for a target consisting of a thick layer of carbon, sufficiently thick to stop the ions. The red line shows the distribution for a target made of  $0.5\text{ mg/cm}^2$  carbon followed by a stopping layer (“backing”) made of tantalum. In the simulation of the excitation process, excitation in the tantalum layer was suppressed. For the black line, detection of recoiling carbon ions under laboratory scattering angles from  $30^\circ - 35^\circ$  was demanded.

**Right:** Doppler-broadened lineshapes for the decay of a fictional state of  $^{136}\text{Xe}$  at 1 MeV excitation energy (vertical, dotted line) with a lifetime of 1 ps. Lineshapes for the target layouts as on the left side are shown in the respective colors. The lineshapes are calculated for a cylindrical  $\gamma$ -ray detector placed at an forward angle of  $\theta = 20^\circ$  with respect to the beam axis. They are normalized such that they contain the same number of events.

bution of  $^{136}\text{Xe}$  nuclei Coulomb-excited on a  $0.5\text{ mg/cm}^2$  layer of natural carbon is shown, where the scattered carbon ions are detected in an annular detector covering laboratory scattering angles  $30^\circ < \theta_c < 35^\circ$  (black line). The velocity profile is significantly sharpened compared to the situation where the reaction products are not registered (red line).

---

The Doppler-broadened lineshapes resulting from the decay of a fictional state at 1 MeV excitation energy in  $^{136}\text{Xe}$  with a lifetime of 1 ps for the cases of the thick excitation layer, a thin excitation layer and a thin excitation layer combined with a detector for recoiling target ions covering  $30^\circ < \theta_C < 35^\circ$  is shown on the right-hand side of Figure 4.4. The lower stopping power per distance for  $^{136}\text{Xe}$  of carbon compared to tantalum enhances decays at high velocities in the case of the thick carbon target (blue lineshape). The difference in excitation probability for the different constellations was neglected.

## Feeding

The nuclear state of interest may not (exclusively) be populated directly by a nuclear reaction, but (also) by decays of higher-lying states. In this case, its decay curve  $A(t)$  is no longer given by a simple exponential law, but has a more complicated form (see Section 2.2). In order to extract the lifetime of the state of interest in this case, the lifetimes, branching ratios and populations of all levels in the feeding chain have to be known or have to be described by a model (see [Gro06, Cla98] for example). There exist analysis methods that aim at deducing the complete decay function  $A(t)$  from measured Doppler-broadened lineshapes rather than the lifetime only [Böh93, Pet15]. However, if the transitions feeding the level of interest also exhibit lifetime-sensitive lineshapes, it is possible to fit the lifetimes of the feeding transitions simultaneously to the lifetime of the state of interest. This is the ansatz pursued in the implementation of the continuous-angle Doppler-Shift Attenuation Method presented in this work.

## Range of applicability

The range of nuclear level lifetimes that can be sensitively measured by the Doppler-Shift Attenuation Method is settled by the time scale of the slowing-down process of the excited ions in the target material. This is again demonstrated using the example of 546 MeV  $^{136}\text{Xe}$  ions Coulomb excited on a target made of  $0.5 \text{ mg/cm}^2$  natural carbon backed by tantalum and discussed for the general case. The temporal evolution of the excited ion velocity distribution is shown in Figure 4.5. In this example, the ions come to rest approximately 2 ps after their excitation. Within the first  $\sim 0.7$  ps after their excitation, the ions' velocities are reduced by about 75%.

The condition for the measurement of very short lifetimes is that during the mean time between population and de-excitation of the state of interest the ion velocity is sufficiently reduced to sensitively detect a change in the Doppler shift of the  $\gamma$ -ray energy. In the case of direct population of the state (no feeding), this time

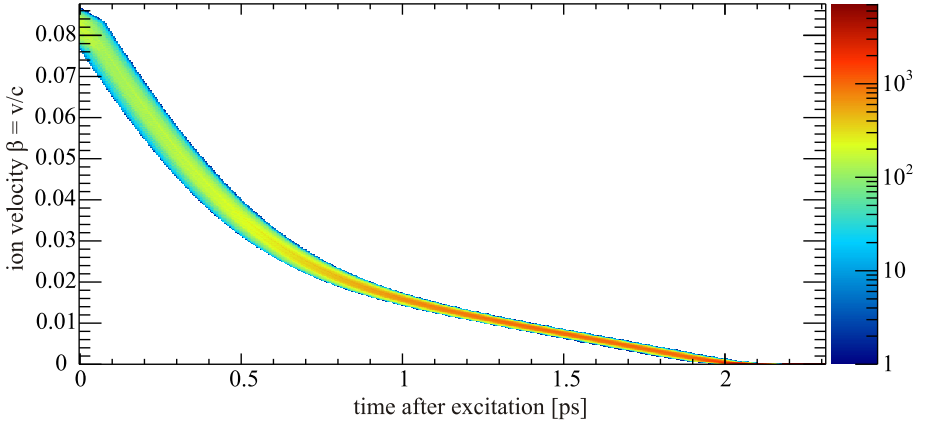


**Figure 4.5.:** Temporal evolution of the velocity distribution of 546 MeV  $^{136}\text{Xe}$  nuclei, Coulomb-excited at  $t = 0$  on a target of  $0.5 \text{ mg/cm}^2$  natural carbon backed by tantalum. The time-scale of the slowing-down process of about 2 ps defines the range of lifetimes that can be sensitively measured by this beam- and target-combination.

is equivalent to the lifetime of the state. The velocity reduction  $\Delta\beta$  necessary to induce a change  $\Delta E$  in the Doppler shift of the energy can be estimated by

$$\Delta\beta \geq \frac{\Delta E}{E_0} \frac{1}{\cos\theta_\gamma} \quad (4.4)$$

where  $E_0$  is the un-shifted  $\gamma$ -ray-energy and  $\theta_\gamma$  is the polar angle of the  $\gamma$ -ray detector with respect to the beam axis. Assuming a detector energy resolution of  $\Delta E/E_0 \sim 2\%$  and assuming that the detector is placed under  $\theta_\gamma = 0^\circ$ , the demand that the energy shift should be at least two times the resolution of the detector yields the condition

$$\Delta\beta \geq 0.004. \quad (4.5)$$

In the example of Figure 4.5, a reduction of the initial average ion velocity at the time of excitation by 4‰ is reached after  $\sim 50 \text{ fs}$ . For the case that the excited state is populated directly in the excitation reaction, this is the lower limit for lifetimes that can be sensitively measured with this particular beam-target combination. Lineshapes for lifetimes close to this lower limit are shown on the left-hand

side of Figure 4.6. In the case that the excited state is substantially fed by higher-lying, longer-lived states, the sensitivity to short lifetimes can be strongly reduced.

The longest lifetime that can be sensitively measured by the DSAM employing a particular beam-target combination can be estimated from the demand that at least a fraction  $f$  of the decays of the excited level should occur at ion velocities that result in a well detectable Doppler shift of the  $\gamma$ -ray energy. Setting the minimum requested Doppler shift to 4‰ of the un-shifted energy at  $\theta_\gamma = 0^\circ$ , inspection of figure 4.5 yields that the demanded fraction  $f$  of decays should occur within  $t_{max} \approx 1.8$  ps after the excitation. The longest lifetime  $\tau_{max}$  fulfilling this condition can be obtained from the relation

$$\int_0^{t_{max}} A(t) dt = f. \quad (4.6)$$

In the case of direct population this yields

$$\begin{aligned} \frac{1}{\tau_{max}} \int_0^{t_{max}} e^{-t/\tau_{max}} dt &= 1 - e^{-t_{max}/\tau_{max}} = f \\ \Rightarrow \tau_{max} &= -\frac{t_{max}}{\ln(1-f)}. \end{aligned} \quad (4.7)$$

A proper choice of the fraction  $f$  sensitively depends on the expected background level and statistics of the respective transition, since in the case of very long level lifetimes the analysis of a DSAM experiment is effectively reduced to the quantification of a "tail" of an un-shifted peak. With  $t_{max} \approx 1.8$  ps and  $f = 30\%$ , the maximum lifetime that can be sensitively measured by the DSAM with the beam-target combination assumed in the discussed example is  $\tau_{max} \approx 5$  ps. Lineshapes for lifetimes close to this upper limit are shown on the right-hand side of Figure 4.6.

The range of applicability of the DSA Method can be influenced by the choice of the beam-target combination. Choosing a target material with a higher (lower) stopping power per distance -not per areal mass density- effectively quenches (stretches) the time scale of the slowing down process, resulting in sensitivity to shorter (longer) level lifetimes. This can be inferred from the right-hand side of Figure 4.4 where the blue curve shows a lineshape for  $^{136}\text{Xe}$  ions stopping in carbon, while the red and black curves show lineshapes of the very same ion species stopping in tantalum. Due to the much lower stopping power per distance of carbon, the de-excitations occur on average at higher velocities than in the case of the tantalum backing. Consequently, longer lifetimes can be measured with the thick carbon target than with the tantalum-backed target.

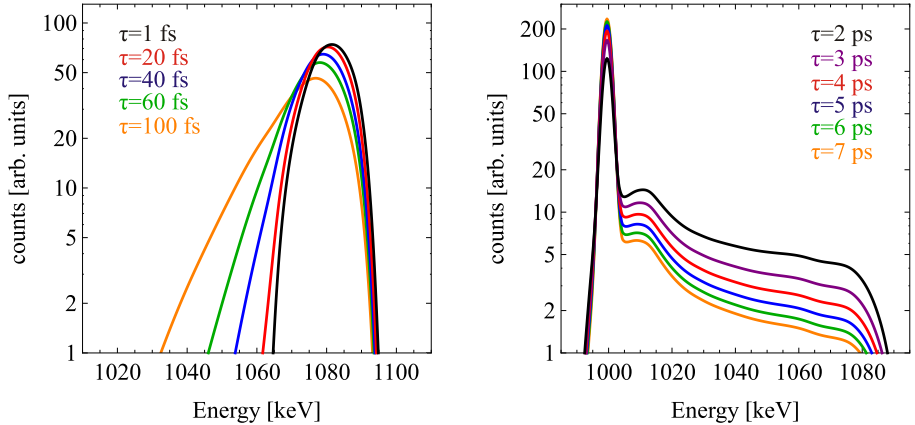


**Figure 4.6.:** Doppler-broadened  $\gamma$ -ray lineshapes for a fictional state of  $^{136}\text{Xe}$  at 1 MeV excitation energy. The excitation and slowing down process was simulated for a beam energy of 546 MeV and Coulomb excitation of  $^{136}\text{Xe}$  ions on a  $0.5 \text{ mg/cm}^2$  carbon target backed by tantalum. Excitations in the tantalum backing were suppressed in the simulation. Lineshapes are shown for short lifetimes close to the estimated lower sensitivity limit of 50 fs (left) and for long lifetimes close to the estimated upper sensitivity limit of 5 ps (right). The lineshapes are calculated for a cylindrical  $\gamma$ -ray detector placed at an forward angle of  $\theta = 20^\circ$  with respect to the beam axis. Note the logarithmic scale of the y-axis and see text for details.

---

## 4.2 Principle of the continuous-angle Doppler-Shift Attenuation Method

---

The development of the *continuous-angle Doppler-Shift Attenuation Method* (caD-SAM) within this work was triggered by the advent of position-sensitive high-purity Germanium (HPGe) detectors, the  $\gamma$ -ray tracking detectors (Chapter 3). In this latest generation of high (energy- and position-)resolution  $\gamma$ -ray detector systems, the subdivision of detector arrays into individual crystals or individual segments is overcome. The ensemble of detector crystals that is arranged in close packing is rather treated as a unity, only electrically and mechanically segmented into co-working cells. Position resolution for the interaction points of  $\gamma$ -radiation within the detector material much finer than the dimensions of the segments is achieved by the technique of Pulse Shape Analysis (see Section 3.2.1) combined with tracking (see Section 3.2.2). This allows to measure the polar angle of  $\gamma$ -ray detection as a continuous quantity. The quantization of detection polar angles that is imposed by individual detectors placed at certain positions does not exist anymore.

The continuous-angle Doppler-Shift Attenuation Method represents a further development of the "conventional" DSAM as it was presented in the previous section. By making use of the precisely measurable polar angle of  $\gamma$ -ray detection as a "newly accessible" experimental observable, it extends the  $\gamma$ -ray lineshapes analysis as a function of  $\gamma$ -ray energy to a lineshape analysis as a function of both  $\gamma$ -ray energy and polar angle of the  $\gamma$ -ray detection.

However, the continuous-angle DSAM can be applied also to data taken with conventional, position insensitive detectors by integrating the two-dimensional lineshapes over the solid angles covered by the individual detectors. In this case, sensitivity is of course reduced to a certain degree.

To summarize, the advantages of the continuous-angle DSAM over the "conventional" DSAM technique are

- Conservation of the sensitivity of  $\gamma$ -ray tracking arrays,
- Careful consideration of the effect of angular distributions on the lineshapes and
- Consistent description of complicated spectra.

These points are discussed in the following, also introducing the principle and concept of the caDSAM as it was developed and implemented within this work.

### Conservation of the sensitivity of $\gamma$ -ray tracking arrays

In the conventional approach, the Doppler-broadened lineshapes are averaged over the solid angles covered by the individual detectors. Transferring this method to

---

the highly position-resolved data obtained with  $\gamma$ -ray tracking detectors neglects the additional information provided by the precise determination of the first interaction points of the radiation and, hence, the precise information on the emission direction of the  $\gamma$ -rays. In this regard, there is no justification for retaining the approach to analyze DSAM data on the basis of individual detector crystals or electric segments, albeit eventually performed as combined fits to the spectra obtained by multiple detectors/segments but with individual normalizations. Principally available sensitivity in terms of peak-to-background ratio would be lost in this way.

In the approach of the continuous-angle Doppler-Shift Attenuation Method, theoretical Doppler-broadened lineshapes are calculated as a function of both  $\gamma$ -ray energy and the detection position of the  $\gamma$ -radiation. Spectra observed under different, continuously measured polar angles of  $\gamma$ -ray detection  $\theta_\gamma$  are naturally connected by the angular distribution of the  $\gamma$ -radiation, which is fitted simultaneously with the level lifetimes in the analysis process. This approach completely conserves the sensitivity of  $\gamma$ -ray tracking detectors by avoiding to average lineshapes over significant ranges of polar detection angle  $\theta_\gamma$ .

### Careful consideration of the effect of angular distributions on the lineshapes

In the  $\gamma$ -ray lineshape calculation, the  $\gamma$ -ray angular distribution enters not only in the normalization of the lineshape as a function of  $\theta_\gamma$ , but also influences the lineshapes at fixed observation angles  $\theta_\gamma$ . This effect originates in the relativistic transformation of the polar  $\gamma$ -ray emission angle from the emitting nucleus' rest frame to the laboratory frame (see Section 2.3). Doppler-broadened  $\gamma$ -ray lineshapes represent a distribution of  $\gamma$ -rays emitted at different emitter velocities. While the "stop-peak" of a lineshape originates from emission at rest, the "shifted" part of the lineshapes originates from  $\gamma$ -ray emissions at different ion velocities that are usually up to at least a few percent of the speed of light. Consequently, different parts of the  $\gamma$ -ray lineshape detected under a fixed polar angle  $\theta_\gamma$  in the laboratory frame represent  $\gamma$ -rays emitted under different polar angles in the rest frame of the emitting nuclei. If the  $\gamma$ -ray angular distribution is not isotropic in the rest frame of the emitting nuclei, the intensity of  $\gamma$ -rays measured under a fixed polar angle  $\theta_\gamma$  in the laboratory system may be decreased or increased, depending on the ion velocity at the time of  $\gamma$ -ray emission, the actual angular distribution of the  $\gamma$ -rays and the observation angle in the laboratory system. This affects the observed  $\gamma$ -ray lineshape, and the effect depends on the polar angle  $\theta_\gamma$  at which the lineshape was observed.

Where the influence of the  $\gamma$ -ray angular distribution on lineshapes is largest depends on the emitter velocities and on the actual form of the angular distribution itself. This is sketched for an example in Figure 4.7. As a function of velocity  $\beta$ ,

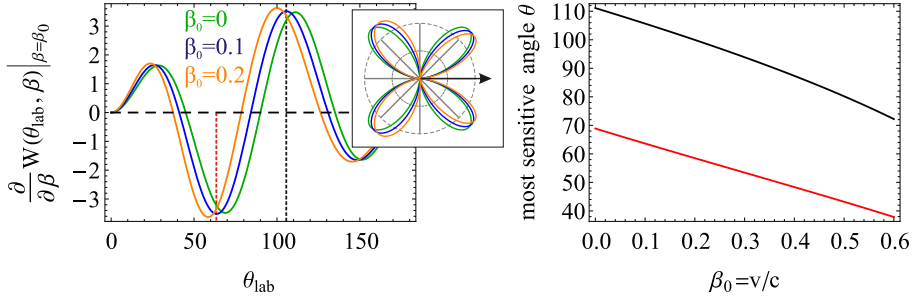


**Figure 4.7.:** Variation of  $\gamma$ -ray intensity observed in the laboratory frame as a function of emitter velocity  $\beta$  (emitter moves along the z-axis).

**Left:** Angular distribution function according to Equation (2.54) for  $A_2 = \frac{5}{7}$ ,  $A_4 = -\frac{12}{7}$  observed in the laboratory system (inset) and its derivative with respect to  $\beta$  at values  $\beta_0 = 0\%$ ,  $10\%$ ,  $20\%$  of the speed of light. The positions of the largest magnitudes of the derivative for  $\beta_0 = 0.1$  are indicated by dashed, vertical lines.

**Right:** Positions of the largest magnitudes of the derivative of the angular distribution function as a function of emitter velocity  $\beta_0$ . Lorentz-boost is neglected in the plotted functions. See text for details.

the  $\gamma$ -ray angular distribution is forward-bended as explained in Section 2.3. This stems solely from the transformation of the polar angle  $\theta$ , not from Lorentz-boost. The derivative of the angular distribution of the  $\gamma$ -radiation emitted from a fully aligned  $2^+$  state (only  $m = 0$  populated) to a  $0^+$  state with respect to the velocity  $\beta$  is shown on the left hand side of Figure 4.7 for  $\beta = 0\%$ ,  $10\%$  and  $20\%$  of the speed of light. Laboratory polar angles where the derivative is largest in magnitude are indicated by the vertical, dashed lines on the left hand side of Figure 4.7 for  $\beta = 0.1$ . These angles where the effect on the lineshape is largest are plotted as a function of  $\beta$  on the right hand side of Figure 4.7. It can be seen on the left hand side of Figure 4.7 that the change of observed  $\gamma$ -ray intensity with respect to the emitter velocity, observed at a given polar detection angle, can be large even at low emitter velocities and the magnitude of that change only weakly depends on the emitter velocity. The detection polar angle where the effect is largest in magnitude in turn strongly depends on the emitter velocity. This means that at different observation angles, different parts of Doppler-broadened  $\gamma$ -ray lineshapes will be dominantly affected.

This effect of  $\gamma$ -ray angular distributions on lineshapes is exemplarily shown in figure 4.8. Lineshapes are drawn for the case of the pronounced angular distri-

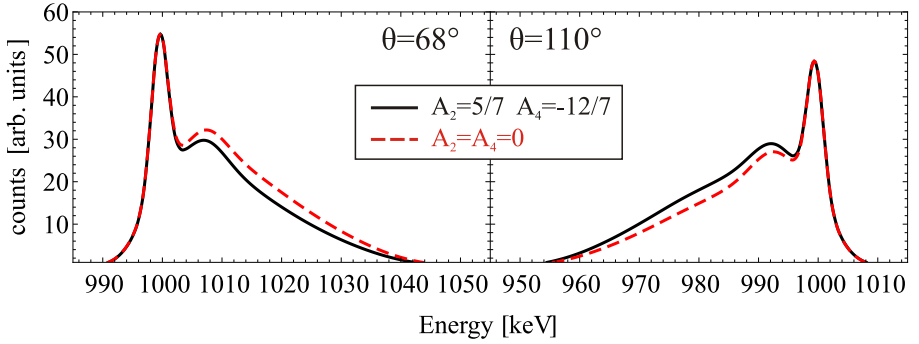


**Figure 4.8.:** Effect of angular distributions on Doppler-broadened lineshapes. Lineshapes calculated with the same parameters as in Figure 4.6 are shown, but for  $\tau = 1$  ps. For the full, black curve, a pronounced  $\gamma$ -ray angular distribution ( $A_2 = \frac{5}{7}$ ,  $A_4 = -\frac{12}{7}$ ) was assumed. For the dashed, red curve, isotropic emission of the  $\gamma$ -rays was assumed. Under the forward detection angle of  $\theta_\gamma = 68^\circ$  (left), the lineshape for isotropic  $\gamma$ -ray emission shows characteristics of a level lifetime *shorter* than for the case of the pronounced  $\gamma$ -ray anisotropy, while for the backward detection angle of  $\theta_\gamma = 110^\circ$  (right), the lineshape for isotropic  $\gamma$ -ray emission shows characteristics of a level lifetime *longer* than for the case of the pronounced  $\gamma$ -ray anisotropy. Lineshapes were normalized such that they have the same height at  $E_0 = 1000$  keV. See text for details.

tribution assumed in Figure 4.7 (solid, black line) and for isotropic emission of the  $\gamma$ -rays (red, dashed lines). The effect of the angular distribution on the lineshapes is significant and at the chosen observation angles, it is very pronounced at basically all Doppler-shifted energies. The corresponding ion velocities at the time of de-excitation range from 0 to  $\sim 8.5\%$  of the speed of light. If the lineshapes calculated for isotropic emission are fitted to the lineshapes assuming pronounced  $\gamma$ -ray angular distribution, significant deviations from the "true" lifetime of 1 ps occur. For the forward angle, a lifetime of 1.11 ps is obtained, for the backward angle a lifetime of 0.90 ps. This demonstrates that the influence of the  $\gamma$ -ray angular distribution on Doppler-broadened  $\gamma$ -ray lineshapes can result in deviations of the lifetime deduced in a DSAM analysis in the order of 10%, even at moderate velocities of the de-exciting ions. How much the  $\gamma$ -ray angular distribution affects the lineshape sensitively depends on the polar observation angles in the laboratory frame and, of course, on the actual form the  $\gamma$ -ray angular distribution function

$W(\theta)$ . To the knowledge of the author,  $\gamma$ -ray angular distributions are usually not considered in DSAM analyses. Their careful consideration is a natural feature of the continuous-angle Doppler-Shift Attenuation Method as it is introduced in this work.

### Consistent description of complicated spectra

It occurs frequently that experimentally observed  $\gamma$ -ray spectra exhibit transitions close in energy. In spectra obtained in DSAM experiments, the Doppler-broadened lineshapes of these close-lying transitions will overlap. This hinders their analysis, since the information contained in the lineshapes is not isolated for each transition. A combined analysis of overlapping lineshapes observed at different observation angles  $\theta_\gamma$  alleviates this problem, since different parts of the overlapping lineshapes are accessible isolated at different observation angles. This is demonstrated in Figure 4.9.

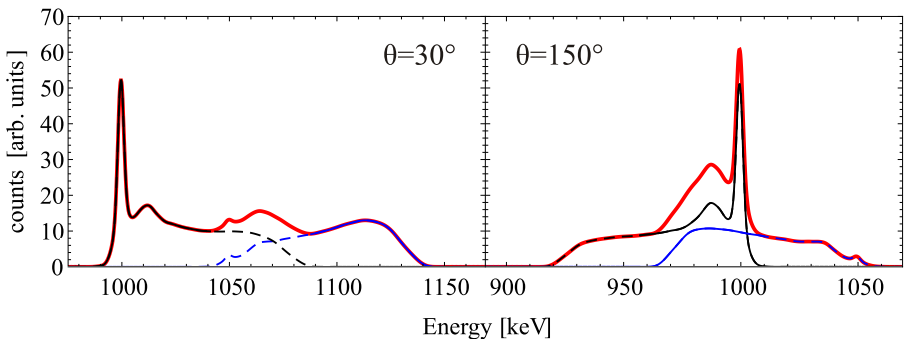


**Figure 4.9.:** Nearby  $\gamma$ -ray transitions resulting in overlapping Doppler-broadened lineshapes. The spectra are calculated for the same conditions as in Figure 4.6, but for a  $\gamma$ -ray transition at 1 MeV de-exciting a level with a lifetime of 1 ps (black lines) and a  $\gamma$ -ray transition at 1.05 MeV de-exciting a level with a lifetime of 0.4 ps (blue lines). The lineshapes are observed with cylindrical detectors at polar angles  $\theta_\gamma=30^\circ$  and  $\theta_\gamma=150^\circ$ . The sum of both lineshapes is drawn as thick, red line. The parts of the lineshapes that are not overlapping at the forward angle of  $\theta_\gamma=30^\circ$  are drawn as thin solid lines. The parts of the lineshapes referring to de-excitations at the corresponding ion velocities, but observed under the backward angle of  $\theta_\gamma=150^\circ$ , are also drawn as thin solid line. See text for details.

---

The example in Figure 4.9 demonstrates that the combined analysis of overlapping, Doppler-broadened lineshapes measured at different observation angles  $\theta_\gamma$  can restore information that is hidden by the overlap of the lineshapes at single observation angles. If individual normalizations for each lineshape at each observation angle are used, unphysical individual lineshapes may be accepted. This is avoided by combining the  $\gamma$ -ray spectra for different observation angles by their  $\gamma$ -ray angular distribution in the continuous-angle Doppler-Shift Attenuation Method, enforcing a consistent description of complicated spectra with overlapping lineshapes.

The same "case" as in Figure 4.9 is shown in Figure 4.10 in a two-dimensional spectrum as a function of  $\gamma$ -ray energy and polar  $\gamma$ -ray detection angle as it can be obtained with position-sensitive detector-systems. It is ensured by the ansatz of the continuous-angle DSAM that the information obtained under different observation angles is combined in a physically consistent way. Figure 4.9 demonstrates that the caDSAM provides an extremely powerful and sensitive tool for the analysis especially of complicated spectra.

All Doppler-broadened  $\gamma$ -ray lineshapes presented in this section were calculated by the software program APCAD developed within this work. The implementation of the caDSAM into the program APCAD is discussed in Appendix B.2. The underlying formalism is presented in the following section.

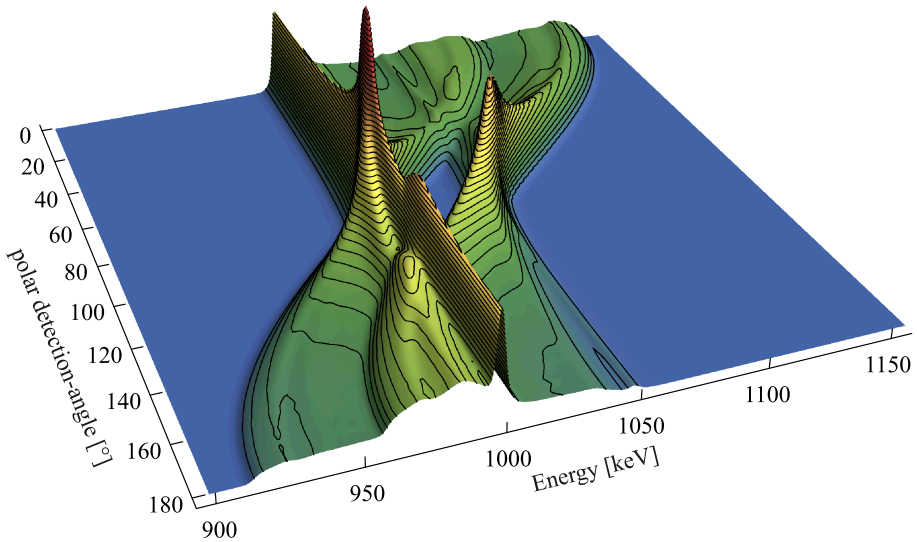


**Figure 4.10:** Two-dimensional Doppler-broadened  $\gamma$ -ray lineshape as a function of  $\gamma$ -ray energy and polar detection angle. The same “case” of overlapping lineshapes as in Figure 4.9 is presented, but in form of a 2D spectrum as it can be obtained by a position-sensitive detector system covering the whole polar angular range from 0-180°. An analysis of the evolution of overlapping lineshapes over a broad range of detection angles represents the best tool for the divestiture of the lineshapes constituting the observed spectrum and a sensitive extraction of the corresponding level lifetimes.

---

---

### 4.3 Formalism of the continuous-angle Doppler-Shift Attenuation Method

---

This section represents a condensed description of the caDSAM formalism. An extensive and detailed description is given in Appendix B.

In the formalism of the continuous-angle Doppler-Shift Attenuation Method, the formation of Doppler-broadened  $\gamma$ -ray lineshapes is strictly separated into three disjunct stages:

- (1) **Simulation of excitation and deceleration of ion beams in targets.** This stage depends solely on the properties of the target, of the ion beam and on the characteristics of the excitation reaction.
- (2) **Description of the experimental setup geometry and modeling of the detectors and their response.** All information on the experimental setup geometry, detector characteristics and experiment-specific properties that are not to be determined by a fit to the experimental spectra containing the Doppler-broadened lineshapes enter at this stage.
- (3) **Calculation of theoretical 2D-lineshapes and their fit to experimental data.** Using the input from stages (1) and (2), theoretical  $\gamma$ -ray spectra for a given set of parameters can be calculated. They are fitted to experimental spectra in order to determine parameters such as level lifetimes, angular distribution coefficients, feeding properties etc. The values and uncertainties of these parameters determined by the fit are the "final product".

The first stage is covered by a Monte-Carlo simulation. Inputs for the simulation are the spatial and energetic profile of the ion beam, the properties of the target and parameters or cross sections describing the excitation process. Such a Monte-Carlo simulation based on the Geant4 framework [Ago03, All06] was developed within this work and is called `StopSim`. It is described in detail in Appendix B.1.

The output of the simulation is a set of ion velocity histories. They contain the velocity vectors of individual ions in an ensemble, sampled in user-defined time steps. The velocity histories start at the time of the excitation of the ions ( $t = 0$ ) and end at the time when the ions come to rest inside the target or leave it. These velocity histories are the starting point for calculating Doppler-broadened  $\gamma$ -ray lineshapes. The temporal evolution of the velocity distribution in an ion ensemble provided by `StopSim` is exemplarily shown in Figure 4.5.

The second and third stage of lineshape calculation are task of the *Analysis Program for Continuous-Angle Dsam* (APCAD) that was also developed within this work.

While the second stage basically comprises further input to APCAD and is described in detail in Appendix B.2, the formalism of the lineshape calculation in the third stage using the input from stage one and two is outlined in the following. A detailed description is again found Appendix B.2.

Experimental data is commonly provided with a certain binning in the continuously measured quantities, such as  $\gamma$ -ray energy. In case of position-sensitive  $\gamma$ -ray tracking detectors, also the detection polar angle is measured continuously and the experimental data is provided with a certain binning also in the detection polar angle. In the case of conventional, position-insensitive  $\gamma$ -ray detectors, spectra are provided either for each detector crystal/segment or for groups of detectors/segments positioned at the same laboratory polar angle. Also the calculated lineshapes are provided with the very same binning in energy and detection angle (or with multiple spectra for the sets of polar angles in the case of position-insensitive detectors) as the experimental data. This has its origin in the employed numerical method for fast calculation of the lineshapes and allows for a fast comparison between experimental and calculated spectra in the fitting procedure.

In the following, both the binning of the  $\gamma$ -ray detection angles that are measured by  $\gamma$ -ray tracking detectors and the spectra for sets of polar angles of detector positions in case of position-insensitive detectors are referred to as "angular bins in detection polar angle".

From the velocity histories provided by the Monte-Carlo simulation, the distributions  $S_i(s_m, t_n)$  of relative Doppler shifts

$$s = E'_\gamma / E_{\gamma,0} - 1 \underset{\beta \ll 1}{\approx} \beta \cos \alpha. \quad (4.8)$$

that would be detected in an angular bin  $i$  for  $\gamma$ -ray emission at time  $t_n$  after the excitation reaction are calculated. The discrete time steps  $t_n$  are given by the sampling of the velocity histories. Discretized relative Doppler shifts are denoted as  $s_m$  and  $E_{\gamma,0}$  is the unshifted  $\gamma$ -ray energy of a transition. The distributions  $S_i(s_m, t_n)$  are denoted as *stopping matrices* and stored in tables. They are calculated for all ion velocity histories that have been selected from the output of the simulation according to experimental constraints such as detection of ions in particle detectors.

The normalization of  $S_i(s_m, t_n)$  for each discretized time,  $\sum_n S_i(s_m, t_n)$ , reflects the enhancement or reduction of  $\gamma$ -ray intensity observed in angular bin  $i$  due to Lorentz-boost (see Section 2.3). This  $\gamma$ -ray intensity is averaged over the solid angle covered by the respective angular bin. In the calculation of  $S_i(s_m, t_n)$  the Doppler-effect, all relativistic effects and effects arising from transformation of reference frames described in Section 2.3 are taken into account *exactly*. Figure 4.11

exemplarily shows a stopping matrix from the analysis of LNL experiment 08.09 (see Chapter 6.1.4) and explains its properties.

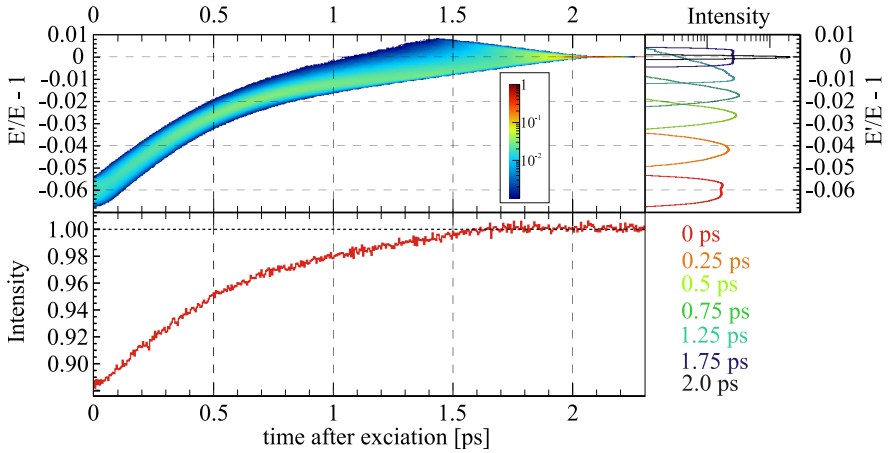


**Figure 4.11.:** Example for a stopping matrix and description of its properties.

**Top left:** Stopping matrix for an angular bin centered at  $\theta_\gamma=137.6^\circ$  from the analysis of LNL experiment 08.09 (see Section 6.1.4). It shows the intensity distribution of relative Doppler shifts  $s_m$  (see Equation 4.8) that would be registered in this angular bin as a function of  $\gamma$ -ray emission time after the excitation reaction.

**Bottom:** Projection of the stopping matrix on the time axis. The deficit in intensity at early times and, hence, high ion velocities is due to Lorentz-boost.

**Top right:** Projections of the stopping matrix on the shift axis, showing the evolution of the relative Doppler shift distribution as time evolves. See text for details.

The stopping matrices  $S_i(s_m, t_n)$  refer to isotropic  $\gamma$ -ray emission in the rest frames of the emitting nuclei. To first order,  $\gamma$ -ray angular distributions can be accounted for by weighting the stopping matrices corresponding to angular bins centered at  $\theta_\gamma$  with the corresponding values of the angular distribution function  $W(\theta_\gamma)$  as defined in Equation 2.50. However, this simple approach neglects the effect of changing emitter velocities on the transformation of the emission polar angle from the rest frame of the emitting nucleus to the laboratory frame and the resulting effects on the lineshapes discussed in Section 4.2. Furthermore, changes of the

emission angle stemming from a displacement of the emitting nuclei from the target center would not be accounted for. An *exact* treatment of the  $\gamma$ -ray angular distribution is provided by the following technique:

Consider an ensemble of excited ions decelerating in matter. The excitation mechanism is the same for all ions in the ensemble. If the nuclear alignment distribution exhibits axial symmetry w.r.t. the beam axis, averaged statistical tensors  $\rho_k(J_i)$  can be found that provide an adequate description of the  $\gamma$ -ray angular distribution in the rest frame of the emitting nuclei (see Section 2.4, the discussion of the case that axial symmetry is not given follows below). For each ion  $j$  emitting  $\gamma$ -radiation, the  $\gamma$ -ray angular distribution can be expressed by

$$W_j(\theta_j^{RN}) = 1 + A_2 P_2(\cos \theta_j^{RN}) + A_4 P_4(\cos \theta_j^{RN}) \quad (4.9)$$

where  $\theta_j^{RN}$  is the  $\gamma$ -ray emission angle with respect to the quantization axis (here: the beam axis) in the rest frame of the emitting nucleus,  $A_0 = 1$  and  $A_k = \rho_k(J_i) F_k$  (compare Eq. 2.50). However, since the velocity vectors and positions of the ions in the ensemble differ, there is a variation of emission angles  $\theta_j^{RN}$  if the  $\gamma$ -rays are detected at fixed polar angles  $\theta_{det}^{lab}$  with respect to the target center and the beam axis in the laboratory frame. In other words, the emission angle  $\theta_j^{RN}$  for a specific ion  $j$  corresponding to the detection angle  $\theta_{det}^{lab}$  has to be considered as a function of the velocity  $\vec{\beta}_j$  and position  $\vec{x}_j$  of the emitting ion, and the same applies vice versa:

$$\begin{aligned} \theta_j^{RN} &= f(\theta_{det}^{lab}, \vec{\beta}_j, \vec{x}_j) \text{ and} \\ \theta_{det}^{lab} &= g(\theta_j^{RN}, \vec{\beta}_j, \vec{x}_j). \end{aligned} \quad (4.10)$$

This is the origin of the effect of the angular distributions on Doppler-broadened lineshapes discussed in Section 4.2. The actual functional dependence between  $\theta_j^{RN}$  and  $\theta_{det}^{lab}$  is discussed in Section 2.3.

Since both ion velocity and position are functions of time for the ions decelerating in matter, also  $\theta_j^{RN}$  as a function of  $\theta_{det}^{lab}$  is a function of time, i.e.  $\theta_j^{RN}(\theta_{det}^{lab}, \vec{\beta}_j, \vec{x}_j)$  may be written as  $\theta_j^{RN}(\theta_{det}^{lab}, t)$ .

Mathematically, the angular distribution observed in the laboratory frame consequently has to be expressed as average over the individual angular distributions for

each ion  $j$  out of the  $N$  ions in the ensemble as a function of laboratory detection angle  $\theta_{det}^{lab}$  and time:

$$\begin{aligned}
 W(\theta_{det}^{lab}, t) &= \frac{1}{N} \sum_{j=1}^N W_j \left( \theta_j^{RN}(\theta_{det}^{lab}, t) \right) \\
 &= \frac{1}{N} \sum_{j=1}^N 1 + A_2 P_2 \left( \cos \theta_j^{RN}(\theta_{det}^{lab}, t) \right) + A_4 P_4 \left( \cos \theta_j^{RN}(\theta_{det}^{lab}, t) \right) \\
 &= 1 + A_2 \frac{1}{N} \sum_{j=1}^N P_2 \left( \cos \theta_j^{RN}(\theta_{det}^{lab}, t) \right) + A_4 \frac{1}{N} \sum_{j=1}^N P_4 \left( \cos \theta_j^{RN}(\theta_{det}^{lab}, t) \right) \\
 &\equiv 1 + A_2 \overline{P_2}(\theta_{det}^{lab}, t) + A_4 \overline{P_4}(\theta_{det}^{lab}, t).
 \end{aligned} \tag{4.11}$$

Equation 4.11 shows that this averaged angular distribution can be expressed by averaged values of the Legendre polynomials evaluated at the corresponding emission angles  $\theta_j^{RN}(\theta_{det}^{lab}, t)$ . These averaged Legendre polynomials are denoted as  $\overline{P_{2,4}}(\theta_{det}^{lab}, t)$ .

For the caDSAM, the values of  $\overline{P_2}(\theta_{det}^{lab}, t)$  and  $\overline{P_4}(\theta_{det}^{lab}, t)$  as defined in Equation (4.11) are calculated along with the stopping matrices for each discrete time step  $t_n$  and are averaged over the detection angles  $\theta_{det}^{lab}$  covered by the respective angular bin  $i$ . These time-dependent averaged Legendre polynomials are denoted as  $\overline{P_{2,i}}(t_n)$  and  $\overline{P_{4,i}}(t_n)$  and stored in tables. Note that the attenuation of angular distributions by finite opening angles of conventional detectors [Gro65, Yam67] is automatically accounted for by averaging  $\overline{P_2}(\theta_{det}^{lab}, t)$  and  $\overline{P_4}(\theta_{det}^{lab}, t)$  over the detector opening angles. Therefore, the expansion coefficients  $A_2$  and  $A_4$  refer to the angular distribution of the ions in the RN reference frame. Calculated values of  $\overline{P_{2,i}}(t_n)$  and  $\overline{P_{4,i}}(t_n)$  are exemplarily shown in Figure 4.12.

The Doppler-shifted energy of  $\gamma$ -ray quanta depends on the velocity  $\beta$  of the emitting ion and on the angle  $\alpha$  between the ion momentum vector and the  $\gamma$ -ray emission direction. Hence, for a given observation position  $(\theta_\gamma^{lab}, \phi_\gamma^{lab})$  and a fixed scattering angle of the emitting particle  $\theta_p^{lab}$  in the laboratory system, the observed Doppler shift depends on the particle azimuth angle  $\phi_p^{lab}$ . If the experimental setup for the detection of scattered particles does not exhibit axial symmetry with respect to the beam axis, the nuclear alignment distribution does in general also not exhibit axial symmetry w.r.t. the beam axis and the  $\gamma$ -ray emission is not isotropic in the azimuth angle  $\phi_\gamma$  (see Section 2.4). The particle- $\gamma$  angular correlation function

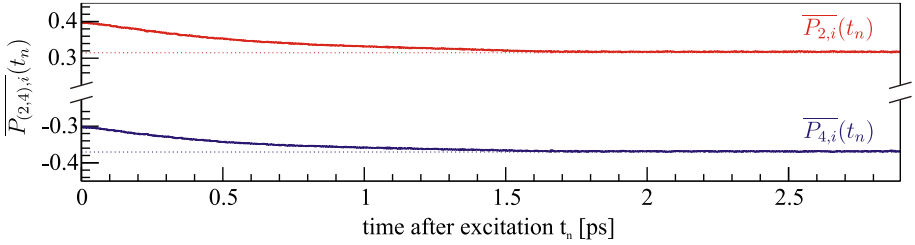


**Figure 4.12.:** Temporal evolution of the averaged  $2^{nd}$  and  $4^{th}$  Legendre polynomials for an ensemble of excited ions,  $\overline{P_{(2,4),i}^{lab}}(t_n)$ , evaluated at  $\gamma$ -ray detection angles  $\theta_{det}^{lab}$  subtended by a position-sensitive detector in an angular bin  $i$  centered at  $\theta_{det}^{lab} = 137.6$ . The shown functions are an example from the caDSAM analysis of LNL experiment 08.09 (see Section 6.1.4). These values of  $\overline{P_{(2,4),i}^{lab}}(t_n)$  are used to calculate angular distributions of  $\gamma$ -radiation emitted in-flight, observed at given polar angles in the laboratory system. The horizontal, dotted lines represent the values of  $P_{2,4}(\cos 137.6^\circ)$  which coincide with  $\overline{P_{(2,4),i}^{lab}}(t_n)$  if the  $\gamma$ -ray emission occurs at the center of the target and at rest. The variation of the  $\gamma$ -ray intensity ratio due to different emitter velocities observed at maximum shift and in the stop peak of a lineshape depends on the values of  $\overline{P_{2,4}}$  at  $t = 0$  and  $t > 2$  ps as well as the angular distribution expansion coefficients  $A_{2,4}$ . See text for details.

$W(\theta_\gamma, \phi_\gamma)$ , Eq. (2.57), applies in this case. It can result in non-trivial distributions of Doppler shift in  $\gamma$ -ray energy observed at a position  $(\theta_\gamma^{lab}, \phi_\gamma^{lab})$  even for fixed ion velocity  $\beta$  and fixed particle polar scattering angle  $\theta_p^{lab}$ . This has to be accounted for in the calculation of Doppler-broadened  $\gamma$ -ray lineshapes<sup>1</sup>.

For the description of particle- $\gamma$  angular correlations in the polar angle  $\theta_\gamma$  and the particle- $\gamma$  azimuth angle  $\phi$  by Equation (2.57), the first term describing the

<sup>1</sup> If the setup is axially symmetric or if the  $\gamma$ -ray emission is isotropic in the azimuth angle, a broadening of the distribution of relative Doppler shifts occurs that is accounted for by the stopping matrices  $S_i(s_m, t_n)$  by construction.

$\gamma$ -ray angular distribution in the polar angle is accounted for by the evaluation of averaged Legendre polynomials as described above. What remains is a term

$$\begin{aligned}
 W'(\theta_j^{RN}, \phi_j^{RN}) &= 2 \sum_{k \geq 2} \sum_{q > 0}^k \hat{\rho}_{kq}(J_i) F_k \cos(q\phi_j^{RN}) C_{kq}(\theta_j^{RN}, 0) \\
 &\equiv \sum_{k \geq 2} \sum_{q > 0}^k A_{kq} \cos(q\phi_j^{RN}) C_{kq}(\theta_j^{RN}, 0).
 \end{aligned} \tag{4.12}$$

Again, the index  $j$  enumerates individual ions in the ensemble. In practice, it is sufficient to regard dipole- and quadrupole radiation, i.e.  $k \leq 4$ . Averaged statistical tensors can be found that provide an adequate description of the particle- $\gamma$ -ray angular correlation in the rest frame of the emitting nuclei.

The  $\gamma$ -ray polar-angular distribution introduces a *re-scaling* of the distribution of relative Doppler shifts observed at a certain observation angle  $\theta_{det}^{lab}$  by the time-dependent factors in Equation (4.11). Apart from its normalization, the Doppler shift distribution that is observed for a fixed  $\gamma$ -ray emission time  $t_n$  is not affected. In contrast, the particle- $\gamma$  angular correlation introduces a *change of the Doppler shift distribution* observed at a certain observation angle  $\theta_{det}^{lab}$  at each time  $t_n$ . As a consequence, a procedure as for the polar-angular distribution can not be applied.

The effect of particle- $\gamma$  angular correlations can be accounted for *exactly* by introducing weighted stopping matrices  $\hat{S}_{ikq}(s_m, t_n)$ . They are calculated in the same way as the (un-weighted) stopping matrices  $S_i(s_m, t_n)$ , but the contribution by every individual ion  $j$  is weighted by the factor  $\cos(q\phi_j^{RN}) C_{kq}(\theta_j^{RN}, 0)$  (see Equations 4.12 and 2.57) at every time  $t_n$ . The weighted stopping matrices have the property

$$\sum_{s_m} \hat{S}_{ikq}(s_m, t_n) = 0. \tag{4.13}$$

The effect of particle- $\gamma$  angular correlations on calculated lineshapes is discussed in detail on the example of LNL-experiment 09.08 in Section 6.1.4.

For a set of angular distribution- and correlation-coefficients  $\{A_k, A_{kq}\}$ , the distributions of relative Doppler shifts  $s_m$  observed in an angular bin  $i$  for  $\gamma$ -ray emission at times  $t_n$  is then given by

$$\mathcal{S}'_i(s_m, t_n) = \left(1 + A_2 \overline{P_{2,i}}(t_n) + A_4 \overline{P_{4,i}}(t_n)\right) \left(S_i(s_m, t_n) + \sum_{k \geq 2} \sum_{q > 0}^k A_{kq} \hat{S}_{ikq}(s_m, t_n)\right). \tag{4.14}$$

As discussed in Section 2.2, the decay function of a nuclear state is determined by the state's lifetime, the lifetimes of states feeding it and fractions  $b$  denoting to what percentage the involved states were populated by the nuclear reaction at time  $t = 0$ . The following discussion is restricted to feeding chains of length two (i.e. a nuclear state that can be populated either directly or by feeders that are populated directly) and can easily be generalized. Let  $N_0$  be the total number of observed decays,  $b_0$  the fraction of direct population of the state under investigation,  $b_f$  the fraction of population via feeders  $f$ ,  $\tau_0$  the lifetime of the state under investigation and  $\tau_f$  the lifetimes of its direct feeders. As discussed in Section 2.2, the decay functions  $A_f(t)$  describing each of the feeding transitions are given by

$$A_f(t) = b_f \frac{N_0}{\tau_f} e^{-t/\tau_f}, \quad (4.15)$$

and the decay function  $A_0(t)$  of the state of interest can be written as

$$\begin{aligned} A_0(t) &= b_0 \frac{N_0}{\tau_0} e^{-t/\tau_0} + \sum_f b_f \frac{N_0}{\tau_0 - \tau_f} \left( e^{-t/\tau_0} - e^{-t/\tau_f} \right) \\ &\equiv A_{0,0}(t) + \sum_f A_{0,f}(t). \end{aligned} \quad (4.16)$$

Here, the decay function  $A_{0,0}(t)$  describes the decay of the fraction of nuclei in the excited state of interest that have been populated by the reaction directly and the decay functions  $A_{0,f}(t)$  describe the decay of fractions that have been populated by the feeder  $f$ .

The decay functions are discretized in time, using the same binning in time as for the stopping matrices. For this purpose, the decay functions are integrated over the time-intervals  $(t_{n,<}, \dots, t_{n,>})$  subtended by each time-bin  $t_n$ :

$$\hat{A}_x(t_n) = \int_{t_{n,<}}^{t_{n,>}} A_x(t) dt, \quad (4.17)$$

where  $A_x(t)$  represents any of the decay functions  $A_{0,0}(t)$ ,  $A_{0,f}(t)$  and  $\hat{A}_x(t_n)$  the corresponding discretized decay functions. A discretized decay function  $\hat{A}_x(t_n)$  is exemplarily shown in the top right of Figure 4.14.

Using Equations (4.14) and (4.17), the distributions  $p_i(s_m)$  of relative Doppler shifts  $s_m$  observed in the angular bins  $i$  for the decay of the state under investigation is given by

$$p_i(s_m) = \sum_{x,n} \hat{A}_x(t_n) \mathcal{S}_i(s_m, t_n). \quad (4.18)$$

This is depicted in the top part of Figure 4.14. Note that for the decay of every differently populated fraction  $x$  of the excited state, a different set of angular distribution and correlation coefficients  $\{A_k, A_{kq}\}$  can be used in the calculation of  $\mathcal{S}_i(s_m, t_n)$  in Equation (4.14). This is necessary because in general, the statistical tensor of a nuclear state is different depending on how the state was populated, i.e. directly or via the decay of a certain, higher-lying state.

By the definition of the relative shifts  $s_m$  (Equation 4.8), the Doppler-shifted  $\gamma$ -ray energies  $E'_{\gamma,m}$  corresponding to the discrete relative Doppler shifts  $s_m$  for an un-shifted energy  $E_{\gamma,0}$  are given by

$$E'_{\gamma,m}(s_m) = E_{\gamma,0}(s_m + 1). \quad (4.19)$$

Hence, the distribution  $p_i(s_m)$  of relative Doppler shifts  $s_m$  can easily be converted into a distribution of Doppler-shifted  $\gamma$ -ray energies  $p_i(E'_{\gamma,m}(s_m))$ . This is depicted in the middle and lower parts of Figure 4.14.

The spacing of the discrete energies  $E'_{\gamma,m}$  depends on the un-shifted  $\gamma$ -ray energy  $E_{\gamma,0}$  and is therefore variable. In particular, it does generally not coincide with the energy binning of the experimental data. This apparent shortcoming is completely abolished after the application of detector response functions  $\rho(E - E_0)$  for a suitably small binning of the relative shifts  $s_m$ . A typical response function for HPGe detectors and its components are shown in Figure 4.13.

The calculation of lineshapes having the same binning in energy as the experimental spectra is achieved by integrating the detector response functions over the energy range  $(E_{l,<}, \dots, E_{l,>})$  covered by an energy bin  $l$  of the experimental data:

$$\hat{\rho}_l(E_0) = \int_{E_{l,<}}^{E_{l,>}} \rho(E - E_0) dE. \quad (4.20)$$

The distributions of  $\gamma$ -ray energies  $p_i(E'_{\gamma,m})$  that are registered in an angular bin  $i$  represent intensities at discrete energies  $E'_{\gamma,m}$ . The theoretical lineshapes are calculated by adding response functions at every energy  $E'_{\gamma,m}$  where the normalization of

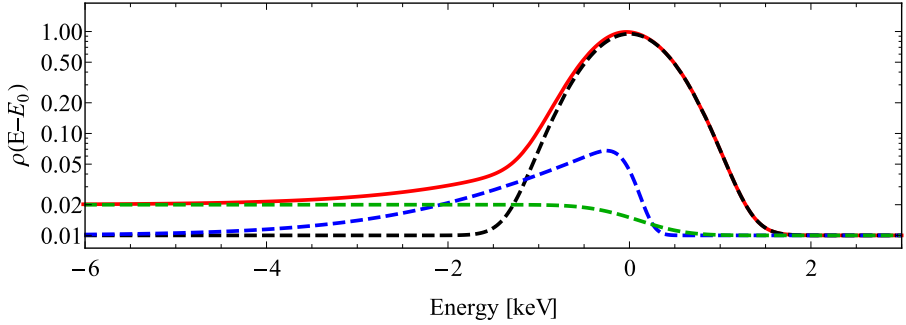


**Figure 4.13:** Typical response function for HPGe detectors consisting of Gaussian part (black, dashed line), low-energy tail (blue, dashed line) and step-function (green, dashed line). The total response function is drawn as red, solid line. The drawn functions were lifted by 0.01 for better visibility in the logarithmic scale.

each contribution is given by  $p_i(E'_{\gamma,m})$ . This is depicted in the lower part of Figure 4.14.

Calculated lineshapes exhibiting the same binning in energy and observation angle as the experimental data are given by the histogram  $T_{il}$  where  $i$  enumerates the angular bins and  $l$  enumerates the energy bins. The content of each bin is given by

$$T_{il} = \sum_m p_i(E'_{\gamma,m}) \hat{\rho}_l(E'_{\gamma,m}), \quad (4.21)$$

where  $p_i(E'_{\gamma,m})$  was defined in Equations (4.18) and (4.19) and  $\hat{\rho}_l(E'_{\gamma,m})$  is given by Equation (4.20). The procedure for the calculation of the lineshapes  $T_{il}$  is visualized in figure 4.14.

Starting from weighted and unweighted stopping matrices  $S_i(s_m, t_n)$ ,  $\hat{S}_{ikq}(s_m, t_n)$  and averaged Legendre polynomials  $\overline{P_{2,i}}(t_n)$  and  $\overline{P_{4,i}}(t_n)$ , the Doppler-broadened lineshapes for an arbitrary number of different  $\gamma$ -decays with individual particle- $\gamma$  angular correlations can be quickly calculated. The procedure of their calculation is basically reduced to summing entries of pre-calculated tables. Note that the weighted and unweighted stopping matrices as well as the averaged Legendre polynomials are independent from the properties of individual  $\gamma$ -decays. Therefore, they have to be calculated only once for all decays of an isotope excited in a certain reaction that is considered in a caDSAM analysis.

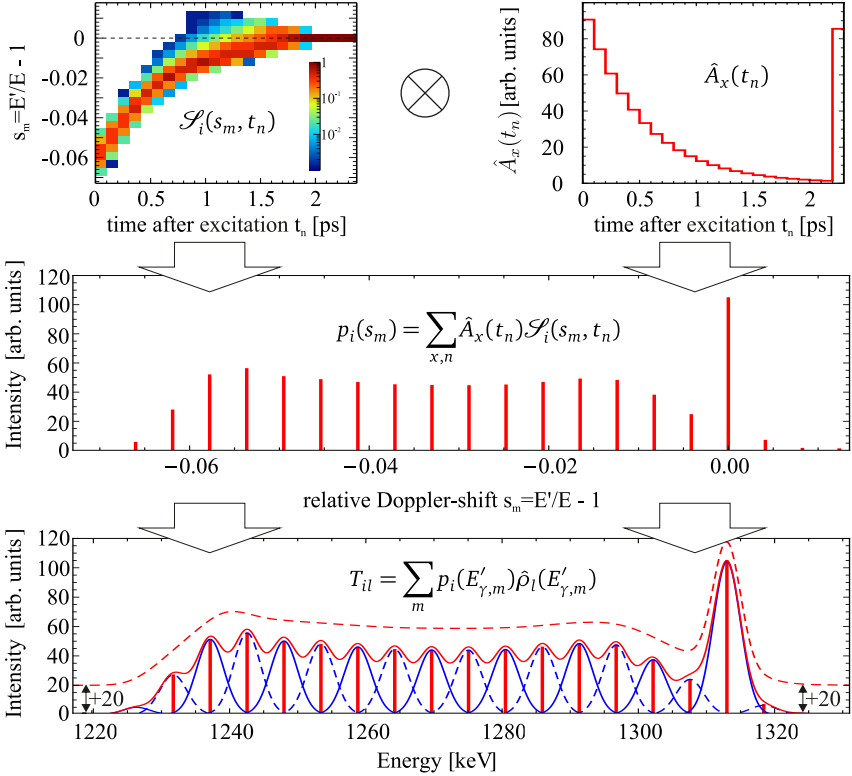


**Figure 4.14.:** Major steps in the calculation of a Doppler-broadened  $\gamma$ -ray lineshape by the caDSAM. The procedure for the lineshape calculation is depicted for one bin in polar  $\gamma$ -ray observation angle. Very coarse binning was chosen for clarity. **Top:** From the distributions  $\mathcal{S}_i(s_m, t_n)$  of relative Doppler shifts  $s_m$  observed in an angular bin  $i$  for  $\gamma$ -ray emission at times  $t_n$  and from the discretized decay functions  $\hat{A}_x(t_n)$ , the distributions  $p_i(s_m)$  of Doppler shifts  $s_m$  observed in angular bin  $i$  are calculated (Equation 4.14). **Middle:** The distributions  $p_i(E'_{\gamma,m})$  of corresponding Doppler-shifted  $\gamma$ -ray energies  $E'_{\gamma,m}$  follow from  $p_i(s_m)$  by use of Equation (4.19). **Bottom:** Application of the detector response function  $\hat{\rho}_l(E'_{\gamma,m})$  to every discrete energy  $E'_{\gamma,m}$  (red, vertical lines), weighted by  $p_i(E'_{\gamma,m})$  (blue curves), yields the final energy spectrum  $T_{il}$  (Equation 4.21). The thin, red line shows the obtained continuous spectrum for a very coarse binning, the dashed red line for a sufficiently fine binning of  $s_m$ . A binning in energy identical to that of the experimental data is introduced at this step (not depicted). See text for details.

---

The calculated Doppler-broadened  $\gamma$ -ray lineshapes for *all* angular bins  $i$  are determined by the following parameters. These are the free parameters entering the fitting procedure described in Appendix B and are listed together with a short note at what point they enter the lineshape calculation.

- **For each  $\gamma$ -ray transition: Intensity  $N_0$ , fractions of population paths  $b_f$ , lifetimes of the state  $\tau_0$  and its feeders  $\tau_f$**  for the calculation of decay functions  $\hat{A}_x(t_n)$  in Equations (4.16) and (4.17). Note that  $N_0$  is the *only normalization* of the lineshapes and applies to all angular bins  $i$ .
- **Angular distribution and correlation coefficients  $\{A_k, A_{kq}\}_x$**  for the decay of every differently populated fraction  $x$  of of the excited state. The coefficients  $\{A_k, A_{kq}\}_x$  enter the calculation of  $\mathcal{S}_i(s_m, t_n)$  in Equation (4.14).
- **Coefficients for the detector response functions** such as resolution (FWHM), fractional area of the low-energy tail, parameters describing the shape of the tail and the height of the step-function. These parameters enter the calculation of the response function  $\rho(E - E_0)$  and, thus, Equation (4.20). They have to be specified for every angular bin  $i$ . Usually, they can be determined from a source measurement and then be fixed during the fitting procedure (see Section 6.1.4).

---

## 4.4 Extensions of the continuous-angle Doppler-Shift Attenuation Method

---

The DSA and continuous-angle DSA Method as they were introduced in the previous sections rely on the complete stopping of ion beams in thick targets. The methods are typically employed for beam energies near the Coulomb-barrier, where maximum ion velocities in the order of 10% of the speed of light occur. The implantation of beams in the target is experimentally very undesirable in some cases. In particular, in experiments with radioactive ion beams the activation of the target area has to be avoided and stopping the beam often prevents the identification of reaction products behind the target.

The DSA Method can be extended such that the ion beam can leave the target in order to avoid the aforementioned restrictions. This experimental technique is dubbed *differential* continuous-angle DSAM and significantly extends the applicability of the caDSA Method to radioactive and relativistic beams.

The second extension of the DSA Method that is discussed in the following is the *geometric* continuous-angle DSAM. It extends the applicability of the caDSAM to level lifetimes up to some hundred picoseconds. It makes use of the dependence of the observed Doppler shifts in  $\gamma$ -ray energy from the vertex of  $\gamma$ -ray emission as excited nuclei proceed their motion after leaving the target.

The modifications of the programs StopSim and APCAD necessary to facilitate the needs of the differential and geometric caDSA Methods were implemented in the course of a Master's thesis [Let13] under the supervision of the author. They are described in Sections B.3 and B.4 of the appendix.

---

### 4.4.1 The differential continuous-angle Doppler-Shift Attenuation Method

---

If a target used in a DSAM experiment is not sufficiently thick to completely stop the excited ions, they will continue their motion with constant velocity vector after leaving the target. If their de-excitation occurs inside the target, the exactly same effects on the measured  $\gamma$ -ray energy spectra can be observed as described above for the caDSA Method, i.e. a pronounced Doppler-broadened  $\gamma$ -ray lineshape originating in  $\gamma$ -ray emission at different emitter velocities as the ions are slowing-down in the target. If the de-excitation occurs after the ions have left the target, a nearly constant Doppler shift of the  $\gamma$ -ray energy will be observed at a given laboratory observation angle<sup>2</sup>. These decays behind the target correspond to the decay after the ions have come to rest in the "conventional" (ca)DSA Method, which result in

---

<sup>2</sup> Effects from varying  $\gamma$ -ray vertices may occur, these are accounted for and are discussed in detail in the section on the geometric caDSA Method and Appendix B.4.

the detection of the un-shifted  $\gamma$ -ray energy  $E_0$ . The range of lifetimes that can be sensitively measured by the differential continuous-angle Doppler-Shift Attenuation Method is comparable to that of the "conventional" (ca)DSA Method and can be estimated by similar considerations.

The differential continuous-angle Doppler-Shift Attenuation Method is especially suitable for experiments with relativistic ion beams at velocities of several ten percent of the speed of light. Therefore, 150 AMeV  $^{136}\text{Xe}$  ions Coulomb-excited on and slowed down in a 500  $\mu\text{m}$  thick gold target will serve as example case for the figures shown in this section. The evolution of the velocity of these ions is shown on the left-hand side of Figure 4.15. The ions enter the target with  $\beta \approx 0.51$  c. The Coulomb excitation cross section changes only slightly as a function of the energy of the ions during their passage through the target. Consequently, approximately the same number of excitations occurs at every depth in the target, resulting in a flat distribution of ion velocities at the time of excitation (at  $t = 0$ ). All ions undergo approximately the same energy loss while traversing the target and leave it with almost the same velocity of  $\beta \approx 0.41$  c. This results in a sharp distribution of ion velocities at the end of the velocity histories at  $t \approx 3$  ps.

Resulting Doppler-broadened  $\gamma$ -ray lineshapes for the decay of a fictional state at 1 MeV excitation energy and a lifetime of 1 ps are shown on the right-hand side of Figure 4.15 as a function of  $\gamma$ -ray energy  $E_\gamma$  and detection polar angle in the laboratory system  $\theta_\gamma$ . Without Doppler correction (top), the registered  $\gamma$ -ray energies spread over a very broad range as a function of  $\theta_\gamma$ . At each detection polar angle, typical Doppler-broadened lineshapes are visible (see figures 4.16 and 4.18 for some projections on the energy-axis at fixed detection angles), yet their "stop-peak" doesn't reside at the transition energy  $E_0$  but is strongly shifted as a function of observation angle. The same spectrum is shown on the lower right side of the same figure, but with a Doppler correction applied. In this Doppler correction, it is assumed that the direction of the ions leaving the target was measured (e.g. by a time-projection-chamber or by a set of segmented Si-detectors) and also that the velocity of the ions *behind* the target was measured with a relative uncertainty of one percent<sup>3</sup>. The decays occurring after the emitting ion has left the target take place at the constant velocities behind the target. These velocities can be measured with good precision. Hence, the Doppler correction properly restores the transition energy  $E_0$  irrespective of the detection polar angle for the decays that occur behind

<sup>3</sup> This is a realistic accuracy. If the velocity is measured e.g. via time-of-flight using a drift-length of 3.5 m (which corresponds approximately to the drift length in the LYCCA-calorimeter at the PreSPEC setup), this requires a time-of-flight resolution of about 230 ps at  $\beta=0.5$  (the TOF resolution in LYCCA is approximately 100 ps).

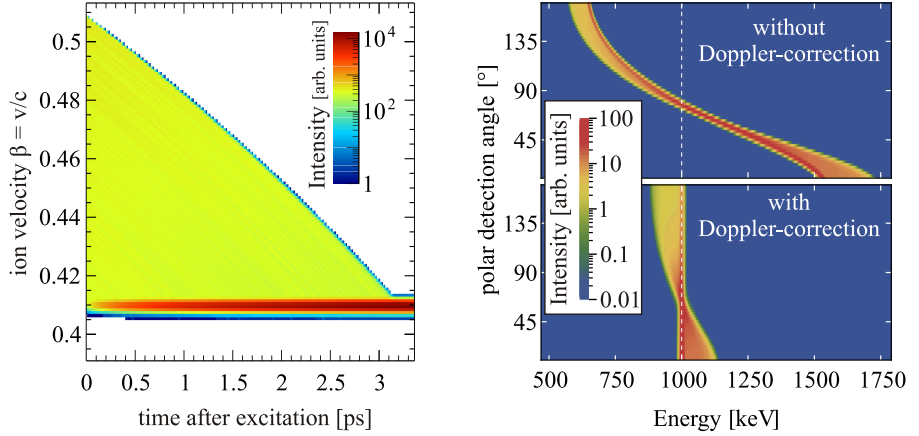


**Figure 4.15.:** **Left:** Temporal evolution of the velocity distribution of 150 AMeV  $^{136}\text{Xe}$  nuclei that have been Coulomb-excited at  $t = 0$  on a 500  $\mu\text{m}$  thick gold target. The excitations occur throughout the target, and all ions leave the target with approximately same velocity.

**Top right:** Calculated spectrum of Doppler-broadened  $\gamma$ -ray lineshapes as a function of  $\gamma$ -ray energy and polar  $\gamma$ -ray detection angle  $\theta_\gamma$ . A decay of a fictional state at 1 MeV excitation energy and a lifetime of 1 ps was assumed. No Doppler correction is applied.

**Bottom right:** Spectrum of the same  $\gamma$ -rays as in the plot above, but after Doppler correction. For the correction it was assumed that the direction of the ions leaving the target is measured and that the velocity of the ions *behind* the target is measured with a relative uncertainty of 1%. See text for details.

the target. If the decay takes place in the target at a higher velocity than the one measured, the instantaneous velocity at the time of de-excitation is experimentally not accessible. The Doppler correction has to be performed assuming the velocity behind the target, and consequently the magnitude of the Doppler shift is underestimated in the correction. This results in higher energies than  $E_0$  observed under forward angles  $\alpha < \alpha_0$  and lower energies under backward angles  $\alpha > \alpha_0$ . Here,  $\alpha_0$  denotes the emitter- $\gamma$ -ray angle at which no Doppler shift occurs:

$$\alpha_0 = \arccos \frac{1 - \sqrt{1 - \beta^2}}{\beta} \underset{\beta \ll 1}{\approx} \frac{\pi - \beta}{2} \text{ rad.} \quad (4.22)$$

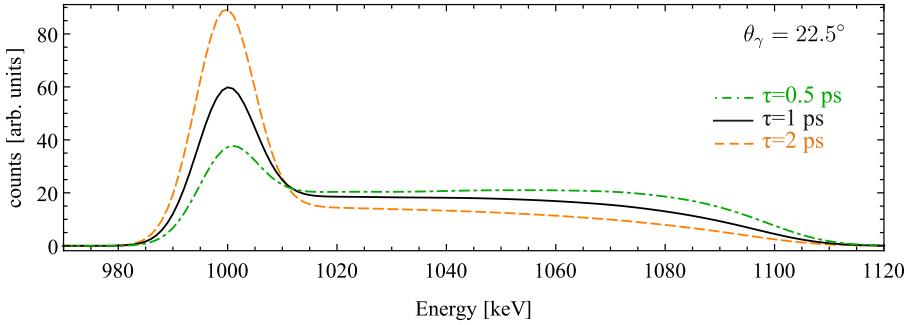


**Figure 4.16.:** Calculated Doppler-broadened  $\gamma$ -ray lineshapes as they are observed when applying the differential caDSA Method. The same experimental conditions as in Figure 4.15 were assumed. Spectra obtained after Doppler correction and for lifetimes of 0.5 ps (green, dashed-dotted line), 1 ps (black, solid line) and 2 ps (orange, dashed line) are shown. They demonstrate the sensitivity of the differential caDSA Method to the lifetime of the de-exciting state. See text for details.

The resulting Doppler-broadened lineshapes after Doppler correction are very similar to those observed in the case where the ions are completely stopped in the target. The sensitivity to the lifetime of the de-exciting state is illustrated in Figure 4.16.

The energy range  $\Delta E_{noDC}(\alpha)$  covered by the Doppler-broadened  $\gamma$ -ray lineshapes observed by the differential caDSAM without the application of a Doppler correction is given by the difference in Doppler shift for the velocity of the ions before and after passing the target,  $\beta_{in}$  and  $\beta_{out}$ :

$$\Delta E_{noDC}(\alpha) = \left| E'(\alpha, \beta_{in}) - E'(\alpha, \beta_{out}) \right|, \quad (4.23)$$

where  $E'(\alpha, \beta)$  is given by the Doppler formula, Equation (2.40).

Application of a Doppler correction assuming that the de-excitation occurs at velocity  $\beta_{out}$  means that the measured  $\gamma$ -ray energy is multiplied by the factor  $E_0/E'(\alpha, \beta_{out})$ . Consequently, the energy-range  $\Delta E_{DC}(\alpha)$  covered by the Doppler-

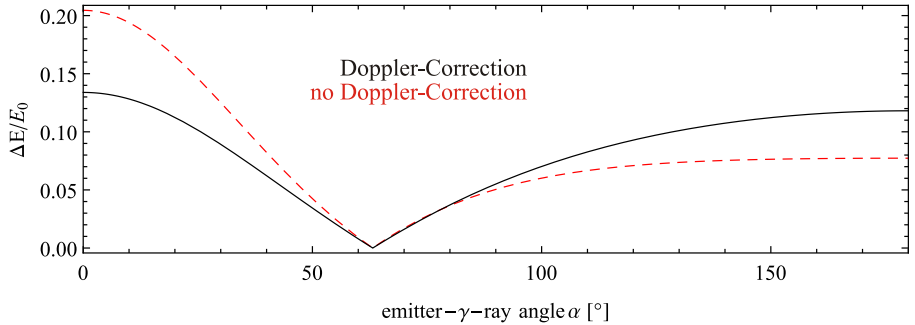


**Figure 4.17.:** Width of the Doppler-broadened lineshape observed in the differential caDSA Method with Doppler correction (black, solid line, Equation 4.24) and without Doppler correction (red, dashed line, Equation 4.23). Ion velocities before and after passage of the target of  $\beta_{in} = 0.5$  and  $\beta_{out} = 0.4$  were assumed. The lineshape is compressed by the Doppler correction under forward angles and expanded under backward angles. See text for details.

broadened  $\gamma$ -ray lineshapes after the application of a Doppler correction is given by

$$\begin{aligned} \Delta E_{DC}(\alpha) &= \left| E'(\alpha, \beta_{in}) \frac{E_0}{E'(\alpha, \beta_{out})} - E'(\alpha, \beta_{out}) \frac{E_0}{E'(\alpha, \beta_{out})} \right| \\ &= \left| E_0 \left( \frac{E'(\alpha, \beta_{in})}{E'(\alpha, \beta_{out})} - 1 \right) \right|. \end{aligned} \quad (4.24)$$

The functions  $\Delta E_{noDC}(\alpha)$  and  $\Delta E_{DC}(\alpha)$  are plotted for  $\beta_{in} = 0.5$  and  $\beta_{out} = 0.4$  in Figure 4.17. Under forward observation angles, the energy range covered by the Doppler-broadened  $\gamma$ -ray lineshape is compressed by the Doppler correction. Under backward observation angles, the opposite is the case. This is illustrated in Figure 4.18 by means of the example of a 150 AMeV beam of  $^{136}\text{Xe}$ , Coulomb-excited and slowed down in a 500  $\mu\text{m}$  thick gold target.

Albeit information on the lifetime of the de-exciting state is contained in both the spectra with and without Doppler correction, there are good arguments for regarding Doppler-corrected spectra for the extraction of level lifetimes:

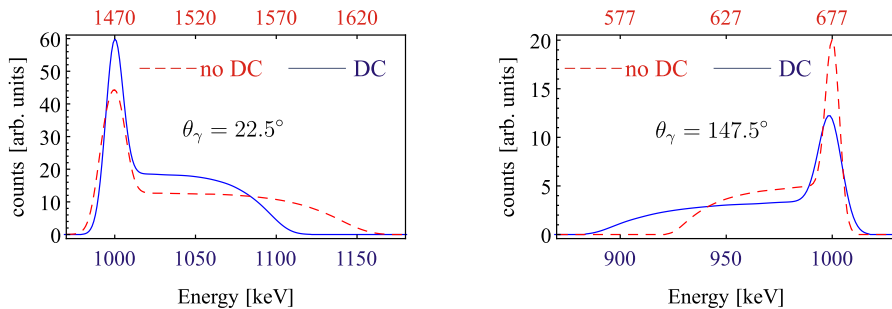


**Figure 4.18.:** Calculated Doppler-broadened  $\gamma$ -ray lineshapes as they are observed when applying the differential caDSA Method. The same experimental conditions as in Figure 4.15 were assumed. For comparison of spectra with (solid, blue lines) and without (dashed, red lines) Doppler correction (DC), the spectra were shifted such that the events corresponding to decays behind the target are plotted at the same position. The energy scale for Doppler-corrected spectrum is on the bottom, the scale for non-corrected spectrum on the top of the plots. Lineshapes observed at forward (left) and backward angle (right) are shown. Under forward angles, the spectra with DC are compressed compared to the spectra without DC. Under backward angles the opposite occurs. See text for details.

### Better resolution

If the ion velocities are measured sufficiently precisely behind the target, the resolution at a *fixed* observation angle is better in the Doppler-corrected spectrum than in the non-Doppler-corrected one. This holds even in the case that the spectrum is sorted as a function of the angle  $\alpha$  between the momentum vector of the emitting ion and the  $\gamma$ -ray emission angle. The origin of the better resolution in Doppler-corrected spectra is additional information that is taken into account, namely the measured velocities of the ions behind the target.

Differences in the ion velocities behind the target inter alia stem from their dependence on the ion scattering angle in the excitation reaction via the reaction kinematics (Appendix C), energy-spread of the incoming beam and energy straggling during the slowing-down process in the target. The influence on the Doppler shift of these differences in the ion velocities behind the target is eliminated by the Doppler correction, if the velocities are measured with sufficient precision. They are not accounted for in the case that the data are sorted as a function of the

emitter- $\gamma$ -ray angle  $\alpha$ , but not Doppler-corrected. Also the differences due to reaction kinematics are *not* removed, since the same angle  $\alpha$  can occur for different particle scattering angles and hence different ion velocities combined with different  $\gamma$ -ray detection angles  $\theta_\gamma$ .

The effect of the velocity spread on the  $\gamma$ -ray energy resolution varies as a function of the emitter- $\gamma$ -ray-angle  $\alpha$ . It is proportional to

$$\left| \frac{1}{E_0} \frac{\partial E'}{\partial \beta}(\alpha, \beta) \right|. \quad (4.25)$$

This value is plotted in Figure 4.19 for different values of  $\beta$ . The effect of the velocity spread on the  $\gamma$ -ray energy resolution is strongest at very forward and backward angles  $\alpha$ , and the same holds for the obtained resolution after Doppler correction. The derivative (4.25) vanishes identically at the angle  $\alpha = \arccos \beta$ . At this angle  $\alpha$ , the observed  $\gamma$ -ray energy resolution is nearly independent from the uncertainty of the measured ion velocity and the velocity spread within the ion ensemble.

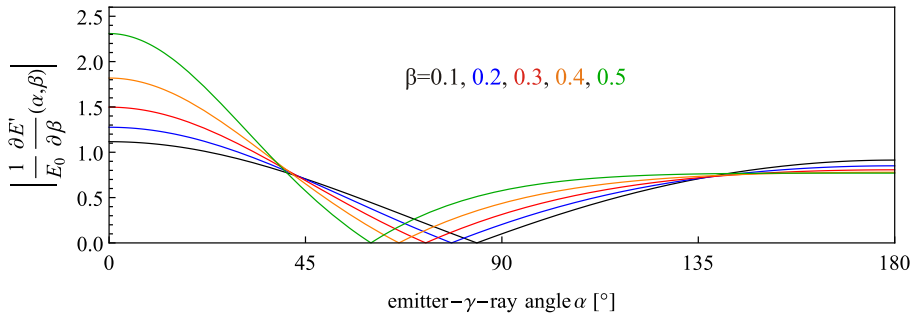


**Figure 4.19.:** Absolute value of the partial derivative of the Doppler-shifted energy  $E'$  with respect to the emitter velocity  $\beta$ , plotted as a function of emitter- $\gamma$ -ray-angle  $\alpha$  for different velocities  $\beta$ . The effect of the velocity spread within an ensemble of emitters of  $\gamma$ -radiation on the observed  $\gamma$ -ray energy resolution is proportional to this quantity.

The better resolution in the Doppler-corrected  $\gamma$ -ray spectra is demonstrated in Figure 4.20. Calculated  $\gamma$ -ray lineshapes are compared for the case that Doppler correction is applied or not applied and for sorting the data as a function of  $\gamma$ -ray polar angle  $\theta_\gamma$  or as a function of emitter- $\gamma$ -ray angle  $\alpha$ . In this example, a relative velocity spread of 1% FWHM of the incoming beam of  $^{136}\text{Xe}$  ions at 150 AMeV was

assumed. In the discussed example, the relative spread of ion velocities behind the target due to energy straggling is about 0.38% (calculated with ATIMA [Gei15]) and the relative velocity spread due to different kinematics within the ion ensemble is about 0.37% (calculated from the reaction kinematics, Equation (C.1), as difference between the velocity corresponding to scattering angles of 0 and  $1.4^\circ$ ). It is carefully checked that the width of the angular bins of  $2.5^\circ$  has no significant influence on the difference in resolution of the two spectra in this case, where a position resolution of the  $\gamma$ -ray detector of 5 mm FWHM was assumed at a detector-target distance of 23.5 cm. The beam was assumed to have a point-like spatial profile. The influence of a broad spatial cross section of the ion beam can be accounted for by both the Doppler correction and sorting the data as a function of  $\gamma$ -ray emission-angle or the emitter- $\gamma$  angle  $\alpha$ , if the transverse beam position close to the target position is measured. The treatment of spatially extended beams in APCAD is discussed in Appendix B.4.

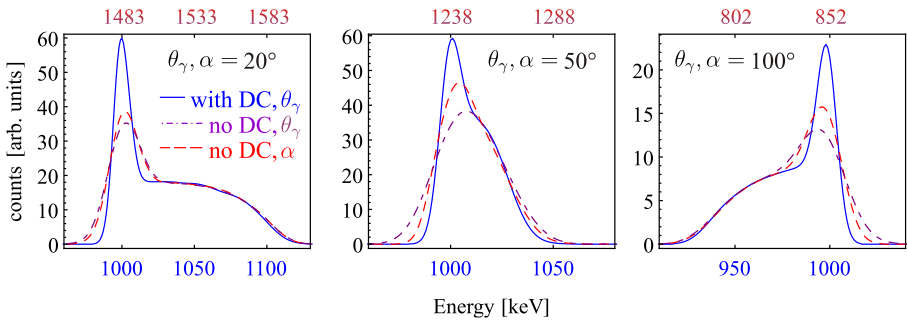


**Figure 4.20.:** Calculated Doppler-broadened  $\gamma$ -ray lineshapes with (blue, solid lines) and without (red/purple, dashed(-dotted) lines) Doppler correction (DC). Apart from an assumed velocity spread of the incoming ion beam of  $\Delta\beta = 1\%$  FWHM, the same experimental conditions as in Figure 4.15 were assumed. The spectra were shifted such that the events corresponding to decays behind the target are plotted at the same position. The corresponding energy scales are indicated by color. Lineshapes without DC are shown as a function of the  $\gamma$ -ray detection angle  $\theta_\gamma$  (dash-dotted, purple line) and as a function of the particle- $\gamma$ -ray-angle  $\alpha$  (dashed, red line). The better resolution after Doppler correction (solid, blue line) is clearly visible. The lineshapes without DC have been corrected for the effect of compression/expansion as shown in Figure 4.18 and described by Equations (4.23, 4.24) for better comparison. See text for details.

---

The better energy resolution after the application of a Doppler correction using the information from a measurement of ion velocities behind the target has two benefits:

- The shape of the Doppler-broadened  $\gamma$ -ray lineshape is better resolved, resulting in higher sensitivity to the underlying level lifetimes and better possibility to disentangle overlapping lineshapes of close-lying transitions.
- The peak-to background ratio is improved, raising the statistical significance of results obtained from the lineshape analyses.

### **Possibility to sum over larger ranges of $\gamma$ -ray detection angles**

The binning of the experimental data in the  $\gamma$ -ray detection angle  $\theta_\gamma$  (or in the particle- $\gamma$ -ray-angle  $\alpha$ ) necessarily implies that each angular bin covers a certain range of angles. In order to preserve the details of the spectrum, the binning has to be chosen sufficiently narrow such that the width of the angular bins is comparable to the angular resolution of the detectors. With the high position resolution of  $\gamma$ -ray-tracking detectors, a large number of very narrow angular bins may result, each with comparably low statistics. This leads to an unsatisfactory situation for the experimenter. If the features of the spectrum (peaks, lineshapes, ..) are not well pronounced due to the low statistics in the individual angular bins, a judgment on the quality of the data or a visual rating of the quality of any fit to the data is hindered. From statistical point of view, in turn, a fit to the experimental data should be performed using such a fully resolved spectrum. In fact, a finer binning resulting in less statistics per channel has no negative influence on a combined fitting procedure including all data or on the uncertainties of the extracted parameters, since the amount of significant data is not changed and no information is lost<sup>4</sup>.

A way to obtain a better signal-to-noise ratio in a single energy-spectrum for a given set of data is to add up data measured under different detection angles. In the case of spectroscopy experiments where no Doppler-broadened lineshapes are observed, the spectroscopic information becomes independent from the detection angle by the Doppler correction, and the spectrum can be summed over the full angular range covered by the detector system.

In the case lineshapes are to be analyzed, summing the spectra of several angular bins necessarily blurs the lineshape due to its dependence on the detection angle. However, the effect is much less severe in the case that a Doppler correction has been applied, as demonstrated in Figure 4.21. Again, the example of the 150 AMeV

---

<sup>4</sup> For low bin contents, normal distribution is not appropriate and the  $\chi^2$  value is not an adequate measure for the goodness-of-fit. Other Log-Likelihood-functions should rather be used, e.g. based on Poisson statistics.

beam of  $^{136}\text{Xe}$ , Coulomb-excited and slowed down in a 500  $\mu\text{m}$  thick gold target, is used for demonstration purposes.

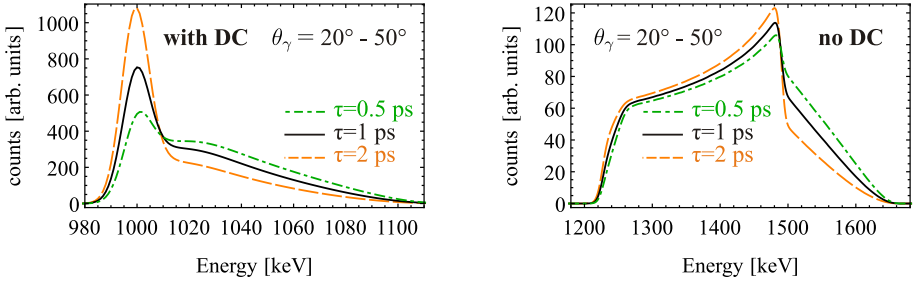


**Figure 4.21.:** Calculated Doppler-broadened  $\gamma$ -ray lineshapes with (left) and without (right) Doppler correction (DC) applied. The same experimental conditions as in Figure 4.15 were assumed. Lineshapes for level lifetimes of 0.5, 1 and 2 ps are shown. The spectra were summed over observation angles from  $20^\circ$  to  $50^\circ$ . Note the width and height of the lineshapes in the cases with and without Doppler correction. While the lineshape adds coherently if a Doppler correction was applied, a very broad and blurred lineshape is obtained in the case without Doppler correction. See text for details.

In the uncorrected spectrum (right), the summed lineshape spreads over a very large energy range. Since the complete lineshape shifts strongly as a function of detection angle, contributions from decays inside and behind the target overlap after summing. The sensitivity to the underlying level lifetime is reduced. Furthermore, the huge width of the summed lineshape results in a poor signal-to-noise ratio, since lineshapes observed under certain angles are added to background observed at other angles. Consequently, the statistical significance of the data is strongly reduced.

In contrast, the lineshapes observed after Doppler correction add in a coherent way, in the sense that for every observation angle the decays behind the target sum up at the same energy,  $E_0$ , and the decays inside the target cover a comparably narrow, adjacent energy range. Since the lineshape is located in overlapping energy ranges at all observation angles, a much smaller number of background events underlie the summed lineshape compared to the case without Doppler correction. The peak-to-background-ratio and, hence, the signal-to-noise ratio is therefore reduced only to a small extent compared to the ratio before summing over the angular range. A certain degree of blurring occurs predominantly at the energies corre-

---

sponding to decays at maximum velocity, since the largest shifts corresponding to these decays are only observed at the most forward angles. The sensitivity to the level lifetime is preserved to a large extend.

It should be stressed again that summing observed Doppler-broadened lineshapes over large ranges of observation angle can only improve the *visual impression* of the lineshape and may help to e.g. identify systematic errors during the fitting procedure like trapping in a local minimum due to poor start parameters, or to judge on the quality of the data. For the statistical analysis of lineshapes by means of a fit, an appropriate binning in  $\gamma$ -ray energy and observation angle preserving the full energy and position resolution should be used in order to use the full information contained in the data.

---

#### 4.4.2 The geometric continuous-angle Doppler-Shift Attenuation Method

---

In the "conventional" and the differential (ca-)DSA Method,  $\gamma$ -ray emission at different emitter velocities is the origin of pronounced Doppler-broadened  $\gamma$ -ray lineshapes that are sensitive to the lifetime of the decaying nuclear state. However, since the Doppler shift of the  $\gamma$ -ray energy depends not only on the velocity of the emitter, but also on the angle  $\alpha$  between the emitter momentum vector and the emission direction of the  $\gamma$ -ray, lifetime sensitive, Doppler-broadened  $\gamma$ -ray lineshapes can also be formed by another mechanism. This mechanism originates in a lifetime-dependent distribution of  $\gamma$ -ray vertices when excited ions leave the target. These different  $\gamma$ -ray vertices affect the angle  $\alpha$  for a given observation position in the laboratory frame. The measurement of level lifetimes by the analysis of the resulting lineshapes will be referred to as the *geometric continuous-angle Doppler-Shift Attenuation Method*.

The principle of the geometric caDSAM is depicted in Figure 4.22. If the target is sufficiently thin, the ions will leave the target after being excited and slowed down. For simplicity of the discussion it is assumed for the moment that the ions travel at constant velocity  $\beta_0$  *inside and behind* the target and that they move along the axis of the incoming beam. The incoming ion beam is assumed to be point-like and to puncture the target at the geometric center of a spherical, position-sensitive detector system with inner radius  $r$ . If the decay of the excited nuclear state occurs at the center of target, let the  $\gamma$ -ray be detected at an forward angle (backward angle)  $\alpha_1$  ( $\alpha_3$ ) with respect to the beam-axis. If in turn the  $\gamma$ -ray is emitted at a

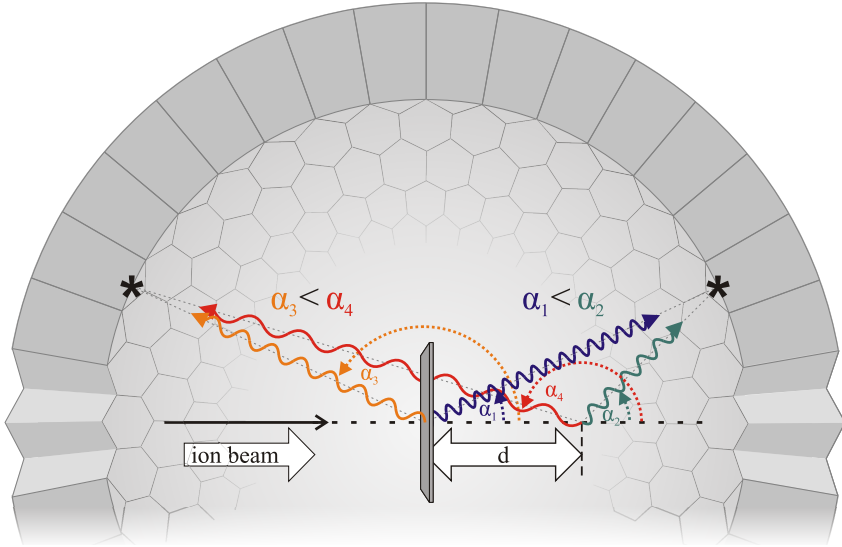


**Figure 4.22.:** Principle of the geometric caDSAM. If the  $\gamma$ -ray emission occurs at a distance  $d$  behind the target, the angle  $\alpha$  between the ion momentum vector and the  $\gamma$ -ray emission direction is reduced compared to  $\gamma$ -ray emission at the target center for a given observation position of the  $\gamma$ -ray. Therefore, the Doppler-shifted  $\gamma$ -ray energy observed at a given detection position is reduced for emission at distance  $d$ . This holds for  $\gamma$ -ray detection under forward and backward direction. A Doppler correction assuming that the  $\gamma$ -ray vertex is located at the target center consequently always results in Doppler-corrected energies  $E_c < E_0$  at all observation angles. See text for details.

distance  $d$  behind the target, then the angle  $\alpha$  for the same observation position of the  $\gamma$ -ray is reduced to

$$\alpha(d) = \tan^{-1} \left( \frac{r \sin \alpha_1}{r \cos \alpha_1 - d} \right) \quad (4.26)$$

In Figure 4.22, the angle  $\alpha$  for  $\gamma$ -ray emission at distance  $d$  from the target center is denoted  $\alpha_2$  ( $\alpha_4$ ) for the emission under forward direction (backward direction). The observation positions of the  $\gamma$ -rays under forward and backward angle are indicated by asterisks.

Since the angle  $\alpha$  depends on the  $\gamma$ -ray vertex, also the observed Doppler shift of the  $\gamma$ -ray energy  $E'$  is a function of  $d$ :

$$\begin{aligned}
 E'(d) &= E_0 \frac{\sqrt{1 - \beta_0^2}}{1 - \beta_0 \cos \alpha(d)} \\
 &= E_0 \sqrt{1 - \beta_0^2} \left( 1 - \frac{1}{\beta_0} \sqrt{\frac{\sin^2 \alpha_1^2}{(d/r - \cos \alpha_1)^2}} \right)^{-1}.
 \end{aligned} \tag{4.27}$$

Equation (4.27) is plotted in Figure 4.23 for different velocities  $\beta_0$  on the left-hand side and for different observation angles  $\alpha_1$  on the right-hand side.

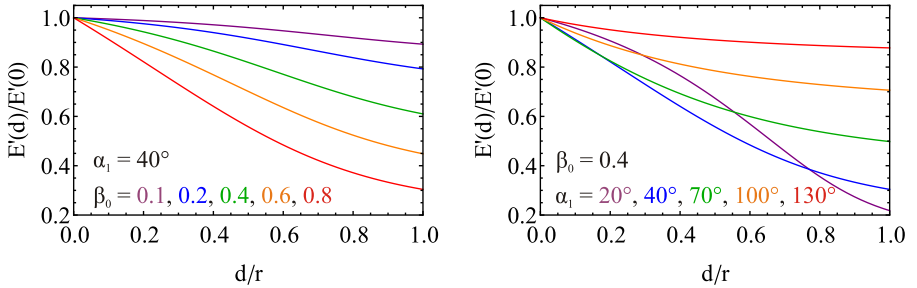


**Figure 4.23.:** Observed shift in  $\gamma$ -ray energy  $E'(d)$  as a function of the vertex position  $d$  along the beam axis behind the target (Equation 4.27, see Figure 4.22 for the geometry). The observed shift  $E'(d)$  is plotted as ratio to the shift observed for decay at the target position  $E'(0)$  and the  $\gamma$ -ray vertex is expressed in terms of the radius  $r$  of the detector system.

**Left:** Observed shift for different emitter velocities  $\beta_0$  at  $\alpha_1 = 40^\circ$ .

**Right:** Observed shift for different observation directions  $\alpha_1$  at  $\beta_0 = 0.4$ .

According to Equation (4.27) and as depicted in Figure 4.23,

$$\begin{aligned}
 E'(d) &< E'(0) \quad \forall d \in (0, r) \quad \text{and} \\
 \frac{\partial}{\partial d} E'(d) &< 0 \quad \forall d \in (0, r).
 \end{aligned} \tag{4.28}$$

In other words, decays that occur behind the target are always registered at lower energies than the decays that occur inside the target. In particular, the further away

from the target the decay occurs, the lower the detected  $\gamma$ -ray energy. This finding is solely due to the change of the  $\gamma$ -ray vertex as the ions leave the target and is independent of the thickness of the target. In particular, it will also be observed for very thin targets.

The decay of excited states will take place at a certain distribution  $\mathcal{A}(d)$  of distances  $d$  behind the target which is given by

$$\mathcal{A}(d) = A(t = \beta_0/d), \quad (4.29)$$

where  $A(t)$  is the decay function of the excited state (see Section 2.2). In the case the excited state with a lifetime  $\tau$  is populated directly (no feeding), the decays will occur on average at a distance

$$d = \beta_0 \tau \quad (4.30)$$

behind the center of the target. The distribution  $\mathcal{A}(d)$  of  $\gamma$ -ray vertices at distances  $d$  behind the target, Equation (4.29), and the dependence of the observed Doppler-shift  $\gamma$ -ray energy  $E'(d)$  from the distance  $d$ , Equation (4.27), result in characteristic distributions of Doppler-shifted  $\gamma$ -ray energies, i.e. Doppler-broadened  $\gamma$ -ray lineshapes. Via the decay function  $A(t)$  of the excited state in Equation (4.29), they are sensitive to the lifetime of the state. Such lineshapes are shown in Figures 4.25 and 4.26.

The range of lifetimes that sensitively affect the observed lineshapes can be estimated by the demand that a significant fraction of the decays occurs at distances  $d$  that result in well-detectable changes in observed Doppler shift.

For example, it is assumed that the ions leave the target with a velocity  $\beta_0 = 0.4$  and  $\gamma$ -rays are detected at an angle of  $\alpha_1 = 60^\circ$ . It is demanded that at least 25% of the emitted  $\gamma$ -rays exhibit a Doppler-shifted energy of at most 98% of the energy of  $\gamma$ -rays emitted from inside the target (i.e., at  $d = 0$ ). It follows from Equation (4.27) that the condition  $E'(d)/E'(0) \leq 98\%$  implies a minimum distance  $d$  of

$$d_{98\%} = 0.052r. \quad (4.31)$$

With  $\beta_0 = 0.4 \approx 120$  mm/ns and  $r = 235$  mm, this drift length of  $d_{98\%} = 12.3$  mm corresponds to a flight-time  $t_{f,min}$  of 102.5 ps. Under the assumption that the decaying state is populated directly (no feeding) at the center of the target at  $d = 0$ , the condition that at least 25% of the decays should occur at  $d \geq d_{98\%}$  or, equivalently, at  $t \geq t_{f,min}$  implies

$$\int_{t_{f,min}}^{\infty} A(t)dt = \frac{1}{\tau_{min}} \int_{t_{f,min}}^{\infty} e^{-t/\tau_{min}} dt = e^{-t_{f,min}/\tau_{min}} \stackrel{!}{\geq} 0.25 \quad (4.32)$$

$$\Leftrightarrow \tau_{min} \stackrel{!}{\geq} t_{f,min}/\ln 0.25 = 74 \text{ ps.}$$

This lifetime  $\tau_{min}$  marks a minimum for the range of sensitivity for the geometric caDSA Method at the given ion velocity behind the target  $\beta_0 = 0.4$  and distance of the  $\gamma$ -ray detectors from the target  $r = 235$  mm.

An upper limit for level lifetimes that can be reasonably measured by the method is set by the demand that no significant fraction of the decays occurs after the ions have left the  $\gamma$ -ray spectrometer, i.e. after they have traveled the distance  $r$ . This maximum lifetime is estimated for the above conditions. It is demanded that at maximum 1‰ of the decays occur after the emitting ions have traveled a distance of  $r$ . The corresponding drift time is  $t_{f,max} = 1.96$  ns, and the corresponding maximum level lifetime is given by

$$\int_{t_{f,max}}^{\infty} A(t)dt = \frac{1}{\tau_{max}} \int_{t_{f,max}}^{\infty} e^{-t/\tau_{max}} dt = e^{-t_{f,max}/\tau_{max}} \stackrel{!}{\leq} 0.001 \quad (4.33)$$

$$\Leftrightarrow \tau_{max} \stackrel{!}{\leq} t_{f,max} / \ln 0.001 = 283.5 \text{ ps.}$$

The range of lifetimes that can be sensitively measured by the geometric caDSA Method strongly depends on the velocity  $\beta_0$  of the ions behind the target and the distance  $r$  of the  $\gamma$ -ray detectors from the target center. However, general sensitivity limits can be calculated for the ratio  $\tau/r$ . They are shown in Figure 4.24 as a function of ion velocity  $\beta_0$ , calculated for the demands as used in the above example.

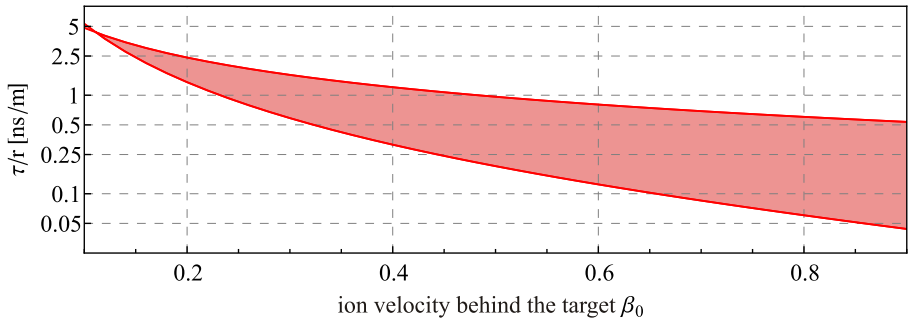


**Figure 4.24.:** Sensitivity range of the geometric caDSA Method in terms of level lifetimes  $\tau$  for a target-detector distance  $r$ . The sensitivity range is plotted as a function of the velocity  $\beta_0$  of the emitting ions behind the target. The demands leading to Equations (4.31)-(4.33) were applied. See text for details.

---

In the discussion of Doppler-broadened lineshapes caused by  $\gamma$ -ray emissions at a distribution of distances  $d$  behind the target, the slowing-down of the ions in the target and the lineshape resulting from  $\gamma$ -ray emission during the slowing-down process were neglected. The resulting lineshapes from the latter process have been discussed in the previous sections. In reality, the lineshape from decays inside the target at different ion velocities and the lineshape from decays behind the target at different  $\gamma$ -ray vertices superpose each other (see Figures 4.25 and 4.26).

As in the case of the differential caDSAM, it is beneficial to perform a Doppler correction of the  $\gamma$ -ray energies. In the correction, it is again assumed that the  $\gamma$ -ray emission occurs at the velocity of the ions measured behind the target. It is furthermore assumed that the decay occurs at the center of the target at  $d = 0$ . For  $\gamma$ -ray emissions that match this assumption, the correct transition energy  $E_0$  is again restored independent of the detection angle. Deviations due to a higher emitter velocity inside the target or due to  $\gamma$ -ray emission at a distance  $d > 0$  behind the target result in an over- or underestimation of the actual Doppler shift in the correction. Consequently, the Doppler-corrected energies deviate from  $E_0$  and the lifetime sensitivity of the lineshape is preserved. For the same reasons as for the differential caDSAM, the Doppler corrections results in an improved resolution and, hence, higher sensitivity.

Calculated lineshapes are shown in figures 4.25 and 4.26 for the previous example case of a 150 AMeV beam of  $^{136}\text{Xe}$ , Coulomb-excited and slowed down in a 500  $\mu\text{m}$  thick gold target. In Figure 4.25, two-dimensional spectra as a function of  $\gamma$ -ray energy and detection angle  $\alpha_1$  are shown for a level lifetime of 110 ps, with and without applied Doppler correction. In Figure 4.26, lineshapes observed at a fixed angle  $\alpha_1 = 45^\circ$  are shown for different lifetimes in the sensitive range of  $\sim 75 - 285$  ps estimated in Equations 4.32 and 4.33.

Lifetime-sensitive, Doppler-broadened lineshapes that are formed by the decay of excited ions behind a target as described above have been successfully used for the determination of level lifetimes in experiments conducted with conventional  $\gamma$ -ray detectors and observation of the lineshapes under discrete polar angles [Ter08, Doo10, Lem12]. As for the "conventional" DSAM, the analysis of those lineshapes highly benefits if it is performed simultaneously as a function of  $\gamma$ -ray energy and observation polar angle. The arguments listed for the continuous-angle DSAM in Section 4.2 apply also to the geometric DSA technique:

- *Conservation of the sensitivity of  $\gamma$ -ray tracking arrays,*
- *Careful consideration of the effect of angular distributions on the lineshapes,*
- *Consistent description of complicated spectra and overlapping lineshapes.*

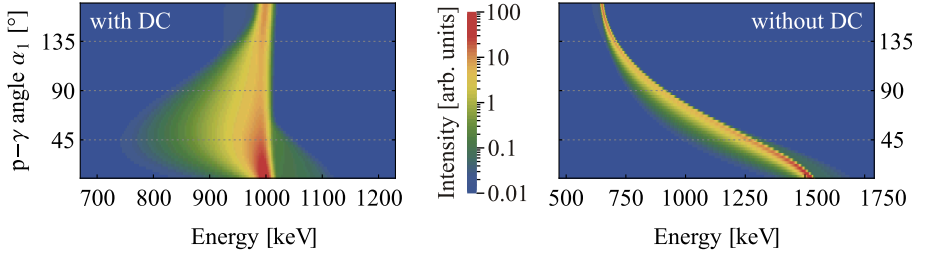


**Figure 4.25.:** Doppler-broadened  $\gamma$ -ray lineshapes for a 150 AMeV beam of  $^{136}\text{Xe}$ , Coulomb-excited and slowed down in a 500  $\mu\text{m}$  thick gold target. A fictional excited state at 1 MeV excitation energy and a level lifetime of 150 ps was assumed here. The calculated spectra are plotted as a function of the detected  $\gamma$ -ray energy  $E_\gamma$  and the particle- $\gamma$  angle  $\alpha_1$ . The angle  $\alpha_1$  is obtained from the measured direction of the emitting ions leaving the target, the detection position of the  $\gamma$ -ray and assuming that the de-excitation occurred at the center of the target. The difference in the obtained spectra with (left) and without (right) application of a Doppler correction (DC) is shown. The lineshapes originate in  $\gamma$ -ray decay at large distances  $d$  behind the target at an almost uniform velocity of  $\beta_0 = 0.41$ . Decays inside the target at higher velocities result in the moderately developed shape that is mainly visible at energies  $> 1$  MeV for the very forward angles. For the Doppler correction, it is assumed that the decays occur in the middle of the target at the ion velocities measured with a relative uncertainty of 1% behind the target. Note the different scales of the energy axes. See text for details.

The last argument is weakened to a certain extent in the case of the geometric caD-SAM. In contrast to the lineshapes originating in different emitter velocities, the lineshapes originating in different  $\gamma$ -ray vertices always extend to energies below  $E_0$  for forward *and* backward angles. The discussed full reconstruction of overlapping  $\gamma$ -ray lineshapes by their observation at forward and backward angles is therefore hindered.

In the aforementioned studies, the analysis was performed in terms of full Monte-Carlo-simulations of the spectra that were compared to the experimental data. This approach has the disadvantage that only a small parameter space for a very limited number of variables can be investigated on, since the full simulation of a spectrum

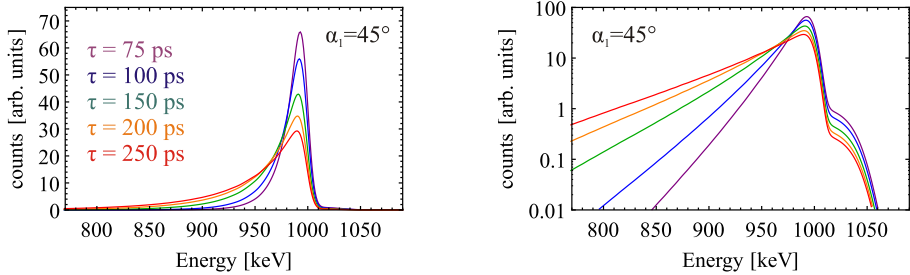


**Figure 4.26.:** Doppler-broadened  $\gamma$ -ray lineshapes calculated for the same situation as in Figure 4.25, but projected on the energy-axis for the angular bin centered at  $\alpha_1 = 45^\circ$  and different level lifetimes from 75 ps to 250 ps. The spectra are plotted on a linear scale on the left-hand side and on a logarithmic scale on the right-hand side. In the logarithmic scale, the contributions from decays occurring at higher emitter velocities inside the target are clearly visible on the high-energy side. See text for details.

for every set of parameters is computationally highly demanding. This inconvenience is removed by the ansatz of lineshape calculation in APCAD (see Section 4.3 and Appendix B), where two-dimensional lineshapes for a given set of parameters can be calculated within few milliseconds. This fast computation of the lineshapes allows for the application of minimization algorithms to scan a large parameter space with several free variables in order to find the optimum description of the experimental data. The extension of the computer program APCAD for the calculation of Doppler-broadened  $\gamma$ -ray lineshapes originating in distributions of  $\gamma$ -ray vertices for excited nuclei recoiling from the target is described in Appendix B.4.

---

## 5 Coulex-Multipolarimetry with relativistic heavy-ion beams

The multipole-mixing ratio  $\delta$  is a measure for the relative contributions of different radiation characters  $\sigma\lambda$  to a certain  $\gamma$ -ray transition. It is defined in Equation 5.1. In this chapter, a novel method suitable to measure  $E2/M1$  multipole mixing ratios of nuclear ground-state transitions is presented. Its development within this work was triggered by the scientific need for identifying the  $J^\pi = \frac{1}{2}^-$   $M1$  spin-flip excitation of the  $\pi 2p_{\frac{3}{2}}$  dominated  $\frac{3}{2}^-$  ground-state of  $^{85}\text{Br}$  (see Chapter 6.2). The new method is based on the comparison of relativistic Coulomb excitation cross sections at different ion velocities. The observation of the Coulomb excitation at different ion velocities can be performed with high-resolution  $\gamma$ -ray detectors in one single measurement by using two targets mounted at a few centimeters distance along the beam axis. Excitation in either of the targets is distinguished by different observed Doppler shifts. This separation of excitations in two target benefits significantly from the position resolution of  $\gamma$ -ray tracking detectors.

The purpose of the method is explicated in Section 5.1, while the measurement principle will be presented in Section 5.2. Section 5.3 is devoted to a detailed description of the method. For being as specific as possible, the description of the method is confronted with simulations relevant for the case of  $^{85}\text{Br}$  as an example throughout the chapter. The method as it is described in this chapter was published in [Sta15].

---

### 5.1 Purpose of the method

---

In-beam Gamma-ray spectroscopy of rare isotopes implies certain challenges to the experimentalists. They stem from the typically low beam intensity compared to stable beam conditions, complications due to the radioactivity of the beam species, high background levels, or broad beam profiles, if the rare ions are produced by fragmentation, for example. The conditions often do not allow to employ established experimental techniques for the extraction of desired spectroscopic information. Adapted methods have to be developed for the performance of state-of-the-art

experiments. The method described in this chapter aims at the measurement of the electromagnetic multipole mixing ratio [Kra73]

$$\delta_{(\sigma\lambda)_>/(\sigma\lambda)_<} = \frac{(2\lambda_{<} + 1)!!}{(2\lambda_{>} + 1)!!} \left( \frac{E_0}{\hbar c} \right)^{\lambda_{>} - \lambda_{<}} \sqrt{\frac{\lambda_{<} (\lambda_{>} + 1)}{\lambda_{>} (\lambda_{<} + 1)}} \frac{\varphi_{\sigma_{>}} \langle J_f \| \mathcal{O}(\sigma\lambda)_{>} \| J_i \rangle}{\varphi_{\sigma_{<}} \langle J_f \| \mathcal{O}(\sigma\lambda)_{<} \| J_i \rangle} \quad (5.1)$$

of transitions between an initial ( $|J_i\rangle$ ) and final ( $\langle J_f|$ ) nuclear state, where  $\langle J_f \| \mathcal{O}(\sigma\lambda)_{>(<)} \| J_i \rangle$  denotes the reduced electromagnetic transition matrix element<sup>1</sup> connecting the states with respect to the electromagnetic transition operator  $\mathcal{O}(\sigma\lambda)_{>(<)}$  of transitions of radiation character  $\sigma$  for the higher (lower) multipole order  $\lambda$  and transition energy  $E_0$ .  $\varphi_E = i^\lambda$  and  $\varphi_M = -i^{\lambda-1}$  are phase factors depending on the electric ( $\sigma = E$ ) or magnetic ( $\sigma = M$ ) character of the transition. In the case  $(\sigma\lambda)_{>} = E2$  and  $(\sigma\lambda)_{<} = M1$ , Eq. (5.1) reads

$$\delta_{E2/M1} = \frac{\sqrt{3} E_0}{10 \hbar c} \frac{\langle J_f \| \mathcal{O}(E2) \| J_i \rangle}{\langle J_f \| \mathcal{O}(M1) \| J_i \rangle}. \quad (5.2)$$

The most common technique for measuring multipole mixing ratios is by analysis of the angular distribution  $W(\theta, \phi)$  of  $\gamma$ -radiation emitted during the transition from an oriented nuclear state (see Ref. [Kra70] and [Rai06] for example), which is a direct function of  $\delta$  as discussed in Chapter 2.4. However, there are cases where this established method is not applicable. Insufficient statistics or strong Lorentz-boost can hinder the analysis of angular distributions, and if the excited state has spin  $\frac{1}{2}$  and is aligned, only, then the method is not applicable at all because the  $\gamma$ -ray emission occurs isotropically and is independent of  $\delta$ .

---

## 5.2 Principle

---

The cross section for Coulomb excitation has different energy-dependence depending on the character  $\sigma\lambda$  of the excitation. For example, the cross section for  $\sigma\lambda = M1$  Coulomb excitation is nearly independent of projectile energy, whereas the cross section for  $\sigma\lambda = E2$  excitation drops with projectile energy. This is evident from Equations (2.25) and (2.26). In consequence,  $M1$  and  $E2$  excitation cross sections may have the same order of magnitude at relativistic beam energies, albeit magnetic excitations are generally suppressed by a factor  $\beta^2 = v^2/c^2$  with respect to electric excitations as discussed in Section 2.1.4. This behavior is sketched in Fig. 5.1 for a situation that is likely to occur in the neutron-rich radioactive nuclide of  $^{85}\text{Br}$ , for example.

---

<sup>1</sup> as defined by Bohr and Mottelson [Boh69, p. 381]

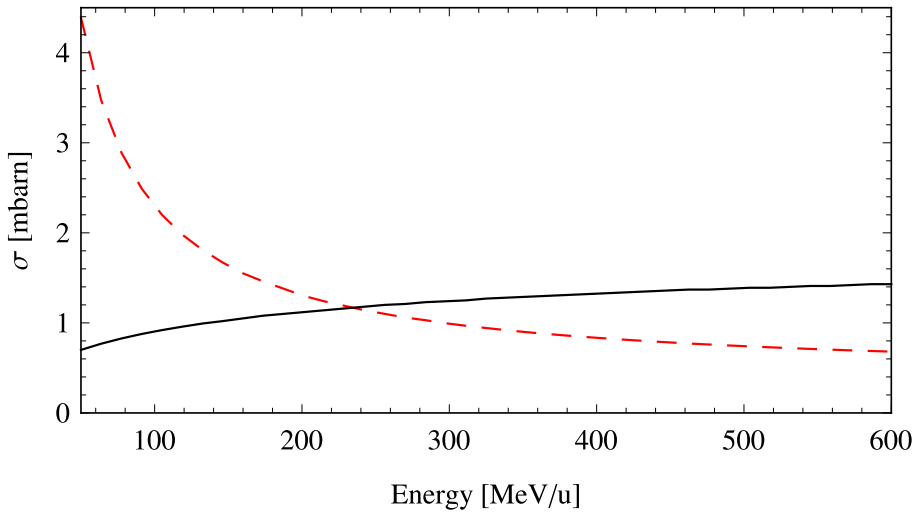


**Figure 5.1.:** Cross section for Coulomb excitation of  $^{85}\text{Br}$  ions impinging on a gold target as a function of beam energy. Cross sections for  $M1$  (solid, black line) and  $E2$  (dashed, red line) excitation of the 1191-keV state of  $^{85}\text{Br}$  are calculated with the computer code DWEIKO [Ber03] for reduced transition strengths  $B(E2, \downarrow) = 1 \text{ W. u.}$  and  $B(M1, \downarrow) = 1 \mu_N^2$ .

Because of the different energy dependence for various excitation characters, the ratio of Coulomb excitation cross sections at different beam energies allows to extract the ratio of the excitation characters contributing to the respective excitation and, hence, the multipole mixing ratio of the transition. The cross sections for one-step Coulomb excitation are independent from the relative signs of the transition matrix elements for the competing excitation characters. Hence, the cross section ratio is sensitive only to the magnitude of the multipole mixing-ratio, but not to its sign. In the following, this principle will be referred to as *Coulex multipolarimetry*. The relation of cross section ratio and  $E2/M1$  multipole mixing ratio is exemplarily shown in Fig. 5.2. There exists a sensitive range of cross section ratios varying by about a factor of two between cases with pure  $M1$  character ( $\delta^2 = 0$ ) and equal share of  $M1$  and  $E2$  character ( $\delta^2 = 1$ ), resulting in sensitivity to multipole mixing ratios between about 0.01 and 0.1 in the shown example case.

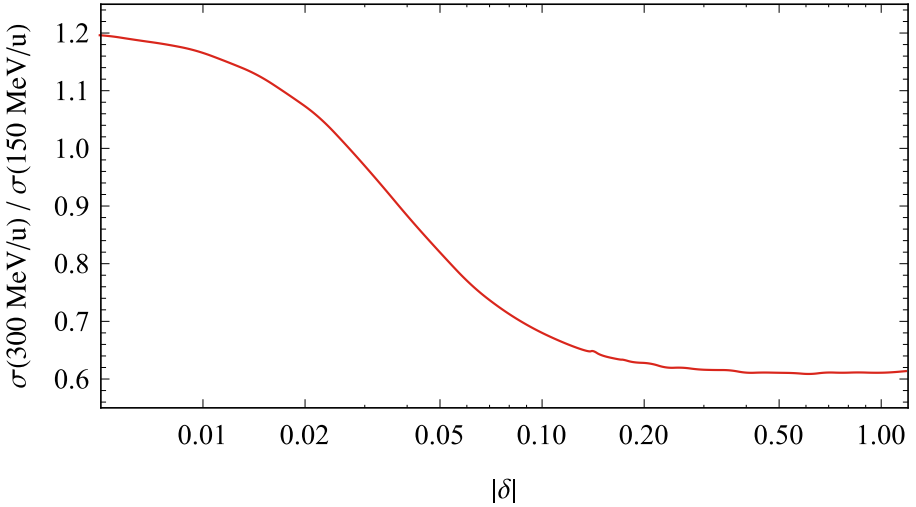


**Figure 5.2.:** Ratio of Coulomb excitation cross sections at 300 MeV/u and 150 MeV/u beam energy as a function of the multipole mixing ratio  $\delta_{E2/M1}$  for the transition between the ground state and 1191-keV  $\frac{1}{2}^-$  excited state in  $^{85}\text{Br}$ .

---

## 5.3 Method

---

### 5.3.1 Experimental setup

---

The straightforward way to apply the Coulex multipolarimetry described above is to perform two Coulomb excitation experiments at different beam energies and calculate the ratio of measured cross sections. This approach demands sufficient beam-time and two absolute cross section measurements, or at least two relative cross section measurements with respect to the same standard. In  $\gamma$ -ray spectroscopy experiments with detectors that have a sufficiently good energy resolution, like HPGe detectors, the two cross section measurements can be combined in one single experiment. The setup for such an experiment is schematically shown in Fig. 5.3.

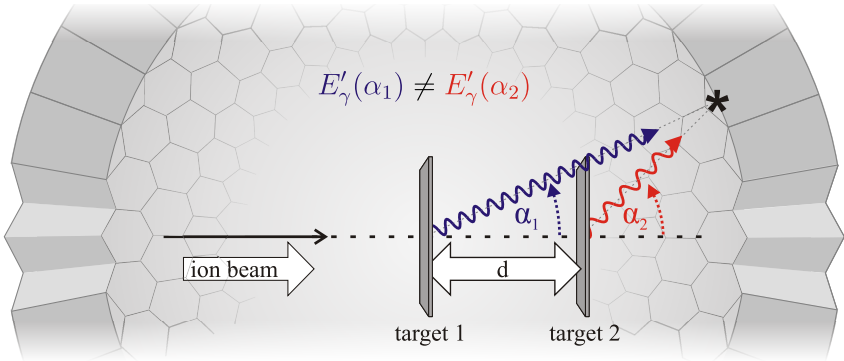


**Figure 5.3.:** Principle experimental setup: The separation  $d$  of the two targets results in different angles  $\alpha$  between beam-axis and the direction of  $\gamma$ -ray detection for excitation in the first or second target. In consequence, the  $\gamma$ -rays are detected with different Doppler shifts.

It corresponds to a standard Coulomb excitation setup with two thick targets in a few centimeter distance instead of one target, typically at the focus of the  $\gamma$ -ray detectors. Coulomb excitation will occur in both targets and the beam will lose energy in both targets. The thickness of the first target has to be chosen such that the energy loss in it leads to a significant change of the Coulomb excitation cross section at entrance- and exit-velocity of the beam as a function of the excitation characters under investigation. The beam must not be stopped in the first target. Coulomb excitation will occur at different average velocities in the first and second target. Therefore, the ratio of yields observed for Coulomb excitation in the first

and second target is a measure for the multipole mixing ratio of the excitation. The evolution of beam energy and cross sections for E2 and M1 excitation while the beam is passing through the two targets is exemplarily shown in Fig. 5.4.

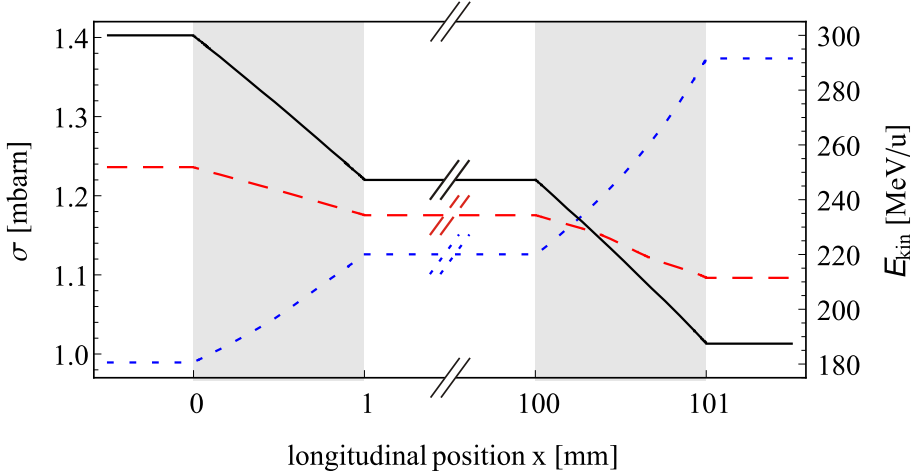


**Figure 5.4.:** Evolution of M1 (red, dashed line) and E2 (blue, dotted line) Coulex cross section and kinetic energy (black, solid line) as a beam of  $^{85}\text{Br}$  with an initial kinetic energy of 300 MeV/u passes through two gold targets with 1 mm thickness each (targets are indicated by shaded areas). Parameters are as in Fig. 5.1

### 5.3.2 Expected yields and peak areas

The expected yield (total number of emitted  $\gamma$ -ray s) from excitations in each target is given by

$$y_i = \rho \frac{N_A}{A_t} \int_{x_{i,1}}^{x_{i,2}} \sigma(E_{kin}(x)) dx. \quad (5.3)$$

The integration runs over the longitudinal extent  $[x_{1(2),1}, \dots, x_{1(2),2}]$  of the first (second) target.  $\sigma(E_{kin}(x))$  denotes the Coulomb excitation cross section as a function of ion kinetic energy,  $E_{kin}(x)$  is the ion kinetic energy as a function of the longitudinal position  $x$  inside the target,  $\rho$  is the target mass density,  $N_A$  is Avogadro's constant and  $A_t$  is the atomic mass number of the target.  $E_{kin}(x)$  can

be calculated with the aid of computer codes for the calculation of stopping power of ions in matter like for example SRIM [Zie10] or ATIMA ([Gei15], included in the program package LISE++ [Tar08, Baz02]). The ratio of yields for Coulomb excitation of the 1191-keV  $\frac{1}{2}^-$  excited state of  $^{85}\text{Br}$  at an initial beam energy of 300 MeV/u on two gold targets with 1 mm thickness each is shown in Fig. 5.5.

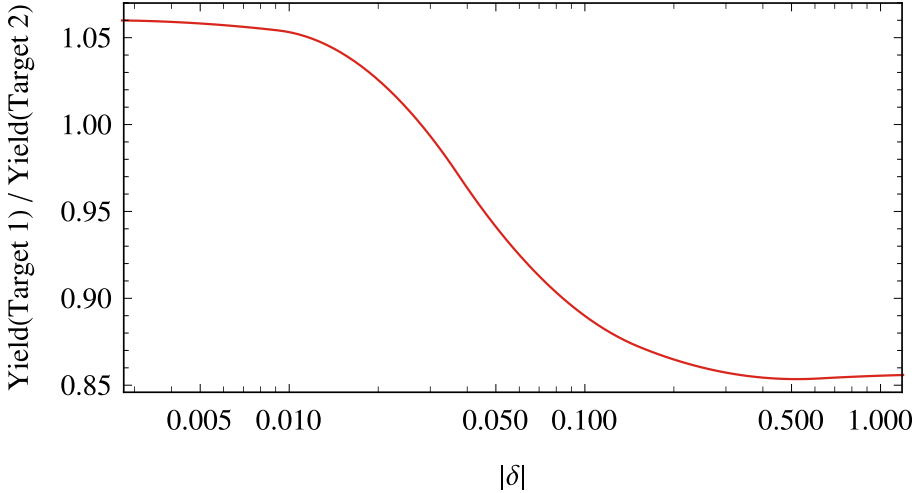


**Figure 5.5.:** Ratio of total  $\gamma$ -ray yields  $\frac{y_1}{y_2}$  for two successively arranged gold targets with a thickness of 1 mm, each. The yields were calculated using Eq. (5.3) for Coulomb excitation of the 1191-keV  $\frac{1}{2}^-$  excited state of  $^{85}\text{Br}$  at an initial beam energy of 300 MeV/u.

The  $\gamma$ -rays are emitted in-flight. Therefore, in the laboratory system their energy is subject to a Doppler shift (Equation 2.40). This shift is a function of the velocity  $\beta = \frac{v}{c}$  of the emitting ion and the angle  $\alpha$  between the ion velocity vector and the emission direction of the  $\gamma$ -quantum in the laboratory frame. Furthermore, the  $\gamma$ -ray angular distribution in the emitter rest-frame  $W(\theta_\gamma^{RN}, \varphi_\gamma^{RN})$  is Lorentz-boosted according to Equation (2.44) and (2.45).

It is a valid assumption that the ions are not significantly deflected in relativistic Coulomb excitation reactions, and therefore the beam-axis, which is chosen to be the z-axis, can be used as quantization axis and  $\alpha = \theta^{lab}$  can be used in Eq. (2.40) and (2.44). In this case, the  $\gamma$ -ray emission angles in the ion rest frame  $(\theta_\gamma^{RN}, \varphi_\gamma^{RN})$  are related to the emission angle in the laboratory system  $(\theta_\gamma^{lab}, \varphi_\gamma^{lab})$  by Equation (2.43). It is straightforward to generalize the analysis to a situation where the

forward-scattering angle of the projectiles is measured on an event-by-event basis using the more general expressions of Equations 2.40 and 2.42.

In the following, it is assumed that the  $\gamma$ -ray detectors are arranged in a fixed distance  $r$  from the origin of the laboratory frame. In the discussed experimental setup, excited ions emit  $\gamma$ -rays at different positions  $x$  along the z-axis. Therefore, it is most convenient to evaluate the  $\gamma$ -ray emission in a reference frame that is not moving with respect to the laboratory frame and has its origin at the position of the emitting nucleus. This reference frame is indicated by the superscript *ion*. A detector polar angle  $\theta_{det}^{ion}$  in that reference frame is related to its polar angle in the laboratory frame  $\theta_{det}^{lab}$  by

$$\tan \theta_{det}^{ion} = \frac{d \sin \theta_{det}^{lab}}{r \cos \theta_{det}^{lab} - x}. \quad (5.4)$$

Eq. (5.3) - (5.4) can be used to estimate the number of  $\gamma$ -rays emitted from ions excited in target  $i$  that are registered in a detector:

$$A_i = \rho \frac{N_A}{A_t} \int_{x_{i,1}}^{x_{i,2}} \sigma(E_{kin}) \int_{\Omega_{det}^{ion}} W(\theta_\gamma^{RN}, \varphi_\gamma^{RN}) \frac{d\Omega^{ion}}{d\Omega^{RN}} \epsilon(E_\gamma^{lab}) d\Omega^{ion} dx \quad (5.5)$$

The inner integral is evaluated in the *ion* reference frame and runs over the solid angle covered by the detector. For clarity, the meaning and dependency of each expression in Eq. (5.5) is listed below:

- $\sigma(E_{kin}) \equiv \sigma(E_{kin}(x), |\delta|)$ : Excitation cross section, depends on the magnitude of the multipole mixing ratio  $\delta$ .
- $E_{kin}(x)$ : Ion kinetic energy as a function of the (z-)position of the ion in the target(s).
- $W(\theta_\gamma^{RN}, \varphi_\gamma^{RN}) \equiv W\left(\theta_\gamma^{RN}\left(\theta_\gamma^{ion}(x, r), \beta(E_{kin}(x))\right), \varphi_\gamma^{RN} = \varphi_\gamma^{ion} = \varphi_\gamma^{lab}, \delta\right)$ :  $\gamma$ -ray angular distribution evaluated in the rest frame of the recoiling ion. It depends also on the multipole mixing ratio  $\delta$ .
- $\epsilon(E_\gamma^{lab}) \equiv \epsilon\left(E_\gamma^{lab}\left(\theta_\gamma^{ion}(x, r), \beta(E_{kin}(x))\right)\right)$ : Detector efficiency at the Doppler-shifted  $\gamma$ -ray energy.
- $\frac{d\Omega^{ion}}{d\Omega^{RN}} = \frac{d\Omega^{ion}}{d\Omega^{RN}}\left(\theta_\gamma^{ion}, \beta(E_{kin}(x))\right)$ : Transformation of Lorentz-boosted solid angle element from the *RN* system moving relative to the *ion* reference frame, which rests in the laboratory frame.

In Eq. (5.5), it is assumed that the de-excitation occurs directly after the excitation (very short lifetime). The formula has to be slightly modified if the mean distance traveled by the excited ions before  $\gamma$ -ray emission implies a significant energy loss or change of detector solid angle due to the different positions of the ions at the time of de-excitation. Furthermore, it is assumed in Eq. (5.5) that the detector efficiency is uniform over the solid angle covered by the detector.

In the discussed case of  $^{85}\text{Br}$ , the excited state has spin  $\frac{1}{2}$  and the  $\gamma$ -ray angular distribution is necessarily isotropic in the  $RN$  reference frame. However, for level spins  $J \neq \{0, \frac{1}{2}\}$ , the nucleus can be spin-aligned by the Coulomb excitation reaction (non-uniform population of the level's magnetic sub-states  $m$ , see Section 2.1.4) leading to a non-uniform angular distribution of the  $\gamma$ -radiation (see Section 2.4). In the discussed setup, a  $\gamma$ -ray detector placed at a certain position is located at different polar angles  $\theta_{det}^{ion}$  for  $\gamma$ -rays emitted in the first or second target. Additionally, the mean ion velocity  $\beta$  differs in the first and second target affecting the Lorentz-boost, Eq. (2.44), and the transformation of polar angle, Eq. (2.42). Therefore, the ratio  $\frac{A_1}{A_2}$  of the number of  $\gamma$ -rays emitted from the first and second target that are registered in a detector is a measure for the ratio of the  $\gamma$ -ray angular distribution  $W(\theta_{\gamma}^{RN})$  at two different values of  $\theta_{\gamma}^{RN}$  (see Fig. 5.6).

Since the angular distribution is also a function of the multipole mixing ratio  $\delta$ , the ratio  $\frac{A_1}{A_2}$  is sensitive to  $\delta$  also if the excitation process itself is not. This sensitivity is exemplarily shown in Fig. 5.7 and 5.8 for the spin-sequence  $\frac{3}{2} \rightarrow \frac{1}{2}$  and different detector polar angles  $\theta_{det}^{lab}$  in the laboratory system.

As expressed by Eq. (5.5), the ratio  $\frac{A_1}{A_2}$  of the number of detected  $\gamma$ -rays (i.e. the ratio of the expected peak areas in the experimental  $\gamma$ -ray spectrum) from the first and second target as a function of the multipole mixing ratio  $\delta$  can be considered as the "product" of the yield ratio shown in Fig. 5.5 and the angular distribution ratio shown in Fig. 5.7, integrated over the detector solid angle (compare Fig. 5.8). The expected peak area ratios for the discussed case of  $^{85}\text{Br}$  and the setup defined in Fig. 5.6 is shown in Fig. 5.9. Expected peak area ratios for the isotropic emission of  $\gamma$ -rays in the  $RN$  reference frame resulting from the spin  $J = \frac{1}{2}$  of the discussed 1191-keV excited state of  $^{85}\text{Br}$  are compared to the peak area ratios for an assumed spin-sequence  $\frac{3}{2} \rightarrow \frac{1}{2}$ .

The influence of the  $\gamma$ -ray angular distribution can have different effects on the sensitivity of the presented method. Depending on the angular range covered by the  $\gamma$ -ray detectors and the positions of the two targets, the sensitivity can be either enhanced or inhibited. The functional dependence of the observed peak area ratios for certain observation angles may also become inconclusive because the same

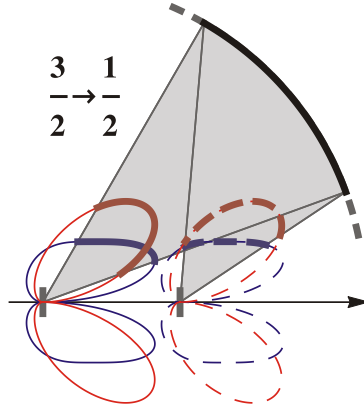


**Figure 5.6.:** Angular distributions of  $\gamma$ -rays emitted from a target at the focus of a spherical detector (solid lines) with radius  $r = 23.5$  cm covering  $\theta_{det}^{lab} = (20^\circ, 60^\circ)$  and a target located 10 cm further downstream along the z-axis (dashed lines). The blue curves correspond to pure  $M1$ -transitions ( $\delta_{E2/M1} = 0$ ), the red curves to pure  $E2$ -transitions ( $\delta_{E2/M1} = \pm\infty$ ). A spin sequence  $\frac{3}{2} \rightarrow \frac{1}{2}$  was assumed for example. The gray areas and bold sections of the angular distribution plots indicate the range in polar angle covered by the detector in the reference frame originating at the center of the first and second target, respectively. Perfect "prolate" spin-alignment ( $p(m) = \frac{1}{2}\delta_{|m|,J}$ ) is assumed in each case. A weighting by  $|\sin \theta_\gamma^{ion}|$  was applied.

peak area ratio can be observed for different values of  $\delta$ . Measurement of peak area ratios at different suitably chosen angles will make a unique determination of the multipole mixing-ratio  $\delta$  possible in most cases. The appropriate detection positions have to be chosen for each experimental case individually.

Apart from the sensitivity to  $\delta$  via the de-excitation process (i.e. the angular distribution of the  $\gamma$ -radiation that is exploited in the well-known angular correlation technique) applicable in cases where  $J \neq \{0, \frac{1}{2}\}$ , the presented method is additionally sensitive to  $\delta$  via the (Coulomb-) excitation process and is, in particular, applicable also in the case of  $J = \frac{1}{2}$  as in  $^{85}\text{Br}$ .

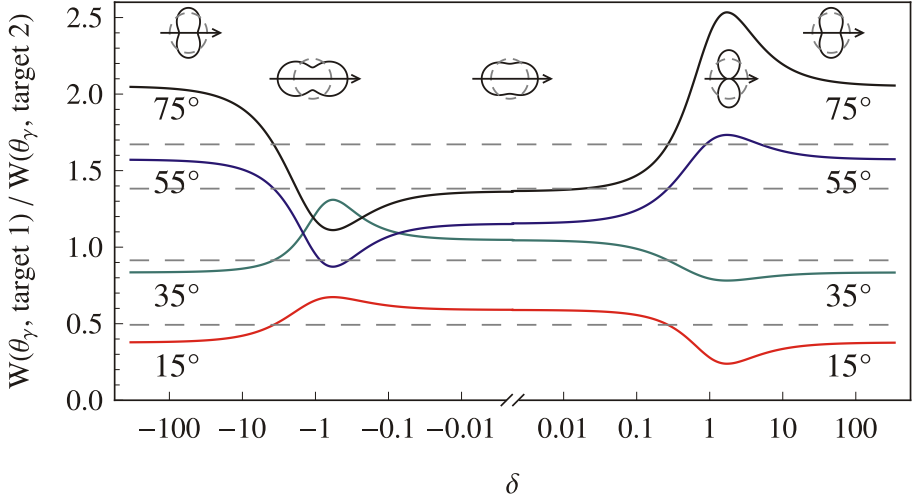


**Figure 5.7.:** Ratio of angular distribution of  $\gamma$ -rays emitted from the first and second target and detected in the same detector (see Fig. 5.6). The angular distribution was integrated over detectors covering  $\Delta\theta^{lab} = 1^\circ$  and the full azimuth-angular range. The ratios are calculated as a function of the multipole mixing ratio  $\delta_{E2/M1}$  for  $\bar{\theta}_{det}^{lab} = 15^\circ, 35^\circ, 55^\circ, 75^\circ$  (full red, green, blue and black lines, respectively) and the spin-sequence  $\frac{3}{2} \rightarrow \frac{1}{2}$  for example. The horizontal dashed lines show the angular distribution ratios for isotropic  $\gamma$ -ray emission in the  $RN$  reference frame. The small insets sketch the angular distribution for the respective values of  $\delta$ . Perfect "prolate" spin-alignment ( $p(m) = \frac{1}{2}\delta_{|m|,\nu}$ ) is assumed in each case for simplicity.

### 5.3.3 Peak separation

The challenge here is to experimentally disentangle excitations in the first and in the second target. The first condition for the separability of excitations in the first and second target is, that ions that have been excited in the first target de-excite before they enter the second target. Corrections for de-excitations after reaching the second target are below one permille if one demands that the drift time from the first to the second target is at least ten half-lives  $T_{1/2}$  of the excited state. For an

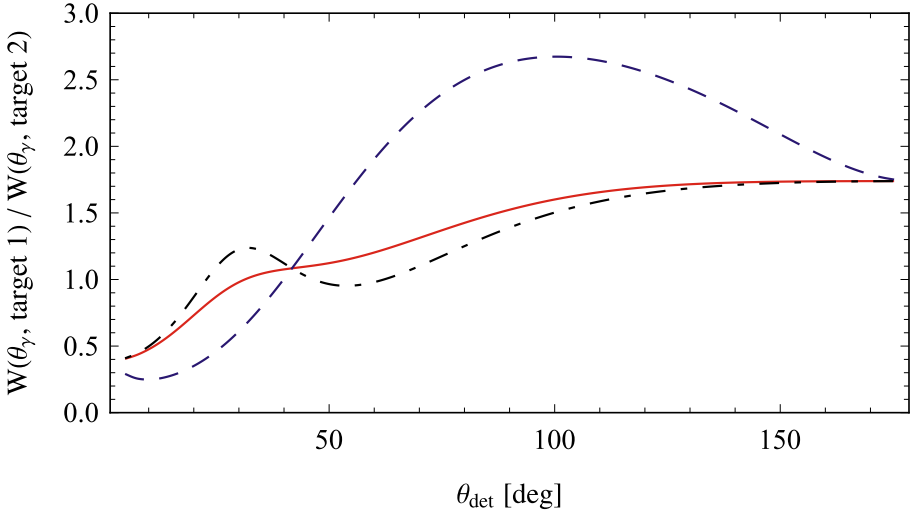


**Figure 5.8.:** Ratio of angular distribution of  $\gamma$ -rays emitted from the first and second target and detected in the same detector (see Fig. 5.6). The same quantity as in Fig. 5.7 is drawn, but for fixed values of  $\delta_{E2/M1} = 0$  (solid line),  $\delta_{E2/M1} = 1$  (blue, dashed line) and  $\delta_{E2/M1} = -1$  (black, dash-dotted line) for the spin-sequence  $\frac{3}{2} \rightarrow \frac{1}{2}$  as a function of the detector polar angle  $\bar{\theta}_{det}^{lab}$ . Perfect “prolate” spin-alignment ( $p(m) = \frac{1}{2} \delta_{|m|,j}$ ) is assumed in each case for simplicity.

exit-velocity off the first target  $\beta_{exit,1} = v_{exit,1}/c$ , this corresponds to a minimum target separation of

$$d_{min,T_{1/2}} = \beta_{exit,1} \gamma(\beta_{exit,1}) \cdot 10T_{1/2} \quad (5.6)$$

where  $\gamma(\beta_{exit,1}) = (1 - \beta_{exit,1}^2)^{-\frac{1}{2}}$  is the Lorentz-factor corresponding to  $\beta_{exit,1}$ . If this condition is fulfilled, excitations in the first and second target can be distinguished by different Doppler shifts of the de-excitation  $\gamma$ -rays. Here, two contributions to the Doppler shift have to be considered, namely the velocity of the emitting ion and the angle  $\alpha$  between the ion velocity vector and the  $\gamma$ -ray emission direction. In the following, it is assumed that the beam ions are not stopped in

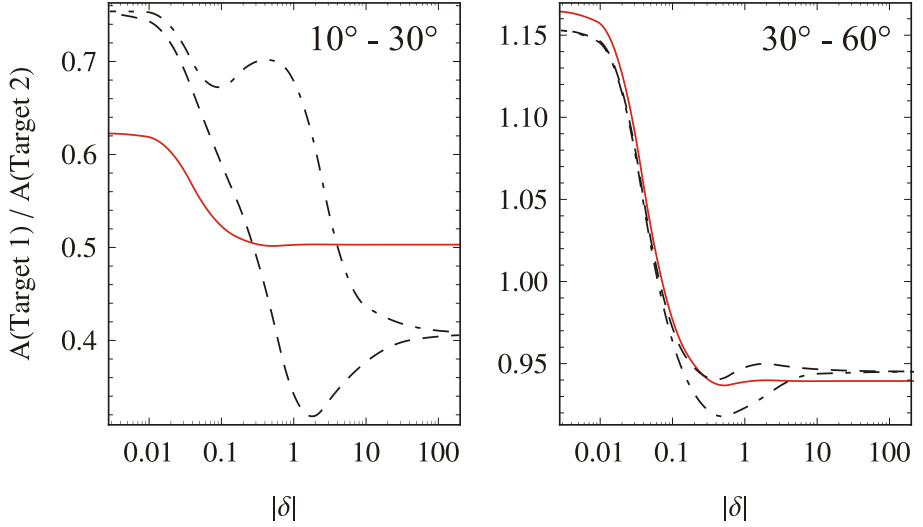


**Figure 5.9.:** Ratio of expected peak areas for  $\gamma$ -rays emitted from the first and second target for the setup depicted in Fig. 5.6, but with a detector covering  $\theta_{det}^{lab}$  from  $10^\circ$  to  $30^\circ$  (left panel) and from  $30^\circ$  to  $60^\circ$  (right panel). The solid, red line shows the peak area ratio as a function of the multipole mixing ratio  $\delta$  for the case of isotropic  $\gamma$ -ray emission that occurs in the discussed example-case of the 1191-keV  $\frac{1}{2}^-$  excited state of  $^{85}\text{Br}$ . The black lines show the expected peak area ratio if the spin sequence was  $\frac{3}{2} \rightarrow \frac{1}{2}$ . Dashed lines correspond to positive values of  $\delta$ , dashed-dotted lines to negative values. Perfect “prolate” spin-alignment ( $p(m) = \frac{1}{2}\delta_{|m|,J}$ ) is assumed in each case for simplicity.

the second target<sup>2</sup>. Because the beam ions have different velocities in and behind the first and second target, the de-excitation  $\gamma$ -rays will be observed with different Doppler shifts by a detector placed at a certain angle  $\theta_{det}$  with respect to the beam axis. However, this difference in Doppler shift is not present (not decisive) for detectors placed at (close to) angles  $\theta_{det} = \arccos(\beta)$ , where the Doppler shift is independent of the emitter velocity. This follows from Eq. (2.40) assuming  $\theta_{det}^{lab} = \alpha$  and demanding  $\partial E_\gamma^{lab} / \partial \beta = 0$ .

<sup>2</sup> The method is, in principle, also applicable if the beam is stopped in the second target. However,  $\gamma$ -rays emitted from ions excited in the second target are eventually not Doppler shifted in that case

---

For a clear separation also at these angles, the targets have to be spatially clearly separated. This results in different angles between the ion velocity vector and the  $\gamma$ -ray emission direction for ions excited in the first and second target, if the de-excitation  $\gamma$ -rays are observed in a detector at a given angle relative to the beam axis (see Fig. 5.3 and 5.6). Figure 5.10 (top panel) demonstrates the principle for a small detector. It is assumed that the center of the first target is located at the focus of the  $\gamma$ -ray array and the detector under consideration covers the polar angle range of  $59^\circ$  to  $61^\circ$  from the perspective of the center of the first target. The second target is located 10 cm further downstream (as depicted in Fig. 5.3) and the same detector covers an polar angle range of  $84^\circ$  to  $86^\circ$  from the perspective of the center of the second target. In the simulated case, the ion velocity after the first target is  $\beta_{exit,1} \simeq 0.61$ . After the downstream target, it is  $\beta_{exit,2} \simeq 0.545$ . Due to relativistic effects, at these velocities the Doppler shift vanishes at an angle  $\alpha$  between ion velocity vector and  $\gamma$ -ray emission direction of about  $71^\circ$ , in contrast to the case  $\beta \ll 1$ , where it vanishes at  $\alpha = 90^\circ$ . Consequently,  $\gamma$ -rays emitted from ions excited in the upstream target are Doppler shifted to energies higher than the  $\gamma$ -ray energy in the ion rest frame  $E_0$  and  $\gamma$ -rays emitted from ions excited in the downstream target are shifted to energies below  $E_0$ .

It is unavoidable that at some detection angle the effects of different emitter velocity and position compensate and the energies of  $\gamma$ -rays emitted in the first or second target overlap (see Fig. 5.12). However, larger spatial separation of the targets allows to shift the detector angle where the peaks overlap to more backward values (see Fig. 5.11). Hence, the separability of the  $\gamma$ -rays emitted in the first and second target can be adjusted for a given experimental setup to the desired physics case. The target separation necessary for a clear separation of excitations in the first and second target depends on the beam energy, detector energy and spatial resolution, detector positions and the half-life of the excited level.

---

### 5.3.4 Lifetime effects

---

Lifetime effects on the energy spectrum (see Section 4 and References [Doo10, DP12]) may complicate the peak separation and reduce the peak-to-background ratio because they can lead to a significant broadening of the observed peaks at angles not in the proximity to  $\theta_{det} = \arccos(\beta)$ . These effects are the same as in the case of the differential continuous-angle Doppler-Shift Attenuation Method (Chapter 4). They can easily be simulated with the aid of the computer program APCAD that was developed within this work (see Appendix B.2). Since Coulomb excitation and slowing down of heavy ions in thick targets can be realistically simulated by the Monte-Carlo simulation program StopSim, corresponding lineshapes can be

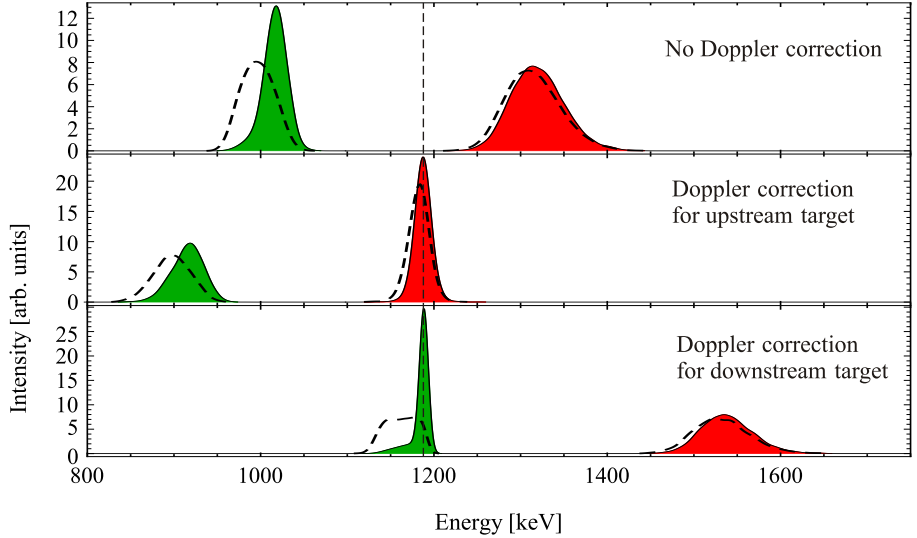


**Figure 5.10.:**  $\gamma$ -ray spectra simulated with the computer code APCAD (see Appendix B.2) for the 1191-keV transition from the  $1/2^-$  excited state of  $^{85}\text{Br}$  to its  $3/2^-$  ground-state (dashed, vertical line). An initial beam energy of 300 MeV/u, level lifetimes of 10 ps (solid line) and 50 fs (dashed line) and a small detector subtending two degrees in polar angle, from  $59^\circ$  to  $61^\circ$ , placed at a distance of 23.5 cm from the center of the upstream target were assumed. The second target is placed 10 cm further downstream. For the excitation cross section, reduced transition strengths of  $B(E2, \downarrow) = 2$  W. u. and  $B(M1, \downarrow) = 0.58 \mu_N^2$ , resulting in  $\delta_{E2/M1} = 0.087$ , were used. Perfect position resolution for  $\gamma$ -ray - and beam-tracking are assumed for simplicity, partially compensated by an assumed intrinsic energy resolution of 10 keV. The top panel shows an energy spectrum without any applied Doppler correction. The central panel shows the same spectrum, but with Doppler correction assuming the average ion velocity after the upstream target and the position of the upstream target as (longitudinal)  $\gamma$ -ray vertex. In the bottom panel, the (measurable, and therefore assumed to be sufficiently well known) ion velocity after the downstream target and the position of the downstream target as (longitudinal)  $\gamma$ -ray vertex were assumed for the Doppler correction. The peaks corresponding to  $\gamma$ -rays emitted in or shortly behind the upstream target have a red filling, the corresponding peaks for the downstream target have a green filling. See text for details.

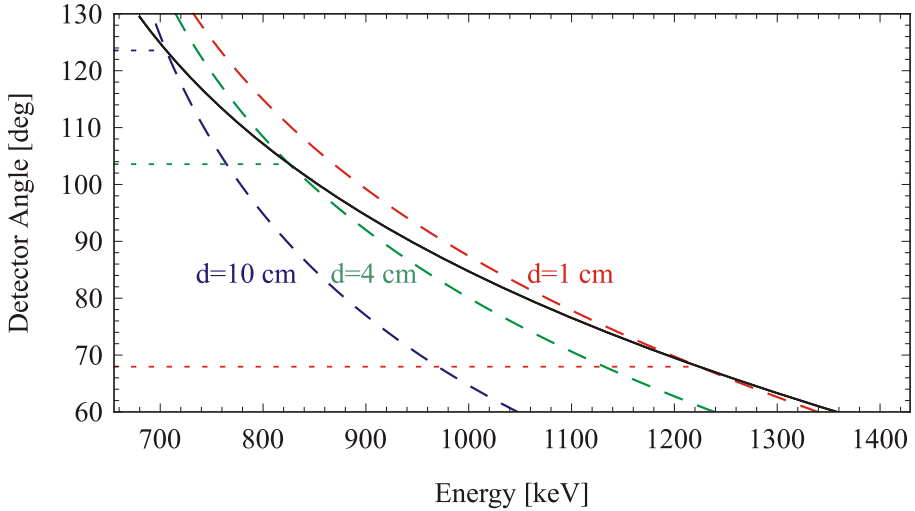


**Figure 5.11.:** Observation angle vs. Doppler-shifted energy of 1191-keV  $\gamma$ -rays emitted directly after the upstream target located at the focus of the detector system (solid, black line) or after the second target mounted at different distances from the upstream target (dashed lines, red: 1 cm, green: 4 cm, blue: 10 cm). An exit velocity off the upstream target of  $\beta_{exit,1} = 0.61$  and off the downstream target of  $\beta_{exit,2} = 0.545$  was assumed. For the calculation, a distance between the center of the upstream target and the detector of 23.5 cm was assumed. The Doppler-shifted  $\gamma$ -rays from upstream and downstream target appear at the same energy at detector angles  $\theta_{det} = 68^\circ$  ( $d = 1$  cm),  $104^\circ$  ( $d = 4$  cm),  $124^\circ$  ( $d = 10$  cm), as indicated by the horizontal, dotted lines.

realistically calculated with APCAD for the planning of experiments employing the Coulex-Multipolarimetry Method. For this purpose, the separation of the two targets is treated as an additional "layer" of the target which consists of the "material" vacuum in the simulation. No modifications to the source code of StopSim or APCAD are necessary, and all relativistic (Lorentz-boost, transformation of angles etc.) and geometrical effects (broad beam-profile,  $\gamma$ -ray vertices in and behind the two targets etc.) are automatically accounted for as described in Appendix B.

---

Lifetime effects are included in the simulated spectra shown in Fig. 5.10, 5.12 and 5.13, and they are best visible in the bottom panel of Fig. 5.10.

For 10 ps level lifetime, the  $\gamma$ -ray emission occurs predominantly behind the targets where the ions move with constant velocity. In this simulation, it is assumed that the ion velocity is measured behind the downstream target and therefore, the velocity of the ions de-exciting behind the second target is well known and allows for a very precise Doppler correction. Consequently, in the 10 ps - case, the  $\gamma$ -rays emitted from ions excited in the downstream target form a very sharp peak after appropriate Doppler correction. The small tail on the low-energy side of the peak stems from  $\gamma$ -rays emitted inside the target at higher ion velocities. Since the velocities inside the target can not be measured, the Doppler correction under-estimates the ion velocities in the case of de-excitation inside the target.

In the 50 fs - case, the ions de-excite predominantly inside the target at different velocities that are not known at the stage of Doppler correction, leading to a broadened peak structure. Since it is assumed that the ion velocities are measured behind the second target only, the ion velocity after the first target is not known exactly due to energy straggling occurring while passing both targets. In this simulation, for the peak from  $\gamma$ -rays emitted from ions excited in the first target, lifetime effects on the peak-shape are diminished by the ignorance of the exact ion velocity after leaving the first target and the fact that the energy loss in the first target is smaller than in the second target due to the higher kinetic energy of the ions.

---

### 5.3.5 Doppler correction / optimization

---

The best separation of excitations in the first and second target and also the best peak-to-background ratio can be expected if two Doppler corrections are applied to the very same data set: One assuming the velocity of the ions leaving the first target as ion velocity at the time of de-excitation and the position of the first target as ion position at the time of de-excitation, and one Doppler correction assuming the respective quantities for the second target. In the first case, de-excitation  $\gamma$ -rays from nuclei excited in the first target will be properly Doppler corrected to the laboratory frame and result in a sharp peak at the unshifted  $\gamma$ -ray energy  $E_0$  (or, depending on the lifetime of the excited state, in a characteristic Doppler-broadened lineshape like in DSAM experiments, see previous sub-section and Section 4). In contrast,  $\gamma$ -rays from nuclei excited in the second target would be transformed to a different energy due to improper Doppler correction. In the second case,  $\gamma$ -rays emitted from nuclei excited in the second target appear as a sharp peak at the unshifted  $\gamma$ -ray energy  $E_0$  while  $\gamma$ -rays from nuclei excited in the first target are transformed to a different energy.

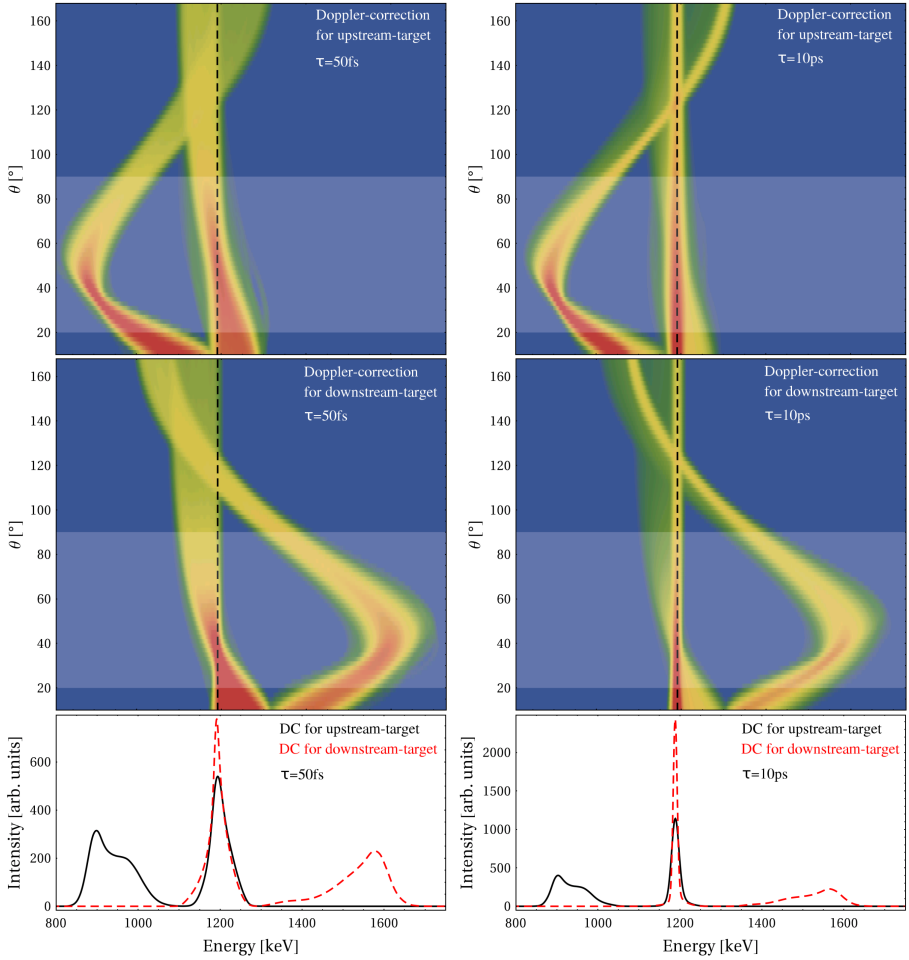


**Figure 5.12.:**  $\gamma$ -ray spectra simulated with the computer code APCAD (see Appendix B.2) for the 1191-keV transition from the  $\frac{1}{2}^-$  excited state of  $^{85}\text{Br}$  to its  $\frac{3}{2}^-$  ground-state. Parameters are as in Fig. 5.10, but the  $\gamma$ -ray energy spectra are shown as a function of the laboratory angle  $\theta$  of the  $\gamma$ -ray detection in a position-sensitive detector system. The bottom panel shows a projection of the shaded areas on the energy-axis. See text for details.

The effect of the two Doppler corrections is exemplarily shown for the case of a small detector subtending only two degrees in polar angle from  $59^\circ$  to  $61^\circ$  in Fig. 5.10. An appropriate Doppler correction for  $\gamma$ -rays emitted from nuclei excited in the upstream target implies a reduction of the measured  $\gamma$ -ray energy. It reproduces the transition energy  $E_0$  (apart from lifetime effects), if the nuclei emitting the  $\gamma$ -radiation were excited in the upstream target. The same Doppler correction applied to  $\gamma$ -rays emitted from nuclei excited in the downstream target results in corrected energies even smaller than  $E_0$ . Vice versa, an appropriate Doppler correction for  $\gamma$ -rays emitted from nuclei excited in the downstream target implies an increase of the  $\gamma$ -ray energy. It reproduces  $E_0$  for  $\gamma$ -rays emitted from nuclei excited in the downstream target and implies a further increase of the energy of  $\gamma$ -rays emitted from nuclei excited in the upstream target to energies even higher than  $E_0$ . In both cases, the position of the peak at the transition energy  $E_0$  arising from the appropriate Doppler correction is independent of the detector polar angle, but the position of the (broad) peak arising from inappropriately Doppler-corrected  $\gamma$ -rays varies strongly with the detector polar angle (see Fig. 5.12).

Since the Doppler-corrected  $\gamma$ -ray spectra will be blurred if the individual  $\gamma$ -ray detectors cover significant intervals of polar angle  $\theta$  with respect to the beam axis (Doppler-broadening), best separability and peak-to-background ratio can be expected with highly granular or position-sensitive HPGe detector-systems like AGATA [Akk12] or GRETA [Lee04, Pas13] (see Section 3.3).

Simulated example  $\gamma$ -ray spectra are shown in Fig. 5.12 for a position-sensitive detector system and in Fig. 5.13 for conventional, position-insensitive detectors. Two gold targets with 1 mm thickness in a distance of 10 cm are assumed in both cases. Transition strengths of  $B(E2, \downarrow) = 2$  W. u. and  $B(M1, \downarrow) = 0.58 \mu_N^2$  were assumed in the simulations, resulting in  $\delta_{E2/M1} = 0.087$ . Spectra have been simulated assuming level lifetimes of 50 fs (left panel in Fig. 5.12 and 5.13) and 10 ps (right panel in both figures). A broadening of the Doppler-corrected spectra can be observed in the case of the short lifetime due to the ignorance of the individual ion velocities at the time of de-excitation. This effect is most prominent at very forward and backward angles. The advantage of the position-sensitive detectors over conventional systems for this kind of measurement is clearly demonstrated by the simulated spectra shown in Fig. 5.12 and 5.13.

The ratio of the peak areas of the properly Doppler-corrected events at the  $\gamma$ -ray rest energy of 1191 keV is the observable used to determine the multipole mixing ratio. Therefore, the sensitivity of the method is limited by the uncertainty of the measured peak areas. This uncertainty may be strongly influenced by the  $\gamma$ -ray background underlying the peaks. The achievable sensitivity for a given physics case

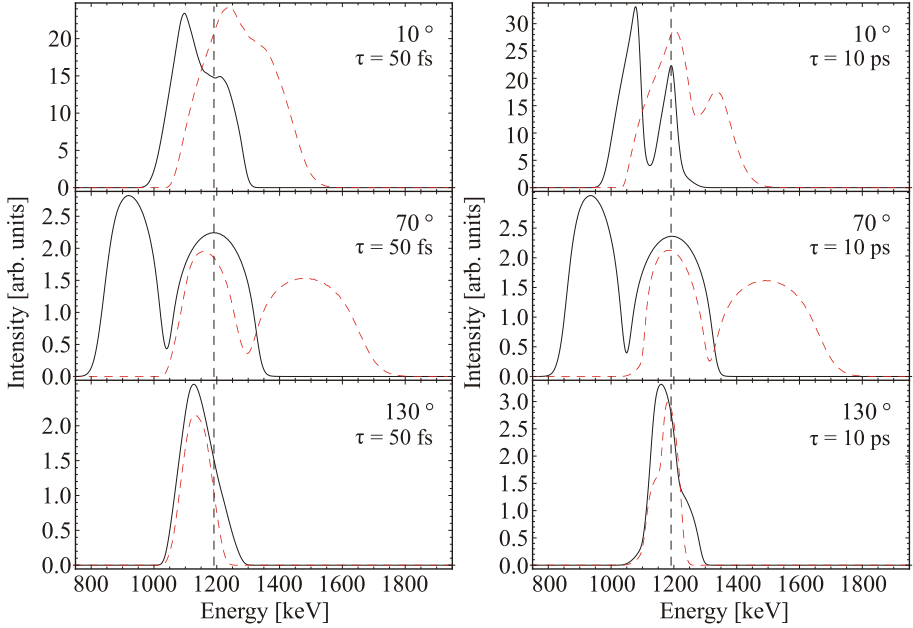


**Figure 5.13:**  $\gamma$ -ray spectra simulated with the computer code APCAD (see Appendix B.2) for the 1191-keV transition from the  $\frac{1}{2}^-$  excited state of  $^{85}\text{Br}$  to its  $\frac{3}{2}^-$  ground-state. Parameters are as in Fig. 5.10, but position insensitive, cylindrical detectors with a diameter of 8 cm placed in a distance of 23.5 cm around the center of the upstream target were assumed. Solid, black lines correspond to spectra obtained after application of a Doppler correction assuming the upstream target as the place of de-excitation, red, dashed lines correspond to Doppler corrections assuming the location of the downstream target as the place of de-excitation. Spectra are shown for detector positions at polar angles of  $\theta = 10^\circ, 70^\circ, 130^\circ$  with respect to the beam axis.

and experimental situation can be relatively easily evaluated by realistic simulations of the expected background level and peak shapes, as shown in Section 6.2.

---

## 6 First experiments employing the new methods

Two novel experimental techniques exploiting the capabilities of  $\gamma$ -ray tracking detectors were developed within this work: The continuous-angle Doppler-Shift Attenuation Method (caDSAM, Chapter 4) and the Coulex-Multipolarimetry Method (Chapter 5). This chapter discusses the first applications of these methods in  $\gamma$ -ray spectroscopy experiments.

The caDSA Method can directly be applied to experiments performed with conventional, position in-sensitive detectors. This was pointed out in Chapter 4 and is substantiated in Appendix B. Also these experiments benefit from the caDSAM via the advantages of the method discussed in Section 4.2. The caDSA Method has already very successfully been used for the analysis of DSAM experiments [Bau12, Bau13, Sta13, Her13] performed with several conventional detector systems such as MINIBALL [War13], EUROBALL Cluster detectors [Sim97] and GAMMASPHERE [Lee97]. The first application of the caDSA Method to data taken with  $\gamma$ -ray tracking detectors, the AGATA demonstrator, is reported in Section 6.1. The aim of the experiment, the experimental setup, the data analysis and the results of this experiment are discussed.

The Coulex-Multipolarimetry Method was applied in an experiment conducted in course of the PreSPEC-AGATA campaign at GSI, Darmstadt, in spring 2014. The data analysis is subject of another doctoral thesis and ongoing while thesis is written. The aim of the experiment, the experimental setup and perspectives for the data analysis are discussed in Section 6.2.

The potential impact of the new experimental techniques in terms of future experiments is discussed in Chapter 7.

---

---

## 6.1 The $2^+$ mixed-symmetry state of $^{140}\text{Ba}$ and level lifetimes of $^{136}\text{Xe}$

---

Mixed-symmetry states (MSSs) are nuclear valence space excitations which are antisymmetric with respect to their proton and neutron part. They are defined in the framework of the proton-neutron version of the Interacting Boson Model (IBM-2) [Ari77] and represent an elementary excitation mode of atomic nuclei that reflects the two-component quantum nature of the system. A prominent example for mixed-symmetry states is the scissors mode, an orbital isovector  $1^+$  excitation that is observed in deformed nuclei [Boh84, Hey10].

In near-spherical nuclei, the one quadrupole phonon mixed-symmetry state,  $2^+_{1,MS}$ , is the mixed symmetric state with lowest energy. It is particularly sensitive to the dominant quadrupole-quadrupole part of the residual proton-neutron interaction. The experimental signature of a  $2^+_{1,MS}$  state is a strong  $M1$  transition to the symmetric one quadrupole phonon state, the  $2^+_1$  state, with a transition strength in the order of  $1 \mu_N^2$  and a small  $E2$  transition strength to the ground state in the order of a few W.u. [Pie08]. Examples for the existence of  $2^+_{1,MS}$  states were first suggested for three  $N = 84$  isotones on the basis of small measured  $E2/M1$  multipole mixing ratios of their decays to the  $2^+_1$  states [Ham84]. The suggested  $2^+_{1,MS}$  states have been identified by lifetime measurements in the two stable isotopes  $^{142}\text{Ce}$  [Van95] and  $^{144}\text{Nd}$  [Hic98]. The  $2^+_{1,MS}$  state in radioactive  $^{140}\text{Ba}$  has not been firmly identified on basis of an absolute value for its  $B(M1, 2^+_{1,MS} \rightarrow 2^+_1)$  transition strength until today (further examples of experimentally identified MSSs and a discussion of  $2^+_{1,MS}$  states in general can be found in [Pie08]).

The population of  $2^+_{1,MS}$  states by  $\alpha$ -transfer reactions has been discussed in the framework of the IBM-2 by Alonso and co-workers [Alo08]. They conclude that in systems with only a few active proton- and neutron-bosons, i.e. in spherical vibrators, the population of  $2^+_{1,MS}$ -states relative to the population of the fully symmetric  $2^+_1$ -states by  $\alpha$ -transfer should be as large as  $1/3$ . In contrast, in systems with many active proton- and neutron-bosons, i.e. in deformed nuclei, the relative population of the  $2^+_{1,MS}$  states relative to the  $2^+_1$ -states should be only in the order of a few percent. In the work of Alonso *et al.*, the radioactive nucleus  $^{140}\text{Ba}$  was identified as an ideal candidate for the scenario where  $2^+_{1,MS}$  states should be strongly populated by  $\alpha$ -transfer. If observed, the strong population of the  $2^+_{1,MS}$  state in  $\alpha$ -transfer reactions could potentially serve as a new experimental signature for their mixed-symmetry character.

In  $\alpha$ -transfer reactions, a Helium nucleus is exchanged between a target and a beam nucleus. The reaction mechanism is not fully understood, and it is not clear

---

whether  $\alpha$ -transfer reactions have to be regarded as successive transfer of two individual protons and neutrons or as the transfer of an  $\alpha$ -"cluster" in one single step [Alo08]. However,  $\alpha$ -transfer reactions have successfully been used for populating excited states in radioactive nuclei close to stability in several experiments (e.g. [Ast10, Les05]). Preferably, low-spin spin states are directly populated by  $\alpha$ -transfer [Ken02]. This makes it a very suitable reaction for measurements of e.g. g-factors or very short level lifetimes where feeding from higher-lying states is not desirable. Maximum cross section for  $\alpha$ -transfer reactions is expected in collisions where the distance of closest approach between projectile and target nuclei equals the nuclear interactions radius [Lem73], i.e. at beam energies close to the Coulomb barrier.

An experiment aiming at the population of the  $2_{1,MS}^+$  state of  $^{140}\text{Ba}$  by  $\alpha$ -transfer was conducted at the Laboratori Nazionali di Legnaro (LNL) in October 2011. In that experiment 09.08, the mixed-symmetric character of the candidate for the  $2_{1,MS}^+$  state of  $^{140}\text{Ba}$ , the  $2_3^+$  state at 1994 keV excitation energy [Ham84], was supposed to be confirmed independently by measurement of its lifetime employing the continuous-angle DSA method. Coulomb-excited states of  $^{136}\text{Xe}$  with well-known lifetimes were designated as test case for the caDSA method.

Hence, two reactions were studied at the same time: The Coulomb excitation of the  $^{136}\text{Xe}$  projectiles and the transfer of one  $\alpha$ -particle from  $^{12}\text{C}$  target ions to the beam ions forming  $^{140}\text{Ba}$  in excited states. The two reactions are distinguished by different energy and kinematics of the carbon ions recoiling from the target after Coulomb excitation reactions and two  $\alpha$ -particles from the instantaneous breakup of  $^8\text{Be}$ , the residual of  $^{12}\text{C}$  after  $\alpha$ -transfer. These target-like recoiling ions are detected in a silicon detector placed behind the target.

Since the exact location of the Coulomb barrier is not well defined (see Appendix A), measurements were performed at two  $^{136}\text{Xe}$  beam energies of 500 MeV and 546 MeV, respectively. For studying the  $\alpha$ -transfer reaction and the population of excited states in  $^{140}\text{Ba}$  by the transfer, measurements were performed with a thin carbon target. For the caDSAM measurements, a carbon target with a thick tantalum backing was employed. The conducted measurements are summarized in Table 6.1.

The experimental setup is sketched in Figure 6.1 and further described in Section 6.1.1. The preparation of the experimental data is described in Section 6.1.2. The  $\gamma$ -ray spectra obtained for  $^{140}\text{Ba}$  populated by  $\alpha$ -transfer are discussed in Section 6.1.3. Determination of level lifetimes of  $^{136}\text{Xe}$  by the caDSA Method is subject of Section 6.1.4, while the determination of further transition strengths in  $^{136}\text{Xe}$  by

---

means of Coulomb excitation yield analysis is discussed in Section 6.1.5. The results for  $^{136}\text{Xe}$  are discussed in Section 6.1.6.

**Table 6.1.:** Experiment 09.08: Beam-target combinations and collected amount of data

beam energy	target	run number	collected data <sup>1</sup>
546 MeV	Carbon	82-97	73.8 GB
546 MeV	DSAM	101-106	21.8 GB
500 MeV	Carbon	107-108	5.1 GB
500 MeV	DSAM	109-110	8.3 GB
-	$^{152}\text{Eu}$	111-113	23.6 GB

---

<sup>1</sup> Data sizes after "replay", excluding AGATA traces. The amount of data is quoted as a measure for the collected statistics because it is independent from varying beam currents at different runs.

---

## 6.1.1 Setup of LNL experiment 09.08

---

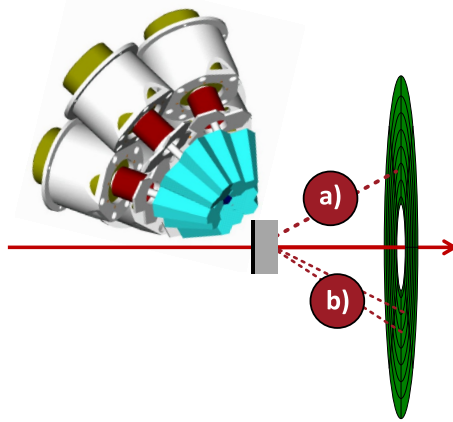


**Figure 6.1.:** Sketch of the setup of experiment 09.08 at LNL. Two reactions were measured at the same time: a) Coulomb-excitation of the  $^{136}\text{Xe}$  beam, identified by the detection of recoiling  $^{12}\text{C}$  ions in a DSSSD behind the target and b)  $\alpha$ -transfer to  $^{140}\text{Ba}$ , identified by the detection of two  $\alpha$ -particles in the DSSSD.  $\gamma$ -rays are detected by the AGATA demonstrator located at backward angles. See text for details.

Beams of  $^{136}\text{Xe}$  were provided by LNL's Tandem-ALPI accelerator complex at energies of 546 MeV and 500 MeV, respectively. These two beam energies are close to the Coulomb-barrier for  $^{136}\text{Xe}$  impinging on carbon targets for the scattering angles covered by the DSSSD (see Fig. 6.33).  $\alpha$ -transfer reactions are expected to occur predominantly in collisions where the distance of closest approach between projectile and target nuclei equals the sum of their radii (see Section 6.1.3). Therefore, the quoted beam energies were chosen in order to maximize the population of excited states of  $^{140}\text{Ba}$  by the  $\alpha$ -transfer reaction in competition to fusion-evaporation, incomplete fusion and other transfer reactions. The beam current was around 0.5-1 pA throughout the measurements.

For reaction studies, the beam was shot on a thin  $0.915\text{ mg/cm}^2$  carbon target, and for lifetime measurements by caDSAM, the beam was shot on a composite target consisting of an excitation layer made of  $0.47\text{ mg/cm}^2$  carbon and a stopping layer made of  $30.6\text{ mg/cm}^2$  tantalum. A thin layer of  $5\text{ }\mu\text{g/cm}^2$  Titanium between the carbon and tantalum layers was added for better adhesion. The thickness of the

stopping layer was chosen such that the primary beam was stopped in the target, but recoiling target-like ions could penetrate it.

Recoiling carbon-ions from Coulomb-excitation reactions and other target-like recoils from other nuclear reactions were detected by a double-sided silicon-strip detector (DSSSD) mounted behind the target. The DSSSD is segmented into 32 rings and 64 segments in azimuth angle  $\phi$ , where each two adjacent channels were electrically combined resulting in effectively 32 segments in  $\phi$ . In the following, the segments in  $\phi$  will be referred to as “sectors”. With its inner active diameter of 32 mm and outer active diameter of 85 mm, the DSSSD subtended polar angles from  $25.6^\circ$  to  $51.8^\circ$  at a distance of 33.4 mm from the target. The thickness of the employed DSSSD is  $\sim 300\ \mu\text{m}$ , sufficient to stop all target-like reaction products. A photograph of the DSSSD is shown in Figure 6.2 and the reaction kinematics is plotted in Figure 6.3.



**Figure 6.2.:** Photograph of the employed DSSSD detector. Energies were measured in the sectors (left) and rings (right) of the detector, times were measured in the sectors, only. The 64 sectors were electrically combined pairwise resulting in effectively 32 sectors.

The AGATA demonstrator consisted of 5 Triple-Clusters, i.e. 15 crystals, at the time of the measurement. It was placed at backward angles covering polar angles from  $\sim 74^\circ$  to  $\sim 164^\circ$ . In order to raise its detection efficiency, it was placed 71 mm closer to the target position than at its nominal target-distance of 235 mm. Plates of 1 mm Copper and 2 mm lead were placed in front of the AGATA detectors in order to shield un-desired low-energy  $\gamma$ - and X-rays that would have caused additional background and unnecessary load of the data acquisition system.

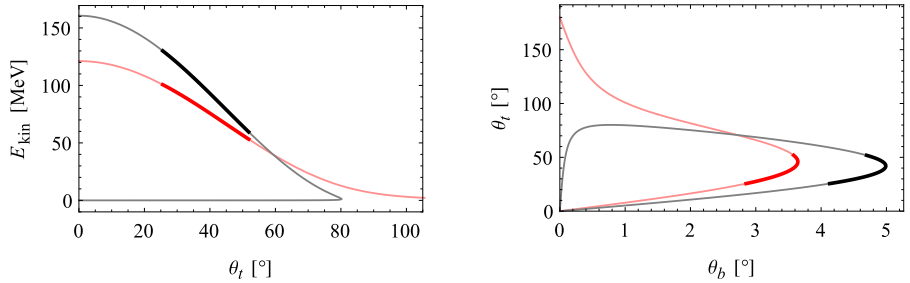


**Figure 6.3.:** Reaction kinematics for the Coulomb-excitation reaction (black) and the  $\alpha$ -transfer reaction (red) at 546 MeV beam energy. Left: Kinetic energy  $E_{kin}$  of the target-like reaction products ( $^{12}\text{C}$ ,  $^8\text{Be}$ ) as a function of their laboratory scattering angle  $\theta_t$ . Right: Laboratory scattering angle  $\theta_t$  of the target-like reaction products ( $^{12}\text{C}$ ,  $^8\text{Be}$ ) as a function of the laboratory scattering angle  $\theta_b$  of the beam-like reaction products ( $^{136}\text{Xe}$ ,  $^{140}\text{Ba}$ ). The angular range covered by the DSSSD is marked by bold lines. The low-energy branch of the recoiling  $^{12}\text{C}$  ions can not be detected by the DSSSD. See Appendix C for the calculation of the reaction kinematics.

Events were recorded in particle- $\gamma$  coincidence mode, i.e. the detection of at least one  $\gamma$ -ray and one particle within a hardware coincidence gate with a width of  $\sim 600$  ns was required to trigger the data acquisition.

---

## 6.1.2 Data Preparation

---

For the preparation of the experimental data, the following steps were carried out:

- Correction of radiation-damage of the DSSSD and energy-calibration for each channel,
- Add-back of particle energies measured coincidentally in neighboring channels,
- Energy calibration of all particle detector channels,
- Reaction channel selection via measured particle energies and scattering angles,
- Random subtraction via particle- $\gamma$  time-differences,
- Determination of the exact setup geometry via optimization of the observed energy resolution after Doppler correction,
- Optimization of the parameters for PSA in AGATA and correction for neutron damage of the detectors,
- Extraction of the first interaction points of the  $\gamma$ -ray quanta in AGATA via PSA and tracking,
- Reconstruction of the momentum vectors of the excited  $^{136}\text{Xe}$ -ions after the reaction from the kinematics of scattered  $^{12}\text{C}$  target nuclei.

In the following paragraphs these steps are discussed in detail.

### Particle spectra

The energies of all 32 rings and 32 sectors as well as times for the sectors were recorded. During the experiment, a drastic change of the detected energy spectrum could be observed (see Fig. 6.4). This can be attributed to increasing radiation damage of the crystal structure of the DSSSD or to gradually charging of the DSSSD's oxide layer [Sch14]. This degeneration was corrected on an event-by-event basis by introducing correction factors as a function of event-number. Corrected spectra of the summed energies registered in all rings and sectors of the DSSSD are shown in figures 6.5 and 6.6, respectively.

Figures 6.5 and 6.6 also show that the events with low-energy particles in the exit channel gradually disappear during the course of the experimental run at 546 MeV beam energy. This effect is also attributed to the degeneration of the DSSSD. The

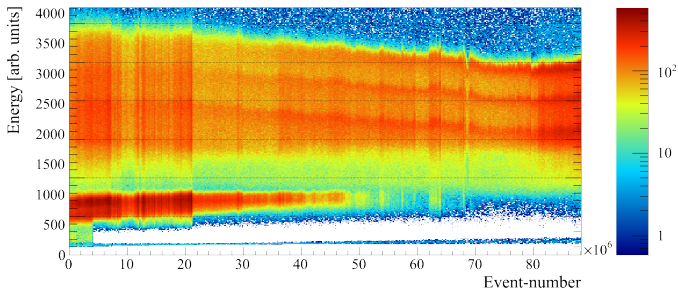


**Figure 6.4.:** Sum-energy spectrum of all DSSSD sectors as a function of the event-number for the experimental run at 546 MeV beam energy and a thin carbon target. A clear degeneration of the detector over the time of the measurement is visible.

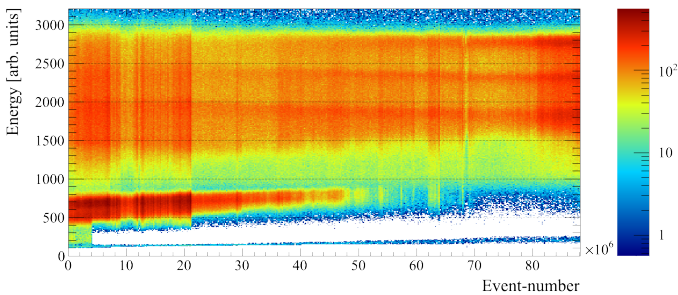


**Figure 6.5.:** Same data as in Figure 6.4, but corrected for the degeneration of the DSSSD.

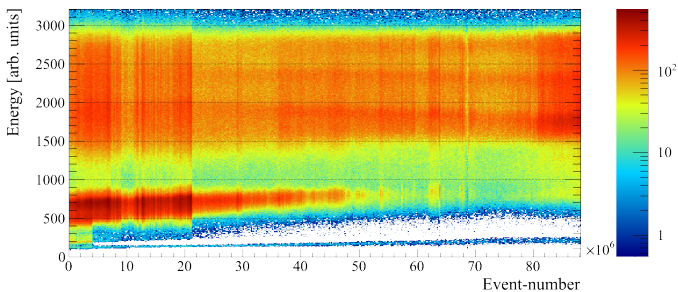


**Figure 6.6.:** Corrected sum-energy spectrum for all DSSSD rings as a function of the event-number for the experimental run at 546 MeV beam energy and a thin carbon target.

---

height of the detected electrical signals gradually decreases. For low-energy particles, it finally drops below the threshold of the constant fraction discriminator creating the particle trigger-signal. Hence, after some time, no particle- $\gamma$  coincidence could be formed for events with low-energy particles in the exit channel and the events were not recorded by the data acquisition system. If this behavior would have been noticed during data taking, gradually increasing the amplifier gain would have remedied this issue. In consequence, the fusion-evaporation reactions are basically absent at the end of the run at 546 MeV with the thin carbon target as well as in the runs with DSAM-target target at both beam energies and the run with thin carbon target at 500 MeV beam energy. At 500 MeV beam energy, the fusion-evaporation reactions would have been strongly suppressed due to the lower beam energy anyways. However, these low-energy particle signals belong to fusion-evaporation reactions that have no significance for the conducted experiment.

A linear calibration was applied to the energies measured in the rings and sectors. It was chosen such that best possible agreement between the energy measured in the rings and segments was achieved. For this purpose, a dedicated computer program was written and used for the automatic calibration of all 64 particle channels.

The pitch between adjacent rings of the DSSSD is relatively large, as can be seen in Figure 6.2. If particles hit this region between two rings, the created charge is collected in two adjacent segments. Only a fraction of the deposited energy is measured in a single channel, and the rest of the deposited energy is measured in a neighboring channel. Therefore, an add-back procedure for the particle detector was implemented in the analysis. Throughout the analysis, it is assumed that the efficiency of the DSSSD is 100%.

The particle energy spectrum measured in the DSSSD's rings during the experimental runs with a thin carbon target is shown as a function of the particle scattering angle in Figure 6.7 for 546 MeV beam energy and in Figure 6.8 for 500 MeV beam energy. Figure 6.9 shows a plot of the particle energy spectrum for the second DSSSD ring against the corresponding energy measured in any segment for both beam energies and the thin carbon target. The spectra for the other DSSSD-rings and the measurements with the layered DSAM target are shown in Appendix D.1.

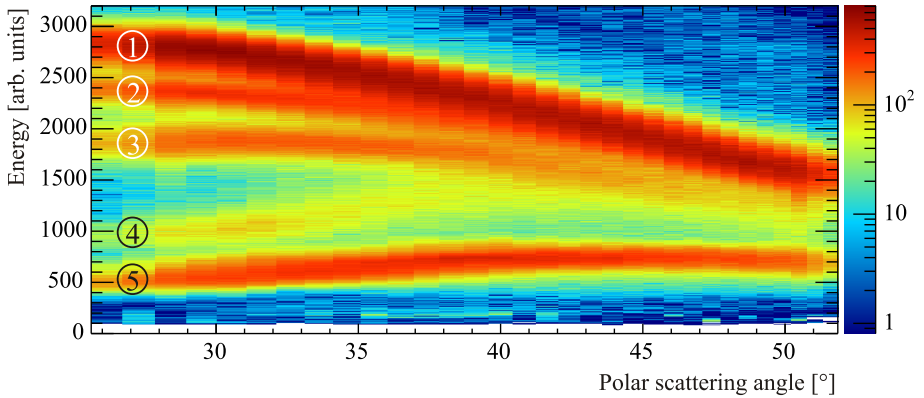


**Figure 6.7.:** Energy spectrum measured in the rings of the DSSSD as a function of the particle scattering angle measured at 546 MeV beam energy with a thin carbon target. Different reaction channels are marked with numbers 1 to 5. Add-back and corrections for the degeneration of the detector were applied. See text for details.

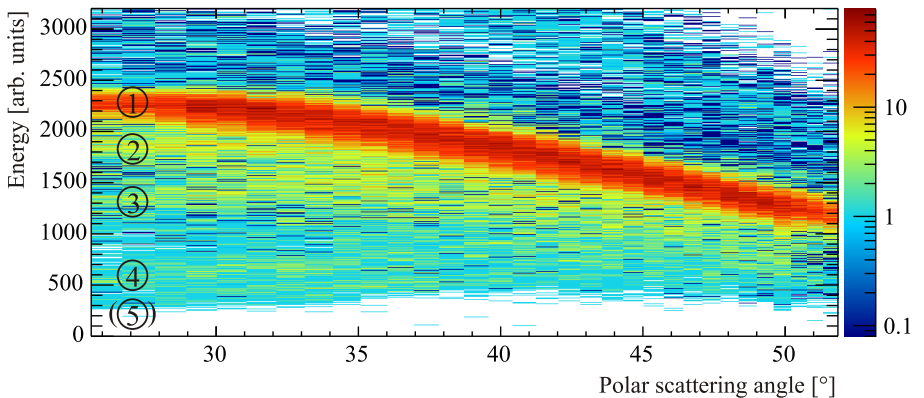


**Figure 6.8.:** Same spectrum as in Figure 6.7 but for the runs at 500 MeV beam energy with a thin carbon target. Different reaction channels are marked with numbers 1 to 5. Add-back and corrections for the degeneration of the detector were applied. See text for details.

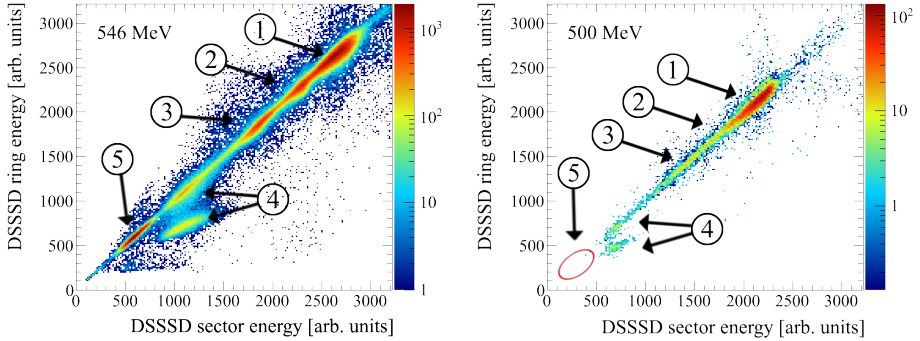


**Figure 6.9.:** Particle energy measured in DSSSD ring 7 (covering scattering angles  $\theta$  from  $32.1^\circ$  to  $33.1^\circ$ ) versus corresponding energy measured in a segment for 546 MeV (left) and 500 MeV (right) beam energy. The spectra correspond to the measurement with a thin carbon target. Different reaction channels are marked with numbers 1 to 5. Add-back and calibration were applied. See text for details.

Different reaction channels are clearly visible. The following reaction channels can be assigned to the particle events marked with number 1 to 5 in figures 6.7, 6.8 and 6.9:

- (1) Coulomb-excitation of the  $^{136}\text{Xe}$  beam:  $^{12}\text{C}(^{136}\text{Xe}, ^{136}\text{Xe}^*)^{12}\text{C}$ .
- (2) Proton pick-up reaction producing  $^{137}\text{Cs}$ :  $^{12}\text{C}(^{136}\text{Xe}, ^{137}\text{Cs}^*)^{11}\text{B}$ .
- (3) Two proton pick-up reaction producing  $^{138}\text{Ba}$ :  $^{12}\text{C}(^{136}\text{Xe}, ^{138}\text{Ba}^*)^{10}\text{Be}$ .
- (4)  $\alpha$ -transfer reaction producing  $^{140}\text{Ba}$ :  $^{12}\text{C}(^{136}\text{Xe}, ^{140}\text{Ba}^*)^8\text{Be}$ , contaminated by incomplete fusion reaction producing  $^{139}\text{Ba}$ :  $^{12}\text{C}(^{136}\text{Xe}, ^{139}\text{Ba}^*)\alpha + an$ .
- (5) Fusion-evaporation reactions with  $\alpha$ -particles in the exit channel producing  $^{140}\text{Ba}$ :  $^{12}\text{C}(^{136}\text{Xe}, ^{140}\text{Ba}^*)2\alpha$  and producing  $^{142}\text{Ce}$ :  $^{12}\text{C}(^{136}\text{Xe}, ^{142}\text{Ce}^*)\alpha + 2n$ .

This assignment of reaction channels was based on the  $\gamma$ -ray spectra observed in coincidence with the respective particles as discussed in the paragraph "  $\gamma$ -ray spectra" at the end of this section.

It can be clearly seen in figures 6.7, 6.8 and 6.9 that the nuclear reactions (pick-up, fusion-evaporation and transfer reactions) are significantly reduced with respect to the Coulomb-excitation reaction at the lower beam energy.

The  $^8\text{Be}$  target-like ions produced in the  $\alpha$ -transfer reaction immediately break up into two  $\alpha$ -particles with a Q-Value of  $91.8 \text{ keV}^2$ . The opening angle of the two  $\alpha$ -particles with respect to the scattering direction of the  $^8\text{Be}$  target-like recoil can be calculated from the Q-value of the break-up and the kinetic energy of the  $^8\text{Be}$  ions as a function of their scattering angle. This opening angle is maximum if emission of the two  $\alpha$ -particles is assumed to happen perpendicular to the direction of motion of the  $^8\text{Be}$  target-like recoil. For the angular range covered by the DSSSD, this maximum opening angle is in the range of  $3^\circ$  to  $4^\circ$ . It is plotted in Figure 6.10 together with the maximum spatial separation of the two  $\alpha$ -particles when they are detected by the DSSSD.

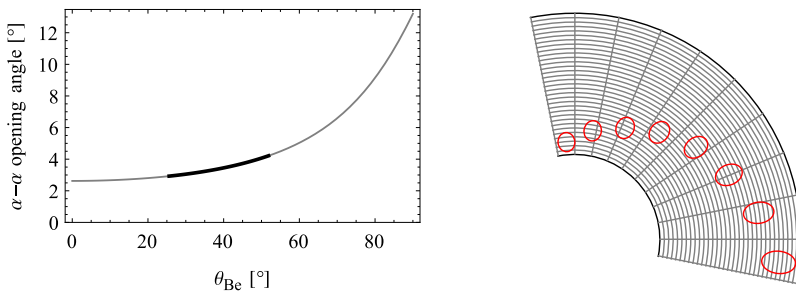


**Figure 6.10.: Left:** Maximum opening angle of the two  $\alpha$ -particles produced by the breakup of  $^8\text{Be}$  as a function of the  $^8\text{Be}$  scattering angle  $\theta_{\text{Be}}$  after an  $\alpha$ -transfer reaction.

**Right:** Maximum spatial separation of the two  $\alpha$ -particles as they are detected by the DSSSD.

For the population of  $^{140}\text{Ba}$  by the fusion-evaporation reaction  $^{12}\text{C}(^{136}\text{Xe}, ^{140}\text{Ba}^*)2\alpha$ , this strong directional correlation of the two  $\alpha$ -particles is not present. Hence, the coincident detection of two  $\alpha$ -particles in nearby segments of the DSSSD is a clean condition for the  $\alpha$ -transfer reaction. It is apparent from Figure 6.10 that the two  $\alpha$ -particles from an  $\alpha$ -transfer reaction will be detected in one single sector or in two neighboring sectors. Consequently, the add-back algorithm will recover their full sum energy in the sectors. However, there is a significant probability that two  $\alpha$ -particles from an  $\alpha$ -transfer reaction will be detected in non-neighboring rings of the DSSSD. In this case, the add-back algorithm will not recover the full sum-energy of the two  $\alpha$ -particles deposited in the rings, and only the energy of one  $\alpha$ -particle will be measured in the rings. This leads to the off-diagonal events in

<sup>2</sup> Q-value calculated from the masses of  $^4\text{He}$  and  $^8\text{Be}$  from the 2012 atomic mass evaluation [Wan12] and the value for the atomic mass unit from [NIS14]

---

Figure 6.9. In events where two coincident  $\alpha$ -particles are registered in the same or in neighboring rings and segments, the sum energy of both  $\alpha$ -particles is measured in the ring and segment and can be clearly distinguished from events where only one  $\alpha$ -particle was detected. In Figure 6.9, events with two coincident  $\alpha$ -particles detected in the same or in neighboring rings and segments form the peak at an energy of  $\sim 1000$  arb. units in both rings and sectors at 546 MeV beam energy and at  $\sim 700$  arb. units at 500 MeV beam energy. These and the off-diagonal events can be considered as a clean condition for the  $\alpha$ -transfer reaction. In the case of the population of  $^{140}\text{Ba}$  by fusion-evaporation, the missing directional correlation of the two  $\alpha$ -particles makes a detection of both particles in the same or neighboring segments very unlikely. In this case, only the energy of one  $\alpha$ -particle is registered in both the rings and segments of the DSSSD. These events form the peak at an energy of  $\sim 500$  arb. units in both rings and sectors for 546 MeV beam energy in Figure 6.9.

Gates on the different reaction channels were set in the two-dimensional spectra of particle energy measured in the sectors and rings of the CD (see Fig. 6.9 for example). These gates were defined separately for every ring of the CD, since the energy of the target-like recoils changes as a function of scattering angle as shown in Fig. 6.7 and 6.8. These reaction channel gates are plotted in Appendix D.1.

### Particle- $\gamma$ time-differences and random subtraction

The time-information from the DSSSD and the AGATA detectors was used to calculate the time-differences between the detection of the target-like reaction products and the detection of the  $\gamma$ -rays from the de-excitation of excited states of beam-like reaction products. The resulting time-difference spectrum is shown in Figure 6.11. The detection of physically and, therefore, temporally correlated particles and  $\gamma$ -rays results in a clear "prompt" peak of true coincidences. It is situated on top of a flat background of "random" events. These stem from physically and temporally un-correlated particles and  $\gamma$ -rays, e.g. Rutherford-scattered target nuclei and  $\gamma$ -rays from the room background. Their temporal coincidence is inherently random.

Prompt events are selected by setting a gate around the prompt peak in the time-difference spectrum. The background of random events underlying the prompt peak is removed by setting a "random"-gate on the flat background in the time-difference spectrum. The prompt and random gate that were used in this work are also indicated in Figure 6.11.

Random subtracted  $\gamma$ -ray spectra are then created by subtracting weighted  $\gamma$ -ray spectra corresponding to events within the "random"-gate in the time-difference spectrum from the  $\gamma$ -ray spectra corresponding to events within the

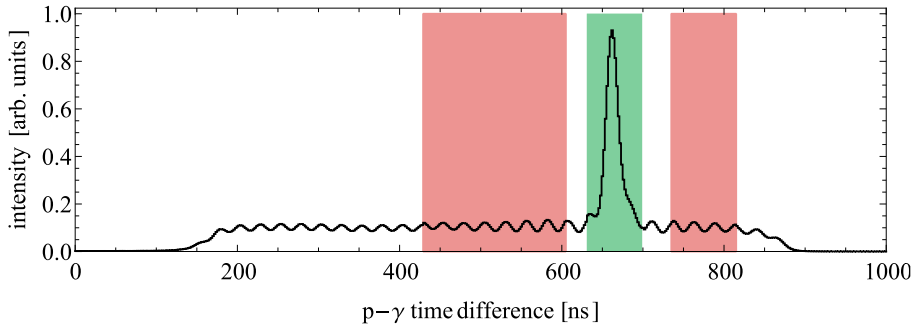


**Figure 6.11.:** Spectrum of time-differences between the detection of a target-like recoil and a  $\gamma$ -ray for the experimental runs with 546 MeV beam energy and thin carbon target. Prompt coincidences based on physical correlations between particle and  $\gamma$ -ray form the pronounced peak at  $\sim 630$  ns. Random coincidences between particles (e.g. Rutherford-scattered target nuclei) and  $\gamma$ -rays (e.g. from the room background) form the background of random coincidences. The periodic structure of the background is caused by the time structure of the ion-beam. Prompt- and random gate used in the analysis are indicated by the green and red areas, respectively. The absolute value of the time difference is caused by the different path lengths of the signals from the particle and  $\gamma$ -ray detectors and has no meaning here. Higher values of the time-difference correspond to later detection of the  $\gamma$ -ray with respect to the particle.

prompt gate. The weighting factor is given by the ratio of the widths of the random- and the prompt gate. The uncertainty of the bin contents of random subtracted spectra is no longer given by the square-root of the bin content (i.e. it does not obey Poisson statistics) and error propagation has to be applied.

This procedure of random subtraction presumes that the  $\gamma$ -ray spectrum corresponding to the random events is uniform throughout the regions in the time-difference spectrum used for the gates. This may not be the case if there is beam-induced, delayed background-radiation, e.g. from activation. It was carefully checked that this is not the case in the discussed experiment.

### Doppler correction and determination of the setup geometry

From the high granularity of the DSSSD and the equations describing the reaction kinematics (Appendix C), the momentum vector of the excited beam-like reaction

---

products can be calculated with high accuracy on an event-by-event basis for a given beam energy. Together with the superior position resolution of the AGATA detectors, this offers excellent conditions for a precise correction of the Doppler-shift of  $\gamma$ -radiation emitted in-flight (see Section 2.3). Especially at the level of precision achievable under these conditions, precise knowledge of the geometry of the experimental setup is very crucial. The setup geometry is determined by the following parameters (compare to Fig. 6.12):

- (1) Distance of the AGATA demonstrator from the nominal target position
- (2) Angle of the AGATA demonstrator with respect to the beam axis
- (3) Position of the ion beam
- (4) Transversal position of the DSSSD relative to the beam axis
- (5) Distance of the DSSSD from the nominal target position
- (6) Rotation of the DSSSD around the beam axis

These parameters define

- the reaction vertex in the target (via parameter 3 and neglecting the  $-\mu\text{m}$ -thickness of the target)
- the momentum vector of the excited ion (via the reaction vertex and parameters 4,5,6 plus the relations for the reaction kinematics)
- the emission direction of the  $\gamma$ -ray (via the reaction vertex and parameters 1,2)
- finally, the angle  $\alpha$  between the momentum vector of the emitting ion and the emitted  $\gamma$ -ray needed for the Doppler correction.

The nominal target position defines the origin of the laboratory frame. The beam axis defines its z-axis and the plumb line its x-axis. The reference frame of the AGATA demonstrator is defined such that the nominal target position coincides with the focus of the AGATA detectors (i.e. the center of the full AGATA sphere) when parameter 1 is zero. The demonstrator is arranged symmetric around the beam axis and positioned upstream of the target when parameter 2 is  $0^\circ$ . The z- and x-axis of the AGATA reference frame are aligned with those of the laboratory frame when parameter 1 is zero and parameter 2 is  $0^\circ$ . The rotation of AGATA (parameter 2) is around the x-axis. Its translation (parameter 1) is along the z-axis of its own reference frame. The parameters for the definition of the setup geometry and the reference frames are illustrated in Figure 6.12.

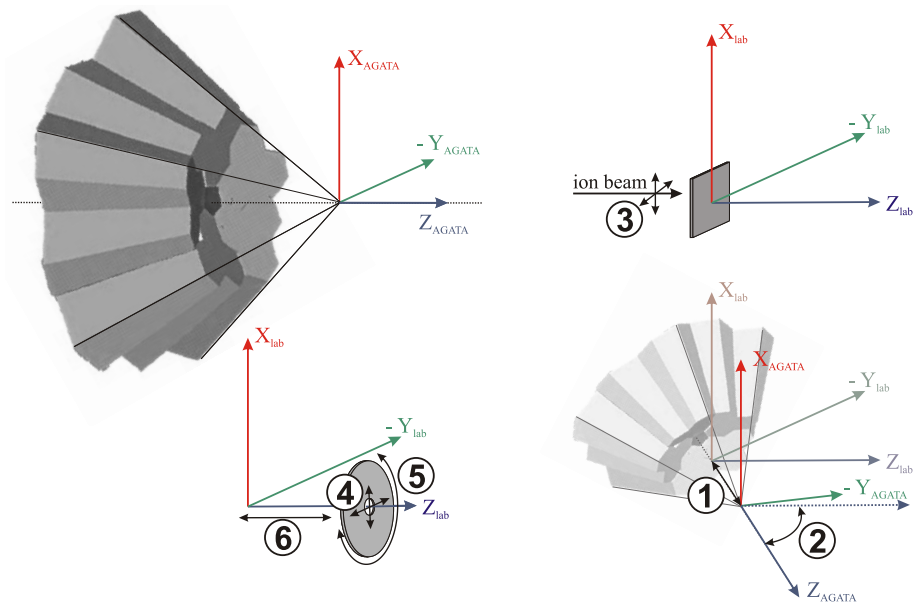


**Figure 6.12.:** Illustration of the parameters defining the experimental setup and the reference frames used for its description. The circled numbers refer to the parameters defining the setup geometry as defined in the text.

**Top left:** AGATA reference frame. The origin is at the focus of the AGATA detectors, the Z-axis is given by AGATA's symmetry axis (coincides with the beam axis if parameter two is zero) and the X-axis is parallel to the plumb line.

**Top right:** Laboratory frame. The origin is at the center of the nominal target position, the Z-axis parallel to the beam axis and the X-axis parallel to the plumb line.

**Bottom left:** Position of the DSSSD in the laboratory frame and related parameters.

**Bottom right:** Position of AGATA with respect to the laboratory frame and related parameters.

---

It was not possible to determine these quantities with the required precision on site. However, the high position resolution of AGATA and the DSSSD provides a powerful tool to determine the setup geometry by optimizing the Doppler correction of  $\gamma$ -rays with known un-shifted energy. This procedure is based on the reasonable presumption that the optimum resolution after Doppler correction is obtained when emanating from the correct setup geometry.

Within this work, a dedicated software program was written for this purpose. The concept of the program is as follows:

The data from the experimental runs with the thin carbon target are used, selected for the Coulomb-excitation of  $^{136}\text{Xe}$  (see the following paragraph on reaction channel selection). A subset with the same number of  $2_1^+ \rightarrow 0_{gs}^+$  transitions was taken for 500 MeV and 546 MeV beam energy. Each datum in this set contained the following information:

- Reconstructed first interaction point of the  $\gamma$ -ray in AGATA, expressed in the reference frame of the AGATA demonstrator
- Ring and sector number of the DSSSD in which the recoiling target ion ( $^{12}\text{C}$ ) was registered
- A boolean flag whether the event belongs to the prompt or random gate
- Beam energy

In contrast to the target for the caDSAM-measurement, the thickness of the thin carbon target was not known exactly. It has strong influence on the observed Doppler-shifts since it changes the velocity of the excited ions after leaving the target and entered as another parameter to be determined by the program. Furthermore, the position of the beam on the target was slightly different during the runs at 546 MeV and 500 MeV beam energy by about 1 mm and had to be determined separately for both beam energies.

For a given set of the parameters defining the setup geometry, a Doppler correction was applied to the data for 500 MeV and 546 MeV beam energy. The resulting spectra for both beam energies were added. The mean of the summed peak of the  $2_1^+ \rightarrow 0_{gs}^+$  transition was adjusted to its un-shifted energy of 1313 keV by varying the angle of the AGATA demonstrator with respect to the beam-axis (parameter 2). This angle was chosen as "adjustment-parameter", because among all parameters, it has the most direct and linear influence on the mean of the peak after Doppler correction.

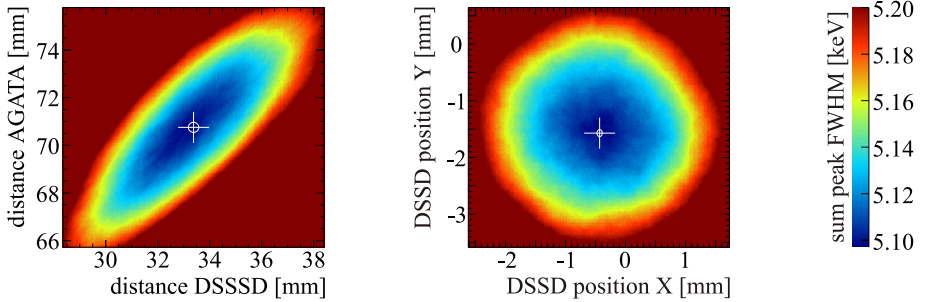


**Figure 6.13.:** Determination of parameters defining the setup geometry by optimization of the  $\gamma$ -ray resolution after Doppler correction. Pronounced minima in the FWHM of the  $2_1^+ \rightarrow 0_{gs}^+$  peak of  $^{136}\text{Xe}$  summed for both beam energies of 500 and 546 MeV were found. Here, the optimization of the distance of the AGATA demonstrator and the DSSSD from the nominal target position (left) and the transverse position of the DSSSD with respect to the beam axis (right) are shown exemplarily. The white crosses mark the locations of the minima and the white circles their uncertainties. The plots for all other parameters are shown in Appendix D.2.

The width of the summed peak of the  $2_1^+ \rightarrow 0_{gs}^+$  transition is the quantity to be minimized by the program. This was done by

- a) use of the MIGRAD minimizer of the MINUIT package [MIN14] and
- b) changing the parameters pairwise and adopting the values yielding the smallest width until the procedure converged.

The validity of the parameter set yielding the smallest width was checked by scanning the parameter space around the minimum. The change of the width of the peak of the  $2_1^+ \rightarrow 0_{gs}^+$  transition under variation of pairs of the parameters is shown in Figure 6.13. Each point in this parameter scan represents the width of the peak of the  $2_1^+ \rightarrow 0_{gs}^+$  transition for a given set of parameters. The uncertainty of each of these data-points is given by the uncertainty of the width of a Gaussian plus low-energy tail fitted to the peak. The locations of the minima with respect to each parameter and their uncertainties were determined by fitting two-dimensional polynomials of second order to the results of the parameter scans. The determined minima are unique in the entire parameter space that is compatible with the survey of the setup geometry on site.

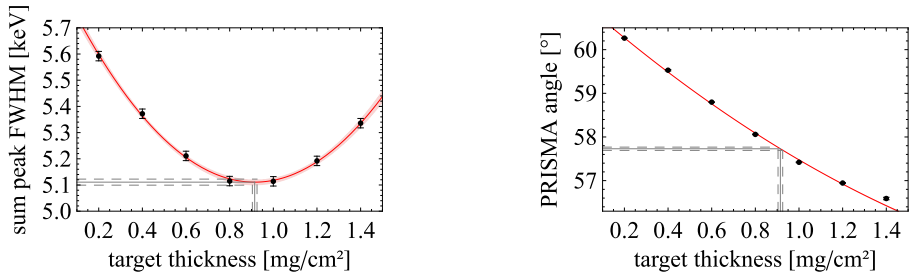


**Figure 6.14.:** Left: Determination of the carbon target thickness. For each data point, parameters 1-6 discussed in the text have been optimized in order to yield the optimum Doppler correction, assuming different target thicknesses. At the true target thickness, the best  $\gamma$ -ray resolution is obtained. Right: Once the target thickness is determined, all parameters 1-6 can be derived. Here, the determination of the polar angle of the AGATA demonstrator with respect to the beam axis is shown exemplarily. The plots for all other parameters are shown in Appendix D.2.

The assumed thickness of the carbon target is strongly correlated to the values of parameters 1-6 yielding the smallest width of the peak after Doppler correction. However, also the smallest width of the peak after Doppler correction (after optimizing all other parameters) correlates with the assumed target thickness and exhibits a pronounced minimum (see Figure 6.14 left). This allows to fix the true target thickness and then to fix all other parameters describing the geometry of the experimental setup. This is shown in Figure 6.14. The final values of the parameters and their uncertainties are listed in Table 6.2. It has to be emphasized that *all* parameters could be determined with *sub-millimeter precision*.

### $\gamma$ -ray spectra

The determination of  $\gamma$ -ray interaction points within the segments of the AGATA detectors by *pulse shape analysis* (PSA, see Section 3.2.1) and the subsequent reconstruction of the path of the individual  $\gamma$ -ray quanta in the crystals by means of *tracking* (see Section 3.2.2) were performed online during the experiment. The *adaptive grid search* algorithm [Ven04] was used for PSA and the *Orsay Forward Tracking-Algorithm* (OFT) [LM04] was used for tracking.

However, the waveforms of the electrical signals measured in the core and segments of the AGATA crystals ("*traces*") were written to disk. This allowed for a

**Table 6.2.:** Parameters defining the setup geometry. Their determination was done by a dedicated computer program developed within this work. See text for details.

No.	Parameter	Value
1	Target thickness	0.915(11) mg/cm <sup>2</sup>
2	distance AGATA	70.7(2) mm
3	polar angle AGATA	57.73(3) <sup>°</sup>
3	beam position X (500 MeV)	0.3(1) mm
3	beam position Y (500 MeV)	-1.26(7) mm
3	beam position X (546 MeV)	0.03(4) mm
3	beam position Y (546 MeV)	-0.23(4) mm
4	DSSSD position X	-0.43(5) mm
4	DSSSD position Y	-1.57(6) mm
5	distance DSSSD	33.4(2) mm
6	rotation DSSSD	-0.53(14) <sup>°</sup>
	resolution at 1313 keV	5.10(2) keV FWHM

later optimization of the parameters for the PSA and subsequent corrections (e.g. for correction of neutron damage [Bru13]), and both PSA and tracking were repeated in an *offline-replay* of the data using the recorded traces. This data replay was conducted under the direct instruction of Dr. Caterina Michelagnoli and Dr. Dino Bazzacco at LNL. The process of data replay and the different optimizations are described in great detail in ref. [Mic13] and will not be further discussed in this thesis. Figure 6.15 exemplarily shows the effect of the optimizations performed in the data replay.

The produced  $\gamma$ -ray spectra were corrected for the detection-efficiency of the AGATA demonstrator. Detection-efficiencies were deduced from measurements with a <sup>152</sup>Eu radiation source placed at the target position and the known relative  $\gamma$ -ray intensities emitted after its  $\beta$ -decay, taken from [Mar13].

The analysis of the measurements with the thin carbon target was made in terms of  $\gamma$ -ray spectra summed over the complete  $\gamma$ -ray detector-array. For this purpose, an efficiency calibration was made for each of the 15 physical germanium crystals of the AGATA demonstrator. This efficiency calibration was applied to all  $\gamma$ -ray spectra summed over the complete  $\gamma$ -ray detector array.

For the caDSAM-analysis, two-dimensional spectra in  $\gamma$ -ray energy and polar  $\gamma$ -ray detection angle were used. These spectra were sorted with a particular bin-

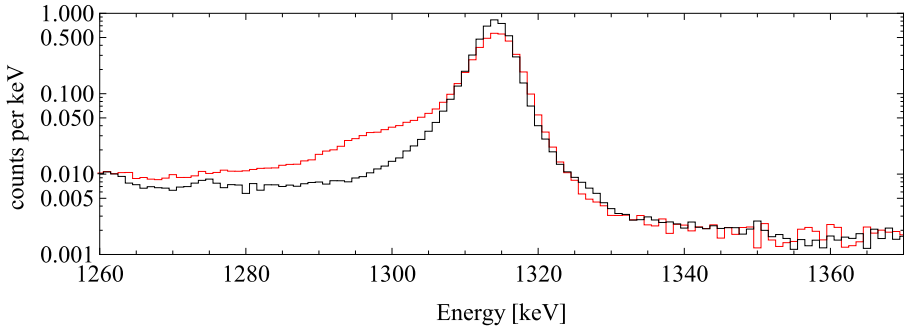


**Figure 6.15.:** Random subtracted, Doppler-corrected  $\gamma$ -ray-spectrum showing the  $2_1^+ \rightarrow 0_{gs}^+$  transition of  $^{136}\text{Xe}$  before (red) and after (black) the “replay” of the experimental data. The neutron damage correction manifests itself in a drastic reduction of the low-energy tail and the optimization of the parameters for PSA results in an improved resolution. The spectrum shows a fraction of the data taken at 546 MeV beam energy and the thin carbon target. See text for details.

ning in the polar angle (see Section 6.1.4.1). The data from the  $^{152}\text{Eu}$  calibration source measurement were sorted with the very same binning in polar  $\gamma$ -ray detection angle as the data for the caDSAM analysis. An independent efficiency calibration was made for all 35 angular bins and applied to all two-dimensional spectra in  $\gamma$ -ray energy and polar  $\gamma$ -ray detection angle.

In total,  $15 + 35 = 50$  efficiency calibrations had to be performed. Therefore, for both the efficiency calibration on the basis of the physical crystals and on the basis of the bins in polar  $\gamma$ -ray detection angle, an automatic script was used. This script was developed within this work and is based on the root-framework [Bru97]. It automatically determines the positions and intensities of the decay lines in the respective  $^{152}\text{Eu}$  spectra by a least-squares fit. The intensities and their uncertainties obtained this way are then used by the script to determine the parameters and their uncertainties of an efficiency function by another least-squares fit. In this work, an efficiency-function of the form

$$\epsilon_i(E_\gamma) = a_i \cdot e^{-b_i \cdot \ln(E_\gamma - c_i + d_i \cdot e^{-e_i E_\gamma})} \quad (6.1)$$

was used. The index  $i$  identifies either a physical Germanium-crystal or a bin in polar  $\gamma$ -ray detection angle. The positions of the  $^{152}\text{Eu}$  decay lines determined by the script were used for a final energy-calibration by a polynomial of second order.

---

Gaussian error propagation was used to calculate the uncertainty of each bin content in every spectrum when the efficiency-calibration and/or random subtraction was applied.

By the application of the gates in particle energy,  $\gamma$ -ray spectra for the different reaction channels can be created. They are shown for the measurements with the thin carbon target at 546 MeV beam energy in Fig. 6.16 and at 500 MeV beam energy in Fig. 6.17. The reaction channel selection is not perfect because the energies of the target-like recoils from the different reactions converge with increasing laboratory scattering angle as shown in Fig. 6.7 Appendix D.1.

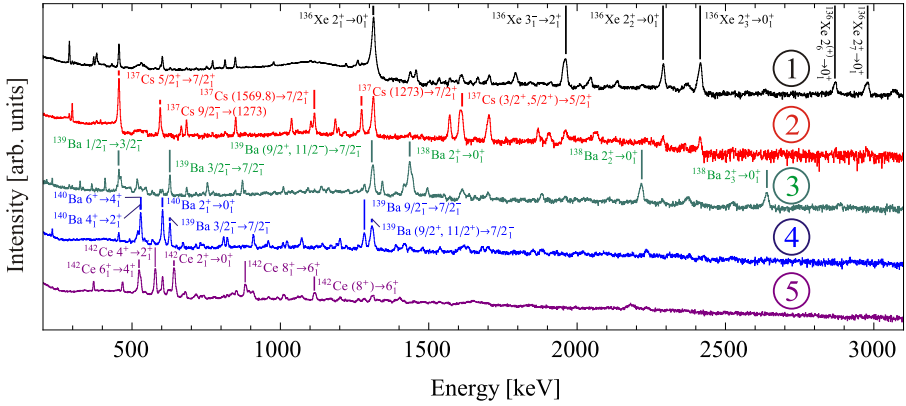


**Figure 6.16.:** Comparison of  $\gamma$ -ray spectra for all reaction channels observed at 546 MeV beam energy using the thin carbon target. The reaction channels are separated by gates on the measured energy of the target-like recoils as indicated in figures 6.7 and 6.9 (left) and discussed in the text. Dominant transitions for each reaction channel are marked and labeled. The spectra are shifted along the y-axis for better visibility.

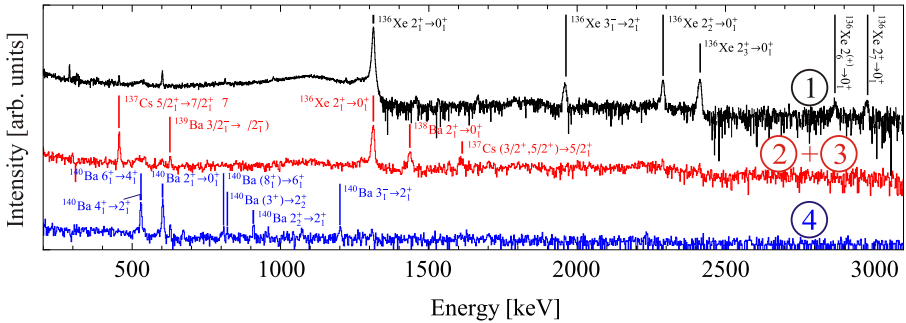


**Figure 6.17.:** Comparison of  $\gamma$ -ray spectra for all reaction channels observed at 500 MeV beam energy using the thin carbon target. The reaction channels are separated by gates on the measured energy of the target-like recoils as indicated in figures 6.8 and 6.9 (right) and discussed in the text. Dominant transitions for each reaction channel are marked and labeled. The spectra are shifted along the y-axis for better visibility.

### 6.1.3 Analysis of the data for $^{140}\text{Ba}$ populated by $\alpha$ -transfer

In LNL experiment 08.09, excited states of  $^{140}\text{Ba}$  were populated by the inverse-kinematics  $\alpha$ -transfer reaction  $^{12}\text{C}(^{136}\text{Xe}, ^{140}\text{Ba}^*)^8\text{Be}$  at beam energies of 500 and 546 MeV.  $\gamma$ -ray spectra produced after gating on the measured energy of the target-like recoils (see previous section) are shown in Figure 6.19 for 546 MeV and in Figure 6.20 for 500 MeV beam energy. A direct comparison of both spectra is shown in Figure 6.18.

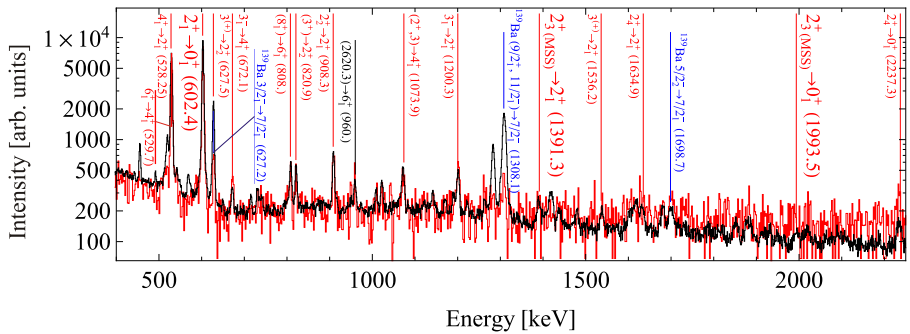


**Figure 6.18.:** Comparison of  $\gamma$ -ray spectra for  $^{140}\text{Ba}$  populated by  $\alpha$ -transfer reactions at 500 MeV beam energy (red) and 546 MeV (black). The spectra were normalized such that they contain the same number of events in the  $2_1^+ \rightarrow 0_{gs}^+$  transition of  $^{140}\text{Ba}$ . To a large extent, the relative population of states in  $^{140}\text{Ba}$  is independent from the beam energy. See text for details.

The spectra are contaminated by decays of excited states in  $^{139}\text{Ba}$ , presumably produced in the incomplete fusion reaction  $^{12}\text{C}(^{136}\text{Xe}, ^{139}\text{Ba}^*)\alpha + an$ . In this reaction, the carbon ion breaks up into an  $\alpha$ -particle and an  $^8\text{Be}$  nucleus which fuses with the  $^{136}\text{Xe}$  ion. The residual  $\alpha$ -particle is ejected with relatively high velocity and detected by the DSSSD (see e.g. [Ill14]). Due to its high energy, it cannot be distinguished from the events with two  $\alpha$ -particles from the  $\alpha$ -transfer reaction. Excited states in  $^{139}\text{Ba}$  are then populated in the  $(\alpha, n)$  exit-channel. If the evaporated  $\alpha$ -particle was detected by the DSSSD, there would not be a correlation between its emission direction and the momentum of the excited  $^{139}\text{Ba}$  nucleus. In consequence, the Doppler correction would be less precise, resulting in broader peaks.

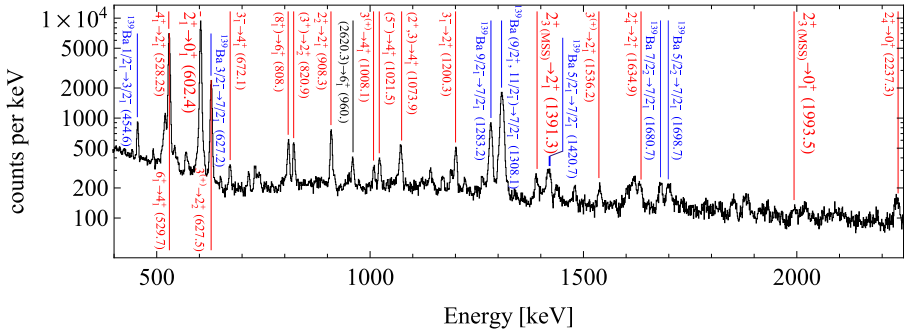


**Figure 6.19.:**  $\gamma$ -ray spectrum for  $^{140}\text{Ba}$  produced in an  $\alpha$ -transfer reaction at 546 MeV beam energy. Low-spin states are excited preferably. Decays of excited states of  $^{140}\text{Ba}$  are marked with red lines. The spectrum is contaminated by transitions in  $^{139}\text{Ba}$  (blue lines), populated by an incomplete fusion reaction. See text for details.

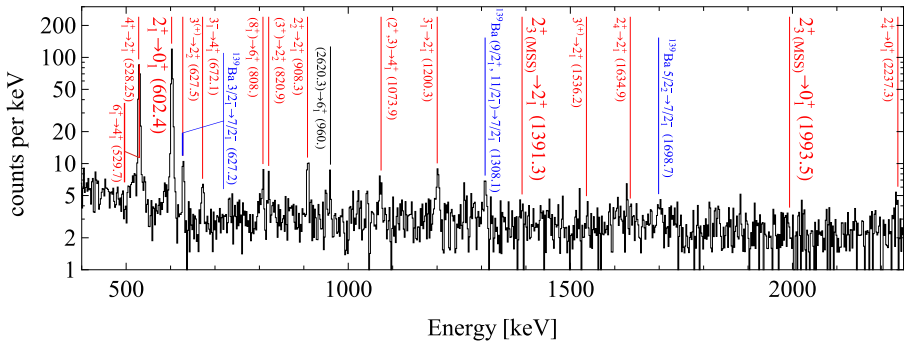


**Figure 6.20.:** Same as in Figure 6.19, but for 500 MeV beam energy. Here, the content of each two neighboring energy-bins was averaged and the spectrum was lifted by one count per keV for better visibility in logarithmic scale. See text for details.

It is apparent from Figure 6.18 that the relative intensity of the decays from excited states of  $^{140}\text{Ba}$  is practically identical for both beam-energies. The intensities of the decays  $2_2^+ \rightarrow 2_1^+$ ,  $3_1^- \rightarrow 2_1^+$  and  $2_{3(MSS)}^+ \rightarrow 2_1^+$  relative to the intensity of the ground-state decay of the  $2_1^+$ -state are shown in Table 6.3 for  $\alpha$ -transfer at both beam-energies and for the population of these states by the fusion-evaporation reaction  $^{12}\text{C}(^{136}\text{Xe}, ^{140}\text{Ba}^*)2\alpha$  at 546 MeV beam energy.

**Table 6.3.:** Intensities of transitions in  $^{140}\text{Ba}$  relative to the  $2_1^+ \rightarrow 0_{gs}^+$  transition. Comparison is made for population of the excited states by  $\alpha$ -transfer at two different beam-energies and population by a fusion-evaporation reaction at 546 MeV beam energy.

	$2_2^+ \rightarrow 2_1^+$	$3_1^- \rightarrow 2_1^+$	$2_{3(MSS)}^+ \rightarrow 2_1^+$
$\alpha$ -transfer, 500 MeV	7.9(14)%	6.5(16)%	2.2(18)%
$\alpha$ -transfer, 546 MeV	7.9(2)%	5.5(2)%	2.3(2)%
fusion-evaporation, 546 MeV	18.1(14)%	6.8(5)%	4.1(6)%

The quantitative analysis confirms that the excitation pattern of the  $\alpha$ -transfer is, within the experimental uncertainties and for the transitions regarded here, independent from beam energy. The excitation pattern by fusion-evaporation is clearly different. This proves that the two different cuts on measured energy of the target-like recoil distinguish two different reaction mechanism populating excited states in  $^{140}\text{Ba}$ .

The third  $2^+$ -state of  $^{140}\text{Ba}$  at 1994 keV excitation-energy is the candidate for the  $2_{MSS}^+$ -state [Ham84]. This is founded on its  $0_{gs}^+/2_1^+$  decay branching ratio of 0.28(2) [Nic07], the small E2/M1 multipole mixing ratio of the  $2_3^+ \rightarrow 2_1^+$  transition of  $+0.18_{-0.06}^{+0.05}$  [Nic07] and the systematics of the energies of  $2_{MSS}^+$ -states in nearby nuclei [Möl14].

The population of this candidate for the  $2_{MSS}^+$ -state of  $^{140}\text{Ba}$ , relative to the population of the  $2_1^+$ -state, is 10.4(10)%. This is about 1/3 of the relative population expected in the work of Alonso *et al.* [Alo08]. In the calculation of this value both decay branches of the  $2_3^+$ -state were considered and feeding of the  $2_1^+$ -state by higher-lying states was accounted for.

Furthermore, also no other  $2^+$ -state below 3 MeV excitation energy was as strongly populated as expected by theory. In consequence, either the predicted strong population of the  $2_{MSS}^+$ -state in  $^{140}\text{Ba}$  by  $\alpha$ -transfer is not correct, or the  $2_{MSS}^+$ -state in

---

$^{140}\text{Ba}$  is strongly fragmented. The latter can basically be excluded, since no other  $2^+$ -states with suitable characteristics at nearby energies have been found [Nic07].

Due to the weak population of the third  $2^+$ -state of  $^{140}\text{Ba}$ , the collected statistics was insufficient for a DSAM measurement of its lifetime. In combination with the known multipole-mixing and branching ratio, the level lifetime would have allowed for the determination of the absolute  $M1$  strength connecting the  $2_3^+$ -state with the  $2_1^+$ -state. Together with an  $E2$  transition strength to the ground state in the order of  $B(E2) \approx 1$  W.u., a strong  $M1$ -transition to the  $2_1^+$ -state in the order of  $B(M1) \approx 1 \mu_N$  is the experimental signature for the mixed-symmetry character of the state [Pie08]. Hence, in order to identify the  $2_{MSS}^+$ -state of  $^{140}\text{Ba}$ , this transition strengths will have to be measured in an upcoming experiment, e.g. by Coulomb excitation at the HIE-ISOLDE facility.

---

#### 6.1.4 caDSAM measurement: Level lifetimes of $^{136}\text{Xe}$

---

For the purpose of lifetime measurements employing the caDSA Method (see Chapter 4), measurements have been performed with a composite target consisting of an excitation layer made of  $0.47\text{ mg/cm}^2$  carbon and a stopping layer made of  $30.6\text{ mg/cm}^2$  tantalum. A thin layer of  $5\text{ }\mu\text{g/cm}^2$  titanium between the carbon and tantalum layers was added for better adhesion. The thickness of the stopping layer was chosen such that the primary beam was stopped in the target, but recoiling target-like ions could penetrate it and be detected in the DSSSD. Measurements with this target have been performed at both beam energies of 500 MeV and 546 MeV.

The following steps were carried out for the caDSAM analysis:

- Data selection and preparation
- Simulation of the excitation and deceleration process
- Description of the experimental setup in APCAD
- Validation of the setup description in APCAD
- Analysis of transitions feeding the excited states of  $^{136}\text{Xe}$  under investigation
- Fit of calculated 2D-lineshapes to the experimental data and extraction of level lifetimes
- Quantification of systematic errors.

These steps are discussed in detail in the following subsections.

---

### 6.1.4.1 Data selection and preparation

---

For the determination of level lifetimes of  $^{136}\text{Xe}$  by the DSAM, the "safe Coulex" criterion (see sections 2.1, 6.1.5.1 and Appendix A) does not have to be obeyed, since it is not required that states of  $^{136}\text{Xe}$  are excited by electromagnetic interaction exclusively. Hence, the full statistics collected at both beam-energies is available for the caDSAM analysis (see Table 6.1).

Data preparation as described in Section 6.1.2 for the thin carbon target was also applied to the data obtained with the thick composite target. Recapitulatory, the main steps of data preparation include

- Correction of radiation-damage of the DSSSD and energy-calibration for each channel,
- Add-back of particle energies measured coincidentally in neighboring channels,
- Reaction channel selection via measured particle energies and scattering angles,
- Reconstruction of the momentum vectors of the excited  $^{136}\text{Xe}$ -ions after the reaction from the kinematics of scattered  $^{12}\text{C}$  target nuclei,
- Random subtraction via particle- $\gamma$  time-differences,
- Extraction of the first interaction points of the  $\gamma$ -ray quanta in AGATA via PSA and tracking.

The parameters defining the setup geometry that have been determined from the observed Doppler-shift in the measurement with the thin target (see Section 6.1.2) are valid also for the measurement with the thick, layered target. The cuts applied to the particle-spectra in order to select reaction channels are shown in Appendix D.1. Events where excited states of  $^{136}\text{Xe}$  were populated are selected by cuts around the particle events corresponding to scattered  $^{12}\text{C}$  target nuclei. These cuts were made spaciuously in order to maximize statistics and in order to avoid any bias on the reaction kinematics. The price for the spaciuous cuts is that the resulting  $\gamma$ -ray spectra are not "clean" on the best possible level, contaminations from competing reactions are present to a certain degree.

For the caDSAM analysis,  $\gamma$ -ray spectra are sorted as a function of  $\gamma$ -ray energy  $E_\gamma$  and polar  $\gamma$ -ray detection angle  $\theta_\gamma$  in the laboratory frame. For the calculation of  $\theta_\gamma$ , the origin is chosen to be in the center of the target at the calculated beam-position. The binning in  $\theta_\gamma$  is chosen such that the Doppler-shifted  $\gamma$ -ray energy  $E'_\gamma$

of the  $2_1^+ \rightarrow 0_1^+$  transition of  $^{136}\text{Xe}$  with  $E_0 = 1313$  keV varies by 3 keV throughout the range of  $\theta_\gamma$  covered in each bin. The resulting bin widths vary from  $\Delta\theta_i \approx 1.7^\circ$  for the polar angles close to  $90^\circ$  to  $\Delta\theta_i \approx 5.5^\circ$  for the very backward angles. This is depicted in Figure 6.21. An efficiency-correction was performed for each angular bin individually using data taken with a standard  $^{152}\text{Eu}$  source at the target position.

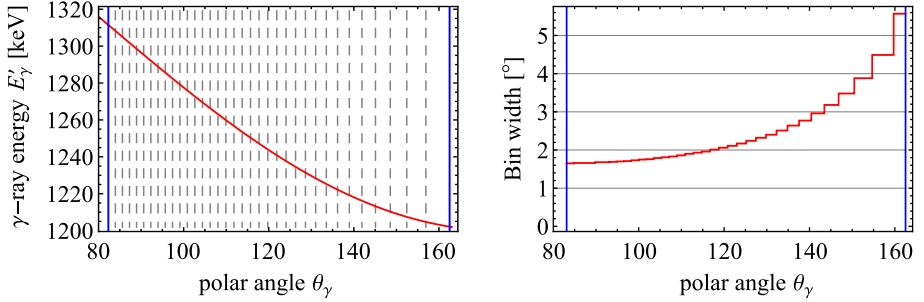


**Figure 6.21.:** Choice of the widths  $\Delta\theta_i$  of the bins of the experimental spectra in polar  $\gamma$ -ray detection angle  $\theta_\gamma$ . The bins are chosen such that the change of the Doppler-shifted  $\gamma$ -ray energy  $E'_\gamma$  of the  $2_1^+ \rightarrow 0_1^+$  transition of  $^{136}\text{Xe}$  with  $E_0 = 1313$  keV is altered by 3 keV throughout the range of  $\theta_\gamma$  covered in each bin. The angular range covered by the AGATA demonstrator is indicated by the blue, vertical lines.

**Left:**  $E'_\gamma$  as a function of  $\theta_\gamma$  (red line). The borders of the angular bins are indicated by vertical, dashed gray lines.

**Right:** Width  $\Delta\theta_i$  of the bins as a function of  $\theta_\gamma$ .

#### 6.1.4.2 Simulation of the excitation and deceleration process

The Coulomb-excitation of  $^{136}\text{Xe}$ -ions on the carbon layer of the composite target and the slowing-down of the excited nuclei in the target was simulated using the software-program StopSim developed within this work (see Appendix B.1). Those velocity-histories were written to file where a Coulomb-excitation reaction occurred in the carbon layer of the target and where the recoiling  $^{12}\text{C}$  target ions had sufficient kinetic energy to leave the target under forward-direction. In the simulations, it is generally assumed that the  $2_1^+$ -state of  $^{136}\text{Xe}$  is excited. This is justified since the reaction kinematic depends only very weakly on the energy of the excited state in the relevant range of scattering angles. A quadrupole moment

---

of zero was assumed for the calculation of the Coulomb-excitation cross section. Hence, the transition matrix element  $\langle 2_1^+ | E2 | 0_1^+ \rangle$  assumed for the calculation of the cross section represents a scaling factor only (see Section 2.1) and has no influence on the energetic and angular distribution of the ions excited throughout the thin carbon layer. Deviations of the experimental excitation cross section from that assumed in the simulation may occur, e.g. due to Coulomb-nuclear interference. These are not relevant for this caDSAM analysis for two reasons:

- Deviations in the energy-dependence of the cross section are negligible, since the energy-loss of the  $^{136}\text{Xe}$ -ions in the thin  $0.47 \text{ mg/cm}^2$  carbon layer is very small, i.e. all excitation happen at approximately the same kinetic energy of the  $^{136}\text{Xe}$ -ions.
- Any deviation in the scattering angle dependence of the cross section is eliminated by selection of ion velocity-histories according to the experimentally observed hit-pattern in the DSSSD as described in Appendix B.2.

Electronic and nuclear stopping powers extracted from the software SRIM [Zie10] were used in StopSim. They are calculated from the semi-empirical model by Ziegler, Biersack and Littmann [Zie85]. The values are plotted for the stopping of  $^{136}\text{Xe}$  in tantalum in Figure 4.3.

Comparison of the SRIM values to experimental data for the stopping of xenon in various materials is shown in Figure 6.22, and for the stopping of various ions in tantalum in Figure 6.23. Unfortunately, no experimental data for the stopping power of tantalum for xenon is available for the energies relevant to this case. The average relative deviation of the SRIM values from experimental data for the stopping of xenon in various materials is 9.8%. This mean relative error is dominated by one experimental data-set for stopping of xenon in lead and by experimental data at energies below 10 keV/u. For the stopping of various ions in tantalum, the mean relative deviation of the values calculated by SRIM from experimental values is 3.8%. In both cases, the relative deviations between experimental data and calculated values are generally largest for ion energies below  $\sim 100 \text{ keV/u}$ . Based on these comparisons, it is estimated that the electronic stopping power of tantalum for xenon provided by SRIM is correct within 5% and the nuclear stopping power within 10%, resembling the higher uncertainty at low beam energies.



---

### 6.1.4.3 Description of the experimental setup in APCAD

---

For modeling the experimental setup of LNL-experiment 09.08 in the software-program APCAD, the following steps were undertaken:

- The range in azimuth angle covered by AGATA in each angular bin is extracted from the experimental hit-pattern of first interaction points (see Figure B.1).
- The DSSSD is implemented as circular particle detector.
- The experimental hit-pattern of the DSSSD is used for further selection of simulated ion velocity-histories.
- The parameters determining the experimental setup, such as distance of the DSSSD from the target, position of the ion-beam on the target etc. (see Section 6.1.2) are entered in APCAD.
- The response function of the  $\gamma$ -ray detectors are fitted for each angular bin to data taken with a standard  $^{152}\text{Eu}$  source at the target position (see Figure 6.24).

The data from the  $^{152}\text{Eu}$  source-measurement was used to fit the detector response function for each angular bin (see Figure 6.24). The response function is described by a main Gaussian component, a low-energy tail and a step-function (see Figure 4.13). The intrinsic energy resolution  $\Delta E$  is assumed to be related to the  $\gamma$ -ray energy  $E_\gamma$  by

$$\Delta E(E_\gamma) = \Delta E_0 + c \sqrt{E_\gamma}. \quad (6.2)$$

$\Delta E_0$ ,  $c$ , the slope and fractional area of the low-energy tail and the height of the step-function are the parameters varied in the fit of the response function. 13 transitions with energies between 344 keV and 2614 keV were included in the fit.

---

### 6.1.4.4 Validation of the setup description in APCAD

---

The validity of the description of the experimental setup in APCAD was checked by fitting the data obtained with the thin carbon target. For this purpose, also for this data  $\gamma$ -ray spectra were sorted as a function of  $\gamma$ -ray energy  $E_\gamma$  and polar  $\gamma$ -ray detection angle  $\theta_\gamma$  using the binning discussed in Section 6.1.4.1. No Doppler correction was applied. The angular correlation in  $\gamma$ -ray polar detection angle  $\theta_\gamma$  and in the particle- $\gamma$  azimuth angle  $\phi$  was included in the fit. Fits to data taken at 500 MeV beam energy are shown in Figure 6.25.

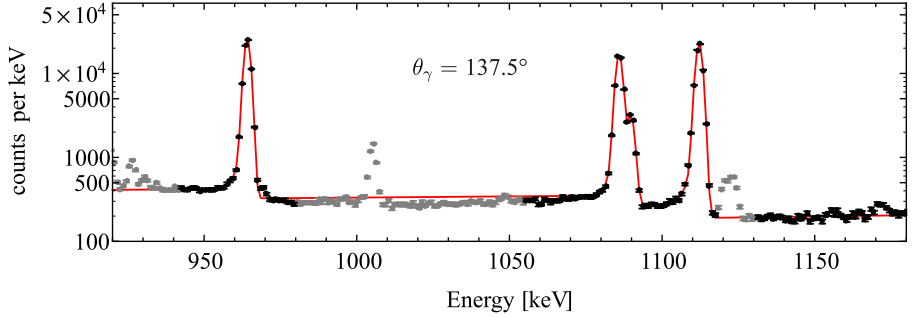


**Figure 6.24.:** Detector response function for the angular bin centered at  $\theta_\gamma = 137.5^\circ$ . At  $E_\gamma \sim 1085$  keV a double-peak structure is visible. The fit to the data (red curve) was performed directly in APCAD. Obtained parameters of the response function for each angular bin were then used in the lineshape-analysis. The data was taken with a standard  $^{152}\text{Eu}$  calibration source. Gray data points were not included in the fit.

At angles  $\theta_\gamma$  in the proximity to  $90^\circ$ , a double-peak structure arises. It is due to the fact that different angles  $\alpha$  between emitter velocity vector and  $\gamma$ -ray emission direction are observed for a given observation angle  $\theta_\gamma$ . Recall that the distribution of ion velocities at the time of  $\gamma$ -ray emission is very narrow in this case, since the data was taken with a thin carbon target. The resulting spread in observed Doppler-shifts at a given angle  $\theta_\gamma$  is therefore only determined by the reaction kinematic, and the shape of the resulting broadened peak is determined by the particle- $\gamma$  angular correlation in the azimuth angle  $\phi$ . The latter is also fitted in APCAD as described in Section 4.3 and Appendix B.2. The widths and tail parameters of the detector response function were not free parameters. They were fixed to the values obtained from the fit to source data.

A very good description of the peak-shapes observed in the measurement with the thin carbon target is achieved consistently for the whole polar-angular range covered by the AGATA demonstrator. Both the observed spread in Doppler-shift and the peak-shapes are well reproduced. The former point proofs that

- (a) the reaction kinematics is properly described,
- (b) the geometry of the AGATA-demonstrator is appropriately accounted for in APCAD and that
- (c) the assumed position resolution of AGATA of 5 mm FWHM reproduces the observed spectra.

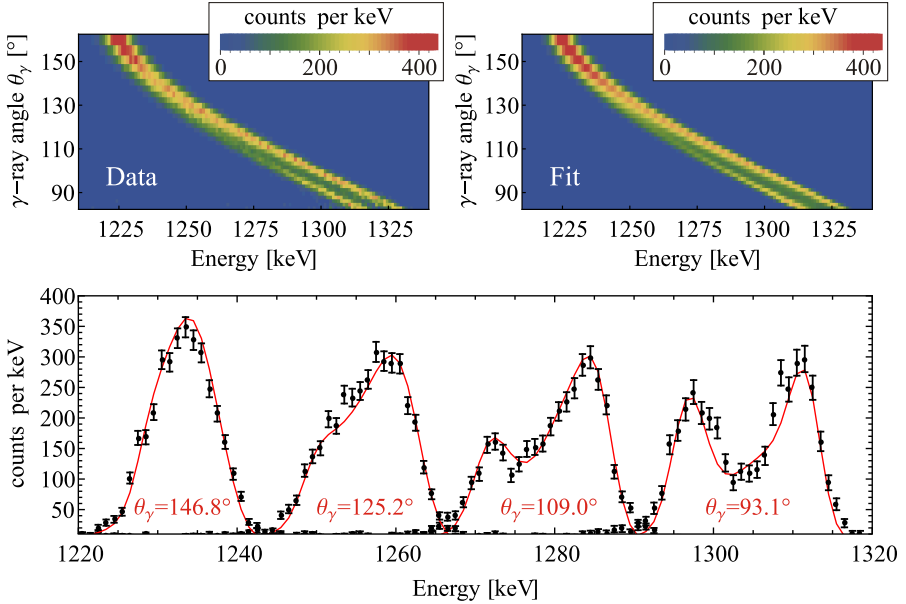


**Figure 6.25.:** Fit to the data measured with 500 MeV beam energy and the thin carbon target. No Doppler correction was applied. **Top:** Data and fit as a function of  $\gamma$ -ray energy  $E_\gamma$  and polar  $\gamma$ -ray detection angle  $\theta_\gamma$ . **Bottom:** Experimental data points (black) and fit (red line), superposed for four angular bins in  $\theta_\gamma$ . See text for details.

The fact that the shapes of the broadened peaks are well reproduced for all observation angles  $\theta_\gamma$  proves that the particle- $\gamma$  angular correlation can be well described in APCAD.

Summarizing the above, the successful reproduction of the broadened  $\gamma$ -ray peak-shapes observed in the measurement with the thin carbon target shows that all effects determining the experimental spectra *except* for lifetime effect stemming from the slowing-down of the ions in a thick target are modeled realistically for the lineshape calculation in APCAD. In particular, the setup of LNL-experiment 08.09 is well described and all effects on the observed Doppler-shifts in  $\gamma$ -ray energy are appropriately accounted for.

---

### 6.1.4.5 Experimental spectra

---

In the  $\gamma$ -ray spectra of  $^{136}\text{Xe}$  taken with the spectra measured with the thick, layered target, only the transitions  $2_1^+ \rightarrow 0_1^+$  at 1313 keV and  $3_1^- \rightarrow 2_1^+$  at 1962 keV show a Doppler-broadened lineshape that is sufficiently pronounced for a DSAM analysis. For the  $2_1^+ \rightarrow 0_1^+$  transition, the spectra are shown as a function of  $\gamma$ -ray energy  $E_\gamma$  and polar  $\gamma$ -ray detection angle  $\theta_\gamma$  in Figure 6.26 for the runs with 500 MeV beam energy and in Figure 6.27 for the runs with 546 MeV beam energy.

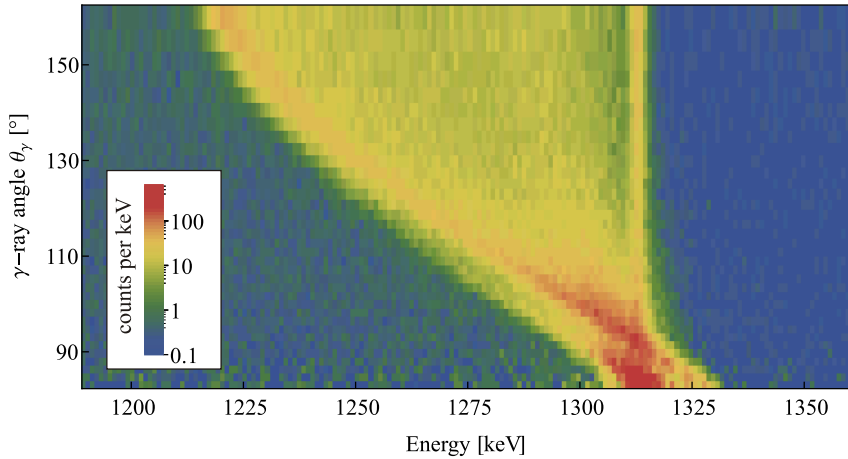


**Figure 6.26.:** Doppler-broadened  $\gamma$ -ray lineshape of the 1313 keV  $2_1^+ \rightarrow 0_1^+$  transition of  $^{136}\text{Xe}$ . Data is shown for the runs at 500 MeV beam energy and irradiation of a composite target with a  $0.47 \text{ mg/cm}^2$  carbon layer where the  $^{136}\text{Xe}$ -ions were excited, backed by a stopping layer made of  $30.6 \text{ mg/cm}^2$  tantalum. The spectrum is shown as a function of  $\gamma$ -ray energy  $E_\gamma$  and polar  $\gamma$ -ray detection angle  $\theta_\gamma$ . See text for details.

At 500 MeV beam energy, the spectrum is very clean. No significant contamination of the pronounced Doppler-broadened lineshape of the 1313 keV  $2_1^+ \rightarrow 0_1^+$  transition of  $^{136}\text{Xe}$  is visible in Figure 6.26. In contrast, the lineshape obtained at 546 MeV beam energy is clearly contaminated by transitions at 1273 keV and 1308 keV. These transitions do not possess a Doppler-broadened lineshape. Hence, they are decays of states that are long-lived on the scale of the slowing-down process of the excited nuclei in the thick target. The 1273 keV transition is the ground-state decay of a known state at 1273 keV excitation energy in  $^{137}\text{Cs}$  with unknown spin and parity [Bro07]. The transition at 1308 keV is the ground-state decay of

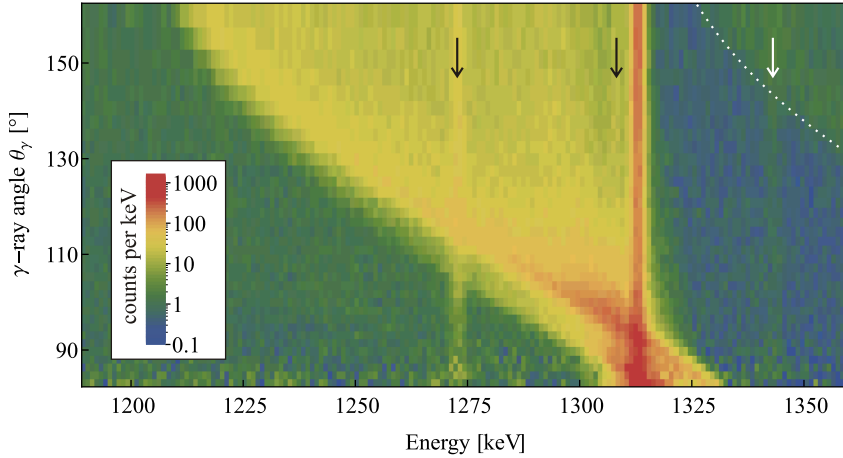


**Figure 6.27.:** Same as in Figure 6.26, but for the runs at 546 MeV beam energy. The arrows mark contaminant transitions of other nuclei than  $^{136}\text{Xe}$ . The dotted, white line marks the Doppler-broadened lineshape of the 1436 keV  $2_1^+ \rightarrow 0_1^+$  transition of  $^{138}\text{Ba}$ . See text for details.

a  $(\frac{9}{2}^+, \frac{11}{2}^-)$ -state of  $^{139}\text{Ba}$  [Bur01]. Also visible in Figure 6.27 is a transition at 1344 keV, which also does not possess a pronounced Doppler-broadened lineshape. This is the  $4_4^+ \rightarrow 2_1^+$  transition of  $^{138}\text{Ba}$  [Son02]. The  $2_1^+ \rightarrow 0_1^+$  transition of  $^{138}\text{Ba}$  at 1436 keV [Son02] is also visible in the spectrum. The  $2_1^+$ -state of  $^{138}\text{Ba}$  is short-lived with a lifetime of 291(12) fs [Ram01]. Therefore, its ground-state transition exhibits a pronounced Doppler-broadened lineshape, which is marked by the white dotted line for the most backward angles in Figure 6.27.

---

#### 6.1.4.6 Feeding of the $2_1^+$ -state of $^{136}\text{Xe}$

---

The data taken with the thin carbon target is also useful to assess the feeding of the states that are to be investigated on in the caDSAM analysis, i.e. the  $2_1^+$  and the  $3_1^-$ -states of  $^{136}\text{Xe}$ . Inspection of  $\gamma$ - $\gamma$  coincidences shows that the  $3_1^-$ -state is populated exclusively directly, while the  $2_1^+$ -state is fed by several transitions. An energy spectrum gated on the  $2_1^+ \rightarrow 0_1^+$  transition is shown for the data taken with the thin carbon target at 546 MeV beam energy in Figure 6.28. In this coincidence spectrum, eight transitions are visible. The transitions directly feeding the  $2_1^+$ -state and the relative populations of the  $2_1^+$ -state by these transitions are listed in Table 6.4. The transitions that are marked by blue lines are accounted for directly in the caDSAM

**Table 6.4.:** Direct feeders of the  $2_1^+$ -state of  $^{136}\text{Xe}$ . The feeding intensities denote the relative populations of the  $2_1^+$ -state by the respective transition. Feeding intensities that are determined from  $\gamma - \gamma$  coincidence data measured with the thin carbon target were obtained by normalizing the observed peak area in the coincidence spectra to one observed for the  $3_1^- \rightarrow 2_1^+$  transition in the same spectrum. The feeding intensity of the latter transition was determined directly in the lineshape fit in APCAD from relative peak areas and include the efficiency correction.

transition	energy	feeding intensity [%]		determined by
		546 MeV	500 MeV	
$4_1^+ \rightarrow 2_1^+$	381 keV	5.54(2)%	0.62(2)%	DSAM fit
$4_2^+ \rightarrow 2_1^+$	813 keV	0.99(2)%	0.27(2)%	DSAM fit
$2_2^+ \rightarrow 2_1^+$	977 keV	0.64(8)%	0.2(1)%	$\gamma - \gamma$ coinc. data
$2_3^+ \rightarrow 2_1^+$	1101 keV	0.36(6)%	0.14(8)%	$\gamma - \gamma$ coinc. data
$4_4^+ \rightarrow 2_1^+$	1247 keV	0.21(6)%	0.06(6)%	$\gamma - \gamma$ coinc. data
$2_7^+ \rightarrow 2_1^+$	1666 keV	0.32(7)%	0.05(5)%	$\gamma - \gamma$ coinc. data
$3_1^- \rightarrow 2_1^+$	1962 keV	5.77(4)%	0.57(2)%	DSAM fit
unobserved (long lived)		2.35(7)%	1.55(6)%	DSAM fit

analysis by fitting their peaks/lineshapes simultaneously to the lineshape of the  $2_1^+ \rightarrow 0_1^+$ -transition. They are treated as direct feeders of the  $2_1^+$ -state. Only the  $3_1^-$ -state has a lifetime short enough to result in a Doppler-broadened  $\gamma$ -ray lineshape. The other two transitions appear as stopped peaks in the spectrum measured with the thick, layered target. Obviously, these transitions occur after the emitting  $^{136}\text{Xe}$ -ions have come to rest in the tantalum layer. Therefore, also the subsequent decays of the  $2_1^+$ -state occur at rest and the corresponding  $\gamma$ -rays contribute to the "stop peak" at  $E_0 = 1313$  keV.

The other transitions feeding the  $2_1^+$ -state that are shown in Figure 6.28 are not included in the fit explicitly, since these transitions are too weak for an analysis in the data taken with the thick, layered target. This originates in the lower statistics collected with the thick target compared to the thin carbon target on one hand (see Table 6.1), on the other hand short lifetimes of the associated states may result in Doppler-broadened lineshapes that lower the signal-to-noise ratio drastically as compared to the measurement with the thin target. Based on the analysis of  $\gamma - \gamma$  coincidences measured with the thin target, it is expected that these transitions feed the  $2_1^+$ -state to a fraction of 1.5(1)%. Their influence on the obtained  $2_1^+$  level lifetime will be accounted for in the systematic error of the lifetime discussed in

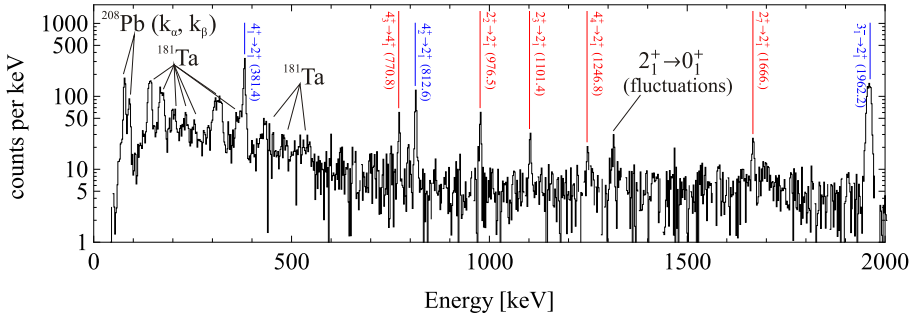


**Figure 6.28.:**  $\gamma$ -ray-spectrum gated on the  $2_1^+ \rightarrow 0_1^+$  transition of  $^{136}\text{Xe}$ . The data was taken at 546 MeV beam energy and with the thin carbon target. Transitions in  $^{181}\text{Ta}$  stem from excitations in the beam dump made of tantalum. These  $\gamma$ -rays are emitted from nuclei at rest. Consequently, they are strongly broadened after Doppler correction. The lead x-rays are emitted from the shielding mounted in front of the  $\gamma$ -ray-detectors. Transitions feeding the  $2_1^+$ -state of  $^{136}\text{Xe}$  are marked. The transitions with blue labels are taken into account explicitly in the fit of the  $2_1^+ \rightarrow 0_1^+$  lineshape in APCAD for both beam energies of 546 MeV and 500 MeV. See text for details.

Section 6.1.4.10. The 771 keV  $4_3^+ \rightarrow 4_1^+$  transition is not included in these considerations, since it decays to the  $4_1^+$ -state and is therefore accounted for in the fit via the transition  $4_1^+ \rightarrow 2_1^+$ . Additional feeding by unobserved transitions is allowed during the fit by contributions to the stop-peak only, i.e. for feeding from long-lived states. These events make up 2.35(7)% of the population of the  $2_1^+$ -state as extracted from the lineshape fit.

In the measurement at 500 MeV beam energy, population of higher-lying states is reduced compared to the measurements at 546 MeV beam energy due to the lower beam energy. Direct feeders of the  $2_1^+$ -state of  $^{136}\text{Xe}$  and their intensities at 500 MeV beam energy are also listed in Table 6.4. Direct feeding of the  $2_1^+$ -state is taken into account by simultaneous fit via the same transitions as in the case of 546 MeV beam energy. Feeding via the other transitions shown in Figure 6.28 that are not explicitly accounted for in the fit is estimated to be 0.44(15)%, based on the analysis of  $\gamma - \gamma$  coincidence data taken with the thin carbon target. Contributions to the stop peak by unobserved feeding from long-lived states amount to 1.55(6)% as extracted from the lineshape fit.

---

### 6.1.4.7 Fit to the data taken at 546 MeV beam energy

---

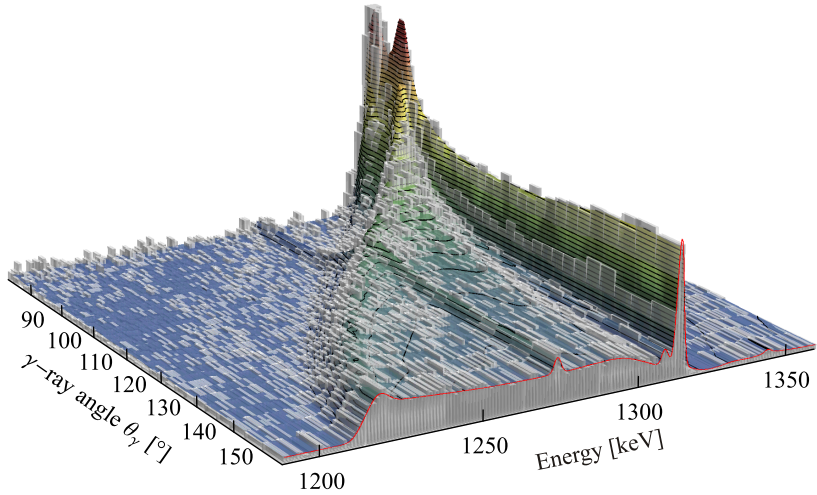


**Figure 6.29.:** Doppler-broadened lineshape of the  $2_1^+ \rightarrow 0_1^+$  transition of  $^{136}\text{Xe}$  observed with the composite target at 546 MeV beam energy (gray bars). The smooth, colored surface represents the best fit to the data obtained with APCAD. See text for details.

The two-dimensional fit to the data taken at 546 MeV beam energy performed in APCAD is shown together with the data in Figure 6.29. One-dimensional spectra are shown for several angular bins in Figure 6.30 for a better assessment of the quality of the fit. The aforementioned contaminant transitions are fitted along with the lineshape of the  $2_1^+ \rightarrow 0_1^+$  transition of  $^{136}\text{Xe}$ . A very good agreement between the fit and the data is obtained for the complete angular range covered by the AGATA-demonstrator in this experiment. The quality of the fit is quantified by a very good reduced  $\chi^2$ -value of  $\chi^2/\text{ndf} = 1.17$ .

The Doppler-broadened lineshape of the  $2_1^+ \rightarrow 0_1^+$ , 1436 keV transition of  $^{138}\text{Ba}$  slightly overlaps that of the  $2_1^+ \rightarrow 0_1^+$  transition of  $^{136}\text{Xe}$  at very backward angles. Therefore, also the lineshape of the  $2_1^+ \rightarrow 0_1^+$  transition of  $^{138}\text{Ba}$  was fitted. The kinematics of the excited  $^{136}\text{Xe}$  and  $^{138}\text{Ba}$  nuclei are very similar. Therefore, the stopping-Matrix calculated for  $^{136}\text{Xe}$  could be used also to qualitatively describe the lineshape of the  $2_1^+ \rightarrow 0_1^+$  transition of  $^{138}\text{Ba}$ . Of course, the stopping powers of the target materials are different for Xe and Ba nuclei. Therefore, the lifetime

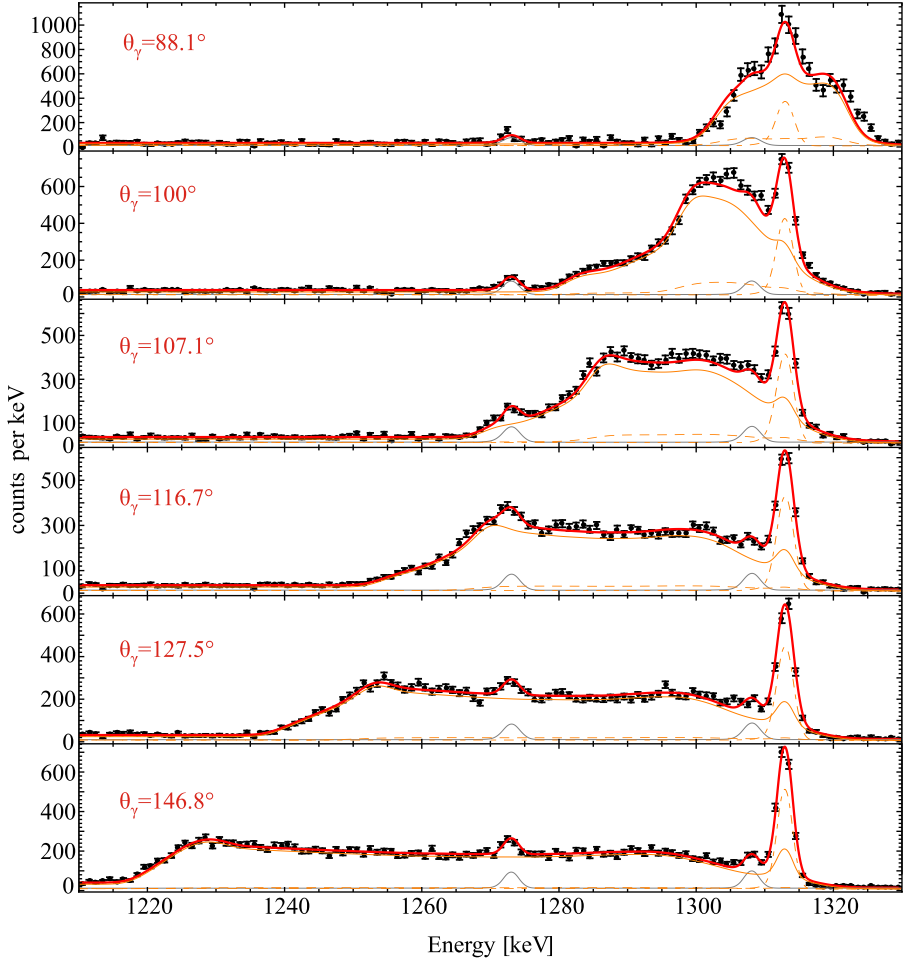


**Figure 6.30.:** Doppler-broadened lineshape of the  $2_1^+ \rightarrow 0_1^+$  transition of  $^{136}\text{Xe}$  observed with the composite target at 546 MeV beam energy. The thick, red line shows the full fit. The fraction of decays that stem from direct population of the  $2_1^+$ -state are drawn as solid, orange line. The fraction of events stemming from population of the  $2_1^+$ -state via the decay of the short-lived  $3_1^-$  state are drawn as orange, dashed lines. Events connected to feeding from long-lived states are drawn as orange, dashed-dotted line. Contaminants are drawn in gray. See text for details.

used in APCAD to describe the lineshape of the Ba-transitions is not realistic. The aim of fitting the lineshape of the  $2_1^+ \rightarrow 0_1^+$  transition of  $^{138}\text{Ba}$  was solely to obtain a qualitative description of the spectrum in proximity to the  $2_1^+ \rightarrow 0_1^+$  transition of  $^{136}\text{Xe}$  at the very backward angles. A realistic fit of the lineshapes of the transitions in  $^{138}\text{Ba}$  would make a nice project for an upcoming Bachelor's or Master's thesis.

The fit of the Doppler-broadened lineshape corresponding to the  $3_1^- \rightarrow 2_1^+$  transition of  $^{136}\text{Xe}$  is shown in Figure 6.31. The level lifetimes obtained from the fit are given in Chapter 6.1.4.9.

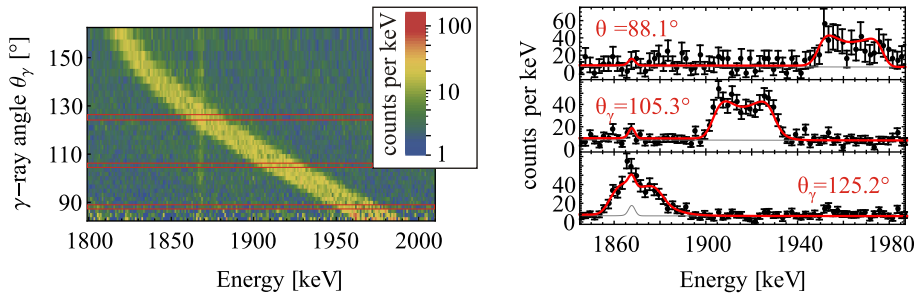


**Figure 6.31.:** Doppler-broadened lineshape of the  $3_1^- \rightarrow 2_1^+$  transition of  $^{136}\text{Xe}$  observed with the composite target at 546 MeV beam energy.

**Left:** Experimental spectrum as a function of  $\gamma$ -ray energy  $E_\gamma$  and polar  $\gamma$ -ray detection angle  $\theta_\gamma$ .

**Right:** Data and fit for three angular bins. These angular bins are marked by red boxes on the left-hand side. Only every second data point is shown for better visibility. The thick, red line shows the full fit. The contaminant peak (gray line) at 1868 keV is the  $9/2_1^- \rightarrow 7/2_1^+$  transition of  $^{137}\text{Cs}$ . See text for details.

#### 6.1.4.8 Fit to the data taken at 500 MeV beam energy

The fits to the data taken at 500 MeV beam energy resulted in an unsatisfying description of the experimental values in the first place. The most Doppler-shifted part of the calculated lineshape was not in accordance with the experimentally observed spectra. With the known thicknesses of the layers of the composite target that were also successfully used in the fit of the data taken at 546 MeV beam energy, a lack of events at maximum Doppler-shift was observed in the fitted function. This is shown on the left-hand side of Figure 6.32.

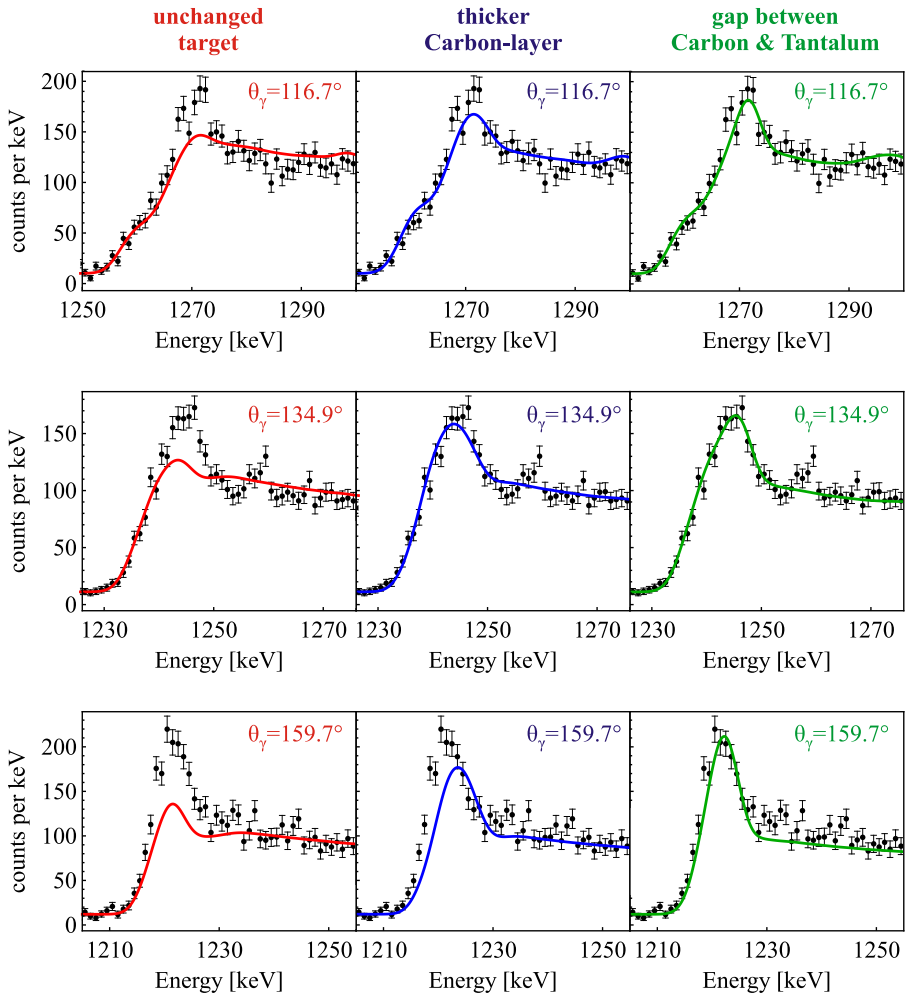


**Figure 6.32.:** Best fits to the Doppler-broadened  $\gamma$ -ray lineshapes measured at 500 MeV beam energy. Spectra and fits are shown for three different angular bins (rows) and different assumptions for the composite target (columns).

**Left column:** Fit assuming the reported thicknesses of the target layer, no gaps.

**Middle column:** Fit assuming a thickness of the carbon layer of  $0.9 \text{ mg/cm}^2$ .

**Right column:** Fit assuming a homogeneous gap of  $0.9 \text{ }\mu\text{m}$  thickness between the carbon and the tantalum layer of the target. See text for details.

---

An accumulation of events at maximum shift can originate in a very strong feeding from a shorter-lived state. This can be excluded from inspection of  $\gamma$ - $\gamma$  coincidence data by gating on the  $2_1^+ \rightarrow 0_1^+$  transition - there is no strong feeding of the  $2_1^+$ -state of  $^{136}\text{Xe}$ . Such a strong feeding would have been present also at the higher beam energy of 546 MeV, which was not observed.

Alternatively, it could be the case that in fact the carbon layer of the target is thicker than assumed. This may have not been recognized at the higher beam energy due to a stronger feeding from a longer-lived state than at the lower beam energy. Again, such a feeding can be excluded from analysis of the  $\gamma$ - $\gamma$  coincidence data, gated on the  $2_1^+ \rightarrow 0_1^+$  transition. Nevertheless, fits have been performed assuming a thickness of the carbon layer of  $0.9 \text{ mg/cm}^2$  instead of the reported  $0.47 \text{ mg/cm}^2$ . They are shown in the central plot of Figure 6.32. The thickness was chosen such that the lineshape was reproduced at several angular bins (e.g. for the angular bin centered at  $\theta_\gamma = 134.9^\circ$  shown in the middle of Figure 6.32). It was, however, not possible to achieve a satisfactory description of the Doppler-broadened  $\gamma$ -ray lineshape of the  $2_1^+ \rightarrow 0_1^+$  transition at *all* angular bins covered by the  $\gamma$ -ray detector.

A consistent description of the lineshape at *all* angular bins covered by the  $\gamma$ -ray detector was achieved by assuming a gap of  $0.9 \text{ }\mu\text{m}$  thickness between the carbon and the tantalum layer of the target. Fits under this assumption are shown on the right-hand side of Figure 6.32. Such a de-lamination of the target layers is indeed conceivable. The target was mounted electrically isolated for the purpose of measuring the beam current. Therefore, heat-transport out of the target may have been poor and irradiation at 546 MeV beam energy may have heated the target significantly. After the run with the layered target at 546 MeV, the beam energy was reduced to 500 MeV and the measurement was continued with the thin carbon target before switching to the layered target, again. During this measurement with the thin carbon target, the layered target cooled down, and thermal stress may have caused a de-lamination of the carbon layer. The data taken with the layered target at 546 MeV beam energy do not show any hint for such a de-lamination, also not at the end of the measurement.

It can, however, not be expected that a potential de-lamination of the carbon layer occurred spatially homogeneous. Therefore, it has to be assumed that the layered target was inhomogeneous during the run with 500 MeV beam energy. The thickness of the gap of  $0.9 \text{ }\mu\text{m}$  reproducing the data has to be considered as an average or effective value. For the  $2_1^+ \rightarrow 0_1^+$  transition of  $^{136}\text{Xe}$ , the effect on the deduced level lifetime is not expected to be dramatic. This is because here, the sensitivity to the level lifetime is mainly given by the evolution of the part of the lineshape that stems from decays while the emitting ions slow down in the thick

tantalum layer. Indeed, under the assumption of the 0.9  $\mu\text{m}$  thick gap between the carbon and the tantalum layer, the lifetime obtained from the run at 546 MeV beam energy is very well reproduced within the very small statistical uncertainties (see the following Chapter 6.1.4.9). In contrast, for the very short lifetime of the  $3_1^-$ -state of  $^{136}\text{Xe}$ , most decays occur already in the carbon layer or shortly after the excited nuclei have left it. A gap between the carbon and tantalum layer therefore significantly affects the obtained level lifetime. Given the fact that the exact geometry of the de-laminated carbon layer is unknown, the level lifetime of the  $3_1^-$ -state obtained from the DSAM-run at 500 MeV beam energy is not trustworthy.

Despite the potentially de-laminated carbon layer of the target, a very good description of the experimental data taken at 500 MeV beam energy has been achieved. This is quantified by a reduced  $\chi^2$ -value of  $\chi^2/\text{ndf} = 1.00$ .

---

#### 6.1.4.9 Results for the level lifetimes

---

The lifetimes obtained for the  $2_1^+$  and  $3_1^-$ -states of  $^{136}\text{Xe}$  are listed in Table 6.5. Because of the issue of possible de-lamination of the carbon layer in the measurement with the composite target at 500 MeV beam energy, the lifetimes measured at 546 MeV beam energy are quoted as final level lifetimes obtained in this work. For comparison, also the values obtained at 500 MeV beam energy under the assumption of a homogeneous, 0.9  $\mu\text{m}$  thick gap between the carbon and the tantalum layer of the composite target are given in parentheses.

The uncertainties of the results are discussed in the following section. The systematic uncertainties include the uncertainty of the stopping powers employed in the calculation of the lineshapes and effects from possible unobserved feeding of the  $2_1^+$ -state of  $^{136}\text{Xe}$ .

**Table 6.5.:** Results for the  $2_1^+$  and  $3_1^-$  level lifetimes of  $^{136}\text{Xe}$  from the caDSAM analysis. The values for 500 MeV beam energy are given for reference only, since the measurement was impaired by a presumed de-lamination of the carbon target layer (see Sections 6.1.4.8 and 6.1.4.10).

beam energy	$2_1^+$ level lifetime $\tau_{2_1^+}$ [fs]	$3_1^-$ level lifetime $\tau_{3_1^-}$ [fs]
546 MeV	$524.3^{+2.2}_{-1.4}(\text{stat})^{+26.6}_{-24.8}(\text{sys})$	$43.8 \pm 1.6(\text{stat})^{+1.7}_{-1.8}(\text{sys})$
500 MeV	$(523.7 \pm 2.1(\text{stat})^{+17.2}_{-19.9}(\text{sys}))$	$(60 \pm 13(\text{stat})^{+0}_{-2}(\text{sys}))$

---

### 6.1.4.10 Uncertainties of the obtained level lifetimes

---

The statistical uncertainty of the level lifetimes of  $^{136}\text{Xe}$  obtained from the fit of Doppler-broadened  $\gamma$ -ray lineshapes in APCAD is inferred using the MINOS-routine of the MINUIT minimization package [Jam75, Jam94]. It performs an analysis of the  $\chi^2$ -surface in the space of the free fit-parameters and accounts for the correlation of fit-parameters in the assessment of statistical uncertainties.

There are generally at least two sources of systematic uncertainties in the analysis of Doppler-broadened  $\gamma$ -ray spectra:

- Uncertainty of the stopping power of the target materials for the beam ions and excited reaction products and
- Incomplete knowledge of the feeding of the levels under investigation.

The first point is discussed in Section 6.1.4.2. The stopping power of the materials employed in the layered target, i.e. carbon and tantalum, for  $^{136}\text{Xe}$ -ions are assumed to be calculated correct by SRIM within 5% for the electronic stopping and 10% for the nuclear stopping. Fits of the experimental spectra have been performed with stopping-Matrices derived from simulations where the electronic and nuclear stopping powers were scaled by  $\pm 5\%$  and  $\pm 10\%$ , respectively. The deviations of the level lifetimes obtained in these fits from the value obtained with un-scaled stopping powers is used as systematic error stemming from the employed stopping powers.

The second point, feeding of the nuclear states under investigation, is discussed in Section 6.1.4.6. It is inferred from inspection of  $\gamma - \gamma$  coincidence data gated on the  $2_1^+ \rightarrow 0_1^+$  transition of  $^{136}\text{Xe}$  that unobserved feeding is responsible for 1.5(1)% of the populations of the  $2_1^+$ -state at 546 MeV beam energy and for 0.44(15)% of the populations at 500 MeV beam energy. The strongest influence on the obtained level lifetime of the  $2_1^+$ -state is given if a lifetime of a feeding state of  $\sim 700$  fs is assumed. At 500 MeV beam energy, this scenario results in a reduction of the  $2_1^+$  level lifetime by 2.4 fs, at 546 MeV beam energy in a reduction by 9 fs. These values are taken as systematic errors stemming from unobserved feeding. They represent a "worst case scenario", since all feeding that occurs after the ions have come to rest is accounted for in the fits (see discussion in Section 6.1.4.6).

Due to the possible de-lamination of the carbon layer of the composite target, the lifetimes obtained from fit to the data taken at 500 MeV may be tainted with another systematic error. This error is hard to quantify reliably, since the effect of the de-lamination depends on the actual geometry of the de-laminated layer. This af-

---

fects the lifetimes of the  $3_1^-$ -state of  $^{136}\text{Xe}$  in particular. However, the uncertainties of the lifetimes obtained at 546 MeV beam energy are strongly dominated by the uncertainty of the employed stopping powers. Since the same stopping powers are the source of systematic errors for the run at 500 MeV, the systematic uncertainty of an averaged result from data taken at both beam-energies would not be reduced compared to the individual uncertainties. Only the very small statistical uncertainties would reduce by averaging the results. Consequently also a reliable result from the analysis of data taken at 500 MeV beam energy would not appreciably reduce the uncertainty of final, averaged values of the lifetimes.

---

## 6.1.5 Coulex analysis: Transition strengths in $^{136}\text{Xe}$

---

Precise values for the level lifetimes of the  $2_1^+$ - and  $3_1^-$ -state of  $^{136}\text{Xe}$  were obtained by the caDSA Method as discussed in the previous section. Using the data collected with the thin carbon target, transition strengths of further transitions can be obtained by analysis of Coulomb excitation yields, relative to the yield observed for the  $2_1^+ \rightarrow 0_1^+$  transition. Transition strengths of all decays of the  $2_i^+$ -states with  $i = 1, 2, 3, 6, 7$  and the  $3_1^-$ -state of  $^{136}\text{Xe}$  were obtained, and limits on the transition strengths of the decays of the  $2_{4,5}^+$ -states were determined. The data selection, extraction of transition strengths and the results are discussed in the following sub-sections.

---

### 6.1.5.1 Data selection and determination of peak areas

---

The experiment focused on the  $\alpha$ -transfer reaction populating excited states in  $^{140}\text{Ba}$ . It is expected that the  $\alpha$ -transfer occurs predominantly at beam energies close to the Coulomb barrier, where projectile and target nuclei are in close proximity (see introduction of Section 6.1). Consequently, the conditions for "safe" Coulomb excitation (see Appendix A) are not always satisfied. The distance between the centers of target and beam nuclei as a function of the center-of-mass scattering angle is plotted for both beam energies of 500 and 546 MeV in Figure 6.33. The minimum distances of closest approach for "safe" Coulomb excitation and the corresponding scattering angles for the "safe" Coulomb excitation criteria of Cline and Wollersheim (see Appendix A) are summarized in Table 6.6.

For 546 MeV beam energy, Cline's criterion for "safe" Coulomb excitation is not fulfilled for any scattering angle covered by the DSSSD, whereas according to Wollersheim's criterion, "safe" Coulomb excitation is given for center-of-mass scattering angles below  $86.9^\circ$ . For 500 MeV beam energy, Cline's criterion is fulfilled for center-of-mass scattering angles below  $84.8^\circ$  and Wollersheim's criterion for angles below  $106.5^\circ$ .

For this Coulex analysis, the more restrictive criterion of Cline was applied. This also accounts for the observation that for very light reaction partners such as carbon, the additional safe distance in Wollersheim's approach should be in the order of 7 fm, in contrast to the value of 5 fm value for heavier systems [Wol92]. The respective maximum center-of-mass scattering angle of  $84.8^\circ$  corresponds to a minimum laboratory scattering angle of the  $^{12}\text{C}$  target-like recoil of  $47.0^\circ$  at 500 MeV beam energy.

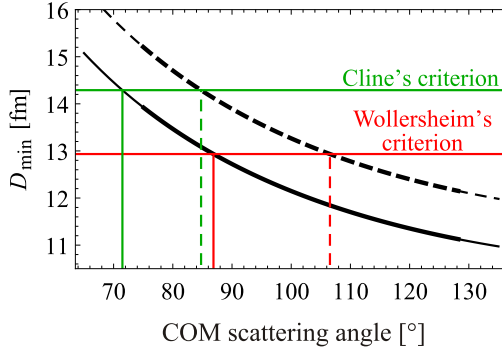


**Figure 6.33.:** Distance of closest approach between the centers of  $^{12}\text{C}$  target and  $^{136}\text{Xe}$  beam nuclei as a function of center-of-mass scattering angle for beam energies of 500 MeV (dashed black line) and 546 MeV (solid black line). The scattering angles covered by the DSSSD are drawn bold. The green horizontal line indicates the “safe” distance according to Cline’s criterion (Eq. A.5 with  $d_{extra} = 5$  fm). The red horizontal line corresponds to the “safe” distance according to Wollersheim’s criterion (Eq. A.6). The colored, vertical lines indicate the corresponding center-of-mass scattering angles. See text for details.

Figure 6.34 shows a  $\gamma$ -ray energy spectrum from the run at 546 MeV beam energy. A gate in the particle energy spectrum was applied in order to select events where  $^{136}\text{Xe}$  was excited in the reaction  $^{12}\text{C}(^{136}\text{Xe}, ^{136}\text{Xe}^*)^{12}\text{C}$ . This was done by setting a gate on scattered  $^{12}\text{C}$  nuclei registered in the DSSSD (see Fig. 6.9 and Section D.1). Since the criterion for “safe” Coulomb excitation is not fulfilled at this beam energy, also nuclear interactions may contribute to the excitation of  $^{136}\text{Xe}$ . The spectrum is dominated by decays of Coulomb excited states of  $^{136}\text{Xe}$ . However, various “contaminant” peaks from other reactions are present in the spectrum. This stems from an imperfect reaction channel selection, since the different reaction channels can not be clearly distinguished in the particle spectra especially at small scattering angles (see Fig. 6.7 and the plots in Appendix D.1).

The spectrum measured at 500 MeV beam energy with the events satisfying the condition for “safe” Coulomb excitation as defined in the Cline criterion is shown in Figure 6.35. In comparison to the spectra taken at 546 MeV beam energy (Fig. 6.34), the contamination by additional reactions is strongly reduced. Also, the relative population of different excited states varies with respect to the 546 MeV case, since the Coulomb excitation amplitudes depend on the beam energy and scatter-

**Table 6.6.:** Minimum distance of closest approach for "safe" Coulomb excitation and corresponding scattering angles in the center-of-mass system (COM) and for the target-like recoil  $^{12}\text{C}$  in the laboratory frame. See text for details.

Criterion by	546 MeV		500 MeV		$D_{safe}$ [fm]
	$\theta_{COM}$ [°]	$\theta_{lab}$ [°]	$\theta_{COM}$ [°]	$\theta_{lab}$ [°]	
Cline	71.5	53.6	84.8	47.0	14.3
Wollersheim	86.9	46.0	106.5	36.3	12.9

ing angle (see Section 2.1). However, also Coulomb-nuclear interference occurring at the higher beam energy may be partly responsible for the difference in relative population of excited states at "safe" conditions and at 546 MeV beam energy.

Because the run at 546 MeV beam energy was significantly longer than the one at 500 MeV beam energy (see Table 6.1) and the limit on the scattering angle excludes a large part of the data at 500 MeV beam energy, only about 1.6% of the recorded events<sup>3</sup> match the "safe" Coulomb excitation criterion. Nevertheless, several transition strengths could be determined from observed peak areas also with this fraction of the total statistics. All peak areas have been determined by integrating the spectrum over a suitable energy range and subtracting a background fitted to the data in proximity of the respective peaks. Their uncertainties were determined from the uncertainties of the bin contents that were summed up and the fluctuations of the fitted background in these bins. The latter was estimated from the square-root of the background-level in the summed bins. The uncertainties of the bin contents of course account for the random subtraction and the efficiency correction.

All determined peaks areas and limits on peak areas are listed in table 6.7. The upper limits on peak areas observed for the "safe" Coulex condition and the values for the runs at 546 MeV beam energy were used for the determination of limits on transition strengths where the statistics of the data satisfying the "safe" Coulex condition was insufficient (see Section 6.1.5.3).

<sup>3</sup> in terms of observed intensity of the  $2_1^+ \rightarrow 0_{gs}^+$  transition of  $^{136}\text{Xe}$

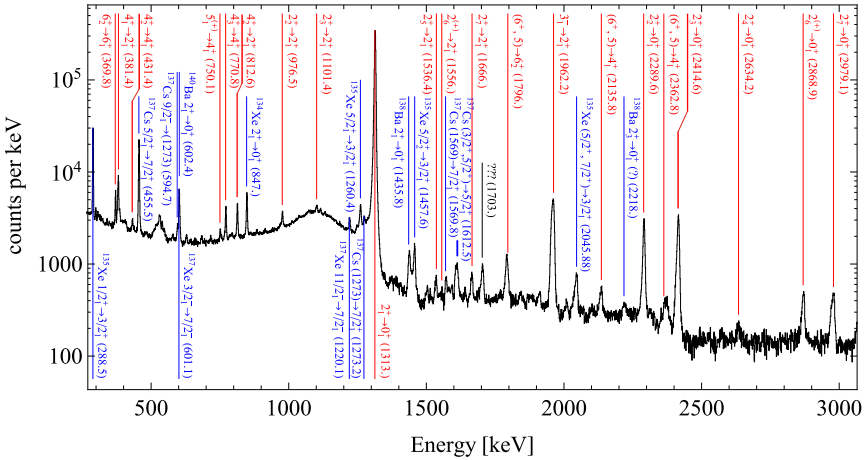


**Figure 6.34.:** Particle-gated  $\gamma$ -ray energy spectrum measured with the thin carbon target at 546 MeV beam energy. Events with  $^{12}\text{C}$  ions detected in the DSSSD were selected. Identified transitions in  $^{136}\text{Xe}$  are marked in red, contaminant transitions in other nuclei are marked in blue. See text for details.

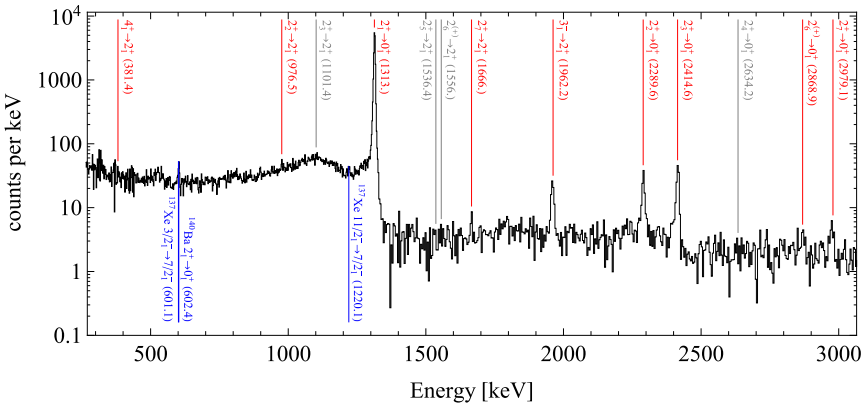


**Figure 6.35.:** Same as in Figure 6.34, but for the run at 500 MeV beam energy and after the application of the "safe" Coulomb excitation criterion. The transitions marked in red were used in the Coulex analysis. In this figure, events in each two neighboring bins were averaged below  $E_{\gamma}=1313$  keV, and events in each four neighboring bins were averaged above  $E_{\gamma}=1313$  keV for better visibility. See text for details.

**Table 6.7.:** Peak areas determined for the Coulex analysis of  $^{136}\text{Xe}$ . The transition energies and relative intensities are taken from [Son02]. “—” means transition was not observed.

transition	energy [keV]	peak area		relative intensity [%]
		500 MeV ”safe” Coulex	546 MeV $\theta_p^{lab} > 42^\circ$	
$2_1^+ \rightarrow 0_1^+$	1313.0	34,448(197)	978,086(1,065)	100
$4_1^+ \rightarrow 2_1^+$	381.4	<80	2,959(227)	100
$2_2^+ \rightarrow 0_1^+$	2289.6	366(23)	12,083(179)	100(5)
$2_2^+ \rightarrow 2_1^+$	976.5	84(31)	3,226(238)	25.6(19)
$2_3^+ \rightarrow 0_1^+$	2414.6	483(26)	16,362(188)	100(5)
$2_3^+ \rightarrow 2_1^+$	1101.4	—	1,188(242)	7.1(11)
$2_4^+ \rightarrow 0_1^+$	2634.2	<39	793(112)	27.2(13)
$2_4^+ \rightarrow 2_1^+$	1321.1	—*	—*	100(7)
$2_4^+ \rightarrow 2_2^+$	344.7	—	—	9.7(8)
$2_4^+ \rightarrow 2_3^+$	219.3	—	—	3.3(3)
$2_5^+ \rightarrow 0_1^+$	2849.2	—	—	2.6(10)
$2_5^+ \rightarrow 2_1^+$	1536.4	<27	888(121)	100(6)
$2_6^+ \rightarrow 0_1^+$	2868.9	49(11)	2,135(117)	100(9)
$2_6^+ \rightarrow 2_1^+$	1556.0	—	277(90)	11.9(9)
$2_6^+ \rightarrow 4_2^+$	309.1	—**	—**	8.6(9)
$2_7^+ \rightarrow 0_1^+$	1979.1	80(12)	2,406(110)	100(9)
$2_7^+ \rightarrow 2_1^+$	1666.0	52(12)	1,275(137)	57(9)
$3_1^- \rightarrow 0_1^+$	3275.2	—	—	<0.32 (this work)
$3_1^- \rightarrow 2_1^+$	1962.2	289(23)	14,300(189)	100

\* The peak of the 1321-keV  $2_4^+ \rightarrow 2_1^+$  transition could not be resolved due to the tail of the dominant peak from the 1313-keV  $2_1^+ \rightarrow 0_1^+$  transition.

\*\* Transition ignored. Decays of the  $4_2^+$  state at 2560 keV were not observed.

---

### 6.1.5.2 Extraction of transition strengths for data satisfying the "safe" Coulomb excitation criterion

---

The Coulex analysis was performed using the software-program GOSIA [Czo83, Cli12]. This program calculates electromagnetic transition matrix elements by a  $\chi^2$ -minimization using different kinds of relevant spectroscopic data. The following values entered the analysis in this work:

- Peak areas of the observed transitions and their uncertainties as discussed above,
- level lifetimes of the  $2_1^+$  and  $3_1^-$  states of  $^{136}\text{Xe}$  and their uncertainties as determined from the caDSAM-analysis in this work (Section 6.1.4),
- the level lifetime of the  $4_1^+$  states of  $\tau = 1.865(25)$  ns from [Son02],
- excitation energies and branching ratios (with uncertainties) for the decays of all involved states from [Son02],
- a branching ratio for the decay of the  $3_1^-$  state of  $I(3_1^- \rightarrow 0_1^+)/I(3_1^- \rightarrow 2_1^+) = 0.0013(13)$  deduced in this work from the  $\gamma$ -ray spectrum observed with the thin carbon target at 546 MeV beam energy.

Using the data satisfying the condition for "safe" Coulomb excitation, statistics is insufficient to determine multipole mixing-ratios from angular distributions (see Figure 6.35). At 546 MeV beam energy, the statistical tensor of the excited states is unknown due to Coulomb-nuclear interference. Therefore, pure  $E2$ -transitions were assumed for all  $2_i^+ \rightarrow 2_1^+$ -transitions and a pure  $E1$ -transition was assumed for the  $3_1^- \rightarrow 2_1^+$  transition. Vanishing diagonal matrix elements (and, hence, quadrupole/octupole moments) were assumed for all considered states. If not all decays of a nuclear state are observed in the experiment, "missing" peak areas of unobserved transitions can be inferred from measured peak areas and known branching ratios. Since in this work all branching ratios of the considered states are known and at least one transition was observed for each of these states (see Table 6.7), the transition matrix elements for all known decay channels of the considered states could be determined.

Coulomb excitation yields were calculated by the program GOSIA for a given set of matrix elements by calculating the excitation- and decay-process of the considered states. For the latter, the geometry of the experimental setup in terms of the geometry of the  $\gamma$ -ray- and particle detectors is taken into account, restricting the reaction kinematics and fixing the fraction of detected  $\gamma$ -rays given the appropriate angular distribution of the  $\gamma$ -rays [Cli12]. In the description of the DSSSD in

GOSIA, the applied cuts on the detection angle of the  $^{12}\text{C}$  recoils were taken into account. The energy-loss of the ions in the target is accounted for via user-provided stopping powers. The values for the energy-loss of  $^{136}\text{Xe}$  in carbon extracted from SRIM [Sri15] were used in this case.

In a minimization process, the assumed matrix elements were varied by GOSIA in order to find the best description of the experimentally observed quantities, i.e. peak areas and level lifetimes. The aforementioned branching ratios and their uncertainties (see Table 6.7) enter as additional data points. Uncertainties of the matrix elements determined in this way were inferred from an error analysis accounting for the uncertainties of all input quantities as well as correlations between them and the determined matrix elements [Cli12]. The global "normalization" of the obtained matrix elements is given in the present case by the lifetimes of the  $2_1^+$ -state of  $^{136}\text{Xe}$ , which exclusively decays directly to the ground-state. Hence, the precision of the  $2_1^+$  level lifetime measured in this work limits the precision that can be achieved for all other matrix elements.

The following sources of systematic errors were accounted for:

- Radiation character of the  $2_i^+ \rightarrow 2_1^+$ -transitions. Calculations were performed also for the case that all of these transitions have  $M1$ -character. In this case, multi-step excitation of the non-yrast  $2^+$ -states via the  $2_1^+$  state is strongly suppressed compared to the case of  $E2$ -transitions. However, excitation of these states by multi-step excitation is suppressed anyway by the light target nuclei (see Chapter 2.1). This is reflected in only small variations of the obtained ground state transition transition matrix elements when assuming pure  $E2$  or  $M1$  character for the  $2_i^+ \rightarrow 2_1^+$  transitions. Deviations in the case of assumed  $M1$ -transitions from the values obtained assuming  $E2$ -transitions were treated as systematic errors.
- In first place, it was assumed that all matrix elements are positive. On the basis of the  $\chi^2$ -value it was not possible to decide on the signs of the matrix elements. Relative signs of the matrix elements in "loops" (i.e. signs of products of transition matrix elements such as  $\langle 0_1^+ | E2 | 2_2^+ \rangle \langle 2_2^+ | E2 | 2_1^+ \rangle \langle 2_1^+ | E2 | 0_1^+ \rangle$ ) lead to constructive or destructive interference (see Section 2.1). This is accounted for by performing fits with all matrix elements defined positive, resulting in obtained matrix elements  $M_+$ . Further fits were performed where the matrix elements were chosen such that the aforementioned loops have negative sign, resulting in obtained matrix elements  $M_-$ . The mean of both values,  $0.5(M_+ + M_-)$  is quoted in this work. The deviations between the obtained transition strengths  $\Delta M = \pm 0.5 |M_+ - M_-|$  were treated as systematic error.

- Interference with / unobserved feeding from higher-lying states was accounted for by introducing "buffer-states" above every considered state (see GOSIA user-manual, [Cli12]). They turned out to have no significant effect on the obtained transition strengths. This is due to the low probability for multi-step excitation using the light target.

The transition strengths obtained using the data satisfying the condition for "safe" Coulomb excitation are listed in Table 6.8 for the  $2_i^+$ -states and in Table 6.9 for the  $3_1^-$ -state of  $^{136}\text{Xe}$ . They are visualized in Figure 6.36.

**Table 6.8.:** Reduced transition strengths determined for decays of  $2_i^+$ -states of  $^{136}\text{Xe}$ . The values were obtained by analysis of data measured under "safe" Coulomb excitation conditions using the software-program GOSIA. See text for details.

Transition	B(E2) [W.u.]	$\sigma_{sys}$ [W.u.]	$\sigma_{stat}$ [W.u.]	Transition	B(E2) [W.u.]	$\sigma_{sys}$ [W.u.]	$\sigma_{stat}$ [W.u.]
$2_1^+ \rightarrow 0_1^+$	9.59	$\pm 0.002$	$\pm 0.35$				
$2_2^+ \rightarrow 0_1^+$	0.623	$^{+0.015}_{-0.003}$	$^{+0.038}_{-0.032}$	$2_2^+ \rightarrow 2_1^+$	11.4	$\pm 0.06$	$\pm 1.2$
$2_3^+ \rightarrow 0_1^+$	0.906	$\pm 0.015$	$\pm 0.058$	$2_3^+ \rightarrow 2_1^+$	3.20	$\pm 0.05$	$^{+0.52}_{-0.56}$
$2_6^+ \rightarrow 0_1^+$	0.234	$\pm 0.008$	$^{+0.048}_{-0.058}$	$2_6^+ \rightarrow 2_1^+$	0.59	$\pm 0.02$	$\pm 0.16$
$2_7^+ \rightarrow 0_1^+$	0.695	$\pm 0.038$	$\pm 0.066$	$2_7^+ \rightarrow 2_1^+$	7.5	$\pm 0.4$	$\pm 1.8$

**Table 6.9.:** Reduced transition strengths determined for the decays of the  $3_1^-$ -state of  $^{136}\text{Xe}$ , obtained under "safe" Coulomb excitation conditions. See text for details.

transition	character	B( $\sigma\lambda$ )	$\sigma_{sys}$	$\sigma_{stat}$	unit
$3_1^- \rightarrow 0_1^+$	E3	14.9	$\pm 0.3$	$\pm 1.3$	W.u.
$3_1^- \rightarrow 2_1^+$	E1	1.114	$\pm 0$	$^{+0.064}_{-0.048}$	mW.u.

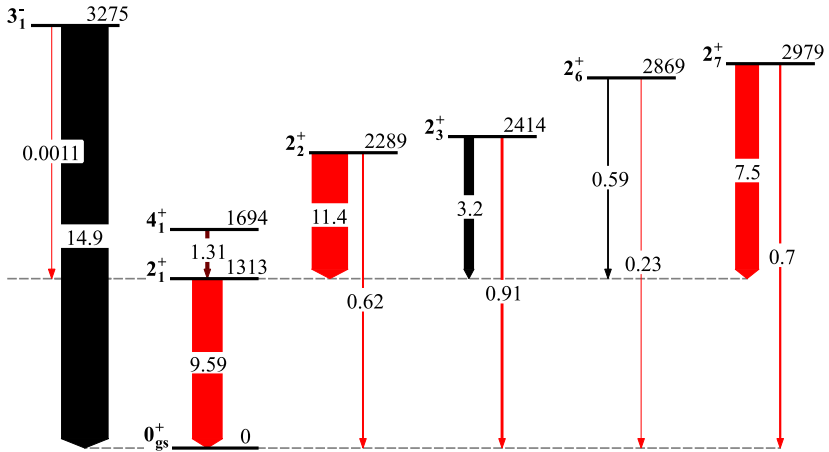


**Figure 6.36.:** Level scheme showing the excited states of  $^{136}\text{Xe}$  considered in the Coulex analysis using the data satisfying the condition for "safe" Coulomb excitation. For each state, spin and parity (left of the lines indicating the level) and excitation energy (on the line) are given. Observed transitions are drawn as red arrows connecting the respective states. The widths of the arrows are proportional to the measured transition strengths. The values of the transitions strength are given on each arrow in Weisskopf-units. Strengths of transitions that were not observed (black arrows) could be determined via the branching ratios of the decays from [Son02].

---

### 6.1.5.3 Limits on transition strengths of decays depopulating the $2_{4,5}^+$ -states of $^{136}\text{Xe}$

---

The transitions  $2_4^+ \rightarrow 0_1^+$  and  $2_5^+ \rightarrow 2_1^+$  were observed at 546 MeV beam energy, but are not sufficiently pronounced in the data satisfying the condition for "safe" Coulomb excitation due to the lower statistics (see Table 6.1). Nevertheless, limits on the transitions strengths for the decays of the  $2_4^+$  and  $2_5^+$  states of  $^{136}\text{Xe}$  can be given.

*Lower* limits on these transition strengths were obtained from a Coulex analysis of data collected at 546 MeV beam energy. For this purpose, the scattering angle of the recoiling  $^{12}\text{C}$  ions was restricted to  $42^\circ$  in the laboratory system, corresponding to a scattering angle of  $95^\circ$  in the center-of-mass system. Peak areas for the  $2_4^+ \rightarrow 0_1^+$  and  $2_5^+ \rightarrow 2_1^+$  transitions could be determined with uncertainties of 14.1% and 13.6% in this data set, respectively. The observed peak areas are summarized in Table 6.7.

These data selection conditions for obtaining *lower* limits on the transition strengths of the decays depopulating the  $2_{4,5}^+$ -states of  $^{136}\text{Xe}$  does not satisfy the criterion for "safe" Coulomb excitation (see Figure 6.33 and the discussion in Section 6.1.5.1). It has to be expected that Coulomb-nuclear interference occurs at the small distances of closest approach occurring for this beam energy and the selected scattering angles. It is reasonable to assume that these interferences may be more pronounced for smaller distances of closest approach between the collision partners, e.g. for smaller laboratory scattering angles of the recoiling  $^{12}\text{C}$  ions. However, choosing a larger minimum angle of the recoiling  $^{12}\text{C}$  ions than  $42^\circ$  would have resulted in drastically higher uncertainties of the determined peak areas. This would not have been beneficial for the determination of lower limits of the excitation strengths.

A general rule for the Coulomb-nuclear interference is, that "*The initial Coulomb-nuclear interference will be constructive (destructive) if the excitation function for pure Coulomb excitation is approaching or at a minimum (maximum)*" [Gui78]. The Coulomb excitation cross section for a  $2^+$ -state of  $^{136}\text{Xe}$  at 2.7 MeV with a ground-state transition strength of 10 W.u. on a carbon target is plotted in Figure 6.37. It is clear that in this case the excitation function for pure Coulomb excitation is approaching a maximum. Hence, the Coulomb-nuclear interference is expected to be destructive. This is the usual case near the Coulomb barrier [Cli12] and also applies to the excitation of the  $2_4^+$ - and  $2_5^+$ -states of  $^{136}\text{Xe}$  at 2634 keV and 2849 keV, respectively. For destructive Coulomb-nuclear interference, the transition strengths obtained assuming pure Coulomb excitation will *underestimate* the

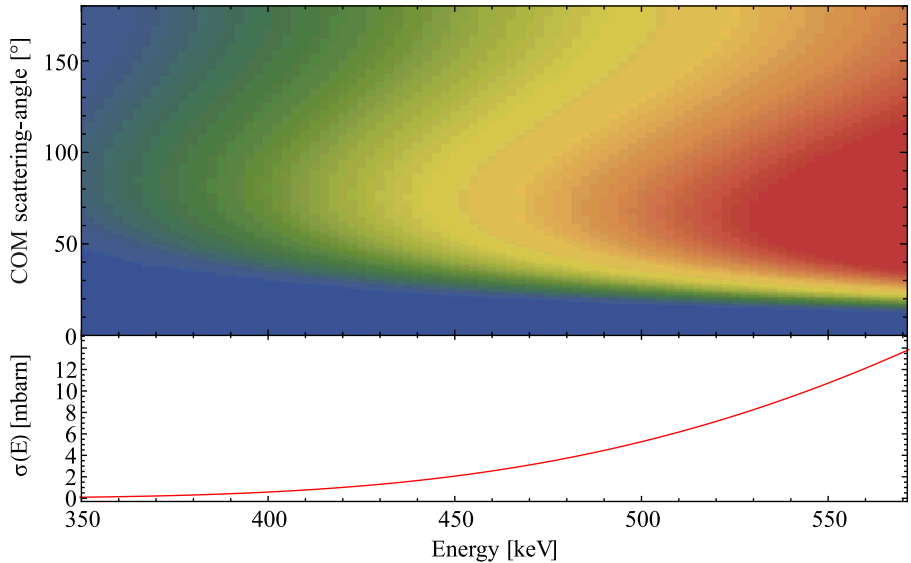


**Figure 6.37.:** **Top:** Differential cross section for Coulomb excitation of a  $2_1^+$ -state of  $^{136}\text{Xe}$  at 2.7 MeV with a ground-state transition strength of 10 W.u. on a carbon target.

**Bottom:** Excitation function (i.e. differential cross section integrated over the full solid angle) for the excitation of the same state as above. Cross sections were calculated using the Coulomb excitation code CLX [Owe].

true value. Following this argumentation, transition strengths of the  $2_4^-$ - and  $2_5^+$ -states of  $^{136}\text{Xe}$  obtained from the Coulex analysis of data taken at 546 MeV beam energy will underestimate the true strengths and therefore serve as lower limit. This has been checked by analysis of the transitions observed also under "safe" Coulomb excitation conditions. The strengths of these transition are all underestimated in the Coulex analysis of the 546 MeV data set, as expected.

*Upper* limits for the transition strengths of the decays of the  $2_4^-$ - and  $2_5^+$ -state of  $^{136}\text{Xe}$  were obtained from data taken at 500 MeV beam energy and satisfying the condition for "safe" Coulomb excitation. For this purpose, upper limits on the peak areas have been determined. The same approach as for the determination of the areas of well pronounced peaks was applied, i.e. integration of the spectrum in the region of the peak and subtraction of a background fitted to the data in proximity

to the peak. For the decays of the  $2_4^+$ - and  $2_5^+$ -state, the integration regions were determined in the spectrum taken at 546 MeV beam energy where the transitions are well visible. The upper  $1\sigma$ -limit of the peak areas determined this way were used as upper limits of the peak areas. These upper limits are also listed in Table 6.7. Resulting upper limits on the respective transition strengths were again obtained by an analysis using the program GOSIA as described in Section 6.1.5.2. Known branching ratios of the decays of the  $2_4^+$ - and  $2_5^+$ -state of  $^{136}\text{Xe}$  from [Son02] (listed in Table 6.7) were used in the analysis.

Obtained transition strengths of both the  $2_4^+$ - and  $2_5^+$ -state of  $^{136}\text{Xe}$  to the  $2_1^+$ -states are strong and it is reasonable to suppose that these transitions have at least partial  $M1$ -character. Therefore, limits of the transition strengths to the  $2_1^+$ -state have been calculated for both pure  $E2$  and pure  $M1$  character. As in the case of the "safe" Coulomb excitation, positive and negative signs of transition loops have been considered (see Section 6.1.5.2) where pure  $E2$  character was assumed for all transitions. The lower (higher) obtained values are quoted for the lower (upper) limits of the strengths.

Transitions of the  $2_4^+$ -state to the  $2_2^+$ - and  $2_3^+$ -state are very strong and they must be dominated by  $M1$  character. If the states would have pure  $E2$  character, the transition strengths to the  $2_2^+$ - and  $2_3^+$ -state would take unrealistic values exceeding 1500 and 4500 W.u., respectively. Therefore, pure  $M1$  character was assumed for these two transitions in all calculations. The results are summarized in Table 6.10.

**Table 6.10.:** Limits on reduced transition strengths determined for decays of the  $2_{4,5}^+$ -states of  $^{136}\text{Xe}$ . Transition strengths for either pure  $E2$  **or**  $M1$  character are quoted for the  $2_{4,5}^+ \rightarrow 2_1^+$  transitions.

Transition	character	$B(\sigma\lambda)$ [W.u.]
$2_4^+ \rightarrow 0_1^+$	E2	0.184 ... 0.354
$2_4^+ \rightarrow 2_1^+$	E2	19.8 ... 39.5
	M1	0.068 ... 0.123
$2_4^+ \rightarrow 2_2^+$	M1	0.31 ... 0.66
$2_4^+ \rightarrow 2_3^+$	M1	0.37 ... 0.82
$2_5^+ \rightarrow 0_1^+$	E2	0.010 ... 0.040
$2_5^+ \rightarrow 2_1^+$	E2	15.7 ... 33.8
	M1	0.17 ... 0.66

---

## 6.1.6 Discussion of the results for $^{136}\text{Xe}$

---

### 6.1.6.1 Quadrupole collectivity in $^{136}\text{Xe}$

---

The lifetime of the  $2_1^+$  state of  $^{136}\text{Xe}$  has been measured in various experiments starting in the mid of the 1970's employing Coulomb excitation [Wol78], DSAM [Wol78, Spe93, Jak02], NRF [Gar06] and  $(\alpha, \alpha')$  [Bur87]. These values are compared to the lifetime obtained in the present work in Figure 6.38. The  $2_1^+$  level lifetime of  $^{136}\text{Xe}$ , measured in this work to be  $524_{-23}^{+27}$  fs, is in excellent agreement with the currently adopted value of  $520 \pm 20$  fs and has comparable uncertainty (which is dominated by systematic uncertainties of the employed stopping powers, see Section 6.1.4).

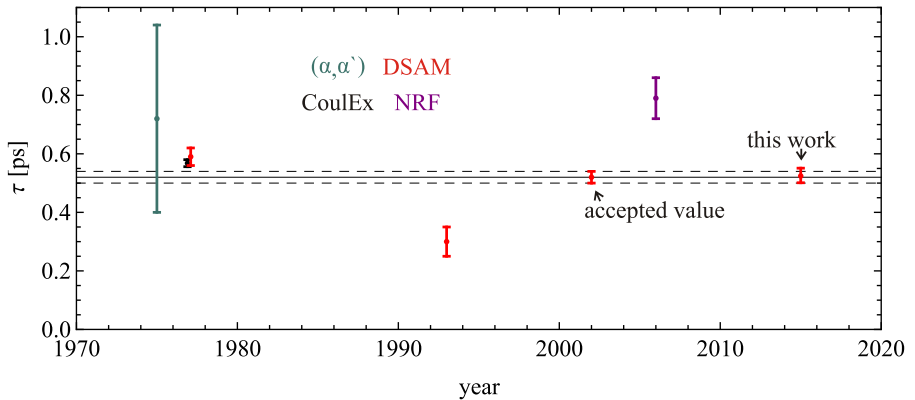


**Figure 6.38.:** Previously measured values for the  $2_1^+$  level lifetime of  $^{136}\text{Xe}$ , plotted against the year of their publication. The currently adopted value of  $0.52(2)$  ps stems from one DSAM measurement in 2002 [Jak02] and is displayed as horizontal lines. It is in perfect agreement with the value obtained in this work. The references are given in the text.

Experimental data on low-spin, off-yrast quadrupole collectivity in  $^{136}\text{Xe}$  is scarce. Only the NRF measurements by von Garrel [Gar06] are available for comparison to the values obtained in this work. As clearly visible in Figure 6.38 and listed in Table 6.11, already the result for the  $B(E2, 0_1^+ \rightarrow 2_1^+)$  from [Gar06] is smaller by a factor of 1.5 than the value determined in this work and the adopted value. It is also visible in Figure 6.38 that among the available experimental data, the value from [Gar06] has the largest deviation from the currently accepted value. Also for

the off-yrast  $2^+$ -states, the ground state transition strengths reported in [Gar06] are smaller than the values measured in this work by approximately the same factor. An exception is the value for the  $2^+$  level at 2869 keV where the measurements agree. The experimental results from this work and [Gar06] are compared in Table 6.11.

The valence nucleons of the neutron-closed shell nucleus  $^{136}_{54}\text{Xe}_{82}$  are the four protons above the  $Z = 50$  proton shell-closure. In the ground-state, they predominantly occupy the  $g_{7/2}$  orbit. This can be inferred from the  $7/2^+$  ground states of its isotones  $^{137}\text{Cs}$ ,  $^{135}\text{I}$  and  $^{133}\text{Sb}$  and was extracted from ( $^3\text{He}, d$ ) and ( $d, ^3\text{He}$ ) transfer reactions [Wil71] (see Table 6.12). The lowest excitations can be made by re-coupling two of the four protons to higher spins. Since both protons occupy the same orbit, the parity of those states is necessarily even. According to the Pauli principle, two identical particles with spin  $7/2$  can couple to total, non-zero finite spins of 2, 4, 6. Since these states involve exactly two nucleons that are not coupled pairwise to spin zero, their seniority is  $\nu = 2$ . As will be discussed below, these states generated by two protons in the  $g_{7/2}$  orbit are the dominant constituents of the  $J^\pi = 2^+, 4^+, 6^+$  yrast states of  $^{136}\text{Xe}$  at excitation energies of 1313 keV, 1694 keV and 1891 keV, respectively [Son02]. By the re-coupling of all four protons in the  $g_{7/2}$  orbit ( $\nu = 4$  states), additional states with  $J^\pi = 2^+, 4^+, 5^+, 8^+$  can be build. This can easily be reenacted by the application of the  $m$ -scheme [Cas00, chapter 6.1].

The seniority scheme [Rac52, Tal93] predicts strong suppression of transitions between states with  $\Delta\nu = 0$  at mid-shell, which is the case in  $^{136}\text{Xe}$  with four out of eight possible protons in the  $g_{7/2}$  orbit<sup>4</sup>. Indeed, the  $6_1^+$  state of  $^{136}\text{Xe}$  is isomeric with a half-life of 2.95(9)  $\mu\text{s}$  and also the  $4_1^+$  state is long-lived with a half-life of 1.293(17) ns [Son02], indicating a rather pure  $\{\pi g_{7/2}\}_{\nu=2}^4$  configuration for the  $6_1^+$  and  $4_1^+$  states of  $^{136}\text{Xe}$ . The proton dominance in the configurations of the  $2_1^+$  and  $4_1^+$  states of  $^{136}\text{Xe}$  are indicated experimentally by their large positive g-factors [Jak02, Spe93]. Furthermore, a dominant  $\{\pi g_{7/2}\}_{\nu=2}^4$  configuration reproduces the respective spectroscopic data fairly well in microscopic calculations [Man91, Isa05, and references in Table 6.11].

Empirical shell-model calculations by Isakov *et al.* indicate that the  $2_2^+$  state at 2289 keV has dominantly a  $\{\pi g_{7/2}\}_{\nu=4}^4$  configuration [Isa05]. This is in agreement with the observations in this work. In the seniority scheme, no suppression is expected for  $\Delta\nu = 2$  transitions, but transitions with  $\Delta\nu = 4$  should be suppressed. Indeed, a strong transition between the 2289 keV  $2_2^+$  state and the  $2_1^+$

<sup>4</sup> The  $\pi g_{7/2}$  orbits forms a quite pronounced sub-shell closure with a gap to the next-higher  $d_{5/2}$  orbit of about 950 keV in  $^{133}\text{Sb}$ , see Figure 6.42

state ( $\Delta\nu = 2$ ) is observed, while the ground-state transition strength of the  $2_2^+$  state ( $\Delta\nu = 4$ ) is relatively small. The transition strengths  $B(E2, 2_1^+ \rightarrow 0_1^+)$ ,  $B(E2, 2_2^+ \rightarrow 0_1^+)$  and  $B(E2, 2_2^+ \rightarrow 2_1^+)$  calculated in the empirical shell-model approach of [Isa05] consistently underestimate the experimental values from this work by a factor of 2, but reproduce their ratios. The same holds for the shell-model calculations based on realistic interactions derived from the CD-Bonn potential by Bianco *et al.* [Bia13], yet the  $2_2^+ \rightarrow 0_1^+$  transition strength is more strongly underestimated in that calculation (see Table 6.11).

In [Man91, Isa05], the next higher-lying  $2_i^+$  states of  $^{136}\text{Xe}$  ( $i > 2$ ) are mainly attributed to mixed configurations where the valence protons occupy both the  $g_{7/2}$  and  $d_{5/2}$  orbits. However, the few calculated spectroscopic observables from [Bia13, Isa05] show at best partial qualitative agreement with the experimental findings for the higher-lying  $2^+$  states in this work.

The discussed shell-model calculations generally under-estimate the observed transition strengths for all states, except for the  $B(E2, 2_1^+ \rightarrow 0_1^+)$  value obtained in the shell-model calculation of [Cor09] that is able to fairly reproduce the experimental strength. This may indicate admixtures of collective wave functions that are not covered by the shell-model calculations, which are all restricted to the major proton shell comprising the orbits  $0g_{7/2}$ ,  $1d_{5/2}$ ,  $1d_{3/2}$ ,  $0h_{11/2}$  and  $2s_{1/2}$ . Minor contributions from other orbitals are supposed to be absorbed by the perturbative treatment of the (effective) interactions in shell-model calculations, but significant degrees of freedom may be disregarded.

A comparison between the experimental values and microscopic calculations within the shell-model and the quasi-particle random phase approximation (QRPA) is given in Table 6.11 together with the employed interactions and model spaces. The details of the calculations will not be discussed here, the reader is referred to the cited publications and references therein. The four non-yrast  $2^+$  states with the strongest experimentally observed ground-state transitions (i.e., the transitions observed under safe Coulex conditions, see Chapter 6.1.5) are compared to the calculations. This procedure is motivated by the fact that all  $2^+$  states described by the calculations of [Bia13], the only calculation found that also quotes transition strength for the non-yrast  $2^+$ -states, exhibit substantial ground-state transition strengths. The resulting level assignment between experiment and calculations on the basis of ground-state transition strengths also reasonably matches in terms of the corresponding energies.



The systematics of the  $B(E2, 0_1^+ \rightarrow 2_1^+)$  strength and the energy of the  $2_1^+$  level in the region around  $^{136}\text{Xe}$  show a very regular pattern (see Figure 6.39). The  $B(E2, 0_1^+ \rightarrow 2_1^+)$  strength exhibits no significant asymmetry with respect to the  $N = 82$  shell closure. Only a small enhancement of  $B(E2)$  strength for  $N > 82$  nuclei compared to their respective isotopes with the same number of valence neutrons (neutron holes) and  $N < 82$  can be recognized. An exception is the case of  $^{136}\text{Te}$  which is discussed at the end of this section. All other nuclei show a clear scaling of their  $B(E2, 0_1^+ \rightarrow 2_1^+)$  strength as a function of the product of the number of valence protons and neutrons,  $N_\pi$  and  $N_\nu$  (see Figure 6.40, left). This is interpreted in the  $N_\pi N_\nu$ -scheme as indication that the quadrupole collectivity in these nuclei is predominantly generated by the attractive  $T = 0$  component of the p-n interaction of the few available valence nucleons [Cas85]. For  $^{136}\text{Xe}$ , the  $N_\pi N_\nu$ -scheme doesn't apply ( $N_\nu = 0$ ), yet the dominant  $\{\pi g_{7/2}\}_{\nu=2}^4$  configuration of the  $2_1^+$  state of  $^{136}\text{Xe}$  was already discussed above.

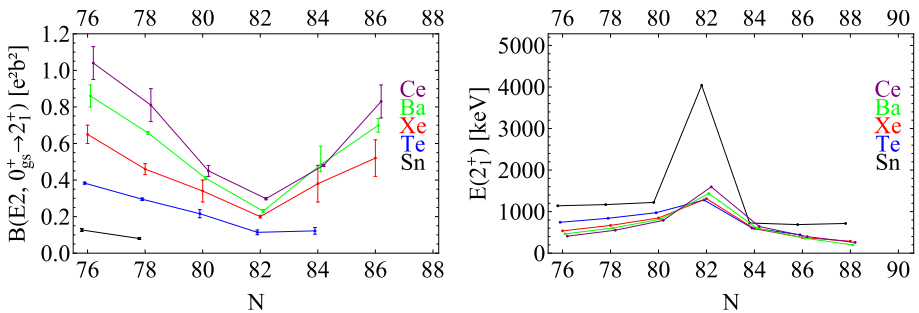


**Figure 6.39.:** Systematics of the  $2_1^+$ -state in nuclei close to  $^{136}\text{Xe}$ . The behavior of  $B(E2, 0_1^+ \rightarrow 2_1^+)$  strengths is shown on the left hand side as a function of neutron number  $N$ , the behavior of the  $2_1^+$  level energies on the right hand side. The lines are drawn to guide the eye and the data points are slightly shifted along the x-axis for better visibility. The data is taken from [Ram01] with the following exceptions:  $^{132-136}\text{Te}$ : [Dan11];  $^{124-126}\text{Sn}$ : [All11];  $^{136}\text{Xe}$ : this work;  $^{138-142}\text{Xe}$ : [Krö07];  $^{140}\text{Ba}$ : [Bau12];  $^{140}\text{Nd}$ : [Bau13]

In contrast to the  $B(E2)$  values, the energies of the  $2_1^+$  states show a clear asymmetry with respect to the  $N = 82$  shell closure (see Figure 6.40, right). Nuclei with  $N > 82$  show a systematically lower  $2_1^+$  level energy than their isotopes with  $N < 82$  and the same number of valence neutrons (neutron holes). The lowered energies indicate a higher collectivity of these states which is, however, barely reflected in

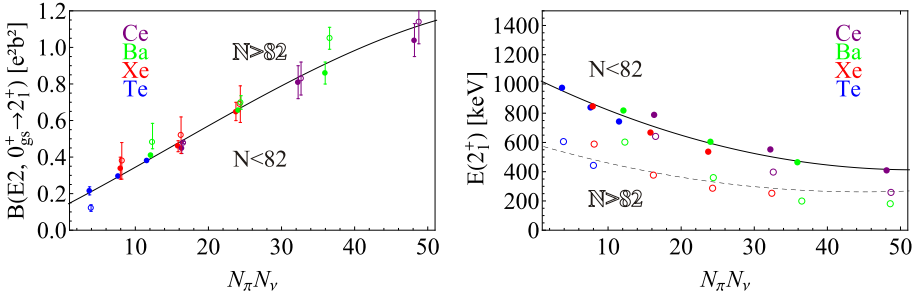


**Figure 6.40.:** Same data as in Figure 6.39, but plotted against the product  $N_{\pi}N_{\nu}$  of the number of valence protons and neutrons. For the  $B(E2, 0_{gs}^+ \rightarrow 2_1^+)$  values, the black line represents a cubic fit to all data points ( $^{136}\text{Te}$  was excluded from the fit). All experimental values are very close to this line. A small enhancement of  $B(E2)$  strength for  $N > 82$  (open symbols) with respect to their isotopes with the same number of valence neutrons (holes)  $N_{\nu}$  and  $N < 82$  (full symbols) can be recognized. For the energies, the full line represents a quadratic fit to the data for nuclei with  $N < 82$  (full symbols), the dashed line for nuclei with  $N > 82$  (open symbols). Clearly, the energies of the  $2_1^+$  states of nuclei with  $N > 82$  are lower than those of their isotopes with  $N < 82$  and the same number of valence neutrons (holes)  $N_{\nu}$ . This indicates enhanced collectivity for  $N > 82$ .

the  $B(E2)$  values. This can be understood by an increased neutron collectivity that originates in a reduced neutron pairing gap for  $N > 82$  [Ter02]. The reduced neutron pairing gap and increased neutron collectivity clearly lower the level energies, but make only a small contribution to the proton-generated electromagnetic transition strength via the neutron-proton quadrupole-quadrupole residual interaction.

The energies of the  $2_1^+$  states of  $N = 82$  isotones above  $^{132}_{50}\text{Sn}$  rise moderately as a function of the number of protons filling the  $g_{7/2}$  and  $d_{5/2}$  orbitals. At the same time, the  $B(E2)$  values rise. This contradicts Grodzins' rule that states an anti-proportionality between  $B(E2, 0_1^+ \rightarrow 2_1^+)$  and  $E(2_1^+)$  [Gro62]. It is also in contrast to the almost constant  $2_1^+$  energies of light tin isotopes, where neutrons also gradually fill the  $d_{5/2}$  and  $g_{7/2}$  orbitals. While the constancy of  $2_1^+$  energies of light tin isotopes is *inter alia* attributed to the near degeneracy of the  $\nu g_{7/2}$  and  $\nu d_{5/2}$  orbitals near  $^{100}\text{Sn}$  [Gra95] resulting in strong pairing, the deviating behavior of the  $N = 82$  isotones is explained by the larger separation of the  $\pi g_{7/2}$  and  $\pi d_{5/2}$

---

orbitals near  $^{132}\text{Sn}$  [Hol97] (see Figure 6.42). Also, the ordering of these orbitals is interchanged for protons and neutrons.

A very conspicuous exception to the very regular behavior of the  $B(E2, 0_1^+ \rightarrow 2_1^+)$  strength of nuclei around  $^{136}\text{Xe}$  is the case of  $^{136}\text{Te}$ . Its transition strength from the  $2_1^+$  state to the ground state remains at nearly the same level as the one of its  $N = 82$  isotope  $^{134}\text{Te}$  [Rad02, Dan11]. At the same time,  $^{136}\text{Te}$  exhibits a significantly lower energy of the  $2_1^+$  state than  $^{134}\text{Te}$ , contradicting Grodzins' rule. The odd behavior of the  $B(E2, 0_1^+ \rightarrow 2_1^+)$  strength is also peculiar in terms of the  $N_\pi N_\nu$ -scheme, as clearly visible in Figure 6.40 (left, lower value at  $N_\pi N_\nu = 4$ ).

The exceptionally low  $B(E2)$  strength of  $^{136}\text{Te}$  is interpreted as manifestation of a clear neutron dominance of the wave function of the  $2_1^+$  state. It originates in a strong reduction of the neutron pairing gap when crossing  $N = 82$  that is not compensated by proton pairing and the proton-neutron quadrupole-quadrupole residual interaction as in the higher- $Z$  elements [Ter02, Shi04].

If this is so, the "mirror state" with respect to the proton and neutron part of the  $2_1^+$  state, the one-phonon mixed-symmetry state  $2_{ms}^+$  [Pie08], should exhibit just the opposite characteristics, namely a dominant proton part of its wave function [Sev14]. This would manifest itself in an enhanced E2 transition strength between the  $2_{ms}^+$  and the ground state and a reduced M1 transition strength between the  $2_{ms}^+$  and the  $2_1^+$  state, compared to the case of a balanced proton and neutron contingent in the wave functions of the  $2_{ms}^+$  and the  $2_1^+$  states. This phenomenon is known as Configurational Isospin Polarization (CIP) [Hol07, Wer08] and discussed in the context of the anomalous behavior of  $^{136}\text{Te}$  [Dan11, Sev14]. An experiment aiming at the identification of the  $2_{ms}^+$  of  $^{136}\text{Te}$  and the measurement of its transition strengths to the  $2_1^+$  and ground-state is planned at the HIE-ISOLDE facility. The accepted proposal to this experiment was elaborated during this work [Sta14].

---

#### 6.1.6.2 $B(E3, 0_1^+ \rightarrow 3_1^-)$ strength of $^{136}\text{Xe}$

---

The value of the  $B(E3, 0_1^+ \rightarrow 3_1^-)$  strength in  $^{136}\text{Xe}$  has so far only been inferred from the  $\beta_3$  deformation parameter obtained in a  $(p, p')$  experiment [Sen72] to be  $17 \pm 6$  W.u. [Kib02]. The value of  $14.9 \pm 1.3$  W.u. measured in this work is in excellent agreement with the  $(p, p')$  value, but has highly reduced uncertainty. In fact, the large uncertainty of the value deduced from  $(p, p')$  did not allow to draw any quantitative conclusions and in this respect, this work provides the first sensitive measurement of the  $B(E3, 0_1^+ \rightarrow 3_1^-)$  strength in  $^{136}\text{Xe}$ . It is put into context by comparison with the  $B(E3)$  strength in neighboring nuclei in Figure 6.41.

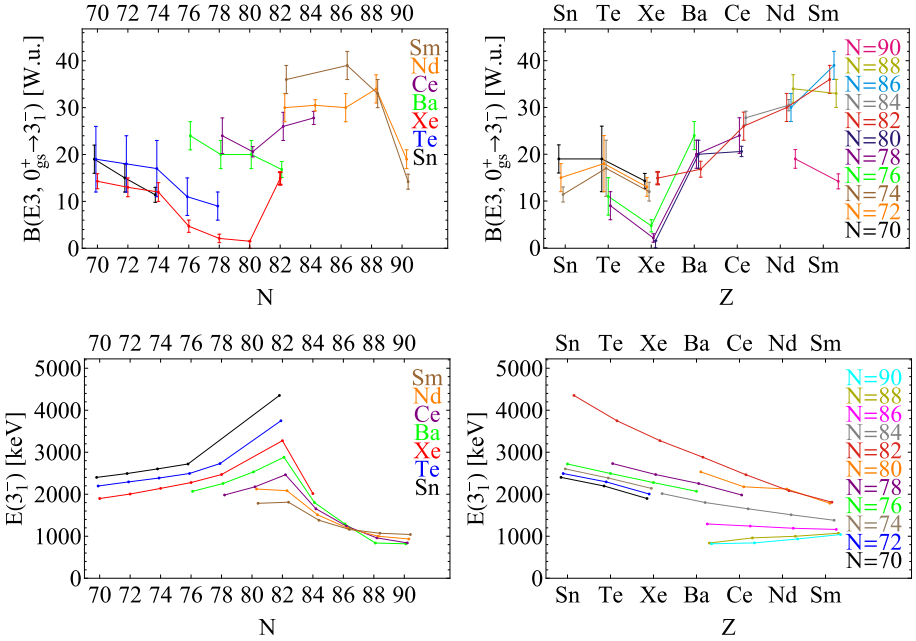


**Figure 6.41.:** Systematics of the  $3_1^-$ -state in nuclei close to  $^{136}\text{Xe}$ . The behavior of  $B(E3, 0_1^+ \rightarrow 3_1^-)$  strengths is shown in the upper plots, the behavior of the  $3_1^-$  level energies in the lower plots. On the left hand side, the systematics is shown as a function of neutron number  $N$  and on the right hand side as a function of atomic number  $Z$ . The lines are drawn to guide the eye and the data points are slightly shifted along the x-axis for better visibility. The data is taken from [Kib02] with the following exceptions:  $^{134}\text{Te}$ : [All12] ( $E(3^-)$  only);  $^{124-134}\text{Xe}$ : [Mue06];  $^{136}\text{Xe}$ : this work;  $^{136}\text{Ce}$ : [Ahn12];  $^{138}\text{Ce}$ : [Rai06];  $^{140}\text{Ce}$ : [Pit70];  $^{142}\text{Ce}$ : [Kim91]. The  $B(E3, 0_1^+ \rightarrow 3_1^-)$  value of  $^{134}\text{Xe}$  represents an upper limit.

When comparing the measured  $B(E3, 0_1^+ \rightarrow 3_1^-)$  strength in  $^{136}\text{Xe}$  and the energy of the  $3_1^-$ -state to available data in neighboring nuclei, some striking features become apparent:

- (1) For  $N < 82$ , the  $B(E3)$  strength drops with increasing neutron number in the  $_{52}\text{Te}$  and  $_{54}\text{Xe}$  isotopes. This trend is also present in the available data of  $_{50}\text{Sn}$  isotopes.
- (2) The decrease of  $B(E3)$  strength when approaching  $N = 82$  is either not present in the  $_{56}\text{Ba}$  and  $_{58}\text{Ce}$  isotopes, or they "start" from a much higher  $B(E3)$  strength at  $N < 76$ .
- (3) For  $82 < N < 90$ , the behavior of  $B(E3)$  strength is very regular. It is almost independent from the neutron number  $N$  and in the isotonic sequence it increases monotonically as a function of proton number  $Z$  by  $\sim 2.5$  W.u. per proton pair (upper right part of Fig. 6.41). At  $N = 90$ , the  $B(E3)$  strengths drop sharply.
- (4) For  $N < 82$  there is no such regularity in the  $_{52}\text{Te}$  and  $_{54}\text{Xe}$  isotopes. The known  $B(E3)$  values of  $_{56}\text{Ba}$  and  $_{58}\text{Ce}$  are significantly higher than the values of  $_{52}\text{Te}$  and  $_{54}\text{Xe}$  for  $N < 82$ . In particular, the  $B(E3)$  values of  $_{54}\text{Xe}$  do not follow the trend of monotonically rising  $B(E3)$  strength with increasing proton number  $Z$  (upper right part of Fig. 6.41).
- (5) The  $B(E3)$  value of  $^{136}\text{Xe}_{82}$  is very much larger than the values of  $^{132,134}\text{Xe}_{78,80}$  - there is a factor of  $\sim 10$  between the strengths. This sudden increase at the neutron shell closure is not present in Ce and Ba, the only other elements where relevant data exist.
- (6) The energies of the  $3_1^-$ -states in the regarded sector of the nuclear chart behave extremely regular. They are elevated at the  $N = 82$  shell closure for all elements with  $50 \leq Z \leq 62$  and decrease monotonically as a function of  $Z$  in all isotonic chains with  $70 \leq N \leq 86$ . Towards  $N = 88$ , this decrease is reduced; at  $N = 88$  and at the  $\nu(1f_{7/2})$  subshell closure at  $N = 90$ , the energies of the  $3_1^-$ -states rise slowly as a function of  $Z$ . In general, the energies evolve in an asymmetric way with respect to  $N = 82$ : Above  $N = 82$ , the energies of the  $3_1^-$ -states are significantly lower than below  $N = 82$ .

In the following, these observations are discussed in detail.

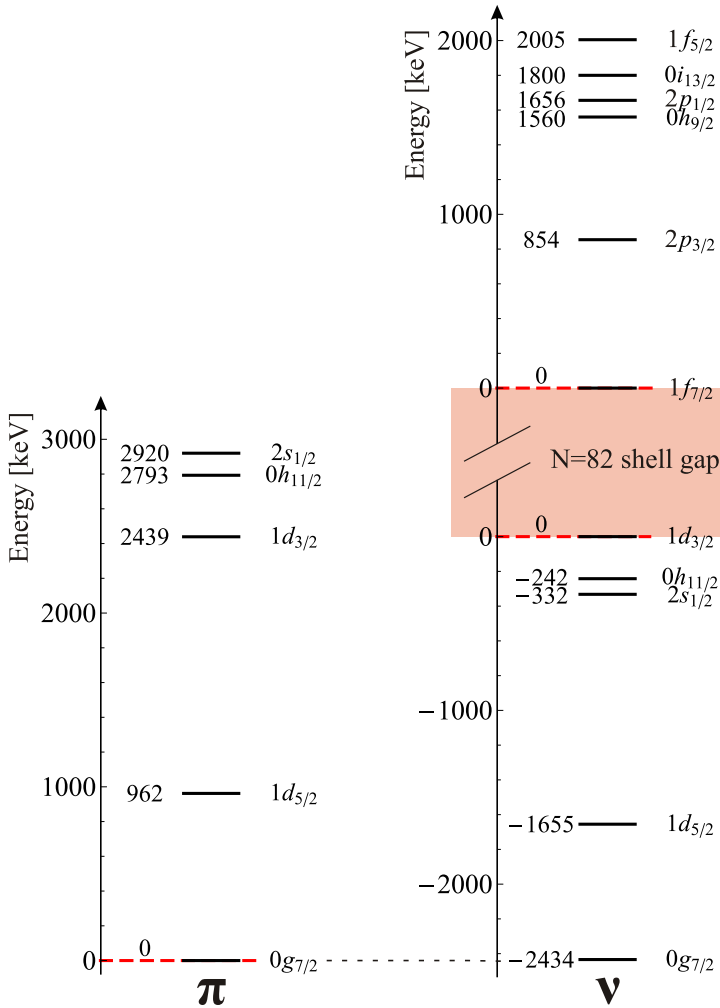


**Figure 6.42.:** Single-particle energies for protons ( $\pi$ ) and neutrons ( $\nu$ ) relative to the  $Z = 50$  and  $N = 82$  shell closures of a  $^{132}\text{Sn}$  core. The energies for  $N, Z \leq 82$  are taken from single-particle states of  $^{133}\text{Sb}$  ( $\pi$ ) and  $^{131}\text{Sn}$  ( $\nu$ ) [Jak02] and for  $N > 82$  from single-particle states of  $^{133}\text{Sn}$  [Pit13]. The width of the  $N = 82$  shell-gap decreases when adding protons from  $\sim 6.4$  MeV in  $^{132}\text{Sn}$  to  $\sim 4$  MeV in Ce and Nd [Dwo08].

### **B(E3) strength below N = 82**

Just below the  $N=82$  shell closure, the neutrons fill the very close-lying orbits  $2s_{1/2}$ ,  $0h_{11/2}$  and  $1d_{3/2}$  (see Figure 6.42). Octupole correlations are formed between orbits with  $\Delta l = 3$  and  $\Delta j = 3$ . In the  $N = 50 - 82$  major shell, only the pair  $1d_{5/2} \leftrightarrow 0h_{11/2}$  fulfills this requirement. Consequently, neutrons in the  $1d_{5/2}$  orbit can form octupole correlations with the  $0h_{11/2}$  orbit, as long as the  $0h_{11/2}$  is not completely filled [Ahm93].

The evolution of the  $B(E3)$  strength in Xe isotopes below  $N = 82$  has been qualitatively explained on the basis of neutron  $d_{5/2} \otimes h_{11/2}$  octupole correlations and the presence of a soft quadrupole mode of the mean field [Mue06]. In this picture, the decreasing trend of  $B(E3)$  strength when approaching  $N = 82$  is caused by the decreasing availability of the  $h_{11/2}$  orbit to form octupole correlations. At  $N = 82$  the major neutron shell is completely filled and  $d_{5/2} \otimes h_{11/2}$  octupole correlations cannot be formed. Hence, this mechanism cannot be responsible for any significant octupole strength in  $^{136}\text{Xe}_{82}$ .

The decreasing trend of  $B(E3)$  strength towards  $N = 82$  is also present in the  $_{52}\text{Te}$  isotopes and is indicated by the available data on  $_{50}\text{Sn}$  isotopes. In the  $_{56}\text{Ba}$  isotopes, this decrease is not apparent in the presently available data. It is not expectable that the  $B(E3, 0_1^+ \rightarrow 3_1^-)$  strengths of  $^{126,128,130}\text{Ba}$  exceeded 30 W.u. and the high experimental values for  $^{132,134,136}\text{Ba}$  were in fact reduced as a function of neutron number as much as the strengths in Te and Xe. The same holds for the available data on Ce isotopes.

### **B(E3) strength above N = 82**

After crossing the  $N = 82$  shell gap, octupole correlations can be made up by the neutron orbit pair  $1f_{7/2} \leftrightarrow 0i_{13/2}$ . Beyond  $N = 82$ , the neutron  $1f_{7/2}$  orbit is the first orbit filled by the neutrons, as it is apparent from the  $J^\pi = 7/2^-$  ground-states of all known even- $Z$ ,  $N = 83$  isotones. In  $^{133}\text{Sn}_{83}$ , the gap to the next orbit,  $2p_{3/2}$ , is well pronounced with 854 keV (see Fig. 6.42). The available  $B(E3, 0_1^+ \rightarrow 3_1^-)$  values of  $_{58}\text{Ce}$ ,  $_{60}\text{Nd}$  and  $_{62}\text{Sm}$  show an almost constant behavior as the  $\nu(1f_{7/2})$  orbit is being filled. However, at  $N = 90$ , the  $\nu(1f_{7/2})$  shell is completely filled and a sudden drop in  $B(E3)$  strength occurs in the elements where data is available, i.e.  $_{60}\text{Nd}$ ,  $_{62}\text{Sm}$  and  $_{64}\text{Gd}$ . The reduction of strength has a magnitude of  $\sim 20$  W.u. in all three cases. This is indicative for that at least part of the octupole strength in these  $82 < N < 90$  isotopes is generated by the neutrons in the  $\nu(1f_{7/2})$  orbit or by collective modes that are suppressed when pronounced deformation sets in for these isotopes at  $N \gtrsim 90$ . The mechanisms leading to the reduction of strength in Xe towards  $N = 82$  (after the  $\nu 0h_{11/2}$  orbit is half-filled) doesn't apply here, since the higher-lying partner-orbital for octupole correlations,  $0i_{13/2}$ , is still depleted.

**Table 6.12.:** Occupation numbers of protons in the  $Z = 50 - 82$  major shell in some  $N = 80$  and  $N = 82$  isotones. The values for  $N = 80$  stem from shell model calculations [Sie09] based on the GCN5082 interaction ([Sie09]-A) and on the same interaction, but with a modified pairing interaction ([Sie09]-B). The values for the  $N = 82$  isotones are extracted from ( ${}^3\text{He}, d$ ) and ( $d, {}^3\text{He}$ ) transfer reactions [Wil71].

Nucleus	Source	$d_{5/2}$	$g_{7/2}$	$s_{1/2}$	$d_{3/2}$	$h_{11/2}$
${}^{132}\text{Te}$	[Sie09]-A	0.32	1.41	0.02	0.08	0.17
	[Sie09]-B	0.41	1.38	0.03	0.11	0.07
${}^{134}\text{Xe}$	[Sie09]-A	0.85	2.57	0.04	0.16	0.38
	[Sie09]-B	1.01	2.54	0.07	0.21	0.18
${}^{136}\text{Xe}$	[Wil71]	$0.5 \pm 0.2$	$3.5 \pm 0.4$	-	-	-
${}^{136}\text{Ba}$	[Sie09]-A	1.53	3.48	0.08	0.25	0.66
	[Sie09]-B	1.73	3.48	0.12	0.32	0.35
${}^{138}\text{Ba}$	[Wil71]	$0.7 \pm 0.3$	$4.3 \pm 0.4$	-	-	$1.0^{+1.0}_{-0.7}$
${}^{138}\text{Ce}$	[Sie09]-A	2.21	4.31	0.13	0.35	1
	[Sie09]-B	2.43	4.33	0.18	0.44	0.62
${}^{140}\text{Ce}$	[Wil71]	$1.8 \pm 0.2$	$5.6 \pm 0.3$	$\leq 0.2$	$\leq 0.2$	$1.3^{+0.6}_{-0.2}$
${}^{140}\text{Nd}$	[Sie09]-A	2.88	5.03	0.19	0.47	1.43
	[Sie09]-B	3.04	5.05	0.26	0.58	1.07
${}^{142}\text{Nd}$	[Wil71]	$2.6^{+0.2}_{-0.3}$	$5.7^{+0.2}_{-0.4}$	$\leq 0.2$	$\leq 0.2$	$1.3^{+0.6}_{-0.4}$
${}^{144}\text{Sm}$	[Wil71]	$3.6 \pm 0.2$	$6.3 \pm 0.2$	$0.2 \pm 0.1$	$0.3 \pm 0.1$	$1.6 \pm 0.3$

As a function of proton number, a general increase of the  $B(E3)$  strength can be observed for  $N \geq 82$  (and generally also for  $N < 82$ , but here the  ${}_{54}\text{Xe}$  isotopes exhibit a consistently reduced strength compared to the neighboring  ${}_{52}\text{Te}$  and  ${}_{56}\text{Ba}$  isotopes). This can be understood by the gradual filling of the  $\pi 1d_{5/2}$  orbit, which can form octupole correlations with the higher-lying  $\pi 0h_{11/2}$  orbit. The gradual filling of the  $\pi 1d_{5/2}$  orbit already occurs before the  $\pi 0g_{7/2}$  orbit is completely filled, i.e. also for  $52 \leq Z \leq 58$ . This is documented by measurements of occupation numbers of the ground-states of the  $Z = 54 - 62$ ,  $N = 82$  isotones [Wil71] and shell-model calculations in the  $N = 80$  isotones [Sie09]. The measured and calculated occupation numbers are summarized in Table 6.12. However, Nd and Sm

already possess 10 and 12 protons outside the closed shell and clearly show collective behavior. Their  $B(E3)$  strengths for their deformed  $N = 90$  isotopes have been very successfully described by a collective model of nuclear quadrupole-octupole vibrations and rotations [Str12].

### **$B(E3)$ strength at $N = 82$ and in the Xe isotopes, Conclusions**

The available data on  $B(E3, 0_1^+ \rightarrow 3_1^-)$  strength in the  $N = 82$  isotonic chain including the value for  $^{136}\text{Xe}$  determined in this work show a smooth behavior with a monotonic increase of the strength as a function of proton number. This may at last partly be attributed to strength generated by  $\pi(1d_{5/2}) \otimes \pi(0h_{11/2})$  octupole correlations by the mechanism described in [Mue06] and discussed in the previous paragraph. However, the  $B(E3, 0_1^+ \rightarrow 3_1^-)$  strength of the Xe-isotopes below  $N = 82$  behaves qualitatively different than the strength in the Ba and Ce isotopes. It is not clear why the octupole strength generated by the protons, which are presumably the dominant source for the  $B(E3, 0_1^+ \rightarrow 3_1^-)$  strength of  $^{136}\text{Xe}_{82}$ , does not persist below  $N = 82$ . In contrast to Xe, the strength in the Ba and Ce isotopes is not significantly reduced when crossing the neutron shell closure from above. Furthermore, the shell-model calculations in Ref. [Sie09] suggest that the neutron configurations in the  $N = 80$  isotones are basically unaffected by adding protons to  $^{134}\text{Xe}$ . This can be interpreted as a hint that the  $B(E3, 0_1^+ \rightarrow 3_1^-)$  strength of  $^{138}\text{Ba}_{80}$  and  $^{140}\text{Ce}_{80}$  is not generated by neutrons dominantly, since the values of Xe and Te at the same neutron number are significantly lower.

The fact that the energies of the  $3_1^-$ -states are systematically lower in *all* isotopic chains for  $N > 82$  than for  $N < 82$  is also indicative for larger collectivity at the neutron rich side of the neutron shell closure. Surprisingly, the energies seem to behave in the same way for Xe, Ba and Ce, albeit there is clearly "missing" collectivity for  $N < 82$  only in one case (Xe). No data beyond  $N = 82$  is currently available for  $_{52}\text{Te}$ .

Holt *et al.* have calculated  $B(E3, 0_1^+ \rightarrow 3_1^-)$  ground-state transition strengths in  $N = 82$  isotones within the shell-model and the QRPA based on the same interactions derived from the Bonn-A potential [Hol97]. While the shell-model calculation is restricted to the proton orbitals  $0g_{7/2}$ ,  $1d_{5/2}$ ,  $1d_{3/2}$ ,  $0h_{11/2}$ , the QRPA calculation additionally comprises the same orbitals also for neutrons, the proton orbitals  $1p_{3/2}$ ,  $1p_{1/2}$ ,  $0f_{7/2}$ ,  $0f_{5/2}$  as well as the neutron orbitals  $1f_{7/2}$ ,  $2p_{3/2}$ ,  $0h_{9/2}$ ,  $2p_{1/2}$ ,  $0i_{13/2}$  and  $1f_{5/2}$ .

In the shell-model calculations, the energy of the  $3_1^-$  state is consistently over-estimated while the ground-state transition strength is strongly under-estimated throughout the  $N = 82$  isotonic chain. The QRPA calculations in turn are able to reproduce both energy and ground-state transition strength of the  $3_1^-$  states of the

$N = 82$  isotones nicely. The authors state that these two approaches yield information on two differently structured  $3^-$  states, where the lower-lying  $3^-$  states are not accessible by the shell-model due to the limited configurational space. The  $3^-$  states emerging in the shell-model calculations are proton valence-space configurations involving the  $h_{11/2}$  intruder orbital. They are mostly identified as the  $3_2^-$  states in the  $N = 82$  isotones.  $3^-$  states at similar energies emerge from the QRPA calculations which have two-quasiparticle character and are pure proton-excitations.

The experimentally observed yrast  $3^-$  states of the  $N = 82$  isotones with consistently strong ground-state transitions are associated with the lowest-energy states emerging from the QRPA calculations<sup>5</sup>. These are collective core excitations involving both proton and neutron degrees of freedom. While the work of Holt *et al.* is the only shell-model calculation found that quotes the obtained  $B(E3, 3_1^- \rightarrow 0_1^+)$  strength for  $^{136}\text{Xe}$ , a collective strength close the experimental value as it is obtained in the QRPA calculations of Holt *et al.* is found also in other RPA calculations [Ero01, Isa05]. They all predict a collective  $3_1^-$  state also for  $^{134}\text{Te}$ .

The evolution of the energies of the  $3_1^-$  and  $3_2^-$  states of  $N = 82$  isotones are plotted in Figure 6.43. It is clearly visible that the energies of the yrast  $3^-$  states drops quickly for larger proton number  $Z$ , while the energies of the  $3_2^-$  state drop more slowly. In consequence, the energies of the  $3_1^-$  and  $3_2^-$  states of the  $N = 82$  isotones approach each other for smaller proton numbers towards  $Z = 50$ .

In summary, the picture of two competing, non-mixing structures of  $3^-$  states emerges. It is clearly visible in Figure 6.43 that they approach in the  $N = 82$  isotones as the number of protons is reduced. The case of  $^{136}\text{Xe}$  seems to represent the cornerstone of a transition where either of the structures becomes yrast. Nuclei "south-west" of  $^{136}\text{Xe}$  exhibit a valence-nucleon generated, non-collective  $3_1^-$  state, while nuclei "north" and "east" of  $^{136}\text{Xe}$  exhibit a collective first  $3^-$  state. The microscopic mechanisms leading to this very abrupt change of the structure of the  $3_1^-$  state close to  $^{136}\text{Xe}$  is not clear at the moment.

In order to obtain a satisfactory, microscopic understanding of the behavior of the  $B(E3, 0_1^+ \rightarrow 3_1^-)$  strength in the proximity of the  $N = 82$  shell closure around  $^{136}\text{Xe}$ , measurements of this transition strength in the nuclei  $^{138,140}\text{Xe}$ ,  $^{134-138}\text{Te}$  and  $^{140,142}\text{Ba}$  are indicated. Gyromagnetic ratios ("g-factors") would be sensitive to the proton and neutron contribution of the wave functions of the  $3_1^-$ -states, but their measurement is strongly hindered by the short level lifetimes due to fast  $E1$  transitions to the  $2_1^+$  state. The experimentally most interesting cases are

<sup>5</sup> Unfortunately, the discussion in [Hol97] is confused by the fact that the  $B(E3, 3_1^- \rightarrow 0_1^+)$  strength of  $^{138}\text{Ba}$  in units of  $e^2 b^3$  is misinterpreted as being in Weisskopf units and by a wrong, unreferenced "very weak  $E3(3^- \rightarrow 0^+)$  transition [...] measured in  $^{136}\text{Xe}$ ".

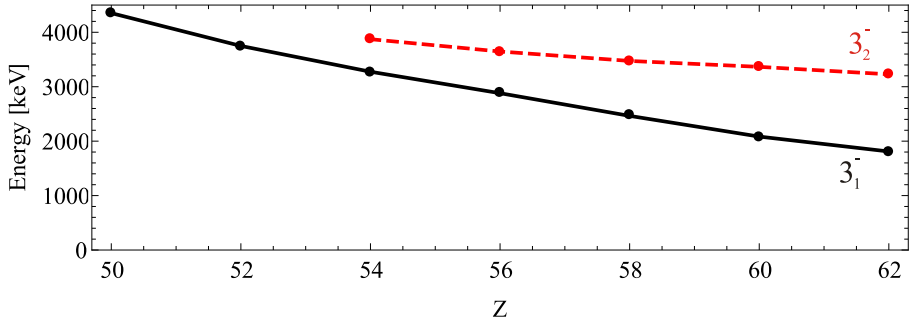


**Figure 6.43.:** Energy of the  $3_1^-$  and  $3_2^-$  states of  $N = 82$  isotones as a function of proton number  $Z$ . For  $^{140}_{58}\text{Ce}$ , the energy of the  $3_3^-$  state is plotted, as suggested in [Hol97]. The energies of the  $3_1^-$  states are taken from the same references as in Figure 6.41, the energies of the non-yrast  $3^-$  states are taken from [Son02].

$^{138,140}\text{Xe}$  and  $^{134-138}\text{Te}$ . Their investigation would answer the question whether low  $B(E3, 0_1^+ \rightarrow 3_1^-)$  strength is found also above  $N = 82$  in these elements and whether there is also a sudden jump in octupole collectivity at  $N = 82$  in Te. Detailed microscopic calculations in a large configurational space for Te, Xe, Ba and Ce isotopes across the neutron shell closure would also be highly pertinent.

Since all of these nuclei are unstable, sub-barrier Coulomb-excitation in inverse kinematics at a RIB facility would be the experimental method of choice. Light targets should be used in order to suppress multi-step Coulomb excitation via intermediate ( $2_1^+$ ,  $4_1^+$ ) states. Additionally, the lifetime of the  $3_1^-$  states and the branching ratios of their decays should be measured in order to firmly pin down the  $B(E3, 0_1^+ \rightarrow 3_1^-)$  strengths. The method of the differential caDSAM (see Chapter 4.4) would be ideally suited for the measurement of these very short lifetimes and can be performed together with a Coulex measurement in one single RIB experiment.

If the  $3_1^-$  state of  $^{136}\text{Te}$  is similarly collective as the one in  $^{136}\text{Xe}$  (which is expected from the above considerations), the aforementioned upcoming experiment at HIE-ISOLDE [Sta14] may already yield the  $B(E3, 0_1^+ \rightarrow 3_1^-)$  strength of  $^{136}\text{Te}$ .

---

## 6.2 Identification of the $\pi p_{3/2} \rightarrow \pi p_{1/2}$ spin-flip transition in $^{85}\text{Br}$

---

The investigation of the evolution of nuclear shell structure as a function of proton and neutron number is a major subject of nuclear structure physics. Nowadays, a main focus is on the shell evolution in nuclei with large proton-neutron asymmetry, i.e. far off stability [Gad08]. For understanding the structure and the properties of atomic nuclei in terms of the very successful nuclear shell model [Cau05, Bro88], the nucleon-nucleon interaction and the energies of the single-particle orbits are major ingredients. Single-particle energies are altered by the nucleon-nucleon interaction [Ots10a] and they are experimentally accessible especially in nuclei in vicinity of doubly-closed shells.

In this context, the single-particle structure of nuclei in proximity to the doubly-magic nucleus  $^{78}\text{Ni}$  is of current interest. The evolution of the proton single-particle energies in the Nickel isotopic chain has been subject of extensive experimental [Fra98, Fra01, Fla09] and theoretical work [Fra01, Ots05, Ots10a]. Dramatic and rapid changes in the proton single-particle energies are observed when approaching doubly-magic  $^{78}\text{Ni}$  as a function of neutron number, specifically in the relative positions of the  $\pi p_{1/2}$ ,  $\pi p_{3/2}$ ,  $\pi f_{5/2}$  and  $\pi f_{7/2}$  orbitals. The tensor force, a non-central part of the nuclear interaction, has been identified as an impetus of the evolution of these proton single-particle energies as a function of the filling of the  $\nu g_{9/2}$  shell [Ots05, Ots10a].

The evolution of proton single-particle energies of the  $N = 50$  isotones, approaching  $^{78}\text{Ni}$  as a function of (decreasing) proton number, can be studied by the energies of identified single-particle states of the  $N = 50$  isotones with odd proton number. This is depicted in Figure 6.44.

The ground state of  $^{81}_{31}\text{Ga}_{50}$  has spin 5/2 [Che10] and presumably negative parity [Bag08]. The same ground state spin and parity are assumed for  $^{83}_{33}\text{As}_{50}$  [McC15]. The first excited state of both nuclei is expected to be a  $3/2^-$ -state, but no (candidates for) low-lying  $1/2^-$ -states are identified [Bag08, McC15, Sah12]. In the nuclei  $^{85}_{35}\text{Br}_{50}$  and  $^{87}_{37}\text{Rb}_{50}$ , the ground states have adopted spin/parity assignments  $3/2^-$  and the first excited states have adopted spin/parities  $5/2^-$  [Sin14, Hel02]. Under the assumption of the tentative spin/parity-assignments for the states of  $^{81}\text{Ga}$  and  $^{83}\text{As}$  and assuming that all excited states have single-particle character, a quite constant single-particle energy difference between the  $\pi p_{3/2}$  and  $\pi f_{5/2}$  orbitals ranging from  $\sim 300$  keV to  $\sim 400$  keV can be inferred for  $N = 50$  and  $Z = 31 - 37$ .

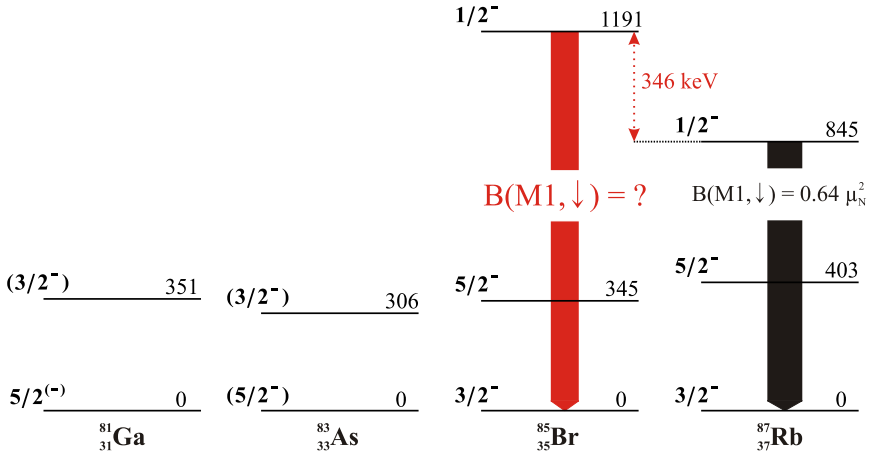


**Figure 6.44.:** Energies of low-lying excited states in  $N = 50$  isotones. Spin/parities in parentheses are tentative assignments. See text for details and references.

In  $^{87}\text{Rb}$ , the second excited state at 845 keV excitation energy could be unambiguously identified as the main component of the  $\pi p_{3/2} \rightarrow \pi p_{1/2}$  spin-flip transition [Sta13]. This identification is based on a firm assignment of the spin  $J = 1/2$  of the 845-keV state and the observation of its strong  $M1$ -transition to the ground state. The spin assignment and the ground state  $M1$  transition strength of  $B(M1, \downarrow) = 0.644^{+0.075}_{-0.053} \mu_N^2$  were pinned down based on a lifetime measurement within this work<sup>6</sup> [Sta13] employing the caDSA Method (Section 4) combined with results from previous experiments employing NRF [Käu02] and transfer reactions [Med75, Com73, Har72].

In fact, single-particle spin-flip transitions exhibit some of the largest  $M1$  transition strengths observed in nuclei in the order of  $\sim 1 \mu_N^2$ . This is exemplarily shown in a calculation in Appendix E for the case of the  $\pi p_{3/2} \rightarrow \pi p_{1/2}$  spin-flip transition of  $^{87}\text{Rb}$ . The large  $M1$  transition strength can serve as a unique signature for single-particle spin-flip transitions.

<sup>6</sup> The respective experiment was performed at the UNILAC accelerator at GSI, Darmstadt, using EUROBALL cluster detectors. The excited state was populated in proton-transfer from a  $^{12}\text{C}$ -target to  $^{86}\text{Kr}$  beam ions. The experiment will not be further discussed in this thesis and the reader is referred to Reference [Sta13].

---

In  $^{85}\text{Br}$ , the first excited  $1/2^-$ -state is at 1191 keV excitation energy [Sin14]. If this state is the main component of the proton  $p_{3/2} \rightarrow p_{1/2}$  spin-flip excitation, there is a sudden and pronounced change in the single-particle energy difference between the  $\pi p_{3/2}$  and  $\pi p_{1/2}$  orbitals of  $\sim 350$  keV when going from  $Z = 35$  to  $Z = 37$ . This conclusion, however, requires the firm identification of the transition between the  $3/2^-$  ground state and 1191-keV  $1/2^-$  excited state of  $^{85}\text{Br}$  as  $\pi p_{3/2} \rightarrow \pi p_{1/2}$  spin-flip transition. The experimental signature for this identification would be a strong  $M1$  transition strength between the 1191-keV  $1/2^-$ -state and the ground state.

The measurement of this  $M1$  transition strength and, hence, the identification of the 1191-keV  $1/2^-$ -state of  $^{85}\text{Br}$  as the main component of the proton  $p_{3/2} \rightarrow p_{1/2}$  spin-flip excitation, is the aim of experiment S426 conducted at GSI's PreSPEC-AGATA setup in spring 2014 [Pie11]. Originally, the ground state  $M1$  transition strength of the 1191-keV state was supposed to be measured by relativistic  $M1$  Coulomb excitation of that state at two different beam energies, as described in the introduction of Section 5. A drastic reduction of the allocated beam time with respect to the beam time originally approved by the G-PAC triggered the development of the Coulex-Multipolarimetry Method within this work (see Chapter 5) and its application in experiment S426. This method allows not only to measure the  $E2/M1$  multipole mixing ratio of the transition from the 1191-keV state to the ground state, but also the absolute  $M1$  transition strength can be inferred relative to the known  $B(E2)$ -strength of the 548-keV  $3/2_{gs}^+ \rightarrow 7/2_1^+$  transition in the utilized gold targets.

The experiment is described in Section 6.2.1. The analysis of the data taken in this experiment is subject of the doctoral thesis of M. Lettmann, TU Darmstadt, and ongoing. Perspectives for the data analysis are discussed in Section 6.2.2.

---

## 6.2.1 PreSPEC-AGATA experiment S426

---

Experiment S426 aiming at the identification of the  $p_{3/2} \rightarrow p_{1/2}$  spin-flip transition in radioactive  $^{85}\text{Br}$  by the Coulex-Multipolarimetry Method (Chapter 5) was conducted at GSI's PreSPEC-AGATA setup in spring 2014. The PreSPEC-AGATA setup is described in Section 6.2.1.1. The planning of the experiment in terms of expected peak shapes, statistics and background is discussed in Section 6.2.1.2. The time structure of the beam, the experimental setup, the DAQ and the way the recorded data will have to be treated in the analysis were modified with respect to the standard procedures applied during the PreSPEC-campaign in order to maximize the

experimental statistics that could be collected within the skimpy beam time. These modifications are described in Section 6.2.1.3.

### 6.2.1.1 The PreSPEC-AGATA setup

Primary beams of relativistic heavy ions are delivered by GSI's Schwerionen-Synchrotron SIS18 [Hen92]. Kinetic energies up to 2 GeV/u can be provided for moderate mass elements and energies up to 1 GeV/u can be provided for all elements up to uranium. Maximum beam intensities are  $\sim 2 \times 10^8 \text{ s}^{-1}$  for Uranium. Intensities higher by up to few orders of magnitude are achieved for lighter elements.

This primary beam impinges on thick production targets, where secondary exotic beams are produced in-flight by fission or fragmentation. Typically, beryllium is used as material of the production target for fragmentation and lead is used for secondary beam production by fission. Typical thicknesses of these targets are 1-4 g/cm<sup>2</sup>. The products of the fission or fragmentation of stable primary beam ions are "cocktails" of secondary, mostly radioactive ions moving preferably in the direction of the primary beam.

Among this cocktail of secondary ions, single isotopic species can be selected in-flight by the FRagment Separator (FRS) [Gei92]. The FRS is a zero-degree magnetic spectrometer consisting mainly of four dipole magnets (green elements in Figure 6.45). In the magnetic field of the dipole magnets, the ions are deflected

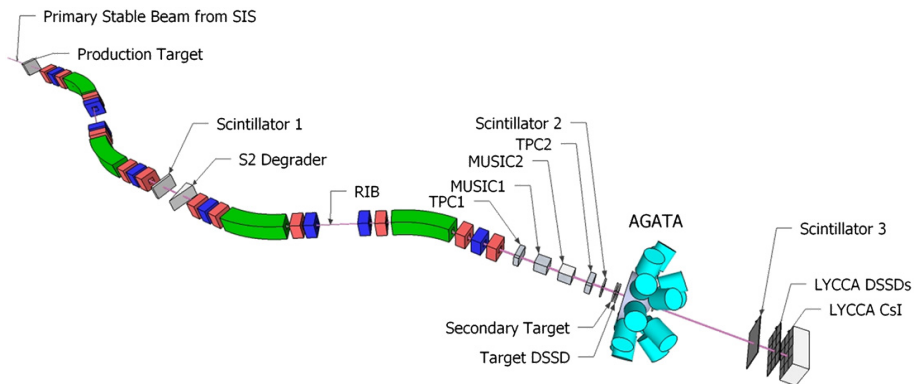


**Figure 6.45.:** Sketch of the PreSPEC-AGATA setup and GSI's Fragment Separator (FRS). The ion beam direction is from left to right. Figure reprinted from [DP12] with permission from Elsevier. See text for details.

---

and spatially separated according to their magnetic rigidity  $B\rho \propto \gamma\beta A/Q$ , where  $B$  is the magnetic field strength,  $\rho$  is the radius of the ion trajectory inside the field,  $A$  is the mass-number,  $Q$  the charge and  $\beta = v/c$  the velocity of the ions. At the central focal plane S2, between the second and third dipole magnet, a degrader made of aluminum imposes a charge-dependent energy loss  $\Delta E$  upon the ions (labeled as "S2 degrader" in Figure 6.45). Hence, ions are first separated in terms of  $B\rho$ , then by  $\Delta E$  and then again by  $B\rho$ . This method of ion separation is called the  $B\rho - \Delta E - B\rho$  method. The isotope of interest is pre-selected by slit systems at the four focal planes of the FRS. For details, the reader is referred to Reference [Gei92].

Detectors for particle identification are mounted at the S2 focal plane and at the final fourth focal plane S4 (behind the fourth dipole magnet) of the FRS (see Figure 6.45). At each of these sites, two time projection chambers (TPC, [Hli98, tpc]) are mounted for the measurement of the position and direction of motion of the ions and a scintillator detector for the measurement of the time-of-flight (TOF) of the ions between S2 and S4. At the fourth focal plane, the charge number  $Z$  of the ions is measured via energy loss by two ionization chambers (MUSIC, [mus]). Each of these quantities is measured on an event-by-event basis, i.e. for each individual ion. The mass-over-charge ratio  $A/Q$  can then be inferred from the ions' magnetic rigidity via the ion positions measured in the TPCs at S2 and S4, the magnetic field strengths of the dipole magnets and the TOF between S2 and S4. Additionally, the ion position at S2 and S4 in the dispersive plane can be measured from time differences of light signals generated by the ions in the scintillators, read out from two sides. The charge number  $Z$  of each ion can be obtained from the ionization chambers and the TOF between S2 and S4. Further details can be found in References [Gei92, Wol05].

The target for secondary reactions and the AGATA  $\gamma$ -ray detectors (see Section 3.3) are mounted downstream of the detectors for ion identification at the fourth focal plane S4 of the FRS. The LYCCA calorimeter [Gol13] is devoted to identify the ions behind the secondary target, e.g. for the selection of reaction channels. It consists of the following parts:

- A segmented double-sided silicon strip detector (DSSSD) mounted directly in front of the secondary target for the determination of the transverse position of each ion at the target.
- Scintillator detectors  $\sim 0.7$  m in front of the target and  $\sim 3.6$  m downstream of the target for the measurement of the velocity  $\beta$  of the ions behind the target.

- A wall of segmented DSSSDs followed by a wall of CsI detectors  $\sim 3.6$  m downstream of the secondary target for the measurement of energy loss  $\Delta E$  and total kinetic energy  $E$  of the ions behind the target.

The following quantities can be derived on event-by-event basis using the FRS and LYCCA detectors:

- Mass number  $A_{in}$  and charge number  $Z_{in}$  of the secondary beam ions in front of the secondary target, i.e. after leaving the FRS, by the time-of-flight (TOF) between S2 and S4 and positions at S2 and S4 yielding  $B\rho$  as well as  $\Delta E$  from the MUSIC detectors.
- Transverse position and direction of motion of the ions when entering the secondary target from positions measured in the TPCs and the target DSSSD.
- Direction of motion of the ions when leaving the secondary target from positions measured in the target DSSSD and the downstream wall of DSSSDs.
- The scattering angle in the secondary target from the ions' directions of motion in front of and behind the target.
- The velocity of the ions behind the secondary target from the TOF between the LYCCA TOF detector in front of the target and  $\sim 3.6$  m further downstream.
- Mass number  $A_{out}$  and charge number  $Z_{out}$  of the ions behind the secondary target from the energy loss measurement in the LYCCA wall of DSSSDs (yielding  $Z_{out}$ ), the velocity behind the target and the total kinetic energy measurement in the LYCCA CsI detectors (yielding  $A_{out}$ ).

In summary, the species, position and momentum vector of every ion can be determined in front of and behind the secondary reaction target. For further details on the experimental setup, the reader is referred to Reference [Wol05]. This reference describes the experimental setup used in the RISING fast beam campaign, which is the predecessor of PreSPEC. Some detectors for ion identification have changed in between the two campaigns, yet most of the discussion in [Wol05] applies to the PreSPEC-setup as well. Differences between the RISING fast beam and PreSPEC setup are discussed in Reference [Pod08]. The data acquisition system (DAQ) used in the PreSPEC-AGATA campaign is described in Reference [Ral15].

For experiment S426 employing the Coulex-Multipolarimetry Method (see Section 5), two thick gold targets were mounted at the secondary target position. Gold was chosen as target material for the following reasons:

- Good mechanical properties.
- High chemical stability (no oxidation) and purity.
- High Coulomb excitation cross section due to high  $Z$ .
- Ground state  $E2$  transition with well-known transition strength at suitable energy for relative Coulomb excitation yield measurement.
- High stopping power for the bromine beam.
- Inexpensive isotopically pure material: Only one stable isotope.

The relative thicknesses of the targets were chosen such that approximately equal sensitivity to the peaks from the decay of the 1191-keV state of  $^{85}\text{Br}$ , Coulomb-excited in both targets, can be expected. Here, equal sensitivity means that the peaks from excitations in both targets are equally high in terms of counts per keV, resulting in a comparable peak-to-background ratio. The absolute target thicknesses are chosen such that good sensitivity to the multipole mixing ratio of the decay of the 1191-keV excited state of  $^{85}\text{Br}$  is achieved (see Section 6.2.1.3) while the expected broadening of the Doppler-corrected  $\gamma$ -ray energies due to different ion velocities at the time of de-excitation is kept at a reasonable level (see Section 5.3.4).

The first target with a thickness of  $2 \text{ g/cm}^2$  was mounted at the nominal target position in the focus of the AGATA detectors. The second target with a thickness of  $1 \text{ mg/cm}^2$  was mounted 10 cm further downstream. Both targets were quadratic with an edge length of 10 cm. A photograph of the mounted targets is shown in Figure 6.46.

---

### 6.2.1.2 Planning of experiment S426

---

In the following discussion, reduced transition strengths of  $B(E2, \downarrow) = 2 \text{ W. u.}$  and  $B(M1, \downarrow) = 0.58 \mu_N^2$  are assumed for the decay of the  $1/2^-$ -state of  $^{85}\text{Br}$  at 1191 keV. According to equation (5.2), this corresponds to an  $E2/M1$  multipole mixing ratio of  $\delta_{E2/M1} = 0.087$ .

A beam energy of 300 MeV/u is chosen for the secondary beam of radioactive  $^{85}\text{Br}$ . It is produced by the fragmentation of a 730 MeV/u primary beam of  $^{86}\text{Kr}$  on a beryllium production target. According to simulations performed with LISE++ [Tar08] and MOCADI [Iwa11, and references therein], a beam purity better than 99.9% is expected at the secondary target position [Pie11]. The primary beam of



**Figure 6.46.:** Targets for experiment S426 mounted in the PreSPEC-AGATA setup. The beam ions enter from the right. Their transverse position is measured in the target DSSD (green PCB frame) before they impinge on the first gold target at the nominal target position in the focus of the AGATA detectors. This target has a thickness of  $2 \text{ g/cm}^2$ . The second target with a thickness of  $1 \text{ g/cm}^2$  is mounted 10 cm further downstream. The quadratic targets have an edge length of 10 cm. See text for details.

$^{86}\text{Kr}$  can be provided by SIS18 with high intensity and the production of the close-to-stability nucleus  $^{85}\text{Br}$  is efficient. Consequently, the particle rate at the secondary target is not limited by the intensity of the primary beam, but rather by the particle rate that can be processed by the detectors used for ion identification (see also discussion in Section 6.2.1.3).

According to ATIMA [Ge15], the bromine ions leave the  $2 \text{ g/cm}^2$  upstream target with an energy of  $242 \text{ MeV/u}$  and the downstream  $1 \text{ g/cm}^2$  target with  $210 \text{ MeV/u}$ . A significant difference in average ion velocity in both targets is therefore ensured by the choice of the target thicknesses.

### Expected peak shapes

Expected peak shapes for the discussed conditions and the geometry of the AGATA detectors in the PreSPEC setup were calculated using APCAD (Appendix B.2) assum-

ing a level-lifetime<sup>7</sup> of 50 fs. They are shown in Figure 6.47. For the Doppler corrections, it was assumed that the ion velocities behind the downstream target are measured with a relative uncertainty of 1%. In the Doppler correction for the upstream target, a fixed offset for the ion velocity with respect to the value measured behind the downstream target was assumed. Significant, but acceptable broadening of the peaks after Doppler correction occurs especially at forward-angles due to the sizable thicknesses of the targets. The peaks stemming from excitations in the upstream and downstream target are clearly separated for all angles covered by the AGATA detectors.

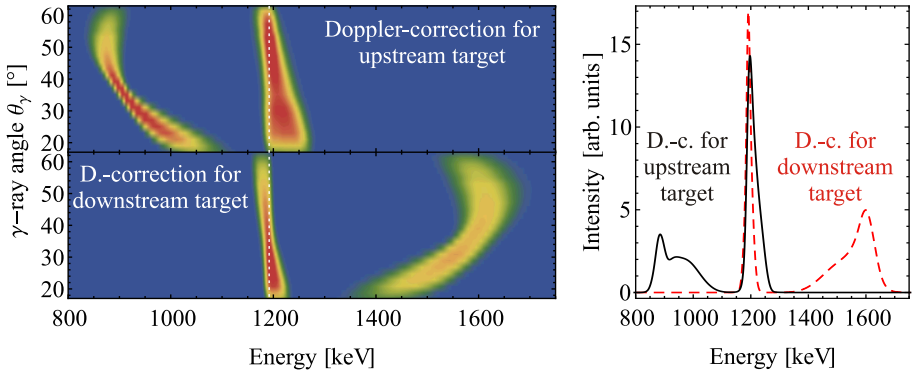


**Figure 6.47.:** Peak shapes expected in experiment S426, simulated using APCAD.

**Left:** Spectra as a function of  $\gamma$ -ray energy and detection polar angle  $\theta_\gamma$ , Doppler-corrected assuming the center of the upstream/downstream target as  $\gamma$ -ray vertex (top/bottom). The unshifted  $\gamma$ -ray energy is indicated by the dashed, white line.

**Right:** Projection of the spectra on the energy axis. See text for details.

### Expected peak areas and sensitivity to $\delta_{E2/M1}$

The cross section for Coulomb excitation of the 1191 keV-state of  $^{85}\text{Br}$  is small for the assumed transition strengths. It drops from 3.3 mbarn at 200 MeV/u to 2.7 mbarn at 300 MeV/u, as calculated with DWEIKO [Ber03]. Nevertheless, the excitation probability is  $2.4 \times 10^{-5}$  due to the very thick targets.

The expected ratio of peak areas from excitations in the first (upstream) and second (downstream) target as a function of the transition's  $E2/M1$  multipole mixing

<sup>7</sup> The assumed transition strength of  $B(M1, \downarrow) = 0.58 \mu_N^2$  alone corresponds to lifetime of the  $1/2^-$ -state of 58 fs.

ratio  $\delta_{E2/M1}$  is shown in Figure 6.48. In that calculation, the different  $\gamma$ -ray vertices for excitation in either of the two targets and the resulting difference in polar angles covered by AGATA and the Lorentz-boost are taken into account. Since the excited state has spin 1/2, the  $\gamma$ -ray emission in the emitter rest frame is necessarily isotropic. In the discussed calculation, it is assumed that AGATA covers polar angles from  $\theta_\gamma = 16^\circ$  to  $\theta_\gamma = 61^\circ$ . The exact geometry of AGATA in the PreSPEC-setup was not taken into account. Also ignored is the spatial profile of the secondary beam. In the final analysis, such a curve of peak-area ratios as a function of multipole mixing ratio should be determined in a detailed Monte-Carlo simulation.

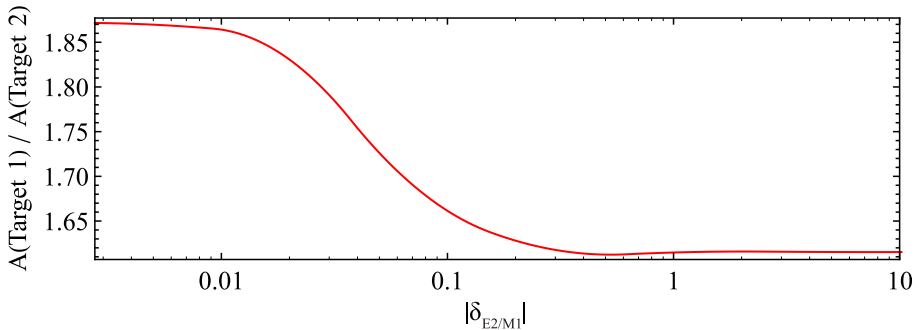


**Figure 6.48.:** Ratio of peak areas expected in experiment S426 from excitation in target 1 (upstream) and target 2 (downstream). See text for details.

24 shifts à 8 hours for data taking were budgeted by the G-PAC for experiment S426. A secondary  $^{85}\text{Br}$  beam intensity of  $2.5 \times 10^4 \text{ s}^{-1}$  on the secondary target is the maximum that can be reasonably handled by the detectors for identification of the incoming beam ions. With this secondary beam intensity, around  $4 \times 10^5$  excitations of the 1191-keV level of  $^{85}\text{Br}$  can be expected. Conservatively assuming a total detection efficiency for the whole setup of 2%, 8000 counts are expected to be detected, sufficient for a reliable measurement of the  $M1$  strength of the decay even at sizable background levels.

### Expected background level

The level of  $\gamma$ -ray background can be estimated from the background observed in a test shift for experiment S426 which was run in 2012. This test was performed with a secondary beam of  $^{85}\text{Br}$  at 300 MeV/u impinging on a single  $400 \text{ mg/cm}^2$  gold target. Data was taken for 8.6 hours with an average beam intensity of  $2.6 \times 10^4 \text{ s}^{-1}$ . A background level of about 20 counts per keV was observed at a  $\gamma$ -ray energy of 1191 keV after Doppler correction [Pie14a, Ree15].  $\gamma$ -ray tracking in AGATA

---

was not employed. Instead, for each  $\gamma$ -ray event the interaction point determined in PSA with the highest energy deposit was assumed to be the first  $\gamma$ -ray interaction point. The energy information was obtained from the core signals. A gate in particle- $\gamma$ -ray time difference was applied. The following scaling was applied for an estimate of the background level expected in experiment S426:

- The performance commissioning of the PreSPEC-AGATA campaign was *inter alia* performed with a 150 MeV/u beam of  $^{80}\text{Kr}$  ions, Coulomb-excited on a 400 mg/cm<sup>2</sup> gold target [Pie14b]. Runs with an empty target frame revealed that the observed background level with target is about 130% of the background level without target. In other words, only about one quarter of the background is produced in the 400 mg/cm<sup>2</sup> gold target. Consequently, with a total of 3 g/cm<sup>2</sup> target mass, a background level higher by only a factor of 2.5 would be expected. Geometrical effects arising from the two targets in experiment S426 and an influence of the beam energy on this ratio are neglected.
- The test shift was run at the nominal beam intensity for experiment S426 and there was beam on target for about 8.6 hours. Hence, scaling for 24 shifts in experiment S426 yields a factor for the time of the measurement of 22.3.
- In the test run, effectively 14 AGATA crystals were available. In experiment S426, 22 crystals were used, resulting in a factor 1.6.

Simulated spectra are shown in Figure 6.49. The background was obtained by scaling the background observed in the 2012 test run as described above. 8000 registered  $\gamma$ -rays from the de-excitation of the 1191-keV state of  $^{85}\text{Br}$  exhibiting the peak shapes after Doppler corrections shown in Figure 6.47 were assumed. The fluctuation of the bin contents was modeled by Gaussian noise where  $\sigma$  is given by the square-root of the total bin contents (peak plus background). These estimates for peak areas and background levels for experiment S426 show that the background level is the limiting factor in this experiment. However, a reduction of the background level and a resulting improvement of the peak-to-background ratio can be expected from  $\gamma$ -ray tracking, which was not taken into in the estimates. As stated before, the discussed estimates imply that peak areas from the excitations in both targets can be measured with sufficient precision for a reliable measurement of the  $M1$  strength of the decay of 1191-keV state of  $^{85}\text{Br}$ .

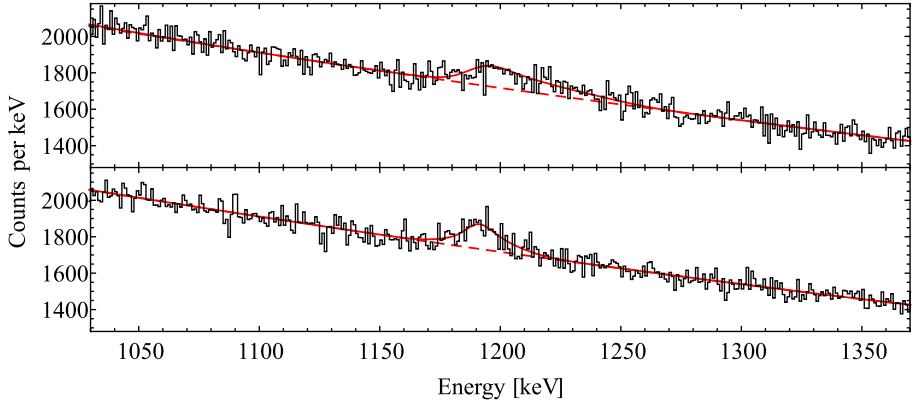


**Figure 6.49.:** Simulation of the  $\gamma$ -ray spectrum expected in experiment S426 for Doppler correction assuming excitation in the upstream target (top) and the downstream target (bottom). 24 shifts of beam on target are assumed. See text for details.

---

### 6.2.1.3 Modifications for experiment S426

---

The allocated beam-time for experiment S426 was reduced to 12 instead of 24 shifts before the experiment started. Whether the experiment should be conducted under these circumstances was decided after data were taken for 4.5 shifts. For these 4.5 shifts, measures were taken in order to reduce the background level and enhance the efficiency of the measurement as much as possible. These measures included optimization of slit positions at the S2 and S4 focal planes of the FRS in terms of observed  $\gamma$ -ray intensity per  $^{85}\text{Br}$  ion identified in LYCCA and removal of the LYCCA target TOF detector. This millimeter thick plastic scintillator was located very close to the target and certainly is a source of background  $\gamma$ -radiation. Its time information is redundant in principle, since a start signal for the TOF from the secondary target to the LYCCA wall detectors can also be obtained from another LYCCA scintillator detector which is located  $\sim 0.7$  m upstream of the secondary target.

Another measure was the modification of the time structure of the primary beam of  $^{86}\text{Kr}$  ions extracted from the SIS18. It had been noticed from particle times measured in the scintillators at the second and fourth focal plane of the FRS that the time differences between consecutive ions in the beam exhibit a certain, unexpected structure. If the ions are spatially longitudinal and time-wise randomly

---

distributed in the beam (following Poisson statistics), an exponential distribution would be expected for the time difference between consecutive ions. The negative exponent of this expected exponential distribution is then given by the time multiplied by particle rate (see e.g. [Fel40, Eq. (1)]).

In contrast, the distribution shown in the top part of Figure 6.50 was observed. Short time differences between consecutive ions are observed more frequently than expected for a random distribution of the ions in the beam. This is indicative for a "clustering" into packets of ions in short time intervals. Within these packets, the instantaneous ion rate is higher and in between the packets it is lower than the average ion rate. In the logarithmic plot of the distribution of time differences in Figure 6.50, this results in different slopes of the curve for short and long time differences. The time differences shown in Figure 6.50 were measured with the scintillator at the second focal plane S2 of the FRS and using a VULOM module [Vul] with a dedicated firmware [Kur14].

The observed time structure of the ion beam extracted from SIS18 is unfavorable from the experimental point of view for several reasons:

- Within the packets of ions, the instantaneous rate is high and eventually exceeds the maximum particle rate that can be taken by the detectors for beam identification, especially the TPC and MUSIC detectors. As a consequence, the average rate has to be reduced.
- The loss of events due to dead time of the data acquisition system (DAQ) is significantly enhanced. The dead time is defined as the fraction of time where the DAQ can not register any event because it is busy with processing a previous event. At the PreSPEC-AGATA setup, the time needed to process an event is at least  $90 \mu\text{s}$  [Ral15]. If an event is registered within a packet of beam ions, the time where the DAQ is busy extends over the rest of the packet. Events caused by the following ions in the packet can not be registered. On the other hand, it is likely to be in a time span *between* two beam ion packets where the DAQ is ready to register events again. In these time spans, the instantaneous ion rate is low and events are unlikely. This means that, effectively, the DAQ is preferably busy while the instantaneous rate is high and many events can not be registered and the DAQ is preferably available when the instantaneous rate is low and only few events occur.
- The high instantaneous rate within the packets of ions results in enhanced  $\gamma$ -ray background. The high probability for very short time differences between consecutive ions makes it likely that multiple ions are registered within one event. In this case, the background generated by all particles in the

---

event is registered. At the same time, eventually only one of the ions fulfills all trigger requirements [Ral15] and may have undergone the desired reaction. If the time difference between the ions can not be resolved by the detectors, contributions by different ions can not be distinguished and the peak-to-background ratio will be reduced.

In order to avoid these disadvantages arising from the clustered structure of the ion beam, the SIS beam was bunched as described in References [For00, For06]. This bunching imprints a new time structure on the ion beam extracted from SIS18 both on short timescales of tens of nanoseconds and also on longer timescales of tens of microseconds. This is shown in the lower part of Figure 6.50. Two striking effects of the bunching are visible:

- 1) The excess of short time differences between consecutive ions is clearly reduced compared to the situation without bunching.
- 2) The time differences are discretized. Only integer multiples of  $\sim 220$  ns appear. This time difference is related to the revolution frequency of the beam in SIS18 [For00].

The first point relaxes the problems described above and allows to measure with higher average beam intensity. The second point offers the following advantage: The slowest detectors in the setup are the AGATA  $\gamma$ -ray detectors with a time resolution of about 10 ns [Cre10]. This is entirely sufficient to distinguish  $\gamma$ -rays emitted at the target positions from two consecutive ions separated by 220 ns. In consequence, the disadvantage of multiple ions being registered in a single event as described above is now resolved. If two consecutive ions with a time difference of at least 220 ns are registered in one event, each detected  $\gamma$ -ray can unambiguously be assigned to one of the ions and the event can be split in the analysis. In this context, splitting the events means that the hits in each detector belonging to one single beam ion are identified, separated and treated as a new event with ion multiplicity one. Then, the problem of background accumulated from multiple ions per event does not persist anymore.

The data shown in Figure 6.50 was taken with one single scintillator at S2. Very short time differences of consecutive ions below  $\sim 100$  ns can not be resolved by this measurement. Therefore, a statement about whether multiple ions are extracted at very small time differences, i.e. within one bunch, has to be derived from another measurement performed with multiple detectors. The CsI-detectors in the downstream wall of LYCCA are well suited for this purpose. The left hand side of Figure 6.51 shows time differences between multiple ions detected in one event, but in different CsI detectors. Note that in Figure 6.51 inherently different data is

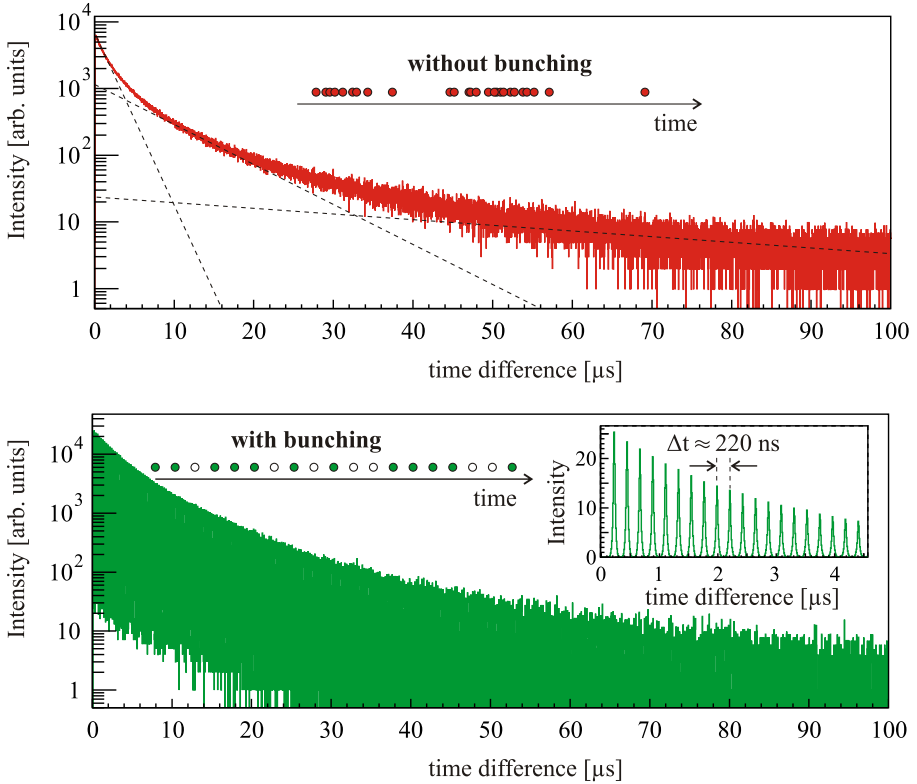


**Figure 6.50.:** Time structure of the  $^{86}\text{Kr}$  beam extracted from SIS18 in experiment S426, measured with the scintillator at the S2 focal plane of FRS.  
**Top:** Time structure without bunching of the SIS beam. The dashed lines visualize the different slopes of the distribution at different time differences and are drawn to guide the eye. The clustering of the ions is depicted on the top of the figure.  
**Bottom:** Time structure with bunching of the SIS beam. The difference in the slope of the distribution for short and long time differences is strongly reduced. Furthermore, only discrete time differences occur (inset). See text for details.

shown than in Figure 6.50. For the former figure, events where exactly two ions were registered in LYCCA were selected and time differences for hits in different CsI detectors of one central module of the downstream LYCCA wall, consisting of nine

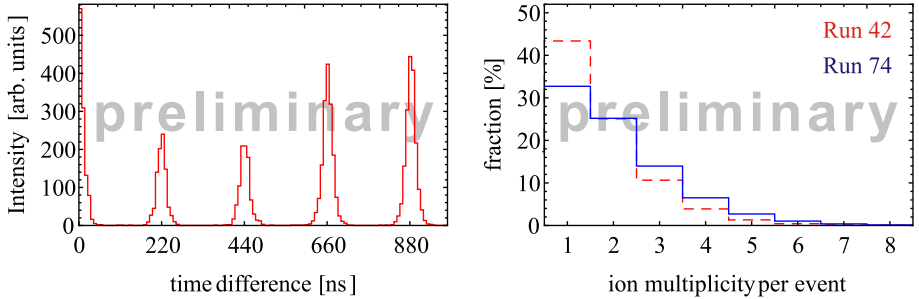


**Figure 6.51.:** **Left:** Time structure of the  $^{86}\text{Kr}$  beam extracted from SIS18 in experiment S426, measured with CsI detectors of the downstream wall of LYCCA. Shown are time differences of multiple ions measured in different CsI crystals of one central LYCCA module in one event. Events with multiplicity two measured in the LYCCA wall DSSSD from experimental run 42 were chosen, where the average ion rate in the spill was  $\sim 3.3 \times 10^4$ .

**Right:** Distribution of ion multiplicities measured in the p-stripes of the LYCCA wall DSSSD in run 42 at a particle rate of  $\sim 3.3 \times 10^4 \text{ s}^{-1}$  (red, dashed line) and run 74 at a particle rate of  $\sim 5.4 \times 10^4 \text{ s}^{-1}$  (blue, solid line).

The preliminary data was kindly provided by Marc Lettmann, TU Darmstadt. See text for details.

individual CsI detectors, are shown. For taking the data shown in the latter figure, a separate DAQ was set up and the time of every ion hitting the S2 scintillator was recorded.

From inspection of the left hand side of Figure 6.51 it is clear that also time differences of quasi-zero occur, i.e. there are bunches containing more than one ion. However, it is also clear from Figure 6.51 that bunches with multiple ions are not significantly more frequent than bunches containing only one ion. Only for events where multiple ions per bunch are registered, time differences of  $\gamma$ -rays emitted from consecutive ions can not be resolved by the AGATA detectors and the corresponding events can probably not be used in the analysis. From the data shown in figures 6.50 and 6.51, it can be estimated that these events make up approximately 5% of the data. They can efficiently be identified due to the high granularity of the CsI and DSSSD detectors of the downstream wall of LYCCA.

---

For the first 4.5 shifts of experiment S426, data was taken at an average particle rate of  $3.1 \times 10^4 \text{ s}^{-1}$ , measured in the S4 scintillator [Let15]. The bunching of the SIS ion beam was used. Deadtime under these conditions was in the order of 25%.

After these first 4.5 shifts, the remaining beam time was distributed between experiment S426 and a competing measurement. Another 4.5 shifts were attributed to experiment S426. In order to be able to take higher beam intensities during these remaining 4.5 shifts, FRS detectors for secondary beam identification were removed from the DAQ. This reduced the readout time of the DAQ and, hence, its dead time. Since the secondary ion beam of  $^{85}\text{Br}$  ions was basically pure (better than 99.9% estimated from simulations in [Pie11]), an identification of the ions before the secondary target was not vital. It was decided to sacrifice the identification of the incoming beam for the sake of increased statistics. The effect of this measure was that the experiment could be performed with a 65% higher average particle rate of  $5.1 \times 10^4 \text{ s}^{-1}$  measured in the S4 scintillator [Let15] at approximately the same level of dead time.

In total, data were taken for 73 hours, corresponding to 9 shifts out of 24 shifts requested and budgeted by the G-PAC. However, from a purely arithmetical point of view, the raise in beam intensity that was made possible by removing the FRS detectors from the DAQ compensated for the additional reduction from 12 to 9 shifts.

---

## 6.2.2 Perspectives for the data-analysis

---

Experiment S426 followed an unconventional way of data taking. The intensity of the secondary beam of up to  $5.3 \times 10^4 \text{ s}^{-1}$  is very high compared to other experiments performed at the PreSPEC-AGATA setup and its predecessor, the RISING fast beam setup. Usually, more exotic secondary beams with orders of magnitude lower intensity are employed. Issues arising from dead time of the DAQ or detection of several particles per event are usually not present in those measurements. However, accepting these unconventional conditions was the only possibility to have the chance to collect sufficient statistics for the determination of the  $B(M1)$  strength of the decay of the 1191-keV state of  $^{85}\text{Br}$  within the beam time available for experiment S426.

These circumstances imply that novel analysis techniques have to be developed for experiment S426. Usually, events with more than one ion registered are not used in the analysis. Since only about 1/3 of the events contain only one ion (see Figure 6.51), it is crucial to develop techniques for splitting events with more than one ion as discussed in Section 6.2.1.3.

It follows from the distribution of ion multiplicities shown in Figure 6.51 that compared to an analysis considering only the events with ion multiplicity one, suc-

successful splitting of the events will increase the available statistics by a factor  $\sim 3.5$  for the runs at  $3.1 \times 10^4 \text{ s}^{-1}$  beam intensity and by a factor  $\sim 5.3$  for the events at  $5.1 \times 10^4 \text{ s}^{-1}$  beam intensity. On average, a gain in statistics by a factor of  $\sim 4.6$  can be expected. It was discussed in the previous section that there are multiple ions with unresolvable time difference only in about 5% of the events.

The  $\gamma$ -ray spectrum shown in Figure 6.52 was obtained by restricting the analysis to events with ion multiplicity one and selecting bromine ions identified in LYCCA via  $\Delta E - E$  measurement. No other conditions were applied. In particular, no tracking and no gate on the particle- $\gamma$  time difference or scattering angle etc. was applied.

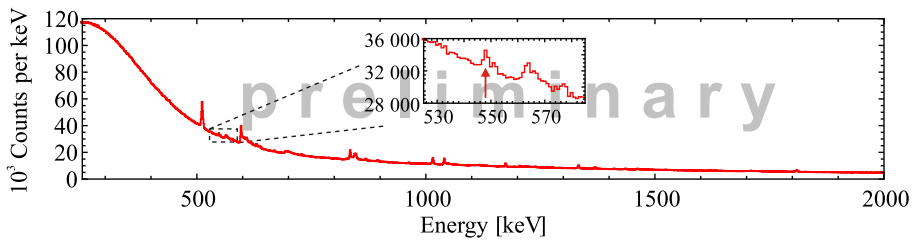


**Figure 6.52.:**  $\gamma$ -ray spectrum observed in experiment S426 without Doppler correction. Only bromine ions identified in LYCCA and an ion multiplicity of one measured in the LYCCA wall DSSSDs were demanded. No tracking and no conditions for cleaning the spectrum were applied. The inset shows the 548-keV decay of the Coulomb-excited  $7/2_1^+$ -state of the gold target nuclei. This preliminary spectrum was kindly provided by Marc Lettmann, TU Darmstadt. See text for details.

In this spectrum,  $\sim 8500$   $\gamma$ -ray events at 548 keV from the Coulomb excitation of the gold targets were observed [Let15]. This number has to be compared to what is expected from estimates for the excitation of the 1191-keV state of  $^{85}\text{Br}$  discussed in Section 6.2.1.2. For 73 hours beam on target with an average intensity of  $4.3 \times 10^4 \text{ s}^{-1}$ , a duty cycle of the SIS beam<sup>8</sup> of 10/12, 25% dead time of the DAQ, a total detection efficiency of the setup of 2% and an excitation probability for the  $7/2_1^+$ -state of gold of  $6.8 \times 10^{-4}$ , a total number of  $9.6 \times 10^4$  registered events are expected. The condition that only events with ion multiplicity one are regarded implies that the target excitations corresponding to  $1/4.6 = 22\%$  of all registered ions were considered, leaving  $2.1 \times 10^4$  expected counts. Hence, a factor of 2.5 less

<sup>8</sup> Accelerating the primary beam in SIS18 took 2 s and the beam was extracted over a duration of 10 s.

---

counts than expected were observed. A similar lack of registered  $\gamma$ -ray intensity has also been observed in the PreSPEC commissioning runs for the Coulomb excitation of  $^{80}\text{Kr}$  [Ree14] and is not understood so far.

From the of observed target excitations, the number of expected  $\gamma$ -ray events from the excitation of the 1191-keV state of  $^{85}\text{Br}$  can be deduced via the ratio of the probabilities for target and projectile excitation of 28.6. Under the condition that ion multiplicity per event is one,  $8500/28.6 = 300$  counts are expected to be registered. Since it is derived from the number of observed decays of excited target nuclei, this estimate contains all detection efficiencies and so far unexplained factors reducing the observed  $\gamma$ -ray intensity. Assuming that all events with multiple detected ions can be split without losses, a number of  $300 \times 4.6 = 1370$  detected  $\gamma$ -rays from the decay of the 1191-keV state of  $^{85}\text{Br}$  can be expected <sup>9</sup>.

Whether this statistics is sufficient to identify the peaks from the decays of ions excited in either of the targets sensitively depends on the level of the  $\gamma$ -ray background. If the background can not be reduced compared to the one observed in the 2012 test shift (which was used for the estimate of the background level in Section 6.2.1.2), there is no chance to see the transitions. However, compared to the situation in the 2012 test shift, the removal of the LYCCA target TOF detector and the optimization of the slits at the S2 and S4 focal planes of the FRS will reduce the background that is produced in matter other than the gold targets.

Additionally, significant reduction of the background level can be expected by the exploitation of AGATA's superb imaging capabilities [Don10, Ced14]. The path of  $\gamma$ -rays that Compton-scatter inside the detector material is reconstructed in terms of ordering the interaction points identified in the PSA by the tracking algorithms (see Section 3.2.2). From this reconstructed path of the  $\gamma$ -rays, a cone of possible  $\gamma$ -ray vertices can be constructed. If the piercing point of the measured ion trajectory through the target is not compatible with that cone, the  $\gamma$ -ray can be considered to not stem from excitation of the respective ion in the target. In this case, the respective  $\gamma$ -ray can be considered to be background and can be rejected. This procedure is ideally suited to reject background that is not produced in the targets. A reduction of the background that is produced outside the target by at least a factor 3 can be expected from this technique [Don10, Ced14]. Additionally, this procedure can be utilized to suppress background generated in the upstream target when performing the Doppler correction for the downstream target (see Section 5) and vice versa. These techniques that in parts still have to be developed can

---

<sup>9</sup> If the factor of 2.5 of missing events can be resolved, 3400 events from the decay of the 1191-keV state of  $^{85}\text{Br}$  can be expected to have been measured.

---

be applied to the data taken in experiment S426 since the electrical signals that were measured in each segment and core of the AGATA detectors (the traces) were written to disc.

The analysis of experiment S426 will also benefit from further improvements for background rejection like for example via improvement of the time resolution of the AGATA detectors based on analysis of the recorded traces (e.g. [Cre10, Sch11b]) or  $\gamma$ -ray-neutron discrimination [Lju05, Ata09, Sen14].

A simulated spectrum with in total 1370 events from the decay of the 1191-keV state of  $^{85}\text{Br}$  is shown in Figure 6.53 for the optimistic case that the background level can be reduced by a factor ten with respect to the assumptions made in Section 6.2.1.2. Under these circumstances - all events with multiple detected ions can be split and the background level can be sufficiently reduced - the peaks from  $\gamma$ -ray decays of the 1191-keV state of  $^{85}\text{Br}$  ions excited in both targets can be clearly identified. A sensitive determination of the multipole mixing ratio of the decay and, hence, its  $B(M1)$  strength is probably not possible with the peak-to-background ratio expected in this scenario. If the factor of "missing events" of 2.5 can be significantly reduced and/or the background level can be reduced even more, there is a chance also to determine a value for  $B(M1)$  for the matrix elements assumed in this study.

It seems worth noting that if the 1191-keV state of  $^{85}\text{Br}$  is *not* the dominant fragment of the  $\pi p_{3/2} \rightarrow \pi p_{1/2}$  spin-flip transition in  $^{85}\text{Br}$ , it will have a much lower  $B(M1)$  strength to the ground state. This would result in a much longer level lifetime than the 50 fs assumed here. In consequence, the ions would predominantly de-excite behind the targets, resulting in well-defined velocities at the time of de-excitation and, hence, in much narrower peaks (compare Figure 5.12). The peak-to-background ratio would highly benefit from such a situation, if the  $B(E2)$  strength to the ground state is sufficiently large.

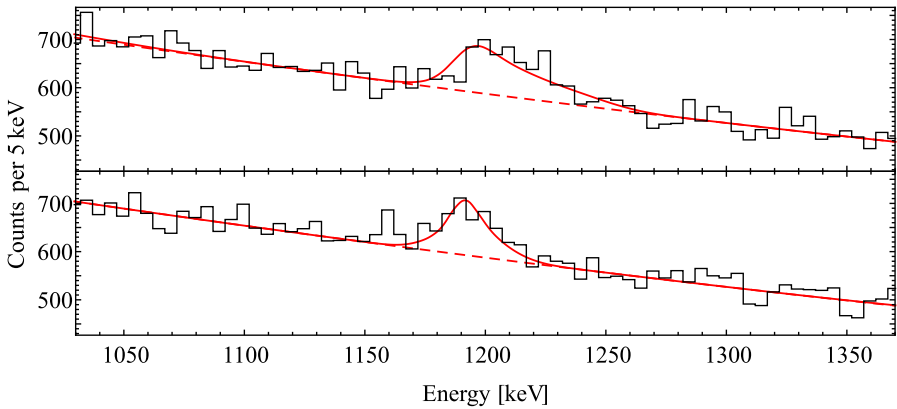


**Figure 6.53.:** Simulation of the  $\gamma$ -ray spectrum expected in experiment S426 for Doppler correction assuming excitation in the upstream target (top) and the downstream target (bottom). The summed peak-area of 1370 events was obtained from scaling to the observed target excitations and the distribution of ion multiplicities per event. A background level reduced by a factor 10 compared to the estimates made in Section 6.2.1.2 was assumed. See text for details.

---

## 7 Potential impact of the new methods

The advent of  $\gamma$ -ray tracking arrays as the next generation of HPGe detector systems for  $\gamma$ -ray spectroscopy will result in a strong increase of sensitivity for the detection of  $\gamma$ -rays and unprecedented accuracy for correcting the Doppler shift observed when  $\gamma$ -radiation is emitted in flight, as discussed in Section 3.3. The European detector array AGATA will be the working horse of the in-beam  $\gamma$ -ray spectroscopy experiment HISPEC at the future next-generation RIB facility FAIR at Darmstadt. Similarly, the US-American  $\gamma$ -ray tracking array GRETA is currently used at experiments at the NSCL, MSU, and will be the central spectroscopic device at the future next-generation RIB facility FRIB which is under construction at the MSU. These experiments will focus on the study of shell-evolution and nuclear properties far off  $\beta$ -stability.

The broadening of the observed peaks of  $\gamma$ -ray transitions stemming from different velocities at the time of de-excitation of excited nuclear states inside the target or from different  $\gamma$ -ray vertices if the decay occurs behind the target are resolvable in these experiments as a function of  $\gamma$ -ray emission angle with high precision. While this broadening is a "nuisance effect" for e.g. Coulomb excitation and transfer or secondary fragmentation experiments, it is the basis of the continuous-angle Doppler-Shift Attenuation Method and its modifications presented in Section 4. Hence, the peak broadening can be used to extract valuable lifetime information as "by-product" in a broad range of experiments at RIB facilities providing relativistic, exotic ion beams.

On the other hand, performing DSAM experiments at relativistic beam energies e.g. by the differential caDSAM (Section 4.4) avoids the main source of systematic errors of DSAM measurements, namely the imprecisely known stopping powers of the target materials for the beam ions and excited nuclei at low velocities. At the relativistic energies and high charge states of the beams provided by facilities such as HISPEC@FAIR and at FRIB, the stopping powers can be calculated with high accuracy as discussed in Section 4.1.2. This allows for performing precision measurements of nuclear level lifetimes in the picosecond range by the caDSAM also in exotic nuclei. If Coulomb excitation is chosen as excitation reaction, the analysis of the observed yields in these experiments can serve as independent validation of

---

the obtained level lifetimes.

Precise and reliable lifetime information is especially interesting and valuable also for nuclei that are not at the very extremes of what can be produced by RIB facilities, but that can be produced with significantly higher intensities than the most exotic isotopes. For example, precise and independent measurements of the  $B(E2, 0_1^+ \rightarrow 2_1^+)$  values of the light tin isotopes is of current interest [Cor15, Doo14, Bad13]. Precise measurements of level lifetimes of non-yrast states in exotic nuclei can also provide highly valuable insight to nuclear structure. Exemplarily, the proton-neutron residual interaction can be probed by the study of one quadrupole-phonon mixed-symmetry states,  $2_{MSS}^+$ , [Pie08] which are identified by strong  $M1$  transitions to the symmetric  $2_1^+$  states, resulting in short lifetimes in the order of  $\sim 100$  fs. Such observables are usually not known in exotic nuclei that are at the limit of production yields of current RIB facilities. The increased intensity of such beams that will be provided by the next-generation RIB facilities will allow their efficient and precise measurement, and the caDSA Method and its modifications are specifically tailored experimental techniques for such measurements that exhaust the capabilities of the next-generation detector arrays.

It is also by the measurement of observables beyond the energies and eventually  $B(E2)$  values of the first excited states of exotic nuclei where the method of Coulex-Multipolarimetry with relativistic ion beams presented in Section 5 can make an impact. Besides the identification of single-particle spin-flip transitions as in the case of  $^{85}\text{Br}$  presented in Section 6.2, also other phenomena involving strong  $M1$  ground-state transitions can be studied by this method in exotic nuclei at relativistic beam energies. An example is the scissors mode, an isovector orbital excitation in deformed nuclei that has only barely been studied in radioactive nuclei [Hey10]. New phenomena involving magnetic dipole excitations are expected at large neutron-to-proton ratios, such as a "soft" scissors mode in the presence of a neutron skin [Isa92, War97]. The standard methods to investigate such  $M1$  excitations are Nuclear Resonance Fluorescence (NRF) and electron or proton scattering. These methods can not (or, at least, not in their usual form) be applied to short-lived radioactive isotopes. Newly developed methods such as the Coulex-Multipolarimetry can therefore be a valuable tool for investigations of phenomena related to  $M1$  excitations at the next generation of RIB facilities.

The  $\gamma$ -ray tracking arrays AGATA and GRETA will also be employed at facilities that do not provide relativistic ion beams, such as the GANIL, France, and LNL, Italy in the case of AGATA and the Argonne National Laboratory in the case of GRETA. Also under the conditions present at these facilities, the caDSAM can make an impact for

---

precision lifetime measurements of excited nuclear states. Especially for lifetimes in the range below a few picoseconds, the DSAM is the only viable method for direct lifetime measurements<sup>1</sup>. It can be employed with a broad range of excitation reactions, and its adaption to the observables that are accessible by  $\gamma$ -ray tracking arrays and the consistent description of the physical effects contributing to the observed lineshapes as discussed in Section 4.2 make it a versatile tool for precise and reliable lifetime measurement also at non-relativistic beam energies. This was demonstrated by the application of the caDSAM for lifetime measurements of excited states in  $^{136}\text{Xe}$  in this thesis.

---

<sup>1</sup> In this context, Coulomb excitation is regarded as indirect method for lifetime measurement because it effectively measures reduced transition strengths  $B(\sigma\lambda)$  or decay widths  $\Gamma$ .



---

## 8 Summary & Outlook

In the course of the next few years, experimental nuclear structure physics and especially in-beam  $\gamma$ -ray spectroscopy will face a substantial advancement of the state-of-the-art instrumentation. The next generation of radioactive ion beam (RIB) facilities is under construction and accompanied by the development of the next generation of high resolution  $\gamma$ -ray spectrometers, the  $\gamma$ -ray tracking arrays. The challenging experimental conditions at RIB facilities call for the adaption and further development of techniques for in-beam  $\gamma$ -ray spectroscopy as well as for the development of new experimental techniques that exhaust the potential of  $\gamma$ -ray tracking detectors.

In this thesis, two such new experimental techniques have been described. One of them is the continuous-angle Doppler-Shift Attenuation Method (caDSAM). It is a further development of the well-known DSAM technique for the direct measurement of nuclear level lifetimes in the picosecond range, adapted to its employment with  $\gamma$ -ray tracking arrays. The caDSAM provides a description of Doppler-broadened  $\gamma$ -ray lineshapes as a function of both detected  $\gamma$ -ray energy and polar detection angle of the  $\gamma$ -rays in position-sensitive detector systems such as AGATA or GRETA. For the implementation of this method into a versatile software program, utmost care is taken of a consistent description of all physical processes affecting the observed  $\gamma$ -ray lineshapes, such as particle- $\gamma$  angular correlations, relativistic effects and properties of employed detectors for  $\gamma$ -ray detection and particle tracking. The semi-analytical approach of the caDSA Method allows for a fast computation of the two-dimensional  $\gamma$ -ray lineshapes. This facilitates efficient and sensitive fits of theoretical lineshapes to observed spectra under the variation of physically significant parameters defining the de-excitation of the nuclear states under investigation and the detection of the emitted  $\gamma$ -rays. The significant enhancement of the sensitivity of the DSA Method by considering the evolution of lineshapes as a function of detection polar angle and the advantages arising from the consequent inclusion of relevant physical effects have been discussed in detail.

The differential caDSA Method is an extension of the caDSAM that adopts it to experiments with radioactive and relativistic ion beams, especially for experiments as they are performed with RIBs produced by in-flight fragmentation or fission. The ansatz of the differential caDSAM circumvents the problem of imprecisely known stopping powers of target materials for ions at low velocities and, hence, the main

---

source of systematic errors in DSAM experiments. This qualifies the method for precision experiments with relativistic, radioactive ion beams. The geometrical caDSA Method extends the range of level lifetimes that can be sensitively measured by the caDSAM to several hundred picoseconds and is completely independent from stopping powers.

The caDSA Method was first employed in an experiment conducted with the AGATA demonstrator at LNL, Italy. The analysis of the experiment was presented, and precise lifetimes of the  $2_1^+$  and  $3_1^-$  state of  $^{136}\text{Xe}$  were determined. Electromagnetic transition strengths of the  $3_1^- \rightarrow 2_1^+$  transition and for four further  $2^+$  states as well as limits on transition strengths for two further  $2^+$  states were extracted by the analysis of observed Coulomb excitation yields. The determined value of the  $2_1^+$  level lifetime is in perfect agreement with the adopted literature value. The lifetime of the  $3_1^-$ -state was determined for the first time. The determined electromagnetic transition strengths were confronted with microscopic calculations and put into context with the systematics in neighboring nuclei. The  $B(E3, 0_1^+ \rightarrow 3_1^-)$  strength in the xenon isotopic chain exhibits a drastic increase at  $^{136}\text{Xe}$ . A competition between non-mixing  $3^-$  states with collective and single-particle character was suggested to be responsible for this new observation. Key experiments to confirm this picture were discussed.

By its layout, the formalism of the caDSAM can easily be extended for further applications. Its employment for the analysis of RDDS measurement of short level lifetimes, where the experimental spectra also show the effects of excited ions slowing down in matter, is straight forward. Also the inclusion of deorientation effects of nuclear alignment into the method is easily feasible. By the use of suitably structured targets, resulting time-dependent variations of  $\gamma$ -ray angular distributions (as they are *inter alia* observed in TDRIV experiments, see e.g. [Stu05, Kus15]) can eventually be sensitively resolved at different subsections of observed  $\gamma$ -ray line-shapes. This would provide the possibility to measure gyromagnetic ratios of short-lived excited nuclear states also in exotic nuclei.

The second experimental technique that was developed within this work is the Coulex-Multipolarimetry Method. It is a novel technique for the measurement of electromagnetic multipole mixing ratios of nuclear ground state transitions. It makes use of the relative energy-dependence of relativistic Coulomb excitation cross sections for transitions with electric and magnetic character. Dedicated experimental setups with two thick targets and the identification of excitations in either of the targets by differences in the Doppler shift of  $\gamma$ -ray energies observed in high-resolution detectors allow to quantify excitation yields at significantly different beam energies in one single measurement. This method can be employed also in cases where the conventional technique for the measurement of mixing ra-

---

tios via  $\gamma$ -ray angular distributions is not applicable. The method and its sensitivity were discussed in a universal manner.

The Coulex-Multipolarimetry Method was employed in experiment S426 performed during the AGATA-PreSPEC campaign at GSI's FRS in spring 2014. Aim of the experiment is to identify the proton  $p_{3/2} \rightarrow p_{1/2}$  spin-flip excitation of  $^{85}\text{Br}$  in order to deduce the effective single-particle energy difference for the corresponding orbitals in that nucleus. The complex experimental setup, the estimates made for planning the experiment and the expected sensitivity were discussed. Dedicated modifications of the PreSPEC setup at GSI were made for the conduction of experiment S426 and discussed in this thesis. They allowed to measure at average secondary beam particle rates of  $\sim 5 \times 10^4 \text{ s}^{-1}$ , a value that to the knowledge of the author is unprecedented for high-resolution in-beam  $\gamma$ -ray spectroscopy experiments with relativistic beams at GSI. The experiment is still under analysis in the course of another doctoral thesis. The perspectives for the data analysis, especially in terms of potential techniques for reducing the observed  $\gamma$ -ray background, were discussed.

The application of the experimental methods developed within this work for future experimental studies was construed. By construction, the main impact of the methods can be expected for experiments with relativistic, radioactive ion beams. It is the conviction of the author that precision measurements of lifetimes of yrast as well as non-yrast nuclear levels in radioactive nuclei that can be produced at substantial intensities at RIB facilities would provide highly significant nuclear structure information. Yet the nuclei that can be produced with sufficiently high abundance for such studies are not at the forefront of technically feasible extreme proton-to-neutron ratios, an in-depth study of these nuclei in terms of e.g. isovector degrees of freedom or cluster structures will promote the understanding of nuclear structure far off  $\beta$ -stability. Also the study of magnetic dipole excitations in exotic nuclei by the Coulex-Multipolarimetry Method, such as the isovector orbital  $M1$  excitations ("scissors mode") may be a promising field of research. This appraisal is fueled in particular by the prediction of hitherto unobserved excitation modes in very neutron-rich nuclei, such as the soft scissors mode.



---

# A Criteria for "safe" Coulomb-excitation

When target nuclei with mass number  $A_t$  and charge number  $Z_t$  are bombarded by projectile with mass number  $A_p$  and charge number  $Z_p$ , projectile and target repel each other by the Coulomb force. Their distance of closest approach  $d$  for a head-on collision is given by

$$d = \frac{e}{4\pi\epsilon_0} \frac{Z_p Z_t}{E_{CM}} \quad (\text{A.1})$$

where  $E_{CM}$  is the kinetic energy of the projectile in the center-of-mass frame. The transformation of the energy to the laboratory frame  $E_{lab}$  is given by

$$E_{lab} = \frac{A_p + A_t}{A_t} E_{CM}. \quad (\text{A.2})$$

For non-central collisionis, the distance of closest approach as a function of the center-of-mass scattering angle  $\theta_{CM}$  can be obtained by multiplying eq. A.1 by a factor  $\frac{1}{2}(1 + 1/\sin(\theta_{CM}/2))$ . Hence, the projectile kinetic energy yielding a distance of closest approach  $d$  at a center-of-mass scattering angle  $\theta_{CM}$  is given by

$$E_{lab}/\text{MeV} = 0.72 \frac{Z_p Z_t}{d/\text{fm}} \frac{A_p + A_t}{A_t} \left( 1 + \frac{1}{\sin(\theta_{CM}/2)} \right) \quad (\text{A.3})$$

The interaction between target and projectile can be considered to be purely electromagnetic if both nuclei are sufficiently separated at all times, i.e.

$$d > D_{safe}. \quad (\text{A.4})$$

Equation A.3 together with the above condition defines the criterion on the maximum beam energy for "safe" Coulomb-excitation. If this "safe" distance is underrun, Coulomb-nuclear interference effects modify the excitation probabilities. Close to the Coulomb-Barrier, usually destructive interference occurs, leading to a reduction of the excitation probability [Spe78]. Coulomb-nuclear interference

dominantly affects second-order processes, such as reorientation or multi-step excitations [Les72].

There exist a variety of definitions for the "safe" distance  $D_{safe}$ . It is often expressed in the form

$$D_{safe} = r_t + r_p + r_{extra} \quad (\text{A.5})$$

where  $r_{t(p)} \approx 1.25 \times A_{t(p)}^{1/3}$  fm is the interaction radius of the target (projectile) nucleus and  $r_{extra}$  is an additional "safety" distance accounting for the diffuse matter distribution of nuclei. In the literature, different values for  $r_{extra}$  can be found: 3 fm [Boe68], 4 fm [Pel82], 5 fm [Cli69, H au74] or 6 fm [Les72]. The value of 5 fm seems to be most accepted and is often referred to as *Cline's criterion*.

An alternative expression for the "safe" distance was given by Wollersheim [Wol92]:

$$D_{safe} = C_t + C_p + 5 \text{ fm} \quad (\text{A.6})$$

where the  $C_i$  are the radii of half density of a Fermi mass distribution

$$C_i = R_i(1 - R_i^{-2}) \text{ fm} \quad (\text{A.7})$$

and  $R_i$  are nuclear radii parametrized from a liquid drop model:

$$R_i = 1.28 \cdot A_i^{1/3} - 0.76 + 0.8 \cdot A_i^{-1/3} \quad (\text{A.8})$$

---

## B Implementation of the caDSA Method

The continuous-angle Doppler-Shift Attenuation Method was implemented into the computer programs `StopSim` and the *"Analysis Program for Continuous Angle DSAM"* (APCAD). First rudimentary versions of both programs were developed in the course of the Master's thesis of the author [Sta11]. They were significantly further-developed within this work.

`StopSim` is a Monte-Carlo simulation based on the Geant4 framework [Ago03, All06]. It simulates the excitation and slowing down of ions in targets.

The program APCAD provides the possibility to calculate Doppler-broadened  $\gamma$ -ray lineshapes as a function of  $\gamma$ -ray energy and its polar detection angle and to fit these two-dimensional lineshapes to experimental data in order to extract nuclear level lifetimes. Special attention is paid to providing precise and realistic descriptions of the experimental conditions and all physical effects influencing the measured lineshapes. A graphical user interface was implemented for operation of the program in order to make it as user-friendly as possible.

Details of the formalism underlying the caDSAM and its implementation into the programs `StopSim` and APCAD are discussed in Sections B.1 and B.2. These sections represent a "long writeup" of Section 4.3. The implementation of the differential and geometric caDSAM in the programs is described in Sections B.3 and B.4, respectively.

---

### B.1 Program `StopSim`

---

The software program `StopSim` is a Monte-Carlo simulation coded in the framework of the Geant4 simulation toolkit [Ago03, All06] in its version 9.6. Descriptions of layered targets, definitions of ion beams in terms of energy, mass- and charge-number, spatial and energetic profiles as well as output routines and mechanisms enhancing the efficiency of the simulation were implemented starting from an example provided with the Geant4 source code. For the simulation of ion excitation, two new interaction classes have been written and integrated into the Geant4 framework: A class for Coulomb excitation and a class for arbitrary binary nuclear reactions employing user-provided cross section tables. Modifications of

---

the Geant4 standard-descriptions of the slowing-down process of ions in matter were undertaken in order to optimize and extend the simulation for the needs of analyses of DSAM data.

The purpose of StopSim is to provide a realistic simulation of the excitation and slowing down process of ions in matter. The programs output is a file containing ion velocity histories, i.e. lists with the components of the ion velocity vectors starting from the time of their excitation and throughout their deceleration in targets. Different aspects of the program StopSim are discussed in the following paragraphs. The focus is on routines/processes that are not standard in Geant4. For general information on simulations based on Geant4 and the implementation of standard processes, the reader is referred to References [Ago03, Gea12].

### Modeling of ion beam and target

It is the great advantage of employing a highly developed, widely used and accepted software framework such as Geant4, that basic routines and processes common to many simulations are provided ready-to-use. This is the case e.g. for the program modules needed to describe the incoming ion beam for the simulation. All beam properties such as ion species, initial charge state, transverse position and spatial profile, kinetic energy and its distribution are accounted for by a build-in class of Geant4 called `G4GeneralParticleSource`. No programming was necessary on this point. The parameters defining the beam are defined by the user via a macro file. Also for the description of the material included in the simulation, in this case a layered target, routines are available that facilitate an easy description within the framework. Up to five layers of a target can be set up by commands in the aforementioned macro file, defining thickness, composition and density of each of the layers. An eventual tilt of the target normal with respect to the beam axis can be set via the macro file.

### Simulation of the excitation process

Since there exists no standard-process for Coulomb excitation in the Geant4 framework and aiming at keeping the range of applicability of the developed programs as broad as possible, two new physics processes were implemented. One is dedicated to arbitrary binary reactions of the type  $A(B, C)D$  such as transfer- or knockout-reactions, requiring user-provided tables with differential cross sections, while the other process is dedicated to Coulomb excitation.

The class providing Coulomb excitation as a process for the Geant4-framework calls the programs CLX [Owe] and DWEIKO [Ber03] for the calculation of differential Coulomb excitation cross sections  $\frac{d\sigma}{d\theta_{CM}}$ . These are calculated for each utilized target material in user-defined steps in energy and steps of  $1^\circ$  in center-of-mass

scattering angle once at the start of the simulation and are stored in tables. For specific beam energies and scattering angles, an interpolation between the stored values is applied. The electromagnetic matrix elements and the excitation-energy of the desired state determining the Coulex cross sections are provided by the user via the macro file. Mass- and proton-number of projectile and target nuclei are defined by the beam species and the target materials.

Since the program CLX is suited for the calculation of Coulex cross sections at moderate energies approximately up to the Coulomb-barrier and DWEIKO is suitable for relativistic beam energies (see Section 2.1), the user has to specify at which range of beam energy which program should be used for the calculation of Coulex cross sections. Interpolation between the cross sections provided by CLX and DWEIKO is applied in the overlap of these ranges. Since in DSAM experiments usually either of the situations holds (energies near the Coulomb-barrier or relativistic energies for differential caDSAM, see Chapter 4.4), the unreliable description of Coulex cross sections at intermediate energies by both programs is usually not a problem. This approach has been chosen in default of a computer program suitable for the calculation of Coulex cross sections at all beam energies. The implementation of the calculation of cross sections at relativistic beam energies from DWEIKO in StopSim and the interpolation with the values from CLX was implemented in the course of a Master's thesis under the supervision of the author of this work [Let13].

For all isotopes  $i$  contained in a given target material as it is defined by the user in the macro file or pre-defined in the program, the partial inverse mean-free paths for Coulomb excitation

$$\lambda_i^{-1}(E) = \rho_i \sigma_i(E) \quad (\text{B.1})$$

are calculated. Here,  $\rho_i$  denotes the density of the isotope  $i$  in the target material (number of nuclei per volume) and  $\sigma_i(E) = 2\pi \int_0^\pi \frac{d\sigma(E)}{d\theta_{CM}} \sin \theta_{CM} d\theta_{CM}$  is the total Coulomb excitation cross section at beam energy  $E$ . For each utilized target material  $M$ , the total inverse mean free path

$$\Lambda_M^{-1}(E) = \sum_{i \in M} \lambda_i^{-1}(E) \quad (\text{B.2})$$

is calculated, where  $i \in M$  denotes the indices of all isotopes making up the material  $M$ . The total inverse mean free path  $\Lambda_M^{-1}(E)$  denotes the average distance that is traversed by a beam ion of energy  $E$  in the material  $M$  until a reaction happens.

$\Lambda_M^{-1}(E)$  is calculated for each material making up the layered target. Like for all discrete processes considered in Geant4 simulations, the occurrence of Coulomb excitation reactions is then sampled from the values of  $\Lambda_M^{-1}(E)$  by the Geant4 Monte-Carlo algorithm (see [Gea12] for details on the Monte-Carlo sampling method applied in Geant4).

If Coulomb excitation occurs in the simulation, another routine of the Coulex class is called. By the call of that method, the current ion position and momentum vectors are known. Therefore, it is also known which target material  $M$  the ion is located in for the sampled Coulomb excitation reaction. In this method, the isotope on which the Coulomb excitation occurs is sampled from the values of  $\lambda_i^{-1}(E)$  for the current target material and the center-of-mass scattering angle  $\theta_{CM}$  is sampled from the differential Coulomb excitation cross section  $\frac{d\sigma}{d\theta_{CM}}$ . Using the kinematics relations (Appendix C), the kinetic energy after the reaction and laboratory scattering angle with respect to the initial momentum vector can be calculated for the excited beam ion from the center-of-mass scattering angle  $\theta_{CM}$ . The azimuth scattering angle is chosen randomly, fixing the momentum vector of the excited beam ion. The momentum vector of the scattered target ion then follows from energy- and momentum-conservation. The properties of the scattered beam ion are updated accordingly and the scattered target ion is created as a "secondary particle" in the simulation.

For the simulation of arbitrary binary reactions of the type  $A(B, C)D$ , the procedure is very similar. This type of reaction is implemented within a separate process class into the Geant4-framework. The difference to the implementation of Coulomb excitation is that the differential reaction cross section  $d\sigma(E)/d\theta_{CM}$  is not automatically calculated by the use of external programs (*CLX*, *DWEIKO*), but is provided by the user in form of a table in an external file. Furthermore, the user specifies the exact reaction partners, i.e. on which specific isotope "B" the reaction can take place and what the reaction products "C", "D" are. Of course, it is sufficient to specify two isotopes out of  $B$ ,  $C$  and  $D$ , since "A" is fixed by the beam species and the process is restricted to binary reactions. It is assumed that the reaction populating the excited state of interest can take place only on one specific isotope  $B$ . Therefore, the total inverse mean free path for each target material is given by

$$\Lambda_M^{-1}(E) = \rho_B \sigma(E) \quad (\text{B.3})$$

where  $\rho_B$  is the number density of the isotope  $B$  in the material  $M$  and  $\sigma(E)$  is the total reaction cross section at projectile energy  $E$ . Again, the occurrence of the reaction  $A(B, C)D$  is sampled from the values of  $\Lambda_M^{-1}(E)$  by the Geant4 Monte-Carlo algorithm. If the reaction occurs, the momentum vectors of the beam-like reaction product  $C$  and the target-like reaction product  $D$  are determined in analogy to the case of Coulomb excitation by randomly sampling the center-of-mass-scattering angle from the differential reaction cross section, randomly sampling the azimuth scattering angle and applying the equations of reaction kinematics (Appendix C).

---

## Simulation of the slowing down process

Since the energy loss of ions in matter is a process frequently needed in the typical Monte-Carlo simulations implemented in the Geant4-framework, there exist standard-classes for electronic and nuclear stopping. The electronic energy loss is implemented as a continuous process, while for the nuclear stopping significant deflections caused by individual collisions are sampled in combination with an average, energy-dependent nuclear stopping power. This procedure represents a compromise between treating nuclear stopping as a continuous process and the computationally very expensive simulation of every individual collision. Yet the correlation between deflection angle and energy loss in individual collisions is neglected by this technique, reasonable descriptions are obtained for average deflections and average energy loss. Since large ensembles of ions are regarded for the purpose of DSAM this seems acceptable, but further investigations on this point may be indicated. Details on this approach can be found in Reference [Gea12]. In the standard implementation in Geant4, the stopping powers are taken from the ICRU tables (Ref. [Int05] for electronic stopping and Ref. [Int93] for nuclear stopping). Intra/extrapolations and scaling algorithms are applied if no data for the respective beam-target-combination is contained in these tables (see [Gea12] for details).

Two modifications to the standard classes for electronic and nuclear stopping have been made for the program StopSim:

- A scaling method for both the electronic and nuclear stopping was introduced. Via the macro setting up the simulation, both stopping powers can be scaled as a function of the velocity of the slowed-down ion. By scaling the stopping powers, the effect of variations in the stopping power on the finally obtained theoretical lineshapes (and, hence, level lifetimes) can be investigated on. This scaling method also provides the opportunity to quantify systematic errors introduced to derived level lifetimes by assumed uncertainties of the stopping powers.
- An interface was programmed to overwrite the standard-values of the stopping powers from the ICRU tables by values provided by the user in an external file. By this means, any parametrization or tabulation of stopping powers can be used for the simulation of ion velocity histories by StopSim. Of course, also the values provided in the external files can be scaled in order to quantify systematic errors introduced by uncertainties of the stopping powers. However, the Geant4 methods for energy- and angular straggling are used also in this case. They are described in [Gea12].

It had turned out that simulation step sizes internally set by Geant4 have significant influence on the simulated slowing-down behavior of ions at very low ener-

---

gies below  $\sim 1\%$  of the speed of light [Sta11]. These step-sizes determine after which traveled path the tables with the inverse mean free path of all considered discrete processes are updated (to the current projectile kinetic energy) and the energy losses introduced by continuous processes are accounted for. Figuratively speaking, the standard mechanism of Geant4 regulating step-sizes at low energies causes the ions to immediately deposit their full kinetic energy, if the energy is too low for any relevant interactions with matter. Here, "relevant interactions" have to be understood as processes such as crossing the interface to another volume (i.e. if an ion enters another target layer or leaves the target) or the creation of secondary particles. This approach is very reasonable for e.g. the simulation of detector responses, because it suppresses the computation of many simulation steps that have no influence on the actual distribution of energy depositions in different detector volumes or number and distribution of generated secondary particles. For the purpose of the simulation of the ion velocity histories for DSAM analyses in turn, the slowing-down process has to be modeled in detail also at these low energies not interesting for other applications. By tuning the provided parameters for the internal standard step-size control (parameters `dRoverRange` and `finalRange`), the behavior at low energies could not be regulated satisfactory without introducing too small simulation steps at high energies, resulting in a massive rise in computational effort. For the cure of this problem, there is no standard procedure available in the Geant4 framework. A workaround is achieved by introducing an "alibi"-interaction. This interaction is constructed such that it occurs in fixed, short time intervals without having an influence on any simulated particle. However, each occurrence of that alibi-interaction forces an update of the tables of inverse mean free paths and the explicit consideration of the continuous energy losses. Comparison of simulations employing the alibi-interaction to the computationally expensive simulations where step-sizes were maximally reduced via the standard parameters show that the results coincide, albeit the alibi-interaction does not raise the computational effort noticeably [Sta11]. An example for the temporal evolution of the velocity distribution for an ion ensemble being excited and slowed-down in a target simulated with StopSim is shown in Figure 4.5.

### Data output

In DSAM experiments, either the properties of excited beam-like or target-like ions are studied. Accordingly, the user can choose to write to file the velocity histories of either target-like or beam-like reactions products. The ion velocity vectors are written to file in fixed, user-defined time steps. The recorded time is the proper time of the moving ions. Additionally, the reaction vertex and the point where target- or the beam-like reaction product escapes from the target and its direction and kinetic energy at this point is written to file for every ion velocity history.

---

This information is used in APCAD to select ion velocity histories that would have been detected in user-defined particle detectors. The way decision is made which particular velocity histories are written to file is inspired by typical triggering modes in DSAM experiments:

- Measurement in  $\gamma$ -ray "singles" mode: Every emitted  $\gamma$ -ray can trigger the data acquisition system and can be registered. In terms of the simulation, this means that every ion impinging on the target should be simulated until it comes to rest, since excitations can, in principle, happen at any energy. If and only if an excitation reaction occurs the ion can emit a  $\gamma$ -ray and the velocity history of the ion is written to file, starting at the time of excitation (i.e. the time of excitation defines time zero of the velocity history of that ion).
- Measurement in particle- $\gamma$  coincidence mode: Only if a particle and a  $\gamma$ -ray are detected within a certain time interval, the data acquisition system is triggered and the event can be recorded. In terms of the simulation this means that only those events can become relevant where the target-like or the projectile-like product of an excitation reaction leaves the target. The effect of a particle detector of certain geometry located at a certain position in the experimental setup is reproduced later on in the program APCAD. There, ion velocity histories can be selected according to the kinematics of reaction products ejected from the target.

Whether higher  $\gamma$ -ray multiplicities have been demanded in an experiment has no meaning for the simulation in StopSim. In APCAD, the decay chain starting from the state initially populated in the nuclear reaction has to be modeled as a function of the lifetimes of all states involved in the decay chain. Therefore, also the ion velocity histories starting from the population of the first state of the decay chain by the nuclear reaction has to be considered in APCAD.

---

## B.2 Details of the caDSAM formalism and the program APCAD

---

The computer program APCAD is written in the object-oriented language C++. For visualization (plots) and the graphical user-interface (GUI), the root framework [Bru97] is employed. The main task of the program is the fast calculation of Doppler-broadened  $\gamma$ -ray lineshapes and their fit to experimental data for the determination of level lifetimes.

Employing the continuous-angle Doppler-Shift Attenuation Method, lineshapes are calculated as a function of  $\gamma$ -ray energy  $E_\gamma$  and polar  $\gamma$ -ray detection angle  $\theta_\gamma$ . The caDSAM and the programs developed within this work can also be applied

---

for a simultaneous analysis of data taken with "conventional", position in-sensitive detectors placed at various polar angles.

Experimental data is commonly provided with a certain binning in the continuously measured quantities, such as  $\gamma$ -ray energy. In case of position-sensitive  $\gamma$ -ray tracking detectors, also the detection polar angle is measured continuously, and the experimental data is provided with a certain binning also in the detection polar angle. In the case of conventional, position-insensitive  $\gamma$ -ray detectors, spectra are provided either for each detector crystal or for groups of detectors positioned at the same laboratory polar angle. Also the calculated lineshapes are provided with the very same binning in energy and detection angle (or with multiple spectra for the sets of polar angles in the case of position-insensitive detectors) as the experimental data. This has its origin in the employed numerical method for fast calculation of the lineshapes and allows for a fast comparison between experimental and calculated spectra in the fitting procedure.

In the following, both the binning of the  $\gamma$ -ray detection angles that are measured by  $\gamma$ -ray tracking detectors and the spectra for sets of polar angles of detector positions in the case of position-insensitive detectors are referred to as "angular bins in detection polar angle".

The philosophy pursued for the numerical calculation of lineshapes by APCAD is as follows:

All available information on detector and setup geometry, excitation and slowing-down process is absorbed into pre-calculated distribution functions that describe theoretical Doppler-shift distributions as a function of the time of  $\gamma$ -ray emission. These distributions are stored in form of numerical tables, the so-called *Stopping-Matrices*. Stopping matrices are calculated for each angular bin in detection polar angle. Sums of these stopping matrices over time, weighted by decay functions, yield the distributions of Doppler-shifts occurring for individual  $\gamma$ -ray transitions. From these distributions of Doppler-shifts and given un-shifted  $\gamma$ -ray energies, the spectra of  $\gamma$ -rays hitting the  $\gamma$ -ray detectors in each angular bin are obtained. Folding these "real"  $\gamma$ -ray spectra with detector response functions and adding suitable backgrounds yields the final calculated spectra with the Doppler-broadened lineshapes that are compared to experimental data.

The source code of APCAD is 36.000 lines long, and the program "core" for line-shape calculation without GUI, data handling etc. still comprises 7.200 lines. The source code of the "core" of APCAD would fill  $\sim 160$  pages of this thesis, and consequently it is not advisable to discuss the complete code in detail. Focus is set on central aspects of the lineshape calculation that provide an understanding of how the program works, what approximations are used for the description of the physi-

---

cal processes and what numerical methods are employed.

In the following paragraphs, the implementation of the caDSAM for lineshape calculation and their fit to experimental data is explained in steps that follow the work-flow when using the program APCAD. These steps are:

- Load experimental spectra into APCAD
- Define the  $\gamma$ -ray detector geometry
- Define particle detectors
- Load velocity histories into APCAD and calculate stopping matrices
- Define  $\gamma$ -ray transitions
- Define detector response functions and calculate lineshapes for a set of parameters
- Fit lineshapes to experimental data and extract best fit parameters and their uncertainties

#### **Loading experimental spectra into APCAD**

Experimental data to be analyzed in APCAD can be provided in several formats, including plain ASCII-data, root-histograms or data in Radware-format. It is expected that the experimental  $\gamma$ -ray spectra have been subject to a relative efficiency correction. For position-sensitive detectors this implies an efficiency correction as a function of detection polar angle, such that  $\gamma$ -rays emitted from an isotropic source resting at the center of the target would result in peaks of same area in all angular bins. For conventional detectors, such a source should result in peaks of the same area in the spectra for all detector polar angles.

#### **Definition of $\gamma$ -ray detector geometry**

In APCAD, the geometry of  $\gamma$ -ray detectors is defined by their front face pointing towards the target. For conventional detectors, cylindrical detector geometry is assumed and the detector is defined by the diameter of its front face and its distance to the target center. It is assumed that all detectors are oriented such that their symmetry axes meet in one point and this point defines the origin of the coordinate system used in APCAD. For position-sensitive detectors, it is assumed that the front faces of the detectors pointing towards the target are all arranged on a sphere. The center of that sphere defines the origin of the coordinate system used in APCAD. The detector geometry is defined by the radius of that sphere and the

azimuth angle subtended by the detectors in each polar angle bin. A detector geometry definition in APCAD is exemplarily shown in Figure B.1.

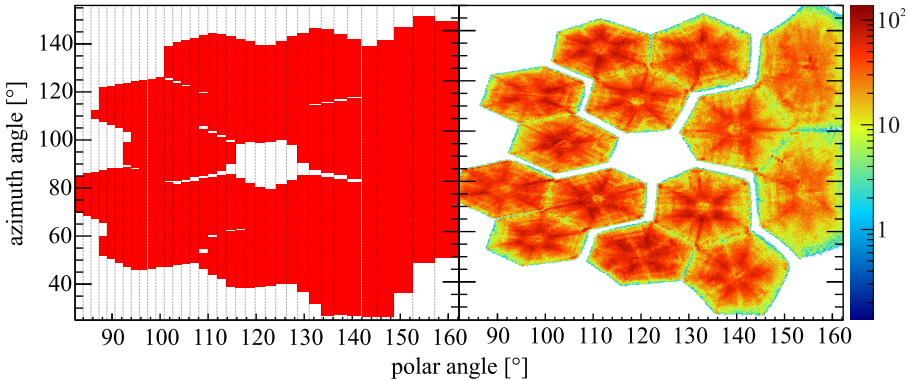


**Figure B.1.:** Definition of the geometry of a position-sensitive detector in APCAD (left) by the azimuth angle covered by the detector at each bin in polar angle. The angular bins are indicated by the vertical dotted lines. The shown geometry definition is derived from the experimental distribution of first interaction points in the AGATA demonstrator shown on the right. It was observed in the experiment described in Section 6.1.

### Definition of particle detectors for the selection of ion velocity histories

Two basic geometries of particle detectors are implemented in APCAD: Annular detectors and rectangular detectors. In the former case, the detector geometry is determined by its inner radius, its outer radius, its minimum and maximum azimuth angle and its distance from the target position along the beam axis. Also a displacement of the annular detector from the beam axis can be set. Rectangular detectors are defined by the polar and azimuth angle of their normal, the coordinates of its top left and bottom right corner in the plane defined by the normal, its rotation around the normal and its distance from the target center. Arbitrary numbers of detectors of both types can be combined.

Ion velocity histories provided by StopSim are selected based on whether beam- or target-like reaction products would have hit any of the defined particle detectors. This procedure assumes an efficiency of 100% of the particle detectors. Additional constraints on the ion velocity histories can be introduced by providing experimental hit-patterns for each particle detectors defined in APCAD. From the velocity his-

---

ories selected based on the geometric "hit-detection" described before, individual histories are selectively removed until the experimental hit-pattern is reproduced. If the excitation reaction is sufficiently well described in StopSim and the real particle detectors have indeed 100% or at least a very uniform efficiency, this selection based on experimental hit-patterns is redundant.

### **Loading velocity histories into APCAD and calculating stopping matrices**

After the file generated by StopSim that contains the simulated velocity histories is loaded into APCAD, velocity histories are selected by the procedure discussed above if particle detectors have been defined. The next step is to calculate the stopping matrices from the velocity histories, which can be considered as the central procedure for the calculation of the lineshapes. Firstly, it requires to specify the position of the target and the (transverse) beam position in the reference frame of APCAD. This reference frame is chosen such that the focus of the  $\gamma$ -ray detectors is at the origin and the beam-axis is parallel to the z-axis. Secondly, it requires to specify how the experimental data have been treated (sorted), because every manipulation done to the experimental data has to be mimicked when the stopping matrices are calculated. Necessary information that are taken into account in the calculation of the stopping matrices are

- Specification of the  $\gamma$ -ray angle in the data. Either this angle can be the polar angle  $\theta$  of the  $\gamma$ -ray detection in position-sensitive detectors, measured from the center of the target or measured from experimentally determined transverse positions of each individual ion, or this angle can be the angle  $\alpha$  between the measured direction of  $\gamma$ -ray emission and the measured momentum vector of the emitting ion, again defined from the center of the target or defined from experimentally determined transverse ion positions. The specification of the  $\gamma$ -ray angle systematically and strongly influences the Doppler-shifts observed at each angular bin.
- Specification of any applied Doppler correction (this is the case for the *differential caDSAM*, see Chapter 4.4). It is crucial to specify what information entered a Doppler correction of the experimental data, i.e. whether the velocity of individual ions were measured before and/or behind the target, if the direction of the ions leaving the target were measured or not, if a fixed ion velocity was assumed for the Doppler correction and if a certain distance of the decay from the target position was assumed. For the *differential caDSAM*, the Doppler correction applied to the experimental data has to be mimicked exactly during the calculation of the stopping matrices.

- In the case of position-sensitive  $\gamma$ -ray detectors, its position resolution has to be specified.

The stopping matrices contain the information of what distribution of Doppler-shifts would be registered in an angular bin  $i$ , if  $\gamma$ -ray emission would occur at a certain time after the excitation reaction. These distributions are discretized in both Doppler-shift and time. The discretization in time is given by the time steps of the velocity histories simulated by StopSim. In the following, the distributions stored in the stopping matrices for angular bins  $i$  are denoted as  $S_i(s_m, t_n)$  where  $t_n$  denotes the discretized times and  $s_m$  the discretized relative Doppler-shifts, given by

$$s = E'_\gamma / E_{\gamma,0} - 1 \approx_{\beta \ll 1} \beta \cos \alpha. \quad (\text{B.4})$$

Here,  $E'_\gamma$  is the Doppler-shifted  $\gamma$ -ray energy observed under an angle  $\alpha$  with respect to the emitter momentum vector and for an emitter velocity  $\beta$  given in Equation 2.40.  $E_{\gamma,0}$  denotes the transition energy that is observed if the emission occurs at rest.

At each time step of the velocity histories, the position of the ions are forward-integrated using their current velocity-vectors and the width of the time steps. The Doppler-shift is calculated for registration at a given observation position if  $\gamma$ -radiation would be emitted at that certain instance of time for each ion in the selected ensemble. The observation positions are sampled within the area in each angular bin, and a contribution is made to the bin of the stopping matrix  $S_i(s_m, t_n)$  corresponding to the current time bin  $t_n$  and the Doppler-shift bin  $s_m$ . This contribution is given by the ratio  $d\Omega_\gamma^{RN} / d\Omega_\gamma^L = (s + 1)^2$  of the solid angle element  $d\Omega_\gamma^{RN}$  in the reference frame of the moving ion for the current velocity  $\beta$ , angle  $\alpha$  and the solid angle element  $d\Omega_\gamma^L$  in the laboratory frame (see Equations 2.44 and 2.45). In the case of position-sensitive detector system, a "measured" detection position is sampled in the calculation of the Doppler-shift, blurred according to the user-defined position resolution of the detector. The contribution for that time step is then added to the stopping matrix  $S_i(s_m, t_n)$  of the angular bin  $i$  corresponding to the sampled "measured" detection-position. For conventional, position insensitive detectors, the angular bin is determined by the detector the detection-position has been sampled from. In the case a Doppler correction is to be applied (see Section 4.4 on the differential caDSAM), the calculated shift is corrected according to the specifications made by the user. In the calculation of  $S_i(s_m, t_n)$  the Doppler-effect, all relativistic effects and effects arising from transformation of reference frames described in Section 2.3 are taken into account exactly.

After the Doppler-shifts have been calculated for all ion-histories and all time steps, the entries in all bins of the stopping matrices  $S_i(s_m, t_n)$  are normalized by the number of contributions, i.e. by the number of ion velocity histories times the number of time steps times the number of sampled detection-positions per angular bin. Hence, the distributions  $S_i(t_m, s_n)$  are not normalized to unity. Their normalization for each discretized time,  $\sum_n S_i(s_m, t_n)$ , rather reflects the enhancement or reduction of  $\gamma$ -ray intensity observed in angular bin  $i$  due to Lorentz-boost (see Chapter 2.3). This  $\gamma$ -ray intensity is averaged over the solid angle covered by the respective angular bin.

Figure B.2 shows a stopping matrix from the analysis of LNL experiment 08.09 (see Chapter 6.1.4). It refers to an angular bin centered at  $\theta_\gamma = 137.6^\circ$ .

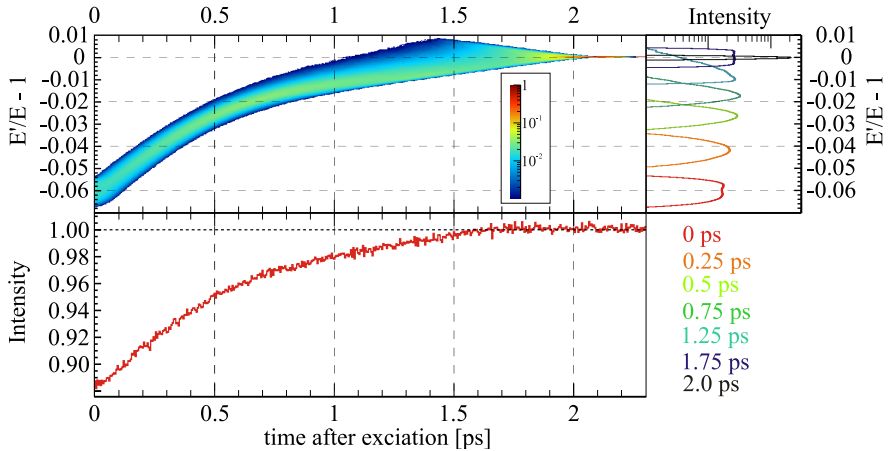


**Figure B.2.:** Top left: Stopping matrix for an angular bin centered at  $\theta_\gamma = 137.6^\circ$  from the analysis of LNL experiment 08.09 (see Chapter 6.1.4). It shows the intensity-distribution of relative Doppler-shifts  $s_m$  (see Equation B.4) that would be registered in this angular bin as a function of the time of the  $\gamma$ -ray emissions after the excitation reaction. Bottom: Projection of the stopping matrix on the time axis. The deficit in intensity at early times and, hence, high ion velocities, is due to Lorentz-boost. Top right: Projections of the stopping matrix on the Shift-axis, showing the evolution of the distribution of relative Doppler-shifts as time evolves. See text for details.

To first order,  $\gamma$ -ray angular distributions can be accounted for by weighting the stopping matrices corresponding to angular bins centered at  $\theta_\gamma$  with the corresponding value of the angular distribution function  $W(\theta_\gamma)$  as defined in Equation 2.50. However, this simple approach neglects the effect of changing emitter velocities on the transformation of the emission polar angle from the rest-frame of the emitting nucleus to the laboratory frame and the resulting effects on the lineshapes discussed in Chapter 4.2. Furthermore, changes of the emission angle stemming from a displacement of the emitting nuclei from the target center would not be accounted for. In order to provide an *exact* treatment of the  $\gamma$ -ray angular distribution, the following technique is applied:

Consider an ensemble of excited ions decelerating in matter. The excitation mechanism is the same for all ions in the ensemble, and averaged statistical tensors  $\rho_k(J_i)$  can be found that provide an adequate description of the  $\gamma$ -ray angular distribution in the rest-frame of the emitting nuclei. For each ion  $j$  emitting  $\gamma$ -radiation, the  $\gamma$ -ray angular distribution can be expressed by

$$W_j(\theta_j^{RN}) = 1 + A_2 P_2(\cos \theta_j^{RN}) + A_4 P_4(\cos \theta_j^{RN}) \quad (B.5)$$

where  $\theta_j^{RN}$  is the  $\gamma$ -ray emission angle with respect to the quantization axis (here: the beam axis) in the rest-frame of the emitting nucleus,  $A_0 = 1$  and  $A_k = \rho_k(J_i) F_k$  (compare Eq. 2.50). However, since the velocity vectors and positions of the ions in the ensemble differ, there is a variation of emission angles  $\theta_j^{RN}$  if the  $\gamma$ -rays are detected at fixed polar angles  $\theta_{det}^{lab}$  with respect to the target center and the beam axis in the laboratory frame. In other words, the emission angle  $\theta_j^{RN}$  for a specific ion  $j$  corresponding to the detection angle  $\theta_{det}^{lab}$  has to be considered as a function of the velocity  $\vec{\beta}_j$  and position  $\vec{x}_j$  of the emitting ion, and the same applies vice versa:

$$\begin{aligned} \theta_j^{RN} &= f(\theta_{det}^{lab}, \vec{\beta}_j, \vec{x}_j) \text{ and} \\ \theta_{det}^{lab} &= f(\theta_j^{RN}, \vec{\beta}_j, \vec{x}_j). \end{aligned} \quad (B.6)$$

This is the origin of the effect of the angular distributions on Doppler-broadened lineshapes discussed in Chapter 4.2. The actual functional dependence between  $\theta_j^{RN}$  and  $\theta_{det}^{lab}$  is discussed in Section 2.3.

Since both ion velocity and position are functions of time for the ions decelerating in matter, also  $\theta_j^{RN}$  as a function of  $\theta_{det}^{lab}$  is a function of time, i.e.  $\theta_j^{RN}(\theta_{det}^{lab}, \vec{\beta}_j, \vec{x}_j)$  may be written as  $\theta_j^{RN}(\theta_{det}^{lab}, t)$ .

Mathematically, the angular distribution observed in the laboratory frame consequently has to be expressed as average over the individual angular distributions for

each ion  $j$  out of the  $N$  ions in the ensemble as a function of laboratory detection angle  $\theta_{det}^{lab}$  and time:

$$\begin{aligned}
 W(\theta_{det}^{lab}, t) &= \frac{1}{N} \sum_{j=1}^N W_i \left( \theta_j^{RN}(\theta_{det}^{lab}, t) \right) \\
 &= \frac{1}{N} \sum_{j=1}^N 1 + A_2 P_2 \left( \cos \theta_j^{RN}(\theta_{det}^{lab}, t) \right) + A_4 P_4 \left( \cos \theta_j^{RN}(\theta_{det}^{lab}, t) \right) \\
 &= 1 + A_2 \frac{1}{N} \sum_{j=1}^N P_2 \left( \cos \theta_j^{RN}(\theta_{det}^{lab}, t) \right) + A_4 \frac{1}{N} \sum_{j=1}^N P_4 \left( \cos \theta_j^{RN}(\theta_{det}^{lab}, t) \right) \\
 &\equiv 1 + A_2 \overline{P_2}(\theta_{det}^{lab}, t) + A_4 \overline{P_4}(\theta_{det}^{lab}, t).
 \end{aligned} \tag{B.7}$$

Equation B.7 shows that this averaged angular distribution can be expressed by averaged values of the Legendre polynomials  $\overline{P_2}$ ,  $\overline{P_4}$  evaluated at the corresponding emission angles  $\theta_j^{RN}(\theta_{det}^{lab}, t)$ .

In APCAD, the values of  $\overline{P_2}(\theta_{det}^{lab}, t)$  and  $\overline{P_4}(\theta_{det}^{lab}, t)$  as defined in Equation (B.7) are calculated along with the stopping matrices for each discrete time step  $t_n$  and are averaged over the detection angles  $\theta_{det}^{lab}$  covered by the respective angular bin  $i$ . These Legendre polynomials averaged over the ion ensemble and the polar angles covered by each angular bin  $i$  are denoted as  $\overline{P_{2,i}}(t_n)$  and  $\overline{P_{4,i}}(t_n)$  and stored in tables. Note that the attenuation of angular distributions by finite opening angles of conventional detectors [Gro65, Yam67] is automatically accounted for by averaging  $\overline{P_2}(\theta_{det}^{lab}, t)$  and  $\overline{P_4}(\theta_{det}^{lab}, t)$  over the detector opening angles. Calculated values of  $\overline{P_{2,i}}(t_n)$  and  $\overline{P_{4,i}}(t_n)$  are exemplarily shown in Figure B.3.

The Doppler-shifted energy of  $\gamma$ -ray quanta depends on the velocity  $\beta$  of the emitting ion and on the angle  $\alpha$  between the ion momentum vector and the  $\gamma$ -ray emission direction. Hence, for a given observation position  $(\theta_\gamma^{lab}, \phi_\gamma^{lab})$  and a fixed scattering angle of the emitting particle  $\theta_p^{lab}$  in the laboratory system, the observed Doppler-shift depends on the particle azimuth angle  $\phi_p^{lab}$ . If the experimental setup for the detection of scattered particles does not exhibit axial symmetry with respect to the beam axis, the nuclear alignment distribution does in general also not exhibit axial symmetry w.r.t. the beam axis and the  $\gamma$ -ray emission is not isotropic in the azimuth angle  $\phi_\gamma$ . The particle- $\gamma$  angular correlation function  $W(\theta_\gamma, \phi_\gamma)$ , Eq. (2.57), applies in this case. It can result in non-trivial distributions of Doppler-shift in  $\gamma$ -ray energy observed at a position  $(\theta_\gamma^{lab}, \phi_\gamma^{lab})$  even for

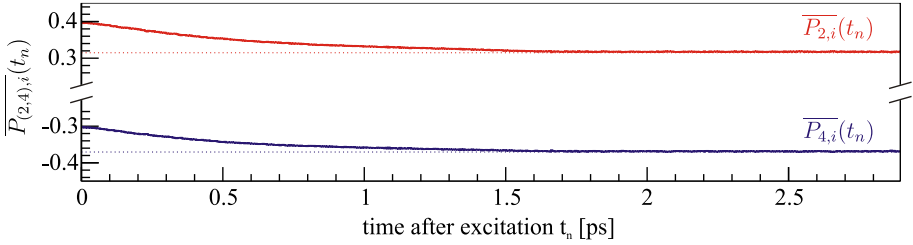


**Figure B.3.:** Average values of the 2<sup>nd</sup> and 4<sup>th</sup> Legendre polynomials  $\overline{P_{(2,4),i}^{(t_n)}}$ , evaluated at  $\gamma$ -ray detection angles  $\theta_{det}^{lab}$  subtended by a position-sensitive detector in an angular bin centered at  $\theta_{det}^{lab} = 137.6^\circ$  from the analysis of LNL experiment 08.09 (see Chapter 6.1.4). These values are used by APCAD to calculate angular distributions of  $\gamma$ -radiation emitted in-flight, observed at given polar angles in the laboratory system. The horizontal, dotted lines represent the values of  $P_{2,4}(\cos 137.6^\circ)$  which coincide with  $\overline{P_{(2,4),i}^{(t_n)}}$  if the  $\gamma$ -ray emission occurs at the center of the target and at rest. The variation of the  $\gamma$ -ray intensity ratio observed at maximum shift an in the stop peak due to different emitter velocities depends on the values of  $\overline{P_{2,4}}$  at  $t = 0$  and  $t > 2$  ps as well as the angular distribution expansion coefficients  $A_{2,4}$ . See text for details.

fixed ion velocity  $\beta$  and fixed particle polar scattering angle  $\theta_p^{lab}$ . This has to be accounted for in the calculation of Doppler-broadened  $\gamma$ -ray lineshapes<sup>1</sup>.

The first term in Eq. 2.57 describing the  $\gamma$ -ray angular distribution in the polar angle is accounted for by the evaluation of averaged Legendre polynomials as described above. What remains is a term

$$\begin{aligned}
 W'(\theta_j^{RN}, \phi_j^{RN}) &= 2 \sum_{k \geq 2} \sum_{q > 0}^k \hat{\rho}_{kq}(J_i) F_k \cos(q\phi_j^{RN}) C_{kq}(\theta_j^{RN}, 0) \\
 &\equiv \sum_{k \geq 2} \sum_{q > 0}^k A_{kq} \cos(q\phi_j^{RN}) C_{kq}(\theta_j^{RN}, 0).
 \end{aligned}
 \tag{B.8}$$

Again, the index  $j$  enumerates individual ions in the ensemble. In practice, it is sufficient to regard dipole- and quadrupole radiation, i.e.  $k \leq 4$ . Again, aver-

<sup>1</sup> If the setup has axial symmetry or if the  $\gamma$ -ray emission is isotropic in the azimuth angle, a broadening of the distribution of relative Doppler-shifts occurs that is accounted for by the stopping matrices  $S_i(s_m, t_n)$  by construction.

aged statistical tensors can be found that provide an adequate description of the  $\gamma$ -ray angular correlation in the rest-frame of the emitting nuclei.

Like for the polar-angular distribution discussed above, the angular correlation-function observed in the laboratory frame has to be derived from Equation (B.8) for each ion  $j$  individually. This is again due to the unique transformation of the angles as a function of the different velocities and positions of the ions in the ensemble. The  $\gamma$ -ray polar-angular distribution introduces a **re-scaling** of the distribution of relative Doppler-shifts observed at a certain observation angle  $\theta_{det}^{lab}$  by the time-dependent factors in Equation B.7. It does not affect the Doppler-shift distribution that is observed for a fixed  $\gamma$ -ray emission time  $t_n$ . In contrast, the particle- $\gamma$  angular correlation introduces a **change of the Doppler-shift distribution** observed at a certain observation angle  $\theta_{det}^{lab}$  at each time  $t_n$ . As a consequence, a procedure as for the polar-angular distribution can not be applied.

To account for the effect of particle- $\gamma$  angular correlations in APCAD, weighted stopping matrices  $\hat{S}_{ikq}(s_m, t_n)$  are introduced. They are calculated in the same way as the (un-weighted) stopping matrices  $S_i(s_m, t_n)$ , but the contribution by every individual ion  $j$  is weighted by the factor  $\cos(q\phi_j^{RN})C_{kq}(\theta_j^{RN}, 0)$  at every time  $t_n$ . The effect of particle- $\gamma$  angular correlations on calculated lineshapes is discussed in detail on the example of LNL-experiment 09.08 in Chapter 6.1.4.

For a set of angular distribution- and correlation-coefficients  $\{A_k, A_{kq}\}$ , the distributions of relative Doppler-shifts  $s_m$  observed in an angular bin  $i$  for  $\gamma$ -ray emission at times  $t_n$  is then given by

$$\mathcal{S}_i(s_m, t_n) = \left(1 + A_2 \overline{P_{2,i}}(t_n) + A_4 \overline{P_{4,i}}(t_n)\right) \left(S_i(s_m, t_n) + \sum_{k \geq 2} \sum_{q > 0}^k A_{kq} \hat{S}_{ikq}(s_m, t_n)\right). \quad (\text{B.9})$$

Along with the simulation of the excitation and deceleration of the ions in the target by StopSim, the calculation of the weighted and unweighted stopping matrices  $S_i(s_m, t_n)$  and  $\hat{S}_{ikq}(s_m, t_n)$  is by far the computationally most intensive part of the lineshape calculation with APCAD. Therefore, the calculation of the stopping matrices was implemented in a parallelized manner. By this, the time needed for the calculation of the stopping matrices can be reduced drastically when performed on computers with many CPUs. If the calculation is distributed to many CPUs, however, the memory consumption may become very high.

It has to be stressed that the ansatz of absorbing all physics and the geometry of the experimental setup into the weighted and unweighted stopping matrices as well as the averaged Legendre polynomials has the huge advantage that these calculations have to be performed only once for each analysis of a caDSAM exper-

iment with APCAD. The computation of lineshapes for a given set of parameters is then very fast, as discussed in the following.

### Definition of $\gamma$ -ray transitions

As discussed in Chapter 2.2, the decay function of a nuclear state is determined by the state's lifetime, the lifetimes of states feeding it and fractions  $b$  denoting to what percentage the involved states were populated by the nuclear reaction at time  $t = 0$ .

In the implementation in APCAD, nuclear states can possess an arbitrary number of *direct* feeders, i.e. the length of chains of states feeding each other is limited to two, the number of "parallel" feeding chains is not limited. This is sufficient for the DSAM experiment analyzed in this work and can easily be extended due to the object-oriented structure of the APCAD source code.

Let  $N_0$  be the total number of observed decays,  $b_0$  the percentage of direct population of the state under investigation,  $b_f$  the percentages of the population via the feeders  $f$ ,  $\tau_0$  the lifetime of the state under investigation and  $\tau_f$  the lifetimes of its direct feeders. As discussed in Chapter 2.2, the decay functions  $A_f(t)$  describing each of the feeding transitions are given by

$$A_f(t) = b_f \frac{N_0}{\tau_f} e^{-t/\tau_f}, \quad (\text{B.10})$$

and the decay function  $A_0(t)$  of the state of interest can then be written as

$$\begin{aligned} A_0(t) &= b_0 \frac{N_0}{\tau_0} e^{-t/\tau_0} + \sum_f b_f \frac{N_0}{\tau_0 - \tau_f} \left( e^{-t/\tau_0} - e^{-t/\tau_f} \right) \\ &\equiv A_{0,0}(t) + \sum_f A_{0,f}(t). \end{aligned} \quad (\text{B.11})$$

In general, the statistical tensor of a nuclear state is different depending on how the state was populated, i.e. directly or via the decay of a certain, higher-lying state. Therefore, the angular distribution of the  $\gamma$ -radiation de-populating the state of interest depends on how the state was populated. Consequently, the decays of the fractions of the state of interest that are populated directly by the nuclear reaction and by feeding from different higher-lying states have to be treated separately. Each of these fractions is described by one of the decay functions  $A_{0,0}(t)$  and  $A_{0,f}(t)$ .

For the numerical calculation of Doppler-broadened  $\gamma$ -ray lineshapes in APCAD, the decay functions are discretized in time, using the same binning in time as for

the stopping matrices. For this purpose, the decay functions are integrated over the time-intervals  $(t_{n,<}, \dots, t_{n,>})$  subtended by each time-bin  $t_n$ :

$$\hat{A}_x(t_n) = \int_{t_{n,<}}^{t_{n,>}} A_x(t) dt, \quad (\text{B.12})$$

where  $A_x(t)$  represents any of the decay functions  $A_{0,0}(t)$ ,  $A_{0,f}(t)$  and  $\hat{A}_x(t_n)$  the corresponding discretized decay functions.

The ion velocity histories provided by StopSim end at the time step when the ions have come to rest in the target or leave it. For the differential and geometric DSAM (see Chapter 4.4), the position of ions leaving the target can be further tracked in the stopping matrices for a user-defined time-span, accounting for effects of the  $\gamma$ -ray vertices on the observed Doppler-shifts. Any decay happening after the last time step  $t_{max}$  covered by the stopping matrices is accounted for by increasing the value of  $\hat{A}_x(t_{max})$  by the amount

$$\hat{A}_x(t_{max})+ = \int_{t_{max,>}}^{\infty} A_x(t) dt. \quad (\text{B.13})$$

These decays enter the further calculations via the distributions of relative Doppler-shift given by the last time bins of the stopping matrices. A discretized decay function  $\hat{A}_x(t_n)$  is exemplarily shown in the top right of Figure B.5.

The distributions  $p_i(s_m)$  of relative Doppler-shifts  $s_m$  observed in the angular bins  $i$  for the decay of the state under investigation is then given by

$$p_i(s_m) = \sum_{x,n} \hat{A}_x(t_n) \mathcal{S}_i(s_m, t_n). \quad (\text{B.14})$$

Note that for the decay of every differently populated fraction of the excited state  $x$  a different set of angular distribution- and correlation-coefficients  $\{A_k, A_{kq}\}$  can be used in the calculation of  $\mathcal{S}_i(s_m, t_n)$  in Equation B.9.

By the definition of the relative shifts  $s_m$  (Equation B.4), the Doppler-shifted  $\gamma$ -ray energies  $E'_{\gamma,m}$  corresponding to the discrete relative Doppler-shifts  $s_m$  for an un-shifted energy  $E_{\gamma,0}$  are given by

$$E'_{\gamma,m}(s_m) = E_{\gamma,0}(s_m + 1). \quad (\text{B.15})$$

Hence, the distribution  $p_i(s_m)$  of relative Doppler-shifts  $s_m$  can easily be converted into a distribution of Doppler-shifted  $\gamma$ -ray energies  $p_i(E'_{\gamma,m}(s_m))$ .

It has to be noted that the spacing of the discrete energies  $E'_{\gamma,m}$  depends on the un-shifted  $\gamma$ -ray energy  $E_{\gamma,0}$  and is therefore variable. In particular, it does not generally coincide with the energy binning of the experimental data. This apparent shortcoming is completely abolished after the application of detector response functions for a suitably small binning of  $s_m$ , as described in the next paragraph.

### Definition of detector response functions and calculation of lineshapes for a set of parameters

High-purity Germanium detectors exhibit a typical response function that can be well described by a Gaussian part, a low-energy tail and a step-function [Hel80]. In APCAD, a simple Gaussian function, an optional additional step-function and low-energy tail of the GAMANAL- or HYPERMET-type as described in [Hel80] can be chosen by the user. A typical response function and its components are shown in Figure B.4.

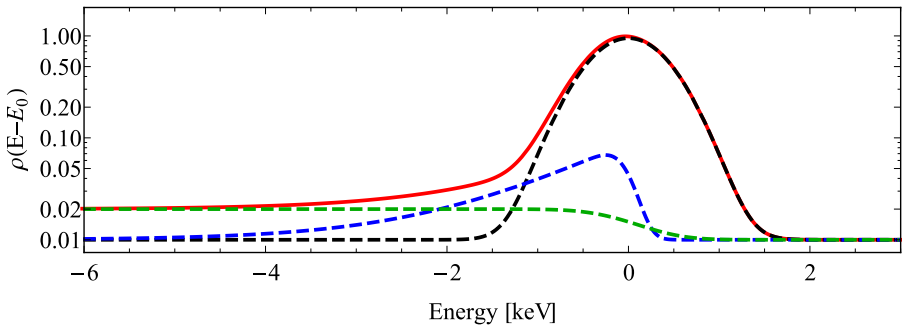


**Figure B.4.:** Typical detector response function for HPGe detectors consisting of Gaussian part (black, dashed line), low-energy tail (blue, dashed line) and step-function (green, dashed line). The total response function is drawn as red, solid line. The drawn functions were lifted by 0.01 for better visibility in the logarithmic scale.

The distributions of  $\gamma$ -ray energies  $p_i(E'_{\gamma,m})$  that are registered in an angular bin  $i$  represent intensities at discrete energies  $E'_{\gamma,m}$ . The theoretical lineshapes are calculated by adding response functions at every energy  $E'_{\gamma,m}$  where the normalization of each contribution is given by  $p_i(E'_{\gamma,m})$ . The procedure is depicted in the lower part of Figure B.5.

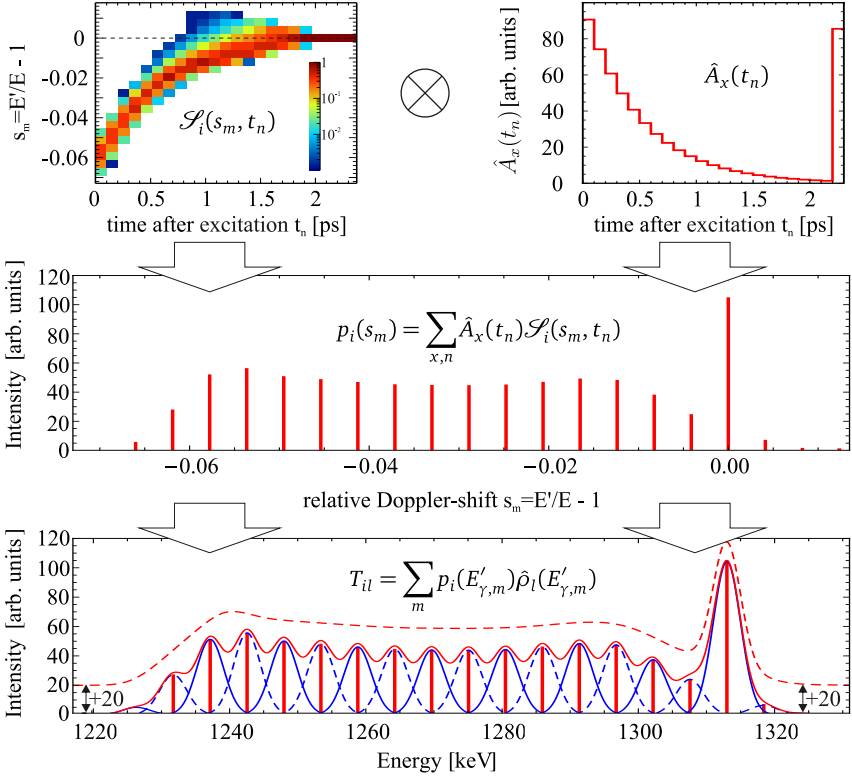


**Figure B.5:** Major steps in the calculation of a Doppler-broadened  $\gamma$ -ray lineshape in APCAD. A very coarse binning was chosen for clarity.

**Top:** From the distributions  $\mathcal{S}_i(s_m, t_n)$  of relative Doppler-shifts  $s_m$  observed in an angular bin  $i$  for  $\gamma$ -ray emission at times  $t_n$  and from the discretized decay functions  $\hat{A}_x(t_n)$ , the distributions  $p_i(s_m)$  of Doppler-shifts  $s_m$  observed in angular bin  $i$  are calculated (Equation B.9).

**Middle:** The distributions  $p_i(E'_{\gamma,m})$  of corresponding Doppler-shifted  $\gamma$ -ray energies  $E'_{\gamma,m}$  follow from  $p_i(s_m)$  by use of Equation (B.15).

**Bottom:** Application of the detector response function  $\hat{\rho}_l(E'_{\gamma,m})$  to every discrete energy  $E'_{\gamma,m}$ , weighted by  $p_i(E'_{\gamma,m})$  (red, vertical lines and blue curves), yields the final energy spectrum  $T_{il}$ . The discrete character of the energies  $E'_{\gamma,m}$  is effectively removed by the application of the response functions, if the binning of  $s_m$  is sufficiently fine. The thin, red line shows the obtained continuous spectrum for a very coarse binning, the dashed red line for a sufficiently fine binning of  $s_m$ . A binning in energy identical to that of the experimental data is introduced at this step by APCAD. See text for details.

In APCAD, the detector response functions  $\rho(E - E_0)$  are implemented as routines returning integrals of the response function over the energy range  $(E_{l,<}, E_{l,>})$  covered by an energy bin  $l$ :

$$\hat{\rho}_l(E_0) = \int_{E_{l,<}}^{E_{l,>}} \rho(E - E_0) dE. \quad (\text{B.16})$$

The energy-binning  $(E_{l,<}, E_{l,>})$  is defined by the binning of the experimental data.

As mentioned throughout this chapter, the final calculated 2D-spectrum of a Doppler-broadened  $\gamma$ -ray lineshape for a certain decay as a function of  $\gamma$ -ray energy  $E_\gamma$  and polar  $\gamma$ -ray detection angle  $\theta_\gamma$  is provided in the same binning as the experimental data. The histogram  $T_{il}$  contains this spectrum, where  $i$  enumerates the angular bins and  $l$  enumerates the energy bins. The content of each bin is given by

$$T_{il} = \sum_m p_i(E'_{\gamma,m}) \hat{\rho}_l(E'_{\gamma,m}), \quad (\text{B.17})$$

where  $p_i(E'_{\gamma,m})$  was defined in Equations (B.14) and (B.15) and  $\hat{\rho}_l(E'_{\gamma,m})$  is given by Equation (B.16).

Starting from weighted and unweighted stopping matrices  $S_i(s_m, t_n)$ ,  $\hat{S}_{ikq}(s_m, t_n)$  and averaged Legendre polynomials  $\overline{P_{2,i}}(t_n)$  and  $\overline{P_{4,i}}(t_n)$ , the Doppler-broadened lineshapes for an arbitrary number of different  $\gamma$ -decays with individual particle- $\gamma$  angular correlations can be quickly calculated. The procedure of their calculation is basically reduced to summing entries of pre-calculated tables.

The calculated Doppler-broadened  $\gamma$ -ray lineshapes for *all* angular bins  $i$  are determined by the following parameters, which are listed with a short note at what point they enter the calculation:

- **For each  $\gamma$ -ray transition: Intensity  $N_0$ , fractions of population paths  $b_f$ , lifetimes of the state  $\tau_0$  and its feeders  $\tau_f$**  for the calculation of decay functions  $\hat{A}_x(t_n)$  in Equations (B.11, B.12, B.13). Note that  $N_0$  is the *only normalization* of the lineshapes and applies to all angular bins  $i$ .
- **Angular distribution- and correlation-coefficients  $\{A_k, A_{kq}\}$**  for the decay of every differently populated fraction  $x$  of of the excited state<sup>2</sup>. The coefficients  $\{A_k, A_{kq}\}$  enter the calculation of  $\mathcal{S}'_i(s_m, t_n)$  (Equation B.9).

<sup>2</sup> The statistical tensor of a nuclear state populated by the decay of a higher-lying state is determined by the statistical tensor of the higher-lying state and the multipole order and character of the transition radiation (see Chapter 2.4). In a further-development of the program APCAD,

- **Coefficients for the detector response functions** such as resolution (FWHM), fractional area of the low-energy tail, parameters describing the shape of the tail and the height of the step-function. These parameters enter the calculation of the response function  $\rho(E - E_0)$  and, thus, Equation (B.16). They have to be specified for every angular bin  $i$ . Usually, they can be determined from a source measurement and then be fixed during the fitting procedure (see Chapter 6.1.4).

### Fit of lineshapes to experimental data

In the above paragraphs, the calculation of Doppler-broadened  $\gamma$ -ray lineshapes as a function of a set of necessary parameters was discussed. Lineshapes for an arbitrary number of  $\gamma$ -ray transitions can be calculated and added to the final spectrum  $T_{il}$ . For the comparison to experimental data, background described by polynomials of arbitrary order can be added to the calculated spectrum  $T_{il}$  for each angular bin  $i$  individually. The parameters of the background functions can be fitted simultaneously to the Doppler-broadened lineshapes or be fitted in a separate dialogue in APCAD and then be fixed during the fit of the lineshapes.

Lineshapes of  $\gamma$ -ray transitions feeding states that are under investigation can be fitted at the same time as the lineshapes from the decay of the fed states. Both lifetimes can be extracted simultaneously from the fit. The sensitivity to the lifetime of the feeding state then arises from both the lineshape of the feeding and the fed transition.

In the fit-procedure, a minimization of the difference between calculated and experimental spectra is done by variation of the parameters entering the calculation of the Doppler-broadened  $\gamma$ -ray lineshapes and the background functions. The difference between calculated and experimental spectra is quantified in terms of the  $\chi^2$ -value

$$\chi^2(\{p\}) = \sum_{i,l \in \mathcal{F}} \left( \frac{M_{il} - T_{il}(\{p\})}{\Delta M_{il}} \right)^2. \quad (\text{B.18})$$

Here,  $T_{il}(\{p\})$  denotes the value of the calculated spectrum in angular bin  $i$  and energy bin  $l$  as a function of the set of parameters  $\{p\}$ , the quantity  $M_{il}$  denotes the value of the experimental spectrum in the same bin and  $\Delta M_{il}$  its uncertainty. Comparison of calculated and experimental spectra is carried out in regions  $\mathcal{F}$  defined by the user. These are specified for each angular bin individually.

---

it would be desirable to exploit the resulting dependence between the particle- $\gamma$  angular correlations of the populating and de-population transition in order to reduce the number of parameters and enforce physically meaningful combinations of these parameters. This would be beneficial especially if the limitation to decay chains of length two is removed.

---

The minimization of the  $\chi^2$ -value is performed using the MINUIT program package [Jam75, Jam94]. MINUIT is included in the root-framework. It provides a variety of minimization methods and routines for the determination of uncertainties of optimum parameters derived from the fit and their correlations. In particular, it provides a method for the determination of *correlated errors* of best parameters obtained from the fit that accounts for correlations of the parameter with all other fit parameters. This "MINOS" error analysis overcomes limitations of the standard-technique for error estimation via a matrix of the second derivatives of the  $\chi^2$ -function with respect to the parameters at its minimum and provides a more realistic error estimate. For further information on the MINUIT program package and its routines and methods of error calculation, reference is made to the detailed MINUIT reference manual [Jam94].

---

### B.3 Implementation of the differential caDSAM

---

In APCAD, Doppler correction of experimental data can be mimicked precisely during the calculation of the stopping matrices. The experimental information that enter the Doppler correction of the data is accounted for during these calculations, resulting in realistic distributions of energy shifts after Doppler correction. The relevant measured values that enter the Doppler correction and that have to be accounted for are:

- Velocity of ions leaving the target:
  - Measured in the experiment with user-defined accuracy or
  - Assumed to have a constant, user-defined value
- Direction of ions leaving the target measured / not measured (beam axis is assumed as direction in this case)
- Longitudinal position of ions at the target position measured / not measured (target center is assumed as  $\gamma$ -ray vertex in this case) → see following section on geometric caDSAM

The uncertainty of the experimentally determined quantities such as ion velocity behind the target and  $\gamma$ -ray detector position resolution can be quantified by the user and are taken into account during the calculation of the stopping matrices. Geometrical effects such as a spatial longitudinal extent of the incoming ion beam and decays at certain distances behind the target are also accounted for in APCAD and are discussed in the following section.

Apart from the calculation of the stopping matrices, the remaining framework of APCAD as described in the previous sections can be used for the analysis of differential caDSAM experiments without modifications.

---

## B.4 Implementation of the geometric caDSAM

---

As discussed in Chapter B, the ion velocity histories simulated by the Monte-Carlo simulation `StopSim` end at the time step when the ions are completely stopped in the target or leave it. To begin with, de-excitations that occur *after* that time are assumed to result in the *same* distribution of Doppler-shifts as at the last time step of the velocity histories. This is exact in the case the ions are stopped in the target, and also a very good approximation if the decay happens at very small distances  $d$  behind the target. In the latter case, the influence of the altered  $\gamma$ -ray vertex on the Doppler-shift is negligible. This assumption no longer holds for the case of the geometric caDSAM, where decays at significant distances  $d$  behind the target resulting in a sizable effect on the Doppler-shift are regarded.

The ions' motion after they left the target is accounted for during the calculation of the stopping matrices in `APCAD`. The points  $\vec{x}_0$  where the ions exit from the target as well as their velocity vectors  $\vec{\beta}_0$  at these points are stored together with the velocity histories by `StopSim`. The position  $\vec{x}_n$  of the ion at each time step  $n$  is then easily obtained from the position  $\vec{x}_{n-1}$  at the previous time step via the relation

$$\vec{x}_n = \vec{x}_{n-1} + \gamma \vec{\beta}_0 \Delta t. \quad (\text{B.19})$$

Here,  $\gamma$  is the Lorentz-factor and  $\Delta t$  is the width of the time bins. The Doppler-shifts that are used for the calculation of the contributions to the stopping matrices (see Section B) can now be computed under consideration of a realistic  $\gamma$ -ray vertex.

If a Doppler correction is applied, the correction factor is computed according to user-specified assumptions, e.g. whether direction and velocity of the ions were measured behind the target and with what accuracy. These assumptions resemble the knowledge that is used for the Doppler correction of the experimental data. In particular, the factor for Doppler correction is calculated in ignorance of the realistic/true  $\gamma$ -ray vertex described above, since it is not accessible experimentally.

For all times after the ions have left the target, the width of the time bins  $\Delta t$  of the stopping matrix can be freely chosen by the user, as well as the time span for which the ions will be "tracked" after they left the target. This time-span is naturally limited by the distance of the  $\gamma$ -ray detector from the target and the velocities  $\beta_0$  of the ions behind the target, as discussed in the assessment of lifetimes measurable by the geometric caDSAM. It makes sense to choose a broader time-binning after the ions have left the target, since here the time-scale for the change of observed Doppler-shifts is much longer than during the rapid deceleration of the ions inside the target. A smaller number of time bins significantly reduces the computational

effort for lineshape-calculation and is justified, if the change of observed Doppler-Shift as a function of time is resolved sufficiently fine.

In the case that all decays occur approximately at the center of the target, it is sufficient to weight the contributions to the stopping matrices by the ratio  $d\Omega_\gamma^{RN}/d\Omega_\gamma^L = (E'_\gamma/E_0)^2$  (see Section B). Here,  $d\Omega_\gamma^{RN}$  denotes a solid angle element subtended by an areal element of the detector surface in the reference frame of an ion moving at velocity  $\beta$ .  $d\Omega_\gamma^L$  denotes the solid angle element subtended by the same areal element in the laboratory frame (see Equations 2.44 and 2.45).

If the  $\gamma$ -ray vertex is no longer at the center of the target (i.e. not in the reference point for which the efficiency correction was performed), the geometrical influence of the  $\gamma$ -ray vertex on the detection efficiency has to be taken into account. This geometrical influence on the detection efficiency is expressed by the solid angle  $\Omega_{det}(\vec{x})$  subtended by a detector surface  $\vec{A}_{det}$  for an ion that is located at the point  $\vec{x}$  w.r.t. the target center:

$$\Omega_{det}(\vec{x}) = \int_{\vec{A}_{det}} d\Omega. \quad (\text{B.20})$$

Since handy analytical expressions for  $\Omega_{det}(\vec{x})$  can be found only in very few special cases, an approximate procedure is used in APCAD.

Consider the case that an ion resides at the geometric center of a spherical detector-array. In this case, an areal element  $\vec{A}_{det}$  subtends the same solid angle in the reference frame of the ion, irrespective of the location of  $\vec{A}_{det}$  on the spherical detector. If the ion resides at the center of the target, it is assumed that any deviations from this situation are accounted for by the efficiency correction demanded for experimental data analyzed in APCAD (see Chapter 4.2, paragraph "Loading experimental spectra into APCAD"). This means that it is assumed that the  $\gamma$ -ray detection efficiency is isotropic in all directions covered by detectors, if the  $\gamma$ -ray vertex is at the target center. If the ion is displaced from the target center and resides at a position  $\vec{x}$ , the detection efficiency is altered geometrically by two factors:

- The ion can be closer to (further away from) an areal element of the detector surface. This raises (lowers) the subtended solid angle  $\Omega_{det}(\vec{x})$ .
- In the picture of the spherical detector and the target center at its focus, the vector from the position of the ion  $\vec{x} \neq 0$  to the center of the areal element  $\vec{a}$  of the detector surface does not coincide with the normal of that area. In other words, the detector surface is "tilted" from the perspective of the ion. This lowers the subtended solid angle  $\Omega_{det}(\vec{x})$ .

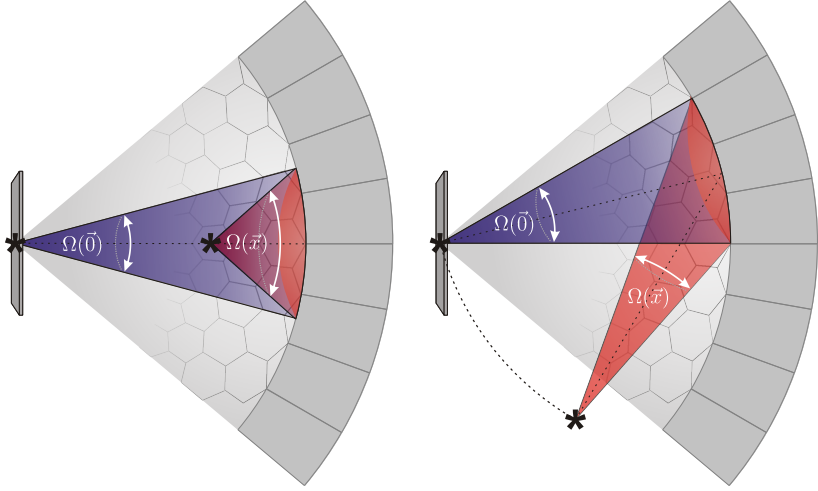


**Figure B.6.:** Effect of the position of an ion  $\vec{x}$  on the solid angle  $\Omega_{det}(\vec{x})$  subtended by an areal element of the detector surface. The solid angle subtended by the same areal element for an ion located at the center of the target is denoted  $\Omega_{det}(\vec{0})$ .

**Left:** If the ion is located closer to the detector than the target center, then  $\Omega_{det}(\vec{x}) > \Omega_{det}(\vec{0})$ .

**Right:** If the ion is at the same distance to the center of the areal element as the target center but displaced from the target center, the detector surface is "tilted" from its perspective. In this case,  $\Omega_{det}(\vec{x}) < \Omega_{det}(\vec{0})$ .

See text for details.

These two effects are visualized in Figure B.6. In APCAD, they are accounted for by the ratio  $\Omega_{det}(\vec{x})/\Omega_{det}(\vec{0})$ . Here,  $\Omega_{det}(\vec{0})$  denotes the solid angle subtended by the detector surface-element if the ion is located at the center of the target:

$$\frac{\Omega_{det}(\vec{x})}{\Omega_{det}(\vec{0})} = \Delta\Omega_D^2 \Delta\Omega_T, \text{ where} \quad (B.21)$$

$$\Delta\Omega_D = \frac{|\vec{a}|}{|\vec{x} - \vec{a}|},$$

$$\Delta\Omega_T = \frac{\vec{a} \cdot (\vec{x} - \vec{a})}{|\vec{a}| |\vec{x} - \vec{a}|}.$$

---

The term  $\Delta\Omega_D$  accounts for the distance of the ion from the detector surface, and the term  $\Delta\Omega_T$  accounts for the "tilting" of the detector surface from the perspective of the ion. This approximation was developed, verified by comparison to a Monte-Carlo integration routine and implemented into APCAD in the course of a Master's thesis supervised by the author [Let13]. It is accurate to better than  $\sim 2\%$  for spherical detector arrangements, if the ion-detector distance  $|\vec{x} - \vec{a}|$  is below  $\sim 0.2r$  where  $r = |\vec{0} - \vec{a}|$  is the distance of the detector from the target center. Deviation for smaller distances arise *inter alia* from the curvature of the assumed spherical detector surface.

The same treatment of ion-positions in the calculation of the stopping matrices is also employed when accounting for spatially extended beams or in situations where the ion beam is known to be displaced with respect to the target center. Therefore, also the continuous-angle DSAM and the differential caDSAM greatly benefit from the meticulous treatment of  $\gamma$ -ray vertices in APCAD. In particular, it makes APCAD a suitable tool for the analysis of any Doppler-shift based lifetime measurements where broad beam profiles occur. Such experimental conditions prevail *inter alia* at RIB facilities where exotic ion beams are produced by fragmentation/fission and in-flight separation.

## C Reaction kinematics

This section is based on Reference [Bal63].

For a reaction of the type  $I+II \rightarrow 1+2$  with initial energies  $E_I$  and  $E_{II}$ , initial masses  $m_I$  and  $m_{II}$ , initial momenta  $p_I$  and  $p_{II}$  as well as the corresponding quantities for the final state with indices 1 and 2, let  $II$  be a particle that initially is at rest in the laboratory frame and let particle  $I$  move in  $z$ -direction (polar angle  $\theta_I = 0$ ). In the following, the unit system is chosen such that  $c = 1$ .

Conservation of energy and momentum yields the relations for energy ( $E_1$ ,  $E_2$ ) and emission angle in the laboratory frame ( $\theta_1$ ,  $\theta_2$ ) of the particles after the collision:

$$E_1 = \frac{A_1 E_G \pm p_I \cos \theta_1 \sqrt{A_1^2 - 4m_1^2 (E_G^2 - p_I^2 \cos^2 \theta_1^2)}}{2 (E_G^2 - p_I^2 \cos^2 \theta_1)} \quad (\text{C.1})$$

$$E_2 = \frac{A_2 E_G \pm p_I \cos \theta_2 \sqrt{A_2^2 - 4m_2^2 (E_G^2 - p_I^2 \cos^2 \theta_2^2)}}{2 (E_G^2 - p_I^2 \cos^2 \theta_2)} \quad (\text{C.2})$$

The coefficients  $A_1$  and  $A_2$  are given by

$$A_1 = E_G^2 - p_I^2 + m_1^2 - m_2^2 \quad (\text{C.3})$$

$$A_2 = E_G^2 - p_I^2 + m_2^2 - m_1^2 \quad (\text{C.4})$$

Here  $E_G = E_I + E_{II} = m_I + E_{kin,I} + m_{II} = E_1 + E_2$  denotes the sum energy of the two particles in the laboratory frame. Excitation of the projectile with an energy  $E_{ex}$  is accounted for by letting  $m_1 = m_I + E_{ex}$ .

The relation between the emission angles of projectile- and target-like recoiling nucleus in the laboratory frame,  $\theta_1$  and  $\theta_2$ , is given by

$$\cot \theta_2 = \frac{-(1 + \rho_1 \rho_2) \cot \theta_1 \pm (\rho_1 + \rho_2) \sqrt{\gamma^2 (1 - \rho_1^2) + \cot^2 \theta_1}}{1 - \rho_1^2} \quad (\text{C.5})$$

with the coefficients

$$\rho_n = \frac{p_I}{\gamma \tilde{p}_n} = \frac{\sqrt{E_I^2 - m_I^2}}{E_I + m_{II}} \frac{A_n}{\sqrt{A_n^2 - 4\tilde{E}_G^2 m_n^2}} \quad (\text{C.6})$$

using the Lorentz-factor  $\gamma = \frac{E_G}{\tilde{E}_G} = \frac{E_I - m_{II}}{\sqrt{(E_I + m_{II})^2 - (E_I^2 - m_I^2)}} = \frac{1}{\sqrt{1 - \beta^2}}$ . Quantities in the center of mass (CM) system are marked by a tilde,  $\beta$  is the relative velocity of laboratory and CM system. In the case of an initially resting (target) nucleus,  $\beta$  is just its velocity in the CM system  $\beta = \frac{p_I}{E_G}$ .

If  $m_I > m_{II}$ , the collision is called to take place in *inverse kinematics*. In this case the coefficients  $\rho_n$  in eq. C.6 may become larger than unity.

For  $\rho_n > 1$ , two values of  $\theta_{2(1)}$  correspond to one value of  $\theta_{1(2)}$ , the dependence branches and is not unique. For that reason, "+"- and "-"-sign have to be accounted for in eq. C.1 and C.2, respectively. Their consideration yields the correct value before and after the cutoff angle of emission  $\theta_{n,max}$ , which is defined by

$$\sin^2 \theta_{n,max} = \frac{A_n^2 - 4m_n^2 \left( (m_I + m_{II})^2 + 2m_{II} E_{kin,I} \right)}{4m_n^2 p_I^2} \quad (\text{C.7})$$

For  $\rho_n \leq 1$ , the "+"-sign has to be used and the correspondence C.5 is unique.

---

## D Additional spectra for LNL exp. 08.09

---

### D.1 Particle spectra and gates for reaction channel selection

---

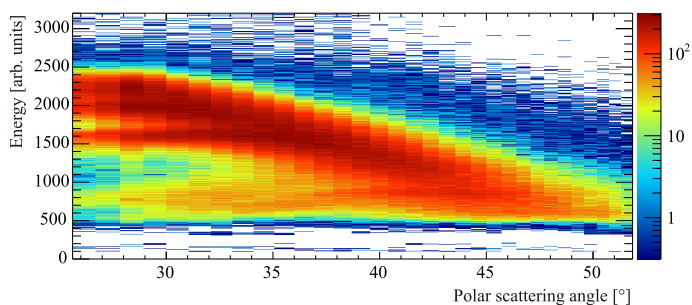


**Figure D.1.:** Energy spectrum measured in the rings of the DSSD as a function of the particle scattering angle, measured at 546 MeV beam energy with the layered DSAM target (carbon + tantalum backing). Add-back and corrections for the degeneration of the detector were applied. See Section 6.1.2 for details.

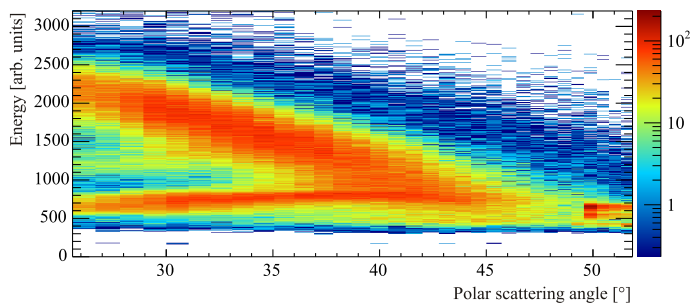


**Figure D.2.:** Same as is Figure D.1, but for 500 MeV beam energy. See Section 6.1.2 for details.

The particle energy spectra as function of polar scattering angle for the measurements with thin carbon target are shown in Section 6.1.2.

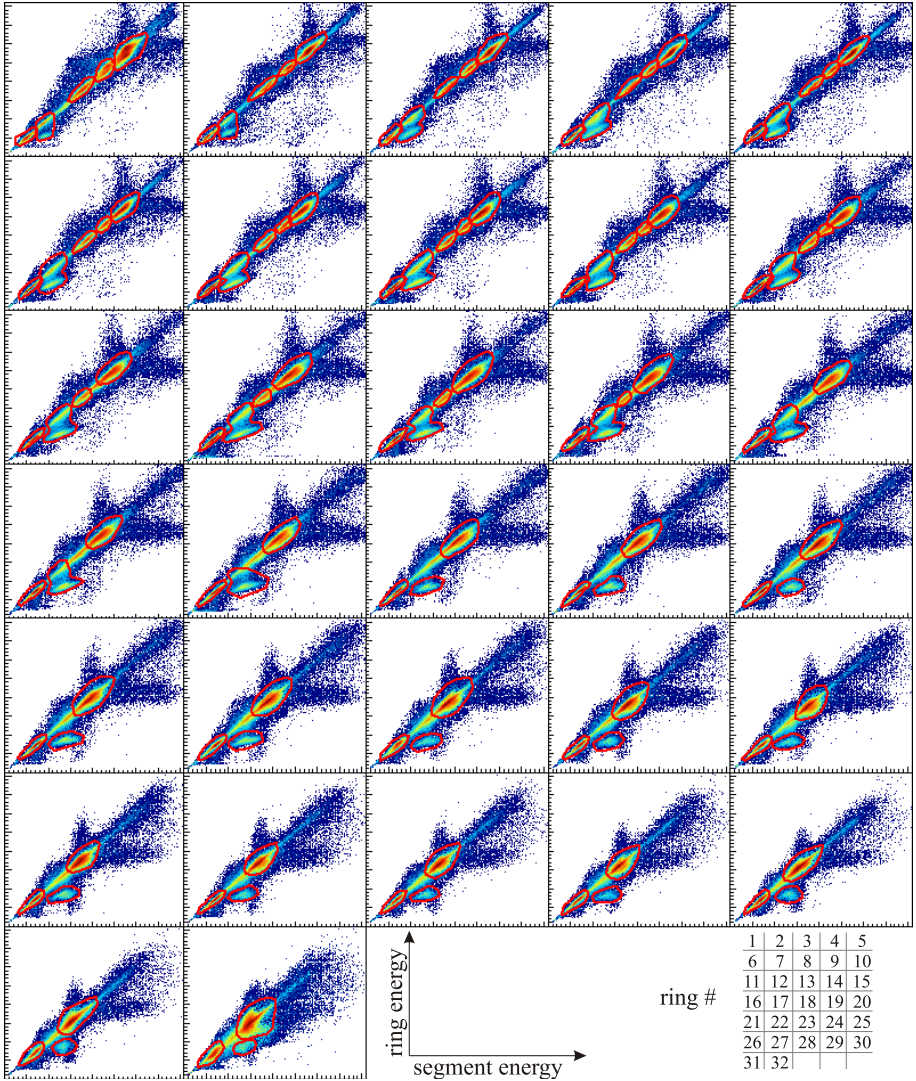


**Figure D.3.:** Particle energy spectra and reaction channel gates for the runs at 546 MeV beam energy using the carbon target. Add-back and corrections for the degeneration of the detector were applied. The energy is given in arbitrary units and the gates are indicated by red lines. See Section 6.1.2 for details.

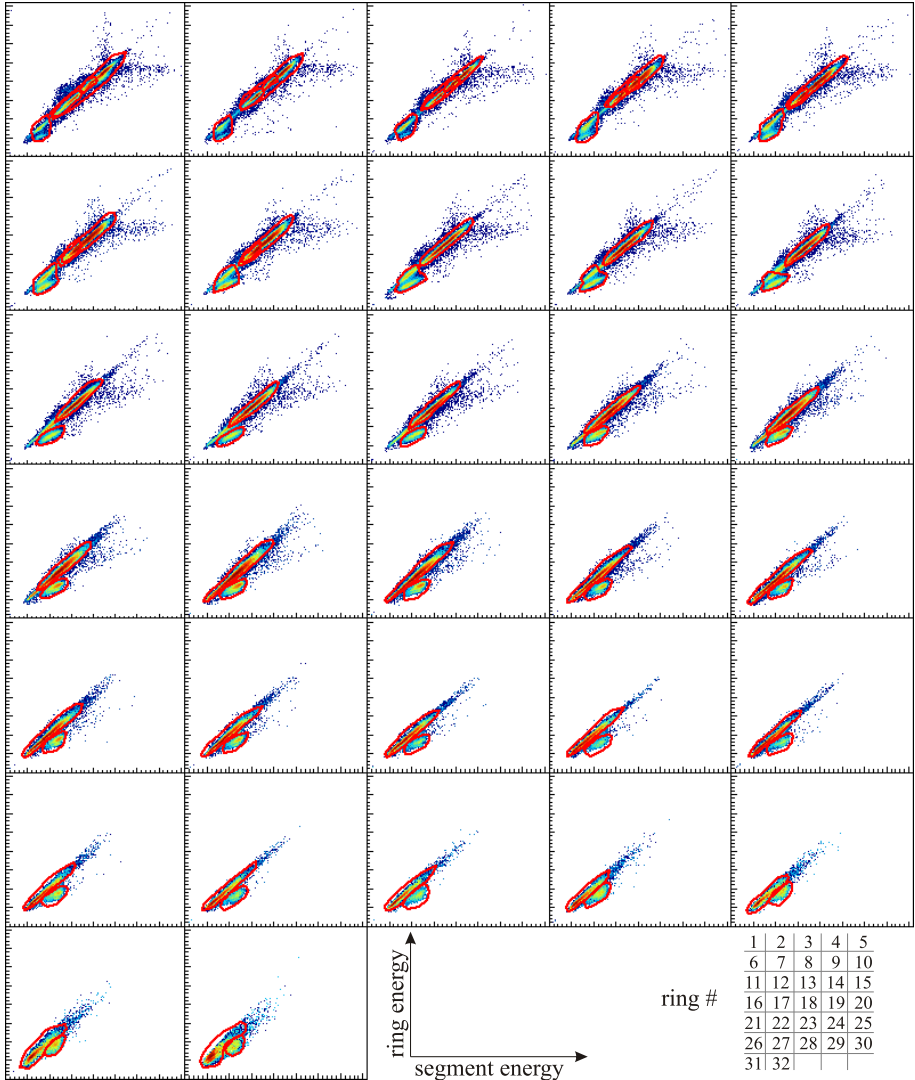


**Figure D.4.:** Particle energy spectra and reaction channel gates for the runs at 546 MeV beam energy using the layered DSAM target (carbon + tantalum backing) for DSAM measurements. Add-back and corrections for the degeneration of the detector were applied. The energy is given in arbitrary units and the gates are indicated by red lines. See Section 6.1.2 for details.

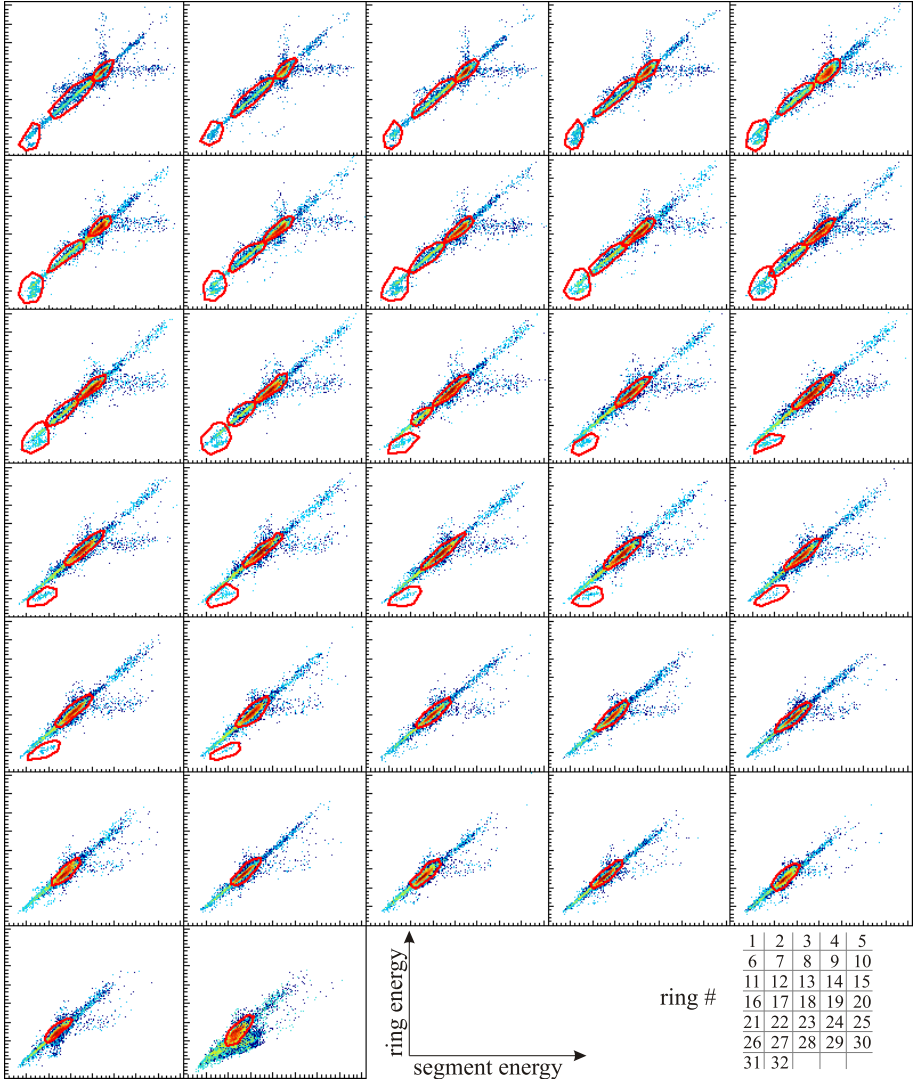


**Figure D.5.:** Particle energy spectra and reaction channel gates for the runs at 500 MeV beam energy using the carbon target. Add-back and corrections for the degeneration of the detector were applied. The energy is given in arbitrary units and the gates are indicated by red lines. See Section 6.1.2 for details.

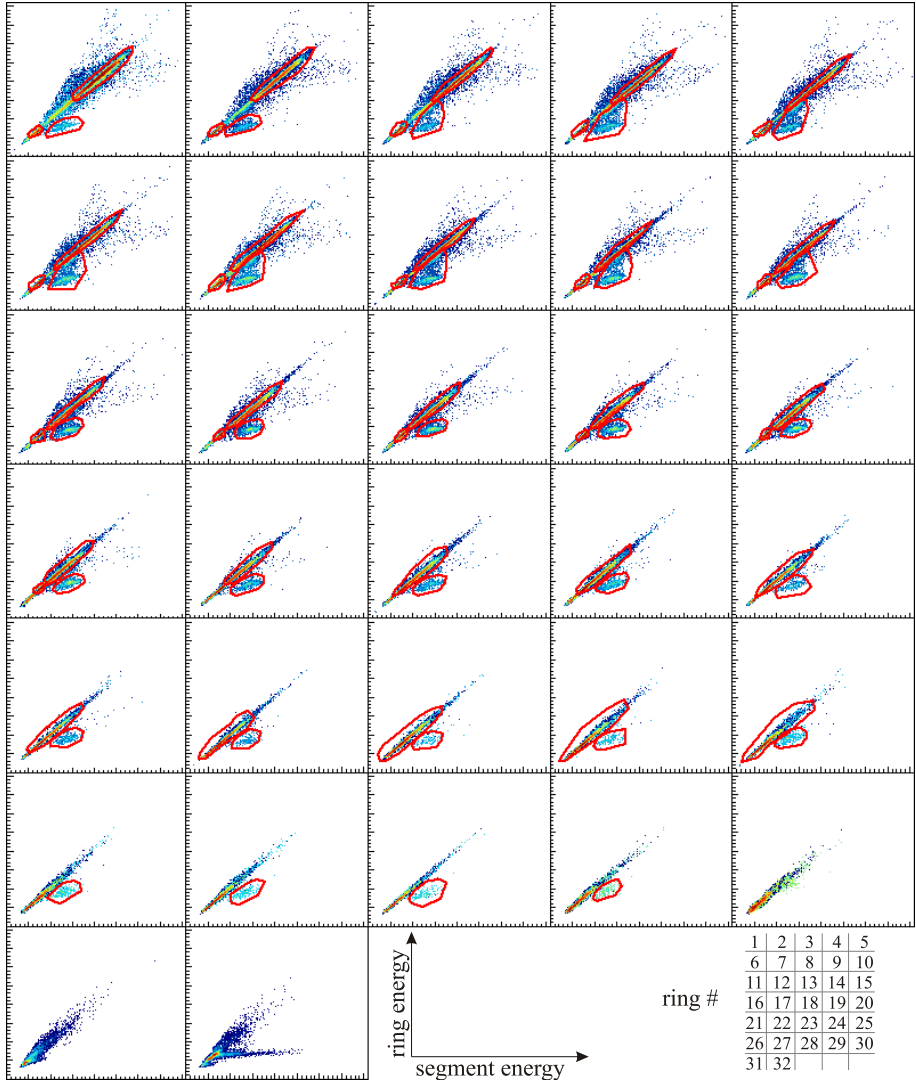


**Figure D.6.:** Particle energy spectra and reaction channel gates for the runs at 500 MeV beam energy using the layered DSAM target (carbon + tantalum backing) for DSAM measurements. Add-back and corrections for the degeneration of the detector were applied. The energy is given in arbitrary units and the gates are indicated by red lines. See Section 6.1.2 for details.

## D.2 Determination of parameters defining the setup geometry

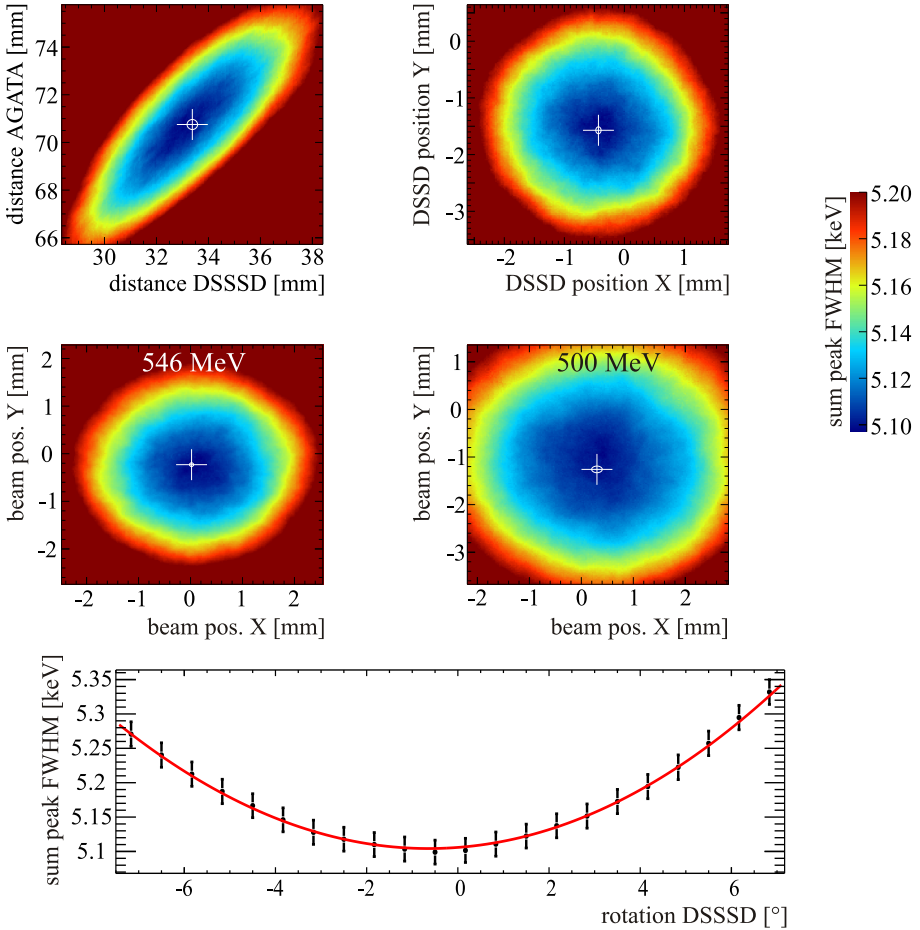


**Figure D.7.:** Determination of parameters defining the setup geometry by optimization of the  $\gamma$ -ray resolution after Doppler correction. The white crosses mark the locations of the minima and the white circles their uncertainties. See Section 6.1.2 for details.

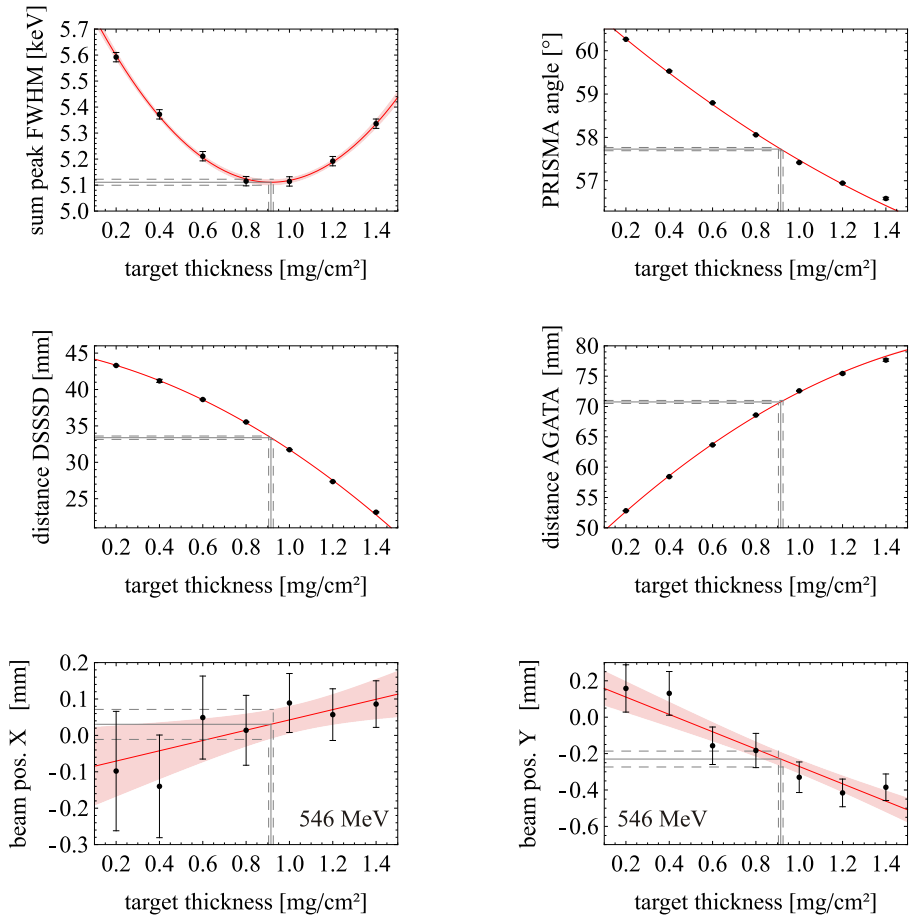


**Figure D.8.:** Top Left: Determination of the carbon target thickness. For each data point, all parameters have been optimized as shown in Figure D.7, assuming different target thicknesses. At the true target thickness, the best  $\gamma$ -ray resolution is obtained. Other plots: Once the target thickness is determined, all parameters can be derived with good precision. The remaining parameters are shown in Figure D.9. See Section 6.1.2 for details.

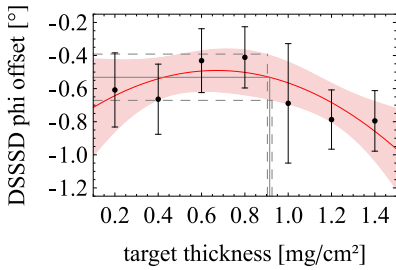
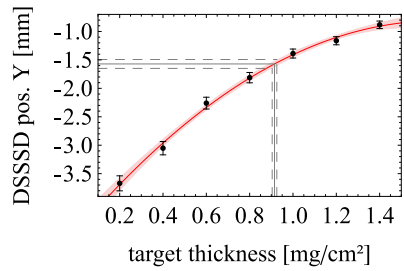
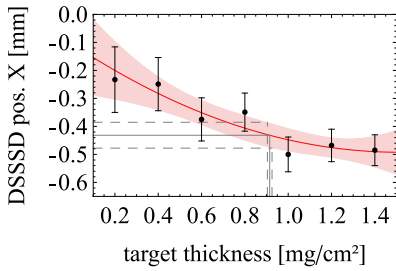
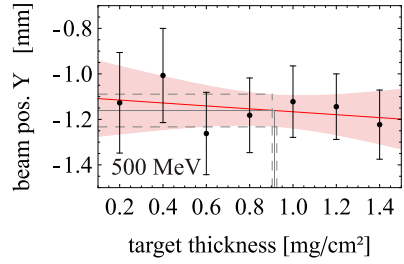
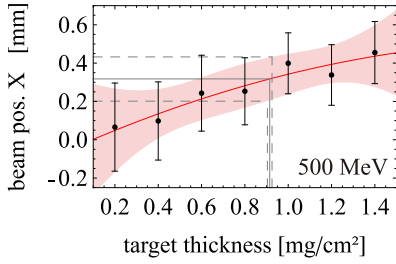


**Figure D.9.:** Continuation of Figure D.8

# E Reduced M1 transition strength for a $p_{1/2} \rightarrow p_{3/2}$ spin-flip transition

The electromagnetic transition strength for a  $(\sigma\lambda)$  transition, for example  $\sigma\lambda = M1$ , is given by

$$B(\sigma\lambda, J_1 \rightarrow J_2) = \frac{1}{2J_1 + 1} |\langle J_2 || \mathcal{O}(\sigma\lambda) || J_1 \rangle|^2 \quad (\text{E.1})$$

The reduced matrix element can be evaluated using the Wigner-Eckart theorem [Boh69, Eq. 1A-60]:

$$\langle J_2 || \mathcal{O}(\sigma\lambda) || J_1 \rangle = \sqrt{J_2 + 1} \left( \mathcal{C}_{J_1 m_1 \lambda \mu}^{J_2 m_2} \right)^{-1} \langle J_2 m_2 | \mathcal{O}(\sigma\lambda, \mu) | J_1 m_1 \rangle \quad (\text{E.2})$$

where  $\mathcal{O}(\sigma\lambda, \mu)$  is the  $\mu$ -component of the operator  $\mathcal{O}(\sigma\lambda)$  and  $\mathcal{C}_{J_1 m_1 \lambda \mu}^{J_2 m_2} = \langle J_1 m_1 \lambda \mu | J_2 m_2 \rangle$  is the Clebsch-Gordan coefficient for coupling  $|J_1 m_1\rangle$  and  $|\lambda \mu\rangle$  to  $|J_2 m_2\rangle$ .

For the case of a M1 transition, let  $\mathcal{O}(\sigma\lambda, \mu) = \mathcal{O}(M1, 0)$ . The operator  $\mathcal{O}(M1, 0)$  doesn't change the magnetic quantum number. By choosing  $m_2 = \frac{1}{2}$ , only the sub-state with  $m_1 = \frac{1}{2}$  of  $|J_1\rangle$  is relevant in the following. Therefore, only the matrix element

$$\langle J_2 m_2 | \mathcal{O}(M1, 0) | J_1 m_1 \rangle = \langle \frac{3}{2} \frac{1}{2} | \mathcal{O}(M1, 0) | \frac{1}{2} \frac{1}{2} \rangle \quad (\text{E.3})$$

has to be evaluated. The 0-component of the magnetic dipole operator is given by

$$\mathcal{O}(M1, 0) = \sqrt{\frac{3}{4\pi}} \left( g_l^\pi \cdot \hat{l}_z + g_s^\pi \cdot \hat{s}_z \right) \mu_N \quad (\text{E.4})$$

where  $g_l^\pi$  and  $g_s^\pi$  are the proton orbital- and spin gyromagnetic ratios, respectively, and  $\hat{l}_z$  and  $\hat{s}_z$  are the z-components of the orbital angular momentum and spin operators, respectively.

The state  $|Jm_J\rangle = |\frac{1}{2}\frac{1}{2}\rangle$  can be expressed as

$$|\frac{1}{2}\frac{1}{2}\rangle = \sum_{l,s,m_l,m_s} \mathcal{C}_{lm_lsm_s}^{\frac{1}{2}\frac{1}{2}} |lm_l\rangle |sm_s\rangle. \quad (\text{E.5})$$

For a single-particle  $p_{\frac{1}{2}}$  state,  $l = 1$  and  $s = \frac{1}{2}$ . For a coupling to a  $|\frac{1}{2}\frac{1}{2}\rangle$  state,  $m_l = 1; m_s = -\frac{1}{2}$  and  $m_l = 0; m_s = \frac{1}{2}$  are the only possibilities and hence

$$|\frac{1}{2}\frac{1}{2}\rangle = \mathcal{C}_{11\frac{1}{2}-\frac{1}{2}}^{\frac{1}{2}\frac{1}{2}} |11\rangle |\frac{1}{2}-\frac{1}{2}\rangle + \mathcal{C}_{10\frac{1}{2}\frac{1}{2}}^{\frac{1}{2}\frac{1}{2}} |10\rangle |\frac{1}{2}\frac{1}{2}\rangle. \quad (\text{E.6})$$

The same applies for a single-particle  $p_{\frac{3}{2}}$  state:

$$|\frac{3}{2}\frac{1}{2}\rangle = \mathcal{C}_{11\frac{1}{2}-\frac{1}{2}}^{\frac{3}{2}\frac{1}{2}} |11\rangle |\frac{1}{2}-\frac{1}{2}\rangle + \mathcal{C}_{10\frac{1}{2}\frac{1}{2}}^{\frac{3}{2}\frac{1}{2}} |10\rangle |\frac{1}{2}\frac{1}{2}\rangle. \quad (\text{E.7})$$

The relevant Clebsch-Gordan coefficients have the following values:

$$\begin{aligned} \mathcal{C}_{11\frac{1}{2}-\frac{1}{2}}^{\frac{1}{2}\frac{1}{2}} &= \sqrt{\frac{2}{3}} \\ \mathcal{C}_{10\frac{1}{2}\frac{1}{2}}^{\frac{1}{2}\frac{1}{2}} &= -\frac{1}{\sqrt{3}} \\ \mathcal{C}_{11\frac{1}{2}-\frac{1}{2}}^{\frac{3}{2}\frac{1}{2}} &= \frac{1}{\sqrt{3}} \\ \mathcal{C}_{10\frac{1}{2}\frac{1}{2}}^{\frac{3}{2}\frac{1}{2}} &= \sqrt{\frac{2}{3}} \end{aligned} \quad (\text{E.8})$$

and, therefore,

$$|\frac{1}{2}\frac{1}{2}\rangle = \sqrt{\frac{2}{3}} |11\rangle |\frac{1}{2}-\frac{1}{2}\rangle - \frac{1}{\sqrt{3}} |10\rangle |\frac{1}{2}\frac{1}{2}\rangle \quad (\text{E.9})$$

and

$$|\frac{3}{2}\frac{1}{2}\rangle = \frac{1}{\sqrt{3}} |11\rangle |\frac{1}{2}-\frac{1}{2}\rangle + \sqrt{\frac{2}{3}} |10\rangle |\frac{1}{2}\frac{1}{2}\rangle. \quad (\text{E.10})$$

The  $\mathcal{O}(M1, 0)$  operator acting on  $|\frac{1}{2} \frac{1}{2}\rangle$  yields

$$\begin{aligned} \mathcal{O}(M1, 0)|\frac{1}{2} \frac{1}{2}\rangle &= \sqrt{\frac{3}{4\pi}} \left( g_l^\pi \cdot \hat{i}_z + g_s^\pi \cdot \hat{s}_z \right) \left[ \sqrt{\frac{2}{3}} |11\rangle |\frac{1}{2} - \frac{1}{2}\rangle - \frac{1}{\sqrt{3}} |10\rangle |\frac{1}{2} \frac{1}{2}\rangle \right] \mu_N \\ &= \sqrt{\frac{3}{4\pi}} \left[ g_l^\pi \sqrt{\frac{2}{3}} |11\rangle |\frac{1}{2} - \frac{1}{2}\rangle \right. \\ &\quad \left. - \frac{1}{2} g_s^\pi \left( \sqrt{\frac{2}{3}} |11\rangle |\frac{1}{2} - \frac{1}{2}\rangle + \frac{1}{\sqrt{3}} |10\rangle |\frac{1}{2} \frac{1}{2}\rangle \right) \right] \mu_N. \end{aligned} \quad (\text{E.11})$$

Evaluating  $\langle \frac{3}{2} \frac{1}{2} | \mathcal{O}(M1, 0) | \frac{1}{2} \frac{1}{2} \rangle$  gives

$$\begin{aligned} \langle \frac{3}{2} \frac{1}{2} | \mathcal{O}(M1, 0) | \frac{1}{2} \frac{1}{2} \rangle &= \sqrt{\frac{3}{4\pi}} \left[ g_l^\pi \frac{1}{\sqrt{3}} \sqrt{\frac{2}{3}} - \frac{1}{2} g_s^\pi \frac{1}{\sqrt{3}} \sqrt{\frac{2}{3}} - \frac{1}{2} g_s^\pi \sqrt{\frac{2}{3}} \frac{1}{\sqrt{3}} \right] \mu_N \\ &= \frac{1}{\sqrt{4\pi}} \sqrt{\frac{2}{3}} (g_l^\pi - g_s^\pi) \mu_N \end{aligned} \quad (\text{E.12})$$

and hence, using Eq. (E.2),

$$\begin{aligned} \langle \frac{3}{2} || \mathcal{O}(M1) || \frac{1}{2} \rangle &= \sqrt{2 \frac{3}{2} + 1} \left( \mathcal{C}_{\frac{1}{2} \frac{1}{2} \frac{1}{2} 10}^{\frac{3}{2} \frac{1}{2}} \right)^{-1} \langle \frac{3}{2} \frac{1}{2} | \mathcal{O}(M1, 0) | \frac{1}{2} \frac{1}{2} \rangle \\ &= 2 \left( \sqrt{\frac{2}{3}} \right)^{-1} \langle \frac{3}{2} \frac{1}{2} | \mathcal{O}(M1, 0) | \frac{1}{2} \frac{1}{2} \rangle \\ &= \frac{2}{\sqrt{4\pi}} (g_l^\pi - g_s^\pi) \mu_N. \end{aligned} \quad (\text{E.13})$$

This results in a reduced transition strength of

$$\begin{aligned} B \left( M1, \frac{1}{2}_{l=1} \rightarrow \frac{3}{2}_{l=1} \right) &= \frac{1}{2 \frac{3}{2} + 1} \left| \langle \frac{3}{2} || \mathcal{O}(M1) || \frac{1}{2} \rangle \right|^2 \\ &= \frac{1}{2\pi} (g_l^\pi - g_s^\pi)^2 \mu_N^2. \end{aligned} \quad (\text{E.14})$$

Inserting the values  $g_l^\pi = 1.0$  and  $g_s^\pi = 0.7 \times 5.58$  where the former is the free proton orbital g-factor and the latter is the free proton spin g-factor quenched by a factor 0.7 (see e.g. [Ala89, Knü86]) yields

$$B \left( M1, \frac{1}{2}_{l=1} \rightarrow \frac{3}{2}_{l=1} \right) = 1.344 \mu_N^2. \quad (\text{E.15})$$



---

# Bibliography

- [Ago03] S. Agostinelli *et al.*, *Geant4 - a simulation toolkit*, Nucl. Instr. Meth. A **506**, 250 (2003)
- [Ahm93] I. Ahmad, P. A. Butler, *Octupole shapes in nuclei*, Ann. Rev. Nucl. Part. Sci. **43**, 71 (1993)
- [Ahn12] T. Ahn *et al.*, *Identification of the  $2_{1,ms}^+$  mixed-symmetry state in  $^{136}\text{Ce}$* , Phys. Rev. C **86**, 014303 (2012)
- [Akk12] S. Akkoyun *et al.*, *AGATA - advanced gamma tracking array*, Nucl. Instr. Meth. A **668**, 26 (2012)
- [Ala89] R. Alarcon, R. M. Laszewski, D. S. Dale, *Giant M1 resonance in  $^{120}\text{Sn}$  and the quenching of the nucleon spin g-factors*, Phys. Rev. C **40**, 1097 (1989)
- [Ald56a] K. Alder, A. Winther, *Tables of the classical orbital integrals in Coulomb excitation*, Dan. Mat. Fys. Medd. **31**, 1 (1956)
- [Ald56b] K. Alder *et al.*, *Study of Nuclear Structure by Electromagnetic Excitation with Accelerated Ions*, Rev. Mod. Phys. **28**, 432 (1956)
- [Ald75] K. Alder, A. Winther, *Electromagnetic Excitation*, North-Holland, 1975
- [Ale78] T. Alexander, J. Forster, *Lifetime measurements of excited nuclear levels by Doppler-shift methods*, in: M. Baranger, E. Vogt (eds.), *Advances in nuclear Physics*, Vol. 10, pp. 197–331, Springer, 1978
- [Ali12] B. Alikhani *et al.*, *Compton polarimetry with a 36-fold segmented HPGe-detector of the AGATA-type*, Nucl. Instr. Meth. A **675**, 144 (2012)
- [All06] J. Allison *et al.*, *Geant4 developments and applications*, IEEE Transactions on Nuclear Science **53**, 270 (2006)
- [All11] J. M. Allmond *et al.*, *Coulomb excitation of  $^{124,126,128}\text{Sn}$* , Phys. Rev. C **84**, 061303 (2011)
- [All12] J. M. Allmond *et al.*, *One-neutron transfer study of  $^{135}\text{Te}$  and  $^{137}\text{Xe}$  by particle- $\gamma$  coincidence spectroscopy: The  $\nu 1i_{13/2}$  state at  $N = 83$* , Phys. Rev. C **86**, 031307 (2012)

- 
- [Alo08] C. E. Alonso *et al.*, *Population of mixed-symmetry states via  $\alpha$  transfer reactions*, Phys. Rev. C **78**, 017301 (2008)
- [Ari75] A. Arima, F. Iachello, *Collective Nuclear States as Representations of a  $SU(6)$  Group*, Phys. Rev. Lett. **35**, 1069 (1975)
- [Ari77] A. Arima *et al.*, *Collective nuclear states as symmetric couplings of proton and neutron excitations*, Phys. Lett. B **66**, 205 (1977)
- [Ast10] A. Astier *et al.*, *Novel Manifestation of  $\alpha$ -Clustering Structures: New “ $\alpha+^{208}\text{Pb}$ ” States in  $^{212}\text{Po}$  Revealed by Their Enhanced  $E1$  Decays*, Phys. Rev. Lett. **104**, 042701 (2010)
- [Ata09] A. Ataç *et al.*, *Discrimination of gamma rays due to inelastic neutron scattering in AGATA*, Nucl. Instr. Meth. A **607**, 554 (2009)
- [Bad13] V. M. Bader *et al.*, *Quadrupole collectivity in neutron-deficient Sn nuclei:  $^{104}\text{Sn}$  and the role of proton excitations*, Phys. Rev. C **88**, 051301 (2013)
- [Bag08] C. M. Baglin, *Nuclear Data Sheets for  $A = 81$* , Nuclear Data Sheets **109**, 2257 (2008)
- [Bal63] A. M. Baldin, W. I. Goldanskij, I. L. Rosental, *Kinematik der Kernreaktionen*, Akademie-Verlag, 1963
- [Bar13] B. R. Barrett, P. Navrátil, J. P. Vary, *Ab initio no core shell model*, Prog. Part. Nucl. Phys. **69**, 131 (2013)
- [Bas07] B. Bastin *et al.*, *Collapse of the  $N = 28$  Shell Closure in  $^{42}\text{Si}$* , Phys. Rev. Lett. **99**, 022503 (2007)
- [Bat10] H. Bateman, *The solution of a system of differential equations occurring in the theory of radioactive transformations*, in: *Proc. Cambridge Philos. Soc.*, vol. 15, pp. 423–427, 1910
- [Bau12] C. Bauer *et al.*, *Prolate shape of  $^{140}\text{Ba}$  from a first combined Doppler-shift and Coulomb-excitation measurement at the REX-ISOLDE facility*, Phys. Rev. C **86**, 034310 (2012)
- [Bau13] C. Bauer, *Level lifetimes and quadrupole moments from projectile Coulomb excitation of  $A \sim 130$  nuclei*, Ph.D. thesis, Technische Universität Darmstadt (2013)
- [Baz02] D. Bazin *et al.*, *The program LISE: a simulation of fragment separators*, Nucl. Instr. Meth. A **482**, 307 (2002)

- 
- [Baz04] D. Bazzacco, *The Advanced Gamma Ray Tracking Array AGATA*, Nucl. Phys. A **746**, 248 (2004)
- [Ben03] M. Bender, P.-H. Heenen, P.-G. Reinhard, *Self-consistent mean-field models for nuclear structure*, Rev. Mod. Phys. **75**, 121 (2003)
- [Ber99] C. Bertulani, V. Ponomarev, *Microscopic studies on two-phonon giant resonances*, Phys. Rep. **321**, 139 (1999)
- [Ber03] C. Bertulani, C. Campbell, T. Glasmacher, *A computer program for nuclear scattering at intermediate and high energies*, Computer Physics Communications **152**, 317 (2003)
- [Bia13] D. Bianco *et al.*, *Spectroscopy of neutron-rich Te and Xe isotopes within a new shell model context*, Phys. Rev. C **88**, 024303 (2013)
- [Bin14] S. Binder *et al.*, *Ab initio path to heavy nuclei*, Phys. Lett. B **736**, 119 (2014)
- [Biz15] P. Bizzeti *et al.*, *Analyzing power of AGATA triple clusters for gamma-ray linear polarization*, Eur. Phys. J. A **51**, 49 (2015)
- [Bla66] A. Blaugrund, *Notes on Doppler-shift lifetime measurements*, Nucl. Phys. **88**, 501 (1966)
- [Blu13] Y. Blumenfeld, T. Nilsson, P. van Duppen, *Facilities and methods for radioactive ion beam production*, Physica Scripta **T152**, 014023 (2013)
- [Boe68] J. de Boer, J. Eichler, *The reorientation effect*, in: M. Baranger, E. Vogt (eds.), *Advances in nuclear Physics*, Vol. 1, pp. 1–64, Plenum Press, 1968
- [Bog10] S. Bogner, R. Furnstahl, A. Schwenk, *From low-momentum interactions to nuclear structure*, Prog. Part. Nucl. Phys. **65**, 94 (2010)
- [Boh52] A. Bohr, B. R. Mottelson, *Beta-decay and the shell model, and the influence of collective motion on nuclear transitions*, Physica **18**, 1066 (1952)
- [Boh69] A. Bohr, B. R. Mottelson, *Nuclear Structure, Vol. I: Single-Particle Motion*, W. A. Benjamin, 1969
- [Boh75] A. Bohr, B. R. Mottelson, *Nuclear Structure, Vol. II: Nuclear Deformations*, W. A. Benjamin, 1975
- [Boh84] D. Bohle *et al.*, *New magnetic dipole excitation mode studied in the heavy deformed nucleus  $^{156}\text{Gd}$  by inelastic electron scattering*, Phys. Lett. B **137**, 27 (1984)

- 
- [Böh93] G. Böhm *et al.*, *The differential decay curve method for the analysis of Doppler shift timing experiments*, Nucl. Instr. Meth. A **329**, 248 (1993)
- [Bro88] B. Brown, B. Wildenthal, *Status of the nuclear shell model*, Ann. Rev. Nucl. Part. Sci. **38**, 29 (1988)
- [Bro07] E. Browne, J. Tuli, *Nuclear Data Sheets for A = 137*, Nuclear Data Sheets **108**, 2173 (2007)
- [Bru97] R. Brun, F. Rademakers, *ROOT - An object oriented data analysis framework*, Nucl. Instr. Meth. A **389**, 81 (1997)
- [Bru06a] B. Bruyneel, P. Reiter, G. Pascovici, *Characterization of large volume HPGe detectors. Part I: Electron and hole mobility parameterization*, Nucl. Instr. Meth. A **569**, 764 (2006)
- [Bru06b] B. Bruyneel, P. Reiter, G. Pascovici, *Characterization of large volume HPGe detectors. Part II: Experimental results*, Nucl. Instr. Meth. A **569**, 774 (2006)
- [Bru13] B. Bruyneel *et al.*, *Correction for hole trapping in AGATA detectors using pulse shape analysis*, Eur. Phys. J. A **49**, 61 (2013)
- [Bur87] T. Burrows, *Nuclear data sheets for A = 136*, Nuclear Data Sheets **52**, 273 (1987)
- [Bur01] T. Burrows, *Nuclear Data Sheets for A = 139*, Nuclear Data Sheets **92**, 623 (2001)
- [Cas85] R. Casten, *NpNn systematics in heavy nuclei*, Nucl. Phys. A **443**, 1 (1985)
- [Cas00] R. F. Casten, *Nuclear structure from a simple perspective*, vol. 6, Oxford University Press Oxford, 2000
- [Cau05] E. Caurier *et al.*, *The shell model as a unified view of nuclear structure*, Rev. Mod. Phys. **77**, 427 (2005)
- [Ced14] B. Cederwall *et al.*, *Technical Report for the Design, Construction and Commissioning of the DESPEC Germanium Array Spectrometer - DEGAS, v12.3* (2014)
- [Che10] B. Cheal *et al.*, *Nuclear Spins and Moments of Ga Isotopes Reveal Sudden Structural Changes between N = 40 and N = 50*, Phys. Rev. Lett. **104**, 252502 (2010)

- 
- [Cla98] R. Clark *et al.*, *The shears mechanism in the lead isotopes*, Physics Letters B **440**, 251 (1998)
- [Cli69] D. Cline, Bull. Am. Phys. Soc. **14**, 726 (1969)
- [Cli12] D. Cline *et al.*, *GOSIA user manual for simulation and analysis of Coulomb-excitation experiments* (2012), [http://www.pas.rochester.edu/~cline/Gosia/Gosia\\_Manual\\_20120510.pdf](http://www.pas.rochester.edu/~cline/Gosia/Gosia_Manual_20120510.pdf), accessed 15/03/2015
- [Com73] J. R. Comfort, J. R. Duray, W. J. Braithwaite,  $^{86,88}\text{Sr}(d, ^3\text{He})^{85,87}\text{Rb}$  Reactions and a Possible Magic Number  $Z = 38$ , Phys. Rev. C **8**, 1354 (1973)
- [Cor09] L. Coraggio *et al.*, *Shell-model study of the  $N = 82$  isotonic chain with a realistic effective Hamiltonian*, Phys. Rev. C **80**, 044320 (2009)
- [Cor15] A. Corsi *et al.*, *Neutron-driven collectivity in light tin isotopes: Proton inelastic scattering from  $^{104}\text{Sn}$* , Phys. Lett. B **743**, 451 (2015)
- [Cre10] F. Crespi *et al.*, *HPGe detectors timing using pulse shape analysis techniques*, Nucl. Instr. Meth. A **620**, 299 (2010)
- [Czo83] T. Czosnyka, D. Cline, C. Wu, *GOSIA, a semiclassical Coulomb-excitation least-squares search code*, Bull. Am. Phys. Soc. **28**, 745 (1983)
- [Dan11] M. Danchev *et al.*, *One-phonon isovector  $2_{1,MS}^+$  state in the neutron-rich nucleus  $^{132}\text{Te}$* , Phys. Rev. C **84**, 061306 (2011)
- [Dea08] D. J. Dean, *Computational nuclear structure: exploring nuclei through INCITE*, J. Phys.: Conf. Ser. **125**, 012062 (2008)
- [Dew12] A. Dewald, O. Möller, P. Petkov, *Developing the Recoil Distance Doppler-Shift technique towards a versatile tool for lifetime measurements of excited nuclear states*, Prog. Part. Nucl. Phys. **67**, 786 (2012)
- [Did10] F. Didierjean, G. Duchêne, A. Lopez-Martens, *The Deterministic Annealing Filter: A new clustering method for  $\gamma$ -ray tracking algorithms*, Nucl. Instr. Meth. A **615**, 188 (2010)
- [Dim09] M. Dimmock *et al.*, *Characterisation Results From an AGATA Prototype Detector*, IEEE Transactions on Nuclear Science **56**, 1593 (2009)
- [Don10] M. Doncel *et al.*, *Experimental test of the background rejection, through imaging capability, of a highly segmented AGATA germanium detector*, Nucl. Instr. Meth. A **622**, 614 (2010)

- 
- [Doo10] P Doornenbal *et al.*, *Lifetime effects for high-resolution gamma-ray spectroscopy at relativistic energies and their implications for the RISING spectrometer*, Nucl. Instr. Meth. A **613**, 218 (2010)
- [Doo14] P Doornenbal *et al.*, *Intermediate-energy Coulomb excitation of  $^{104}\text{Sn}$ : Moderate E2 strength decrease approaching  $^{100}\text{Sn}$* , Phys. Rev. C **90**, 061302 (2014)
- [DP12] C. Domingo-Pardo *et al.*, *Conceptual design and performance study for the first implementation of AGATA at the in-flight RIB facility of GSI*, Nucl. Instr. Meth. A **694**, 297 (2012)
- [Dwo08] M. Dworschak *et al.*, *Restoration of the  $N = 82$  Shell Gap from Direct Mass Measurements of  $^{132,134}\text{Sn}$* , Phys. Rev. Lett. **100**, 072501 (2008)
- [Ebe08] J. Eberth, J. Simpson, *From Ge(Li) detectors to gamma-ray tracking arrays—50 years of gamma spectroscopy with germanium detectors*, Prog. Part. Nuc. Phys. **60**, 283 (2008)
- [Epe09] E. Epelbaum, H.-W. Hammer, U.-G. Meißner, *Modern theory of nuclear forces*, Rev. Mod. Phys. **81**, 1773 (2009)
- [Epe14] E. Epelbaum *et al.*, *Ab Initio Calculation of the Spectrum and Structure of  $^{16}\text{O}$* , Phys. Rev. Lett. **112**, 102501 (2014)
- [Ero01] K. I. Erokhina *et al.*, *On the properties of the  $N = 82$  even-even nuclei*, Particles and Nuclei, Letters **107**, 5 (2001)
- [Far10] E. Farnea *et al.*, *Conceptual design and Monte Carlo simulations of the AGATA array*, Nucl. Instr. Meth. A **621**, 331 (2010)
- [Fel40] W. Feller, *On the time distribution of so-called random events*, Phys. Rev. **57**, 906 (1940)
- [Fla09] K. T. Flanagan *et al.*, *Nuclear Spins and Magnetic Moments of  $^{71,73,75}\text{Cu}$ : Inversion of  $\pi 2p_{3/2}$  and  $\pi 1f_{5/2}$  Levels in  $^{75}\text{Cu}$* , Phys. Rev. Lett. **103**, 142501 (2009)
- [For00] P. Forck *et al.*, *Measurements and improvements of the time structure of a slowly extracted beam from a synchrotron*, Proceedings of EPAC 2000, Vienna, Austria, p. 2237 (2000)
- [For06] P. Forck *et al.*, *Beam Diagnostics Developments for Current Operation of SIS18 and HEBT*, GSI scientific report 2005 p. 129 (2006)

- 
- [Fra98] S. Franchoo *et al.*, *Beta Decay of  $^{68-74}\text{Ni}$  and Level Structure of Neutron-Rich Cu Isotopes*, Phys. Rev. Lett. **81**, 3100 (1998)
- [Fra01] S. Franchoo *et al.*, *Monopole migration in  $^{69,71,73}\text{Cu}$  observed from  $\beta$  decay of laser-ionized  $^{68-74}\text{Ni}$* , Phys. Rev. C **64**, 054308 (2001)
- [Gad08] A. Gade, T. Glasmacher, *In-beam nuclear spectroscopy of bound states with fast exotic ion beams*, Prog. Part. Nucl. Phys. **60**, 161 (2008)
- [Gar06] H. von Garrel *et al.*, *Low-lying E1, M1, and E2 strength distributions in  $^{124,126,128,129,130,131,132,134,136}\text{Xe}$ : Systematic photon scattering experiments in the mass region of a nuclear shape or phase transition*, Phys. Rev. C **73**, 054315 (2006)
- [Gea12] Geant4, *Physics Reference Manual* (2012), accessed 4/11/2015
- [Gei92] H. Geissel *et al.*, *The GSI projectile fragment separator (FRS): a versatile magnetic system for relativistic heavy ions*, Nucl. Instr. Meth. B **70**, 286 (1992)
- [Gei02] H. Geissel *et al.*, *Experimental studies of heavy-ion slowing down in matter*, Nucl. Instr. Meth. B **195**, 3 (2002)
- [Gei15] H. Geissel *et al.*, *ATIMA* (2015), <https://web-docs.gsi.de/~weick/atima/>, accessed 05/01/2015
- [Gla80] S. L. Glashow, *Towards a unified theory: Threads in a tapestry*, Rev. Mod. Phys. **52**, 539 (1980)
- [Goe50] M. Goeppert Mayer, *Nuclear Configurations in the Spin-Orbit Coupling Model. I. Empirical Evidence*, Phys. Rev. **78**, 16 (1950)
- [Goe13] N. Goel *et al.*, *Characterisation of a symmetric AGATA detector using the imaging scanning technique*, Nucl. Instr. Meth. A **700**, 10 (2013)
- [Gol13] P. Golubev *et al.*, *The Lund–York–Cologne Calorimeter (LYCCA): Concept, design and prototype developments for a FAIR-NUSTAR detector system to discriminate relativistic heavy-ion reaction products*, Nucl. Instr. Meth. A **723**, 55 (2013)
- [Gra95] H. Grawe *et al.*, *The shell model at  $^{100}\text{Sn}$  - An experimental status report*, Physica Scripta **T56**, 71 (1995)
- [Gro62] L. Grodzins, *The uniform behaviour of electric quadrupole transition probabilities from first  $2^+$  states in even-even nuclei*, Phys. Lett. **2**, 88 (1962)

- 
- [Gro65] S. R. de Groot, H. A. Tolhoek, W. J. Huiskamp, *Orientation of nuclei at low temperatures*, in: K. Siegbahn (ed.), *Alpha-, Beta-, and Gamma-Ray Spectroscopy*, pp. 1199–1211, North-Holland Publishing Co., 1965
- [Gro05] D. J. Gross, *Nobel Lecture: The discovery of asymptotic freedom and the emergence of QCD*, *Rev. Mod. Phys.* **77**, 837 (2005)
- [Gro06] E. Grodner *et al.*, *Lifetimes and side-feeding population of the yrast band levels in  $^{131}\text{La}$* , *The European Physical Journal A - Hadrons and Nuclei* **27**, 325 (2006)
- [GU93] A. Galindo-Uribarri *et al.*, *First evidence for the hyperdeformed nuclear shape at high angular momentum*, *Phys. Rev. Lett.* **71**, 231 (1993)
- [Gui78] M. W. Guidry *et al.*, *Coulomb-Nuclear Interference for High-Spin States Excited by  $^{86}\text{Kr}$ ,  $^{40}\text{Ar}$ , and  $^{16}\text{O}$  Projectiles*, *Phys. Rev. Lett.* **40**, 1016 (1978)
- [Ha13] T. Ha *et al.*, *New setup for the characterisation of the AGATA detectors*, *Nucl. Instr. Meth. A* **697**, 123 (2013)
- [Ham84] W. D. Hamilton, A. Irbäck, J. P. Elliott, *Mixed-Symmetry Interacting-Boson-Model States in the Nuclei  $^{140}\text{Ba}$ ,  $^{142}\text{Ce}$ , and  $^{144}\text{Nd}$  with  $N = 84$* , *Phys. Rev. Lett.* **53**, 2469 (1984)
- [Har72] J. Harrison, J. Hiebert, *Single-proton transfer reactions on  $N = 50$  nuclei*, *Nuclear Physics A* **185**, 385 (1972)
- [Häu74] O. Häusser, *VII.B - Coulomb Reorientation*, in: J. Cerny (ed.), *Nuclear Spectroscopy and Reactions*, vol. 40, Part C, pp. 55–91, Elsevier, 1974
- [Hax49] O. Haxel, J. H. D. Jensen, H. E. Suess, *On the "Magic Numbers" in Nuclear Structure*, *Phys. Rev.* **75**, 1766 (1949)
- [Hei83] J. Heisenberg, H. Blok, *Inelastic electron scattering from nuclei*, *Ann. Rev. Nucl. Part. Sci.* **33**, 569 (1983)
- [Hel80] R. Helmer, M. Lee, *Analytical functions for fitting peaks from Ge semiconductor detectors*, *Nucl. Instr. Meth.* **178**, 499 (1980)
- [Hel02] R. Helmer, *Nuclear Data Sheets for  $A = 87$* , *Nuclear Data Sheets* **95**, 543 (2002)
- [Hen92] W. Henning, *Physics with SIS/ESR at GSI*, *Nucl. Phys. A* **538**, 637 (1992)

- 
- [Her13] C. Herlitzius, *The Doppler Shift Attenuation Method Facility: Its Design, Setup and Commissioning with the  $^{32}\text{S}(^3\text{He}, ^4\text{He})^{31}\text{S}$  Reaction*, Ph.D. thesis, Technische Universität München (2013)
- [Hey04] K. Heyde, *Basic ideas and concepts in nuclear physics: an introductory approach*, IOP Publishing, 2004
- [Hey10] K. Heyde, P. von Neumann-Cosel, A. Richter, *Magnetic dipole excitations in nuclei: Elementary modes of nucleonic motion*, Rev. Mod. Phys. **82**, 2365 (2010)
- [Hic98] S. F. Hicks *et al.*, *Structural characteristics of  $^{144}\text{Nd}$  through  $\gamma$ -ray spectroscopy following inelastic neutron scattering*, Phys. Rev. C **57**, 2264 (1998)
- [Hli98] V. Hlinka *et al.*, *Time projection chambers for tracking and identification of radioactive beams XX*, Nucl. Instr. Meth. A **419**, 503 (1998)
- [Hol97] A. Holt *et al.*, *Extended shell model calculation for even  $N = 82$  isotones with a realistic effective interaction*, Nucl. Phys. A **618**, 107 (1997)
- [Hol07] J. D. Holt *et al.*, *Microscopic restoration of proton-neutron mixed symmetry in weakly collective nuclei*, Phys. Rev. C **76**, 034325 (2007)
- [Hol13] J. D. Holt, J. Menéndez, A. Schwenk, *The role of three-nucleon forces and many-body processes in nuclear pairing*, J. Phys. G **40**, 075105 (2013)
- [Hol14] J. D. Holt *et al.*, *Three-nucleon forces and spectroscopy of neutron-rich calcium isotopes*, Phys. Rev. C **90**, 024312 (2014)
- [Hoo72] G. 't Hooft, M. Veltman, *Combinatorics of gauge fields*, Nucl. Phys. B **50**, 318 (1972)
- [Ill14] A. Illana *et al.*, *Low-velocity transient-field technique with radioactive ion beams:  $g$  factor of the first excited  $2^+$  state in  $^{72}\text{Zn}$* , Phys. Rev. C **89**, 054316 (2014)
- [Int93] International Commission on Radiation Units and Measurements, *Stopping Power and Ranges for Protons and Alpha Particles: ICRU Report No. 49*, Journal of the ICRU (1993)
- [Int05] International Commission on Radiation Units and Measurements, *Stopping of ions heavier than Helium: ICRU Report, No. 73*, Journal of the ICRU (2005)

- 
- [Isa92] P. van Isacker, M. A. Nagarajan, D. D. Warner, *Effect of the neutron skin on collective states of nuclei*, Phys. Rev. C **45**, 13 (1992)
- [Isa05] V. Isakov *et al.*, *Structure of states and transition rates in the even-even  $N = 82$  nucleus  $^{136}\text{Xe}$* , Physics of Atomic Nuclei **68**, 1487 (2005)
- [Iwa11] N. Iwasa, H. Weick, H. Geissel, *New features of the Monte-Carlo code MO-CADI*, Nucl. Instr. Meth. B **269**, 752 (2011)
- [Jac62] J. D. Jackson, *Classical electrodynamics*, Wiley, 1962
- [Jak02] G. Jakob *et al.*, *Evidence for proton excitations in  $^{130,132,134,136}\text{Xe}$  isotopes from measurements of  $g$  factors of  $2_1^+$  and  $4_1^+$  states*, Phys. Rev. C **65**, 024316 (2002)
- [Jam75] F. James, M. Roos, *Minuit - a system for function minimization and analysis of the parameter errors and correlations*, Comp. Phys. Comm. **10**, 343 (1975)
- [Jam94] F. James, *MINUIT Reference Manual*, CERN Program Library Long Writeup D506 (1994)
- [Kan09] R. Kanungo *et al.*, *One-Neutron Removal Measurement Reveals  $^{24}\text{O}$  as a New Doubly Magic Nucleus*, Phys. Rev. Lett. **102**, 152501 (2009)
- [Käu02] L. Käubler *et al.*, *Influence of the  $N = 50$  neutron core on dipole excitations in  $^{87}\text{Rb}$* , Phys. Rev. C **65**, 054315 (2002)
- [Ken02] O. Kenn *et al.*, *Measurements of  $g$  factors and lifetimes of low-lying states in  $^{62-70}\text{Zn}$  and their shell model implication*, Phys. Rev. C **65**, 034308 (2002)
- [Kib02] T. Kibédi, R. Spear, *Reduced electric-octupole transition probabilities,  $B(E3; 0_1^+ \rightarrow 3_1^-)$  - an update*, At. Data Nucl. Data Tables **80**, 35 (2002)
- [Kim91] W. Kim *et al.*, *Properties of low-lying states in  $^{142}\text{Ce}$  via high resolution electron scattering*, Phys. Rev. C **44**, 2400 (1991)
- [Kne96] U. Kneissl, H. Pitz, A. Zilges, *Investigation of nuclear structure by resonance fluorescence scattering*, Prog. Part. Nucl. Phys. **37**, 349 (1996)
- [Kno10] G. F. Knoll, *Radiation detection and measurement*, John Wiley & Sons, 2010
- [Knü86] W. Knüpfner *et al.*, *Consistent empirical description of magnetic moments and  $M1$  transitions: Quenching of the diagonal and off-diagonal spin matrix elements*, Nucl. Phys. A **457**, 292 (1986)

- 
- [Kog83] J. B. Kogut, *The lattice gauge theory approach to quantum chromodynamics*, Rev. Mod. Phys. **55**, 775 (1983)
- [Kow04] K. Kowalski *et al.*, *Coupled Cluster Calculations of Ground and Excited States of Nuclei*, Phys. Rev. Lett. **92**, 132501 (2004)
- [Kra70] K. S. Krane, R. M. Steffen, *Determination of the E2/M1 Multipole Mixing Ratios of the Gamma Transitions in  $^{110}\text{Cd}$* , Phys. Rev. C **2**, 724 (1970)
- [Kra73] K. S. Krane, R. Steffen, R. Wheeler, *Directional correlations of gamma radiations emitted from nuclear states oriented by nuclear reactions or cryogenic methods*, Nuclear Data Tables **11**, 351 (1973)
- [Kra87] K. S. Krane, *Introductory nuclear physics*, John Wiley & Sons, Inc., 1987
- [Krö07] T. Kröll *et al.*, *Coulomb excitation of neutron-rich  $^{138,140,142}\text{Xe}$  at REX-ISOLDE*, Eur. Phys. J. - Special Topics **150**, 127 (2007)
- [Kur14] N. Kurz (head of GSI data processing department), *private communication* (2014)
- [Kus15] A. Kusoglu *et al.*, *Magnetism of an Excited Self-Conjugate Nucleus: Precise Measurement of the g Factor of the  $2_1^+$  State in  $^{24}\text{Mg}$* , Phys. Rev. Lett. **114**, 062501 (2015)
- [Lee97] I.-Y. Lee, *Physics with GAMMASPHERE and beyond*, Prog. Part. Nuc. Phys. **38**, 65 (1997)
- [Lee03] I.-Y. Lee, M. A. Deleplanque, K. Vetter, *Developments in large gamma-ray detector arrays*, Rep. Prog. Phys. **66**, 1095 (2003)
- [Lee04] I.-Y. Lee *et al.*, *GRETINA: A gamma ray energy tracking array*, Nucl. Phys. A **746**, 255 (2004)
- [Lee13] I.-Y. Lee, *Large gamma-ray detector arrays and electromagnetic separators*, Nucl. Instr. Meth. B **317**, 644 (2013)
- [Lem73] M.-C. Lemaire, *Spectroscopic study of multinucleon transfer reactions induced by heavy ions*, Phys. Rep. **7**, 279 (1973)
- [Lem12] A. Lemasson *et al.*, *Observation of mutually enhanced collectivity in self-conjugate  $^{76}\text{Sr}_{38}$* , Phys. Rev. C **85**, 041303 (2012)
- [Les72] P. Lesser *et al.*, *Static electric quadrupole moments of the first excited states of  $^{56}\text{Fe}$  and the even Titanium nuclei*, Nucl. Phys. A **190**, 597 (1972)

- 
- [Les05] J. Leske *et al.*, *Nuclear structure of the first  $2^+$  state in radioactive  $^{68}\text{Ge}$  based on  $g$  factor and lifetime measurements*, Phys. Rev. C **71**, 044316 (2005)
- [Les10] P. Lesser, D. Cline, *Spherical harmonic expansion of the photon angular distribution in the laboratory frame for photon emission by a rapidly moving source*, Nucl. Instr. Meth. A **614**, 41 (2010)
- [Let13] M. Lettmann, *Differential, continuous-angle DAM for relativistic ion beams*, Master's thesis, Technische Universität Darmstadt (2013)
- [Let15] M. Lettmann (TU Darmstadt), *private communication* (2015)
- [Lin61] J. Lindhard, M. Scharff, *Energy Dissipation by Ions in the keV Region*, Phys. Rev. **124**, 128 (1961)
- [Lin63] J. Linhard, M. Scharff, H. Schiott, *Range concepts and heavy ion ranges*, Mat. Fys. Medd. Dan Vid. Selsk **33** (1963)
- [Lin96] J. Lindhard, A. H. Sørensen, *Relativistic theory of stopping for heavy ions*, Phys. Rev. A **53**, 2443 (1996)
- [Lju05] J. Ljungvall, J. Nyberg, *A study of fast neutron interactions in high-purity germanium detectors*, Nucl. Instr. Meth. A **546**, 553 (2005)
- [LM04] A. Lopez-Martens *et al.*,  *$\gamma$ -ray tracking algorithms: a comparison*, Nucl. Instr. Meth. A **533**, 454 (2004)
- [Loe01] E. V. D. van Loef *et al.*, *High-energy-resolution scintillator:  $\text{Ce}^{3+}$  activated  $\text{LaBr}_3$* , Appl. Phys. Lett. **79**, 1573 (2001)
- [Mac89] H. Mach, R. Gill, M. Moszyński, *A method for picosecond lifetime measurements for neutron-rich nuclei: (1) Outline of the method*, Nucl. Instr. Meth. A **280**, 49 (1989)
- [Mac11] R. Machleidt, D. Entem, *Chiral effective field theory and nuclear forces*, Phys. Rep. **503**, 1 (2011)
- [Mac13] A. O. Macchiavelli, *Selected Aspects of the Structure of Exotic Nuclei and New Opportunities with GRETINA*, Acta Physica Polonica B **44**, 359 (2013)
- [Man91] P. F. Mantica *et al.*,  *$E0$  transitions and  $0^+$  levels in  $^{136}\text{Xe}$* , Phys. Rev. C **43**, 1696 (1991)

- 
- [Mar78] W. Marciano, H. Pagels, *Quantum chromodynamics*, Phys. Rep. **36**, 137 (1978)
- [Mar99] J. van der Marel, B. Cederwall, *Backtracking as a way to reconstruct Compton scattered  $\gamma$ -rays*, Nucl. Instr. Meth. A **437**, 538 (1999)
- [Mar02] J. van der Marel, B. Cederwall,  *$\gamma$ -ray tracking in germanium: the backtracking method*, Nucl. Instr. Meth. A **477**, 391 (2002), 5th Int. Conf. on Position-Sensitive Detectors
- [Mar13] M. Martin, *Nuclear Data Sheets for  $A = 152$* , Nuclear Data Sheets **114**, 1497 (2013)
- [McC15] E. McCutchan, *Nuclear Data Sheets for  $A = 83$* , Nuclear Data Sheets **125**, 201 (2015)
- [Med75] L. R. Medsker *et al.*, *Proton states in  $^{87}\text{Rb}$* , Phys. Rev. C **12**, 1516 (1975)
- [Mel14] Melon, B. *et al.*, *AGATA modules as Compton polarimeters for the measurement of gamma-ray linear polarisation*, EPJ Web of Conferences **66**, 11004 (2014)
- [Mic13] C. Michelagnoli, *The lifetime of the 6.79 MeV state in  $^{15}\text{O}$  as a challenge for nuclear astrophysics and  $\gamma$ -ray spectroscopy: a new DSAM measurement with the AGATA Demonstrator array*, Ph.D. thesis, Università degli Studi di Padova (2013)
- [Mil03] L. Milechina, B. Cederwall, *Improvements in  $\gamma$ -ray reconstruction with positive sensitive Ge detectors using the backtracking method*, Nucl. Instr. Meth. A **508**, 394 (2003)
- [MIN14] MINUIT, *minimization library* (2014), <http://seal.web.cern.ch/seal/snapshot/work-packages/mathlibs/minuit/>, accessed 3/13/2015
- [MK02] T. Mayer-Kuckuck, *Kernphysik, Eine Einführung*, Teubner, 2002
- [Möll14] T. Möller, *Aspects of nuclear collectivity studied in projectile Coulomb excitation experiments*, Ph.D. thesis, Technische Universität Darmstadt (2014)
- [Mor03] L. Moral, A. F. Pacheco, *Algebraic approach to the radioactive decay equations*, American Journal of Physics **71**, 684 (2003)
- [Mos89] M. Moszyński, H. Mach, *A method for picosecond lifetime measurements for neutron-rich nuclei: (2) Timing study with scintillation counters*, Nucl. Instr. Meth. A **277**, 407 (1989)

- 
- [Mue06] W. F. Mueller *et al.*, *Variation with mass of  $B(E3; 0_1^+ \rightarrow 3_1^-)$  transition rates in  $A = 124 - 134$  even-mass xenon nuclei*, Phys. Rev. C **73**, 014316 (2006)
- [mus] *Technical Manual Ionisation Chamber MUSIC80*, [http://www-w2k.gsi.de/frs/technical/FRSsetup/detectors/music80/music80\\_manual.pdf](http://www-w2k.gsi.de/frs/technical/FRSsetup/detectors/music80/music80_manual.pdf), accessed 20/5/2015
- [Ney03] G. Neyens, *Nuclear magnetic and quadrupole moments for nuclear structure research on exotic nuclei*, Rep. Prog. Phys. **66**, 633 (2003)
- [Nic07] N. Nica, *Nuclear Data Sheets for  $A = 140$* , Nuclear Data Sheets **108**, 1287 (2007)
- [NIS14] NIST, *Reference on Constants, Units and Uncertainty* (2014), <http://physics.nist.gov/cgi-bin/cuu/Value?muc2mev>, accessed 18/12/2014
- [Nol79] P. Nolan, J. Sharpey-Schafer, *The measurement of the lifetimes of excited nuclear states*, Rep. Prog. Phys. **42**, 1 (1979)
- [Nor70] L. Northcliffe, R. Schilling, *Range and stopping-power tables for heavy ions*, Atomic Data and Nuclear Data Tables **7**, 233 (1970)
- [Nya84] B. M. Nyakó *et al.*, *Observation of Superdeformation in  $^{152}\text{Dy}$* , Phys. Rev. Lett. **52**, 507 (1984)
- [Ola06] A. Olariu *et al.*, *Pulse shape analysis for the location of the gamma-interactions in AGATA*, IEEE Transactions on Nuclear Science **53**, 1028 (2006)
- [Oli14] K. Olive (Particle Data Group), *Review of Particle Physics*, Chin. Phys. C **38**, 090001 (2014)
- [Ots01] T. Otsuka *et al.*, *Monte Carlo shell model for atomic nuclei*, Prog. Part. Nucl. Phys. **47**, 319 (2001)
- [Ots05] T. Otsuka *et al.*, *Evolution of Nuclear Shells due to the Tensor Force*, Phys. Rev. Lett. **95**, 232502 (2005)
- [Ots10a] T. Otsuka *et al.*, *Novel Features of Nuclear Forces and Shell Evolution in Exotic Nuclei*, Phys. Rev. Lett. **104**, 012501 (2010)
- [Ots10b] T. Otsuka *et al.*, *Three-Body Forces and the Limit of Oxygen Isotopes*, Phys. Rev. Lett. **105**, 032501 (2010)

- 
- [Owe] H. Ower, *Computer program CLX*, unpublished
- [Pas13] S. Paschalis *et al.*, *The performance of the Gamma-Ray Energy Tracking In-beam Nuclear Array GREINA*, Nucl. Instr. Meth. A **709**, 44 (2013)
- [Pel82] D. Pelte, D. Schwalm, *In-beam gamma-ray spectroscopy with heavy ions*, in: R. Bock (ed.), *Heavy Ion Collisions*, North-Holland Publishing Co., 1982
- [Pet15] P. Petkov *et al.*, *New procedures for analyzing Doppler-shift attenuation lifetime measurements*, Nucl. Instr. Meth. A **783**, 6 (2015)
- [Pie08] N. Pietralla, P. von Brentano, A. Lisetskiy, *Experiments on multiphonon states with proton–neutron mixed symmetry in vibrational nuclei*, Prog. Part. Nucl. Phys. **60**, 225 (2008)
- [Pie11] N. Pietralla *et al.*, *Relativistic Coulomb M1 excitation of neutron-rich  $^{85}\text{Br}$*  (2011), experiment proposal to the GSI PAC for the PreSPEC-AGATA campaign
- [Pie14a] N. Pietralla, *First Taste of HISPEC @ FAIR: PreSPEC-AGATA in Operation* (2014), talk at the NUSTAR week 2014
- [Pie14b] N. Pietralla *et al.*, *On the Road to FAIR: 1st Operation of AGATA in PreSPEC at GSI*, EPJ Web of Conferences **66**, 02083 (2014)
- [Piq04] I. Piqueras *et al.*, *A probabilistic  $\hat{I}\hat{s}$ -ray tracking method for germanium detectors*, Nucl. Instr. Meth. A **516**, 122 (2004)
- [Pit70] R. Pitthan, *Unelastische Elektronenstreuung an  $^{140}\text{Ce}$  bis 3,5 MeV Anregungsenergie*, Z. Naturf. **25a**, 1358 (1970)
- [Pit13] S. Pittel *et al.*, *Spherical to deformed shape transitions in the nucleon pair shell model*, J. Phys.: Conf. Ser. **445**, 012031 (2013)
- [Pod08] Z. Podolyák, *From RISING to HISPEC/DESPEC*, Nucl. Instr. Meth. B **266**, 4589 (2008)
- [Pod14] Z. Podolyák, *Studies of exotic nuclei with advanced radiation detectors*, Radiation Physics and Chemistry **95**, 14 (2014), proceedings of the 12th International Symposium on Radiation Physics (ISRP 2012)
- [Pol05] D. Politzer, *Nobel Lecture: The dilemma of attribution*, Rev. Mod. Phys. **77**, 851 (2005)

- 
- [Pre02] D. S. Pressyanov, *Short solution of the radioactive decay chain equations*, American Journal of Physics **70**, 444 (2002)
- [Rac52] G. Racah, I. Talmi, *The pairing property of nuclear interactions*, Physica **18**, 1097 (1952)
- [Rad02] D. C. Radford *et al.*, *Coulomb Excitation of Radioactive  $^{132,134,136}\text{Te}$  Beams and the Low  $B(E2)$  of  $^{136}\text{Te}$* , Phys. Rev. Lett. **88**, 222501 (2002)
- [Rai06] G. Rainovski *et al.*, *Stabilization of Nuclear Isovector Valence-Shell Excitations*, Phys. Rev. Lett. **96**, 122501 (2006)
- [Ral15] D. Ralet *et al.*, *Data-flow coupling and data-acquisition triggers for the PreSPEC-AGATA campaign at GSI*, Nucl. Instr. Meth. A **786**, 32 (2015)
- [Ram01] S. Raman, C. N. Jr., P. Tikkanen, *Transition probability from the ground to the first excited  $2^+$  state of even-even nuclides*, At. Data Nucl. Data Tab. **78**, 1 (2001)
- [Rar07] Rare Isotope Science Assessment Committee, *Scientific Opportunities with a Rare-Isotope Facility in the United States*, National Academies Press, 2007
- [Rec08] F. Recchia, *In-beam test and imaging capabilities of the AGATA prototype detector*, Ph.D. thesis, Università degli Studi di Padova (2008)
- [Rec09a] F. Recchia *et al.*, *Performance of an AGATA prototype detector estimated by Compton-imaging techniques*, Nucl. Instr. Meth. A **604**, 60 (2009)
- [Rec09b] F. Recchia *et al.*, *Position resolution of the prototype AGATA triple-cluster detector from an in-beam experiment*, Nucl. Instr. Meth. A **604**, 555 (2009)
- [Ree14] M. Reese, *Results of the PreSPEC commissioning runs* (2014), talk at the NUSTAR week 2014
- [Ree15] M. Reese (TU Darmstadt), *private communication* (2015)
- [Rei14] P. Reiter, B. Birkenbach, T. Kotthaus, *Spectroscopy of Actinide Nuclei – Perspectives with Position Sensitive HPGe Detectors*, Physics Procedia **59**, 119 (2014)
- [Rot07] R. Roth, P. Navrátil, *Ab Initio Study of  $^{40}\text{Ca}$  with an Importance-Truncated No-Core Shell Model*, Phys. Rev. Lett. **99**, 092501 (2007)

- 
- [Ryb70] F. Rybicki, T. Tamura, G. Satchler, *Particle-gamma angular correlations following nuclear reactions*, Nucl. Phys. A **146**, 659 (1970)
- [Sah12] E. Sahin *et al.*, *Structure of the As, Ge, Ga nuclei*, Nucl. Phys. A **893**, 1 (2012)
- [Sal80] A. Salam, *Gauge unification of fundamental forces*, Rev. Mod. Phys. **52**, 525 (1980)
- [Sch68] A. Schwarzschild, E. Warburton, *The Measurement of Short Nuclear Lifetimes*, Ann. Rev. Nucl. Sci. **18**, 265 (1968)
- [Sch98a] C. Scheidenberger, H. Geissel, *Penetration of relativistic heavy ions through matter*, Nucl. Instr. Meth. B **135**, 25 (1998)
- [Sch98b] C. Scheidenberger *et al.*, *Charge states of relativistic heavy ions in matter*, Nucl. Instr. Meth. B **142**, 441 (1998)
- [Sch99] G. Schmid *et al.*, *A  $\gamma$ -ray tracking algorithm for the GRETA spectrometer*, Nucl. Instr. Meth. A **430**, 69 (1999)
- [Sch11a] M. Schlarb *et al.*, *Pulse shape analysis for  $\gamma$ -ray tracking (Part I): Pulse shape simulation with JASS*, Eur. Phys. J. A **47**, 132 (2011)
- [Sch11b] M. Schlarb *et al.*, *Pulse shape analysis for  $\gamma$ -ray tracking (Part II): Fully informed particle swarm algorithm applied to AGATA*, Eur. Phys. J. A **47**, 131 (2011)
- [Sch14] M. von Schmid, *private communication* (2014)
- [Sen72] S. Sen, P. J. Riley, T. Udagawa,  $^{136}\text{Xe}(p, p')^{136}\text{Xe}$  and  $^{136}\text{Xe}(p, d)^{135}\text{Xe}$  Reactions, Phys. Rev. C **6**, 2201 (1972)
- [Sen14] M. Senyigit *et al.*, *Identification and rejection of scattered neutrons in AGATA*, Nucl. Instr. Meth. A **735**, 267 (2014)
- [Sev14] A. P. Severyukhin *et al.*, *Impact of variational space on  $M1$  transitions between first and second quadrupole excitations in  $^{132,134,136}\text{Te}$* , Phys. Rev. C **90**, 011306 (2014)
- [Shi04] N. Shimizu *et al.*, *Anomalous properties of quadrupole collective states in  $^{136}\text{Te}$  and beyond*, Phys. Rev. C **70**, 054313 (2004)
- [Sie09] K. Sieja *et al.*, *Description of proton-neutron mixed-symmetry states near  $^{132}\text{Sn}$  within a realistic large scale shell model*, Phys. Rev. C **80**, 054311 (2009)

- 
- [Sig83] P. Sigmund, *LSS and the Integral Equations of Transport Theory*, Physica Scripta **28**, 257 (1983)
- [Sig98] P. Sigmund, *Stopping power in perspective*, Nucl. Instr. Meth. B **135**, 1 (1998)
- [Sim97] J. Simpson, *The Euroball Spectrometer*, Z. Phys. A **358**, 139 (1997)
- [Sim08] J. Simpson, J. Nyberg, W. Korten (eds.), *AGATA Technical design report*, 2008
- [Sin14] B. Singh, J. Chen, *Nuclear Data Sheets for A=85*, Nuclear Data Sheets **116**, 1 (2014)
- [Son02] A. Sonzogni, *Nuclear Data Sheets for A = 136*, Nuclear Data Sheets **95**, 837 (2002)
- [Spe78] R. Spear *et al.*, *Systematics of coulomb-nuclear interference: Implications for reliable measurement of the reorientation effect*, Phys. Lett. B **76**, 559 (1978)
- [Spe93] K. Speidel *et al.*, *Measurements of magnetic moments of  $^{134,136}\text{Xe}(2_1^+)$  and the mean life of the  $^{136}\text{Xe}(2_1^+)$  state*, Nucl. Phys. A **552**, 140 (1993)
- [Sri15] *SRIM website* (2015), <http://www.SRIM.org>, accessed 05/05/2015
- [Sta11] C. Stahl, *Continuous-Angle DSAM: A new quality of lifetimes measurements*, Master's thesis, Technische Universität Darmstadt (2011)
- [Sta13] C. Stahl *et al.*, *Identification of the proton  $2p_{1/2} \rightarrow 2p_{3/2}$  M1 spin-flip transition in  $^{87}\text{Rb}$* , Phys. Rev. C **87**, 037302 (2013)
- [Sta14] C. Stahl *et al.*,  *$2^+$  Anomaly and Configurational Isospin Polarization of  $^{136}\text{Te}$*  (2014), proposal to the ISOLDE and Neutron Time-of-Flight Committee, CERN document INTC-P-421
- [Sta15] C. Stahl *et al.*, *Coulex-multipolarimetry with relativistic heavy-ion beams*, Nucl. Instr. Meth. A **770**, 123 (2015)
- [Ste13] D. Steppenbeck *et al.*, *Evidence for a new nuclear “magic number” from the level structure of  $^{54}\text{Ca}$* , Nature **502**, 207 (2013)
- [Str12] M. Strecker, N. Minkov, H. Lenske, *Nuclear Theory, Vol. 31*, Heron Press, Sofia, 2012

- 
- [Stu05] A. E. Stuchbery, P. F. Mantica, A. N. Wilson, *Electron-configuration-reset time-differential recoil-in-vacuum technique for excited-state  $g$ -factor measurements on fast exotic beams*, Phys. Rev. C **71**, 047302 (2005)
- [Sul10] G. Suliman, D. Bucurescu, *Fuzzy clustering algorithm for gamma ray tracking in segmented detectors*, Romanian Reports in Physics **62**, 27 (2010)
- [Tal93] I. Talmi, *Simple models of complex nuclei*, vol. 7, CRC Press, 1993
- [Tar08] O. Tarasov, D. Bazin, *LISE++: Radioactive beam production with in-flight separators*, Nucl. Instr. Meth. B **266**, 4657 (2008)
- [Ter02] J. Terasaki *et al.*, *Anomalous behavior of  $2^+$  excitations around  $^{132}\text{Sn}$* , Phys. Rev. C **66**, 054313 (2002)
- [Ter08] J. R. Terry *et al.*, *Single-neutron knockout from intermediate energy beams of  $^{30,32}\text{Mg}$ : Mapping the transition into the “island of inversion”*, Phys. Rev. C **77**, 014316 (2008)
- [tpc] *TPC technical manual*, <http://www-w2k.gsi.de/frs/technical/FRSsetup/detectors/tpc/tpcmanual.pdf>, accessed 20/5/2015
- [Tsu11] K. Tsukiyama, S. K. Bogner, A. Schwenk, *In-Medium Similarity Renormalization Group For Nuclei*, Phys. Rev. Lett. **106**, 222502 (2011)
- [Van95] J. R. Vanhoy *et al.*, *Structural characteristics of  $^{142}\text{Ce}$  through inelastic neutron scattering*, Phys. Rev. C **52**, 2387 (1995)
- [Ven04] A. Venturelli, D. Bazacco, *Adaptive Grid Search as Pulse Shape Analysis Algorithm for  $\gamma$ -Tracking and Results*, LNL Annual Report 2004, p. 220 (2004)
- [Vul] *Technical information on the VULOM module*, [https://www.gsi.de/work/fairgsi/rare\\_isotope\\_beams/electronics/digitalelektronik/digitalelektronik/module/vme/vulom.htm](https://www.gsi.de/work/fairgsi/rare_isotope_beams/electronics/digitalelektronik/digitalelektronik/module/vme/vulom.htm), accessed 09/05/2015
- [Wal14] P. Walker, *Nuclear physics: Track it to the limit*, Nature Physics **10**, 338 (2014)
- [Wan12] M. Wang *et al.*, *The AME2012 atomic mass evaluation*, Chin. Phys. C **36**, 1603 (2012)
- [War97] D. Warner, P. V. Isacker, *The scissors mode in the presence of a neutron skin*, Phys. Lett. B **395**, 145 (1997)

- 
- [War13] N. Warr *et al.*, *The Miniball spectrometer*, Eur. Phys. J. A **49**, 40 (2013)
- [Wei80] S. Weinberg, *Conceptual foundations of the unified theory of weak and electromagnetic interactions*, Rev. Mod. Phys. **52**, 515 (1980)
- [Wei00] H. Weick *et al.*, *Slowing down of relativistic few-electron heavy ions*, Nucl. Instr. Meth. B **164–165**, 168 (2000)
- [Wei03] D. W. Weißhaar, *MINIBALL - Ein neuartiges Gamma-Spektrometer mit ortsauflösenden Germaniumdetektoren*, Ph.D. thesis, Universität zu Köln (2003)
- [Wer08] V. Werner *et al.*, *Evidence for the microscopic formation of mixed-symmetry states from magnetic moment measurements*, Phys. Rev. C **78**, 031301 (2008)
- [Wie10] A. Wiens *et al.*, *The AGATA triple cluster detector*, Nucl. Instr. Meth. A **618**, 223 (2010)
- [Wie13] F. Wienholtz *et al.*, *Masses of exotic calcium isotopes pin down nuclear forces*, Nature **498**, 346 (2013)
- [Wil71] B. H. Wildenthal, E. Newman, R. L. Auble, *Study of the Level Structure of  $N = 82$  Nuclei via Proton-Transfer Reactions*, Phys. Rev. C **3**, 1199 (1971)
- [Wil05] F. Wilczek, *Nobel Lecture: Asymptotic freedom: From paradox to paradigm*, Rev. Mod. Phys. **77**, 857 (2005)
- [Win79] A. Winther, K. Alder, *Relativistic coulomb excitation*, Nucl. Phys. A **319**, 518 (1979)
- [Wol78] H.-J. Wollersheim *et al.*, *Messung der  $B(E2, 0^+ \rightarrow 2^+)$ -Werte für  $^{128,130,132,134,136}\text{Xe}$* , GSI Annual Report 1977, p. 61 (1978)
- [Wol92] H.-J. Wollersheim, *Kernstruktur schnell rotierender Atomkerne*, habilitation treatise, Frankfurt, 1992
- [Wol05] H. Wollersheim *et al.*, *Rare ISotopes INvestigation at GSI (RISING) using gamma-ray spectroscopy at relativistic energies*, Nucl. Instr. Meth. A **537**, 637 (2005)
- [Yam67] T. Yamazaki, *Tables of coefficients for angular distribution of gamma rays from aligned nuclei*, Nuclear Data Sheets. Section A **3**, 1 (1967)

- 
- [Zie85] J. F. Ziegler, J. Biersack, U. Littmark, *The stopping and range of ions in matter, Vol. 1*, Pergamon, New York, 1985
- [Zie10] J. F. Ziegler, M. Ziegler, J. Biersack, *SRIM – The stopping and range of ions in matter (2010)*, Nucl. Instr. Meth. B **268**, 1818 (2010)



---

# List of Figures

1.1. Measured values of the strong coupling constant $\alpha_s$ as a function of the energy scale $Q$ . . . . .	1
1.2. Rough classification of computational methods suitable to solve the nuclear many-body problem for different regions of the nuclear chart	2
1.3. Present and future major RIB facilities worldwide . . . . .	4
1.4. First $\gamma$ -ray tracking arrays: AGATA demonstrator and GRETINA . . . .	5
2.1. Chains of nuclear decays . . . . .	20
2.2. Different types of axially symmetric nuclear orientation . . . . .	24
3.1. Technical drawing of a part of the GAMMASPHERE detector array . .	30
3.2. Dimensions, segmentation and encapsulation of an AGATA HPGe crystal . . . . .	32
3.3. Sketch of electric signals registered in a segmented detector . . . . .	33
3.4. Cross sections of the main processes for $\gamma$ -ray-interaction with germanium . . . . .	36
3.5. Expected interaction pattern for the three most important interactions of $\gamma$ -rays with matter, criteria for their identification and permutations of subsequent Compton scattering events . . . . .	37
3.6. Simulated interaction point distribution for 30 $\gamma$ -rays with an energy of 1.33 MeV in an ideal $4\pi$ germanium-shell . . . . .	38
3.7. Contributions to the energy resolution $\Delta E$ obtained after Doppler correction . . . . .	40
3.8. Geometry of the three slightly different hexagonal, tapered, 36-fold segmented HPGe crystals of AGATA and geometry of the full array . .	41
3.9. Photographs of the AGATA demonstrator and of GRETINA . . . . .	42
3.10. Doppler-corrected $\gamma$ -ray peak from the decay of the first excited $3/2^-$ -state of $^{49}\text{Ti}$ observed in a prototype AGATA detector . . . . .	43
3.11. Resolving power of different generations of $\gamma$ -ray detectors . . . . .	44
3.12. Simulated spectra for the detection of a rotational cascade of 30 $\gamma$ -rays emitted at a velocity of $\beta = 0.5$ with the full AGATA array . .	46
4.1. Comparison of different experimental techniques for the measurement of nuclear level lifetimes . . . . .	49

4.2. Typical setup for a DSAM measurement and principle of the DSA Method . . . . .	50
4.3. Electronic and nuclear stopping power of tantalum for $^{136}\text{Xe}$ ions . .	53
4.4. Velocity distributions of $^{136}\text{Xe}$ nuclei directly after Coulomb excitation on a thick carbon target, a carbon target backed by tantalum and with restriction of the reaction kinematics by a particle detector. Resulting lineshapes. . . . .	55
4.5. Temporal evolution of the velocity distribution $^{136}\text{Xe}$ nuclei, Coulomb-excited on a thin carbon target backed by tantalum . . . . .	57
4.6. Doppler-broadened $\gamma$ -ray lineshapes for a fictional state of $^{136}\text{Xe}$ with different lifetimes close to estimated sensitivity limits . . . . .	59
4.7. Variation of $\gamma$ -ray intensity observed in the laboratory frame as a function of emitter velocity $\beta$ . . . . .	62
4.8. Effect of angular distributions on Doppler-broadened lineshapes . . .	63
4.9. Overlapping lineshapes resulting from nearby $\gamma$ -ray transitions . . . .	64
4.10. Two-dimensional Doppler-broadened $\gamma$ -ray lineshape as a function of $\gamma$ -ray energy and polar detection angle . . . . .	66
4.11. Example for a stopping matrix and description of its properties . . . .	69
4.12. Temporal evolution of the $2^{\text{nd}}$ and $4^{\text{th}}$ Legendre polynomials for an ensemble of excited ions, averaged over an angular bin in detection polar angle . . . . .	72
4.13. Typical response function and its components for HPGe detectors . .	76
4.14. Major steps in the calculation of a Doppler-broadened $\gamma$ -ray lineshape by the caDSAM . . . . .	77
4.15. Temporal evolution of the velocity distribution of 150 AMeV $^{136}\text{Xe}$ nuclei Coulomb-excited on a 500 $\mu\text{m}$ thick gold target and resulting two-dimensional lineshapes with and without Doppler correction . . . . .	81
4.16. Calculated differential caDSAM lineshapes for different level lifetimes and a fixed forward observation angle . . . . .	82
4.17. Angle-dependent lineshape width observed in the differential caDSA with and without Doppler correction . . . . .	83
4.18. Calculated differential caDSAM lineshapes under a forward and a backward angle with and without Doppler correction . . . . .	84
4.19. Influence of the emitter velocity uncertainty on the observed energy resolution after Doppler correction . . . . .	85
4.20. Calculated differential caDSAM lineshapes with and without Doppler correction for an velocity spread of the incoming beam of 1% . . . .	86

4.21. Calculated differential caDSAM lineshapes with and without Doppler correction for three different level lifetimes, summed over observation angles from 20° to 50° . . . . .	88
4.22. Principle of the geometric caDSAM . . . . .	90
4.23. Shift in $\gamma$ -ray energy at fixed observation angle as a function of $\gamma$ -ray vertex and emitter velocity . . . . .	91
4.24. Sensitivity range of the geometric caDSA as function of ion velocity behind the target . . . . .	93
4.25. Calculated two-dimensional geometric DSAM lineshape with and without Doppler correction . . . . .	95
4.26. Calculated geometric DSAM lineshape for several lifetimes close to the estimated sensitivity limits . . . . .	96
5.1. Cross section for $E2$ and $M1$ Coulomb excitation of the 1191 keV $J^\pi = 1/2^-$ state of $^{85}\text{Br}$ on a gold target . . . . .	99
5.2. Ratio of Coulomb excitation cross sections at 300 MeV/u and 150 MeV/u beam energy as a function of the multipole mixing ratio $\delta_{E2/M1}$ for the 1191 keV $J^\pi = 1/2^-$ state of $^{85}\text{Br}$ . . . . .	100
5.3. Principle experimental setup for the Coulex-multipolarimetry Method employing two targets . . . . .	101
5.4. Evolution of $M1$ and $E2$ Coulex cross section and kinetic energy as a 300 MeV/u beam of $^{85}\text{Br}$ passes through two gold targets with 1 mm thickness each . . . . .	102
5.5. Ratio of expected total $\gamma$ -ray yields from two 1 mm thick gold targets as a function of the multipole mixing ratio $\delta_{E2/M1}$ for the example of an 1191 keV $J^\pi = 1/2^-$ state in $^{85}\text{Br}$ . . . . .	103
5.6. Angular distributions and detection of $\gamma$ -rays emitted from a target at the focus of a spherical detector and target 10 cm further downstream . . . . .	106
5.7. Ratio of angular distribution of $\gamma$ -rays emitted from the first and second target as function of $\delta$ for different detector positions . . . . .	107
5.8. Ratio of angular distribution of $\gamma$ -rays emitted from the first and second target as function of detection polar angle for different values of $\delta$ . . . . .	108
5.9. Ratio of expected peak areas from two 1 mm thick gold targets as a function of the multipole mixing ratio $\delta_{E2/M1}$ for the example of the 1191 keV, $J^\pi = 1/2^-$ state in $^{85}\text{Br}$ . Effects of pronounced angular distributions are shown for two different ranges of observation angle covered by the detector. . . . .	109

5.10. Simulated $\gamma$ -ray spectra expected in an Coulex multipolarimetry experiment for the 1191-keV, $J^\pi = \frac{1}{2}^-$ excited state of $^{85}\text{Br}$ assuming two values for the level lifetime and Doppler corrections for either of the targets . . . . .	111
5.11. Separation between the $\gamma$ -rays from the first and second target as function of the target separation and the observation angle . . . . .	112
5.12. Simulated two-dimensional $\gamma$ -ray spectra expected in an Coulex multipolarimetry experiment for the 1191-keV, $J^\pi = \frac{1}{2}^-$ excited state of $^{85}\text{Br}$ employing position-sensitive detectors, assuming two different values for the level lifetime and Doppler corrections for either of the targets . . . . .	114
5.13. Same as in Figure 5.12, but for position in-sensitive, cylindrical detectors with a diameter of 8 cm . . . . .	116
6.1. Sketch of the setup of experiment 09.08 at LNL . . . . .	121
6.2. Photograph of the employed DSSSD detector . . . . .	122
6.3. Reaction kinematics for the Coulomb-excitation reaction and the $\alpha$ -transfer reaction at 546 MeV beam energy . . . . .	123
6.4. Sum-energy spectrum of all DSSSD sectors as a function of the event-number (546 MeV, carbon target) . . . . .	125
6.5. Same data as in Figure 6.4, but corrected for the degeneration of the DSSSD. . . . .	125
6.6. Sum-energy spectrum of all DSSSD rings as a function of the event-number (546 MeV, carbon target) . . . . .	125
6.7. Energy spectrum measured in the rings of the DSSSD as a function of the particle scattering angle showing the different reaction channels (546 MeV, carbon target) . . . . .	127
6.8. Same spectrum as in Figure 6.7 but for the runs at 500 MeV beam energy with a thin carbon target . . . . .	127
6.9. Particle energy measured in DSSSD ring 7 (covering scattering angles $\theta$ from $32.1^\circ$ to $33.1^\circ$ ) versus corresponding energy measured in a segment (both beam energies and carbon target) . . . . .	128
6.10. Maximum opening angle of the two $\alpha$ -particles produced by the breakup of $^8\text{Be}$ as a function of the $^8\text{Be}$ scattering angle and their maximum separation when detected by the DSSSD . . . . .	129
6.11. Spectrum of time-differences between the detection of a target-like recoil and a $\gamma$ -ray (546 MeV, carbon target) . . . . .	131
6.12. Illustration of the parameters defining the experimental setup and the reference frames used for its description . . . . .	133

6.13. Determination of parameters defining the setup geometry by optimization of the $\gamma$ -ray resolution after Doppler correction . . . . .	135
6.14. Determination of the carbon target thickness and of some setup-defining parameters . . . . .	136
6.15. Random subtracted, Doppler-corrected $\gamma$ -ray-spectrum showing the $2_1^+ \rightarrow 0_{gs}^+$ transition of $^{136}\text{Xe}$ before and after the "replay" of the experimental data . . . . .	138
6.16. Comparison of $\gamma$ -ray spectra for all reaction channels observed at 546 MeV beam energy using the thin carbon target . . . . .	140
6.17. Comparison of $\gamma$ -ray spectra for all reaction channels observed at 500 MeV beam energy using the thin carbon target . . . . .	140
6.18. Comparison of $\gamma$ -ray spectra for $^{140}\text{Ba}$ populated by $\alpha$ -transfer reactions at 500 MeV beam energy and 546 MeV . . . . .	141
6.19. $\gamma$ -ray spectrum for $^{140}\text{Ba}$ produced in an $\alpha$ -transfer reaction at 546 MeV beam energy . . . . .	142
6.20. Same as in Figure 6.19, but for 500 MeV beam energy . . . . .	142
6.21. Choice of the widths $\Delta\theta_i$ of the bins of the experimental spectra in polar $\gamma$ -ray detection angle $\theta_\gamma$ . . . . .	147
6.22. Comparison of stopping powers calculated by SRIM to experimental data for stopping of xenon ions in various targets . . . . .	149
6.23. Comparison of stopping powers calculated by SRIM to experimental data for stopping of various ions in tantalum targets . . . . .	149
6.24. Detector response function for the angular bin centered at $\theta_\gamma = 137.5^\circ$	151
6.25. Fit to the data measured with 500 MeV beam energy and the thin carbon target, verifying the description of the experiment in APCAD .	152
6.26. Doppler-broadened $\gamma$ -ray lineshape of the 1313 keV $2_1^+ \rightarrow 0_1^+$ transition of $^{136}\text{Xe}$ observed at 546 MeV beam energy . . . . .	153
6.27. Same as in Figure 6.26, but for 546 MeV beam energy . . . . .	154
6.28. $\gamma$ -ray spectrum gated on the $2_1^+ \rightarrow 0_1^+$ transition of $^{136}\text{Xe}$ (546 MeV, carbon target) . . . . .	156
6.29. Two-dimensional Doppler-broadened lineshape of the $2_1^+ \rightarrow 0_1^+$ transition of $^{136}\text{Xe}$ observed with the composite target at 546 MeV beam energy and best fit . . . . .	157
6.30. Projection of some angular bins from Figure 6.29 . . . . .	158
6.31. Two-dimensional Doppler-broadened lineshape of the $3_1^- \rightarrow 2_1^+$ transition of $^{136}\text{Xe}$ observed with the composite target at 546 MeV beam energy and projection including best fit for some angular bins . . . .	159
6.32. Best fits to the Doppler-broadened $\gamma$ -ray lineshapes measured at 500 MeV beam energy for different assumptions on the target . . . .	160

6.33.Distance of closest approach between the centers of $^{12}\text{C}$ target and $^{136}\text{Xe}$ beam nuclei as a function of center-of-mass scattering angle for both beam energies and different conditions for "safe" Coulomb excitation . . . . .	166
6.34.Particle-gated $\gamma$ -ray spectrum measured with the thin carbon target at 546 MeV beam energy . . . . .	168
6.35.Same as in Figure 6.34, but for the run at 500 MeV beam energy and after the application of the "safe" Coulomb excitation criterion . . . .	168
6.36.Level scheme showing the excited states of $^{136}\text{Xe}$ considered in the "safe" Coulex analysis . . . . .	173
6.37.Differential cross section and excitation function for Coulomb excitation of a $2_1^+$ -state of $^{136}\text{Xe}$ at 2.7 MeV with a ground-state transition strength of 10 W.u. on a carbon target . . . . .	175
6.38.Previously measured values for the $2_1^+$ level lifetime of $^{136}\text{Xe}$ , plotted against the year of their publication . . . . .	177
6.39.Systematics of the $2_1^+$ -state in nuclei close to $^{136}\text{Xe}$ . . . . .	181
6.40.Same data as in Figure 6.39, but plotted against $N_\pi N_\nu$ . . . . .	182
6.41.Systematic of the $3_1^-$ -state in nuclei close to $^{136}\text{Xe}$ . . . . .	184
6.42.Single-particle energies for protons and neutrons relative to the $Z = 50$ and $N = 82$ shell closures of a $^{132}\text{Sn}$ core . . . . .	186
6.43.Energy of the $3_1^-$ and $3_2^-$ states of $N = 82$ isotones as a function of proton number $Z$ . . . . .	191
6.44.Energies of low-lying excited states in $N = 50$ isotones . . . . .	193
6.45.Sketch of the PreSPEC-AGATA setup and GSI's Fragment Separator .	195
6.46.Photograph of the targets for experiment S426 mounted in the PreSPEC-AGATA setup . . . . .	199
6.47.Peak shapes expected in experiment S426 . . . . .	200
6.48.Ratio of peak areas expected in experiment S426 from excitation in the two targets . . . . .	201
6.49.Simulation of the $\gamma$ -ray spectrum expected in experiment S426 including an estimated background . . . . .	203
6.50.Time structure of the $^{86}\text{Kr}$ beam extracted from SIS18 in experiment S426 with and without primary beam bunching, measured with the scintillator at the S2 focal plane of FRS . . . . .	206
6.51.Time structure of the $^{86}\text{Kr}$ beam and distribution of ion multiplicity per event in experiment S426, measured with CsI detectors of the downstream wall of LYCCA . . . . .	207
6.52. $\gamma$ -ray spectrum and target excitation observed in experiment S426 without Doppler correction . . . . .	209

6.53. Simulation of the $\gamma$ -ray spectrum expected in experiment S426 based on the amount of data taken and an optimistic estimate for the background level . . . . .	212
B.1. Definition of the geometry of a position-sensitive detector in APCAD .	232
B.2. Stopping matrix for an angular bin centered at $\theta_\gamma = 137.6^\circ$ from the analysis of LNL experiment 08.09 . . . . .	235
B.3. Average values of the 2 <sup>nd</sup> and 4 <sup>th</sup> Legendre polynomials $\overline{P_{(2,4),i}}(t_n)$ .	238
B.4. Typical detector response function for HPGe detectors . . . . .	242
B.5. Major steps in the calculation of a Doppler-broadened $\gamma$ -ray line-shape in APCAD . . . . .	243
B.6. Effect of the position of an ion $\vec{x}$ on the solid angle $\Omega_{det}(\vec{x})$ . . . . .	249
D.1. Energy spectrum measured in the rings of the DSSSD as a function of the particle scattering angle (546 MeV, DSAM target) . . . . .	253
D.2. Energy spectrum measured in the rings of the DSSSD as a function of the particle scattering angle showing the different reaction channels (500 MeV, DSAM target) . . . . .	253
D.3. Particle energy spectra and reaction channel gates for the runs at 546 MeV beam energy using the carbon target . . . . .	254
D.4. Particle energy spectra and reaction channel gates for the runs at 546 MeV beam energy using the layered target for DSAM measurements . . . . .	255
D.5. Particle energy spectra and reaction channel gates for the runs at 500 MeV beam energy using the carbon target . . . . .	256
D.6. Particle energy spectra and reaction channel gates for the runs at 500 MeV beam energy using the layered target for DSAM measurements . . . . .	257
D.7. Determination of parameters defining the setup geometry by optimization of the $\gamma$ -ray resolution after Doppler correction . . . . .	258
D.8. Determination of setup-defining parameters from the correct carbon target thickness . . . . .	259
D.9. Continuation of Figure D.8 . . . . .	260



---

# List of Tables

6.1. Experiment 09.08: Beam-target combinations and collected amount of data . . . . .	120
6.2. Parameters defining the setup geometry . . . . .	137
6.3. Intensities of transitions in $^{140}\text{Ba}$ relative to the $2_1^+ \rightarrow 0_{gs}^+$ transition .	143
6.4. Direct feeders of the $2_1^+$ -state of $^{136}\text{Xe}$ . . . . .	155
6.5. Results for the $2_1^+$ and $3_1^-$ level lifetimes of $^{136}\text{Xe}$ from the caDSAM analysis . . . . .	162
6.6. Minimum distance of closest approach for "safe" Coulomb excitation and corresponding scattering angles in the center-of-mass system (COM) and for the target-like recoil $^{12}\text{C}$ in the laboratory frame	167
6.7. Peak areas determined for the Coulex analysis of $^{136}\text{Xe}$ . . . . .	169
6.8. Reduced transition strengths determined for decays of $2_i^+$ -states of $^{136}\text{Xe}$ . . . . .	172
6.9. Reduced transition strengths determined for the decays of the $3_1^-$ -state of $^{136}\text{Xe}$ . . . . .	172
6.10. Limits on reduced transition strengths determined for decays of the $2_{4,5}^+$ -states of $^{136}\text{Xe}$ . . . . .	176
6.11. Comparison of transition strengths measured in this work with results from an NRF measurement and from microscopic calculations in the shell-model and in the QRPA . . . . .	180
6.12. Occupation numbers of protons in the $Z = 50 - 82$ major shell in some $N = 80$ and $N = 82$ isotones . . . . .	188



---

# List of publications

## Publications in refereed journals

R. Stegmann, C. Bauer, G. Rainovski, N. Pietralla, C. Stahl, S. Bönig, S. Ilieva, A. Blazhev, A. Damyanova, M. Danchev, K. Gladnishki, J. Jolie, R. Lutter, J. Pakarinen, D. Radeck, E. Rapisarda, P. Reiter, M. Scheck, B. Siebeck, T. Stora, P. Thöle, T. Thomas, M. Thürauf, M. J. Vermeulen, D. Voulot, N. Warr, F. Wenander, V. Werner and H. De Witte.

**Evolution of quadrupole collectivity in  $N = 80$  isotones toward the  $Z = 64$  subshell gap: The  $B(E2; 2_1^+ \rightarrow 0_1^+)$  value of  $^{142}\text{Sm}$ .**

*Phys. Rev. C* 91, 054326 (2015)

C. Stahl, N. Pietralla, G. Rainovski and M. Reese.

**Coulex-Multipolarimetry with relativistic heavy-ion beams.**

*Nucl. Instr. Meth. A* 770, 123 (2015).

A. Illana, A. Jungclaus, R. Orlandi, A. Perea, C. Bauer, J. A. Briz, J. L. Egido, R. Gernhäuser, J. Leske, D. Mücher, J. Pakarinen, N. Pietralla, M. Rajabali, T. R. Rodríguez, D. Seiler, C. Stahl, D. Voulot, F. Wenander, A. Blazhev, H. De Witte, P. Reiter, M. Seidlitz, B. Siebeck, M. J. Vermeulen and N. Warr.

**Low-velocity transient-field technique with radioactive ion beams:  $g$  factor of the first excited  $2^+$  state in  $^{72}\text{Zn}$ .**

*Phys. Rev. C* 89, 054316 (2014).

N. Warr, J. Van de Walle, M. Albers, F. Ames, B. Bastin, C. Bauer, V. Bildstein, A. Blazhev, S. Bönig, N. Bree, B. Bruyneel, P. Butler, J. Cederkäll, E. Clément, T. Collios, T. Davinson, H. De Witte, P. Delahaye, D. DiJulio, J. Diriken, J. Eberth, A. Ekström, J. Elseviers, S. Emhofer, D. Fedorov, V. Fedosseev, S. Franchoo, C. Fransen, L. Gaffney, J. Gerl, G. Georgiev, R. Gernhäuser, T. Grahn, D. Habs, H. Hess, A. Hurst, M. Huyse, O. Ivanov, J. Iwanicki, D. Jenkins, J. Jolie, N. Kesteloot, O. Kester, U. Köster, M. Krauth, T. Kröll, R. Krücken, M. Lauer, J. Leske, K. Lieb, R. Lutter, L. Maier, B. Marsh, D. Mücher, M. Münch, O. Niedermaier, J. Pakarinen, M. Pantea, G. Pascovici, N. Patronis, D. Pauwels, A. Petts, N. Pietralla, R. Raabe, E. Rapisarda, P. Reiter, A. Richter, O. Schaile, M. Scheck, H. Scheit, G. Schrieder, D. Schwalm, M. Seidlitz, M. Seliverstov, T. Sieber, H. Simon, K.-H. Speidel, C. Stahl,

---

I. Stefanescu, P. Thirof, H.-G. Thomas, M. Thürauf, P. Van Duppen, D. Voulot, R. Wadsworth, G. Walter, D. Weißhaar, F. Wenander, A. Wiens, K. Wimmer, B. Wolf, P. Woods, K. Wrzosek-Lipska and K. Zell.

**The miniball spectrometer.**

*Eur. Phys. J. A* 49, 40 (2013).

C. Bauer, G. Rainovski, N. Pietralla, D. Bianco, A. Blazhev, T. Bloch, S. Bönig, A. Damyanova, M. Danchev, K. A. Gladnishki, T. Kröll, J. Leske, N. Lo Iudice, T. Möller, K. Moschner, J. Pakarinen, P. Reiter, M. Scheck, M. Seidlitz, B. Siebeck, C. Stahl, R. Stegmann, T. Stora, C. Stoyanov, D. Tarpanov, M. J. Vermeulen, D. Voulot, N. Warr, F. Wenander, V. Werner, and H. De Witte.

**Local suppression of collectivity in the  $N = 80$  isotones at the  $Z = 58$  subshell closure.**

*Phys. Rev. C* 88, 021302(R) (2013).

C. Stahl, J. Leske, N. Pietralla, P. R. John, G. Rainovski, J. Gerl, I. Kojouharov, and H. Schaffner.

**Identification of the proton  $2p_{1/2} \rightarrow 2p_{3/2}$   $M1$  spin-flip transition in  $^{87}\text{Rb}$ .**

*Phys. Rev. C* 87, 037302 (2013).

C. Bauer, T. Behrens, V. Bildstein, A. Blazhev, B. Bruyneel, J. Butterworth, E. Clément, L. Coquard, J. L. Egido, A. Ekström, C. R. Fitzpatrick, C. Fransen, R. Gernhäuser, D. Habs, H. Hess, J. Leske, T. Kröll, R. Krücken, R. Lutter, P. Marley, T. Möller, T. Otsuka, N. Patronis, A. Petts, N. Pietralla, T. R. Rodríguez, N. Shimizu, C. Stahl, I. Stefanescu, T. Stora, P. G. Thirof, D. Voulot, J. van de Walle, N. Warr, F. Wenander, and A. Wiens.

**Prolate shape of  $^{140}\text{Ba}$  from a first combined Doppler-shift and Coulomb-excitation measurement at the REX-ISOLDE facility.**

*Phys. Rev. C* 86, 034310 (2012).

S. Akkoyun, A. Algora, B. Alikhani, F. Ameil, G. De Angelis, L. Arnold, A. Astier, A. Ataç, Y. Aubert, C. Aufranc, et al. [AGATA collaboration]

**Agata - advanced gamma tracking array.**

*Nucl. Instr. Meth. A* 668, 26 (2012).

---

## Publications in conference proceedings

N. Pietralla, G. Rainovski, M. Reese, C. Stahl, T. Beck, J. Beller, C. Romig, and V. Werner.

**Progress on M1 research.**

*Journal of Physics: Conference Series 580, 012015 (2015).*

T. Möller, C. Bauer, R. V. F. Janssens, C. J. Lister, E. A. McCutchan, N. Pietralla, G. Rainovski, D. Seweryniak, C. Stahl, and S. Zhu.

**Projectile coulomb excitation of the nucleus  $^{194}\text{Pt}$ .**

*Journal of Physics: Conference Series 366, 012034 (2012).*

C. Bauer, G. Guastalla, J. Leske, O. Möller, T. Möller, J. Pakarinen, N. Pietralla, G. Rainovski, E. Rapisarda, D. Seweryniak, C. Stahl, R. Stegmann, J. Wiederhold and S. Zhu.

**Level lifetimes and quadrupole moments from coulomb excitation in the Ba chain and the  $N = 80$  isotones.**

*EPJ Web of Conferences 38, 10003 (2012).*



---

# Acknowledgements

Zwar ist eine Dissertationsschrift am Ende das Werk eines Einzelnen, eine wissenschaftliche Arbeit ist jedoch eigentlich immer das Ergebnis der Zusammenarbeit von Vielen und auch von gegenseitiger Unterstützung. Zum Glück trifft letzteres auch in meinem Fall zu, denn ohne das Zutun Anderer wäre diese Arbeit so sicherlich nicht zustande gekommen.

An erster Stelle danke ich meinen Eltern Petra und Joachim für ihre ständige, liebevolle und bedingungslose Unterstützung. Gleichzeitig möchte ich mich bei meiner Mutter für die Unannehmlichkeit entschuldigen, Bekannten und Freunden nicht erklären zu können was ihre Kinder eigentlich tun. Nächstes Mal werde ich Arzt. Oder Ingenieur. Vielleicht. ;-)

Auch meine Schwester Julia und meine Lebensgefährtin Annika sind mir stets eine große Unterstützung, wofür ich ihnen sehr dankbar bin.

Meine Begeisterung für die experimentelle Kernstrukturphysik verdanke ich ohne Zweifel Jörg Leske, der mich bereits während meines Bachelorstudiums immer wieder zu anspruchsvollen Strahlzeiten mitgenommen hat. Manche Dinge lernt man einfach nicht im Studium, aus Veröffentlichungen oder Vorträgen, und gerade für diese "Lehrstunden" sowie für seine unendliche Geduld mit mir bin ich Jörg zu großem Dank verpflichtet.

Dass ich meine fachliche Begeisterung, meine Forschungsinteressen und meine Ideen immer frei ausleben konnte verdanke ich "meinem" Professor, Norbert Pietralla. Für diese sicher nicht selbstverständlichen Arbeitsbedingungen und für seine stete Bereitschaft, physikalische Fragen auch dann zu diskutieren, wenn er dafür eigentlich keine Zeit hat, danke ich ihm sehr herzlich.

Das Durchführen kernphysikalischer Experimente war und ist für mich das "Highlight" des Berufs des Kernphysikers. Dass diese arbeitsintensiven Strahlzeiten immer wieder spannend und lehrreich aber auch interessant und unterhaltsam sind ist das Verdienst der vielen tollen Kollegen, mit denen ich zusammenarbeiten durfte. Hierfür danke ich Christopher Bauer, Dino Bazzacco, Sabine Bönig, Mike Bentley, Lililana Cortes, Andrea Gottardo, Tobias Habermann, Andrea Jungclauss, Marc Lettmann, Caterina Michelagnoli, Daniele Mengoni, Thomas Möller,

---

Kevin Moschner, Daniel Napoli, Riccardo Orlandi, Georgi Rainovski, Damian Ralet, Francesco Recchia, Dirk Rudolph, Michael Reese, Henning Schaffner, Jose Javier Valiente-Dobon, Oliver Wieland, Shaofei Zhu und den vielen Anderen, die ich grundlos vergessen habe.

Für zahllose Diskussionen und dafür, die Hoffnung nicht aufgegeben zu haben mir nicht doch noch zumindest etwas Physik beibringen zu können, danke ich Jörg Leske, Marcus Scheck, Georgi Rainovski, Volker Werner, Oliver Möller, Vladimir Ponomarev und natürlich Norbert Pietralla.

Für die stets freundliche und aufgeschlossene Arbeitsatmosphäre bin ich meinen Kollegen aus dem Büro 210, Michael Reese, Christoph Krämer und Christopher Walz sowie der gesamten Arbeitsgruppe (und natürlich auch den anderen Arbeitsgruppen am IKP) dankbar.

---

# Lebenslauf

## Persönliche Daten

Name	Christian Stahl
Geburtsdatum	27.02.1985
Geburtsort	Hadamer
Staatsangehörigkeit	deutsch
Familienstand	ledig

## Schulausbildung

1991 - 1995	Grundschule Offheim
1995 - 2004	Tilemannschule Limburg
2004	Abitur

## Zivildienst

2004 - 2005	Deutsches Rotes Kreuz, Limburg Abteilung "Mobiler sozialer Hilfsdienst"
-------------	--

## Hochschulausbildung

2005 - 2008	TU Darmstadt B.Sc. Physik <i>Entwicklung und Konstruktion eines ortsauflösenden Detektor- systems zur Analyse radioaktiver Schwerionenstrahlen</i>
08/2008 - 07/2009	Hong Kong University of Science and Technology Auslandsstudium
2008 - 2011	TU Darmstadt M.Sc. Physik <i>Winkel-kontinuierliches DSAM: Lebensdauer-Messungen mit ortssensitiven Detektorsystemen</i>
seit November 2011	TU Darmstadt Doktorand, wissenschaftlicher Mitarbeiter AG Pietralla



---

# Erklärung zur Dissertation

Hiermit versichere ich, die vorliegende Dissertation ohne Hilfe Dritter nur mit den angegebenen Quellen und Hilfsmitteln angefertigt zu haben. Alle Stellen, die aus Quellen entnommen wurden, sind als solche kenntlich gemacht. Diese Arbeit hat in gleicher oder ähnlicher Form noch keiner Prüfungsbehörde vorgelegen.

Darmstadt, den 30. Juni 2015

---

(Christian Stahl)

